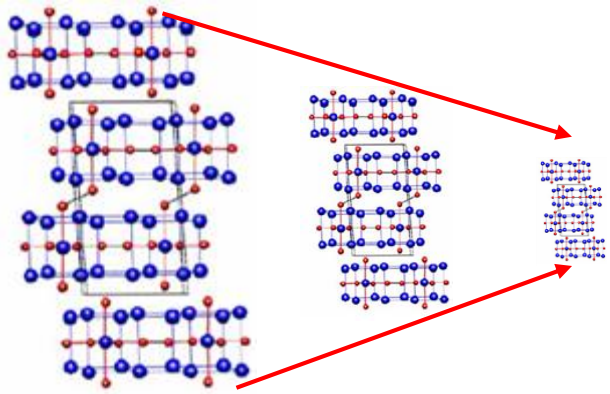

Studies on the multifunctional $Gd_5(Si,Ge)_4$ compounds: from the bulk to the micro and nano scales

Vivian Andrade

MAP-Fis Doctoral Program in Physics

Department of Physics and Astronomy

Faculty of Sciences

University of Porto

2019

Supervisor

Prof. João Pedro de Esteves de Araújo, FCUP

Co-supervisor

Prof. Mario de Souza Reis Jr, IF-UFF

Institutions involved in this thesis:

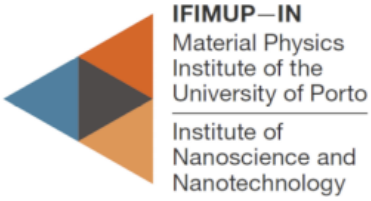

Universidade do Minho
Departamento de Física

INSTITUTO DE FÍSICA
Universidade Federal Fluminense

CBPF
Centro Brasileiro de
Pesquisas Físicas

ESRF
The European Synchrotron

Funded by:

"In this possibly terminal phase of human existence, democracy and freedom are more than just ideals to be valued - they may be essential to survival."

Noam Chomsky

Acknowledgements

This work is the result of a four years journey that was developed at the Multifunctional Magnetic Materials and Nanostructures group of IFIMUP-IN at Porto University in collaboration with the Physics Department of Minho University in Braga, Instituto de Física da Universidade Federal Fluminense (IF-UFF), the LABNANO of Centro Brasileiro de Pesquisas Físicas (CBPF) and the Laboratorio de Magnetismo e Baixas Temperaturas do Instituto de Física Gleb-Wataguin of UNICAMP from Brazil.

More importantly, I thanks the Conselho Nacional de Desenvolvimento Científico e Tecnológico (CNPq) for my scolarship through the *Ciência sem Fronteira* (CsF) program created by President Dilma Roussef and Fernando Haddad that made this PhD project possible.

I would like to previously thanks everyone that somehow was involved in this work and gave me support to finish this PhD directly or indirectly. You were all important for my personal growth and to increase my confidence as a scientist. Even if you're not in this list, know that I thank you very much!

To my supervisor Professor João Pedro Araújo, that readily accepted me to work at IFIMUP, depositing trust in me for the development of this work. I will always be grateful for the opportunity to work with such a wonderful person that has the ability to pass the knowledge of science with the heart and joy, inspiring everyone around it.

A particular thanks to my co-supervisor Professor Mario Reis for the support, friendship and for the long hours of conversation that have show to me how the scientific life can be hard but still worth it.

I would like to thanks Professor Bernardo Almeida to provide the PLD system for the nanoparticle production and for the contagious joy every time that we were working.

To Dr. João Horta Belo a warm thanks for the patience during all of these years to pass me your knowledge on scientific life. I hope that we can keep working towards the construction of a particle size phase diagram for $Gd_5(Si,Ge)_4$ compounds.

To Dr. Raquel Checca a thanks from my heart once your deep knowledge of PLD was critical for the development of this work. Thank you for the patience during my angry moments and to always have a word to calm me down.

To Eng. Francisco for the efficiency on solving my problems with great results and cheerful talks. Your contribution was essential for this work.

To Professor André Pereira, I would like to thanks for the introduction to IFIMUP

research and helping me at my early stages. Without your support, this work would not be possible.

To Dr. Nathalie Barroca thank you so much for allowing me to join the work on the magnetic composites that composes two chapters of this work. It was a hard task, but the results and analysis were a fun puzzle to complete at the end.

A kind thanks to Professor Daniel Bessa for the encouraging conversations and discussions not only about work but also about how to work.

I would like to thanks all the staff from Physics and Astronomy Department: Filomena, Armanda and Florbela for the patience to solve my problems; D. Isabel for the friendship and also patience; Paulo and Felicidade for the daily happy and joy; Pedro and Hernani for always rescuing me on my technological related problems.

To all of my IFIMUP colleagues I would like to thank for the great moments along these years, in particular: to Catarina Dias and Rui Vilarinho for the friendship, advices, python codes, deconvoluted FTIR specs, recipes and for contributing with my environmental conscience. I will have this knowledge forever! My countrywoman and friend Suellen Moraes for the long hours talk and laugh that was essential during this time! The wise Gonçalo Oliveira for always having the latest software versions. I would like also to thank you for the advices and funny talks concerning this academic world that were fundamental for my growth. To Celia Souza and David Navas for being good ears for my struggles during these years, I will be always grateful for this friendship. To Joel Pulga and Bernardo Bordalo, that were my first great friends at IFIMUP, being essential for my adaptation at the group, I would like to thank you for all the laugh and great talks. To Ana Pires for the help during my adaptation time at the lab and for the contamination of joy every time that you are present. To Arlete for showing me how to have strength and persistence on the academic life.

To my colleagues from UNICAMP: Marcos, Kleber, Fanny and Alex for all the help in this final stages of my research, without you guys the finalization of this work would not be possible.

I would like to give a special thanks to my great friends Wagner, Alice, Denise, Marcelo Muniz, Eduardo (mudinho), Renan, Fulapa, Fabiana, Juliana, Caroline, Ana, Massa, Nininha, Jacqueline, Clarinha, Thais Dalloz, Thais Fox and Alana for supporting me since the beginning and for taking care of me when I most needed a comfort to not go crazy! I will be always so grateful to have you all in my life.

Finally, this work is dedicated to my mother, sisters and niece because without all of your love and trust, I would never have the strength to believe that this work would be possible.

Abstract

Recent reports on energy consumption worldwide have shown an increase on the use of renewable sources with an increment of emissions from fossil fuels[1]. It has been evaluated in 2018 that $\sim$25-30% of spent electricity is employed to refrigeration systems and this value is expected to increase along the coming years due to global warming[2,3,15]. In this sense, the development of alternative heating/refrigeration technologies - as well for energy harvesting - is one of the main challenges for industries and, of course, for scientific community. Among the most promising substitutes for conventional gas systems, is thermoelectric, thermoacustic and magnetocaloric refrigeration devices that have been intensively investigated to improve the efficiency during operation[4]. Material scientists have turn their attention mainly to intermetallic compounds that can display multiple ferroic orderings. The larger responses are observed in materials presenting a first order transitions. For these systems, the strong spin-lattice coupling lead to great volume changes during transition that contributes to the thermodynamic parameters variations. A recent research avenue is the combination of multiple fields to induce more than one caloric responses - the so-called multicaloric effect[5]. The effects are classified by the applied field nature like: mechanocaloric due to pressure or tension, electrocaloric as a response of an applied electrical field and magnetocaloric when a magnetic field is applied. Among these promising materials, $Gd_5(Si,Ge)_4$ family compound presents a giant magnetocaloric effect and a great barocaloric response due to its volumetric change during transition[108**?**]. In this sense, the main interest of this PhD work relies on the magnetocaloric effect (MCE) of multifunctional $Gd_5(Si,Ge)_4$ family compounds under different conformations. An evaluation on crystallographic, morphological and magnetic properties was performed on produced samples in three dimensional scales: *i)* chemical substitution in a bulk material, *ii)* fragmentation to the microscale and implementation on polymeric matrices and *iii)* nanostructuring using pulsed laser deposition (PLD).

For the macrometric system, a study on the fundamental properties of $Gd_{5-x}La_xSi_{1.8}Ge_{2.2}$ pseudo-binary compounds with x = 1, 2, 3, 4 and 5 was performed by means of X-ray powder diffraction and magnetic measurements. An evolution from a monoclinic $Gd_5Si_2Ge_2$-type to a tetragonal Zr_5Si_4-type structure, with the addition of La, was observed, finding that the tetragonal phase is stable for x$\geq$2. A monotonic expansion of the unit cell volume with a rate of 28 $Å^3$/La was achieved by increasing the content

of the non-magnetic La ions in the system influence significantly the overall magnetic behaviour. For instance, T_C decreases in a rate of dT_C/dx = -47.8 K/La; and a considerable hysteresis reduction was observed as a result of the change on the nature of the phase transition from a first to a second-order one. Hence, these results reveal the impact of a non-magnetic La substitution on both magnetic and crystallographic properties of this family.

Aiming practical applications of brittle intermetallic materials, a microstructuring through sieving the alloys can reduce these mechanical wear effects after several cycles. For this purpose, we have chosen a Si-rich composition that presents an orthorhombic-I structure with high T_C and a broader working range temperature for the MCE. The performed characterizations have revealed an increase on the detection of secondary monoclinic phase, with a first order magnetic transition at low temperature. After a complete analysis, the processed magnetic materials were implemented in into a flexible poly(methyl methacrylate) (PMMA) thermoplastic. Besides the gain in mechanical properties, the use of PMMA also reduces the powder degradation and oxidation during operation. Different weight fractions of $Gd_5Si_{2.4}Ge_{1.6}$ magnetic material was implemented onto PMMA to perform a study on the structural, magnetic and magnetocaloric effects rising from this blending. The micrometric films were produced through a solvent casting method, presenting a close to homogeneous grains distribution along the polymer surface. Although PMMA does not have influence the magnetic nature of microparticles main phase, a conversion on the amount of secondary monoclinic phase occurs for all produced composite samples is observed. As a consequence, a weakening on the effect of secondary phases on the micropowder magnetocaloric response is observed as a result of hydrostatic pressure arising from the difference between the thermal expansion coefficients of matrix and filler.

Furthermore, we performed a thorough investigation of a multiferroic composite made of small amounts of magnetocaloric and magnetostrictive $Gd_5Si_{2.4}Ge_{1.6}$ microparticles blended into a piezo- and pyroelectric polyvinylidene fluorine (PVDF) matrix. The coupling between electric, magnetic and elastic orders in multiferroic materials is an emerging field on materials science aiming application as alternative solid-state cooling technologies and actuators. Using the same solvent casting technique, it was observed that the increase of filler content from 2 to 12 weight fraction improves the formation and stabilization of PVDF electroactive phases. This effect greatly contributes to the magnetoelectric (ME) coupling, with the ME-coefficient α_{ME} increasing from 0.3 V/cm.Oe to 2.2 V/cm.Oe by increasing the amount of magnetic material. In addition, magnetic measurements revealed that the ME-coupling influence on the magnetocaloric effect with a contribution from the electroactive polymer, leading to a multicaloric effect.

Recent developments on the production of $Gd_5(Si,Ge)_4$ magnetocaloric compounds with reduced nanometric dimension through laser ablation techniques have shown their potential for applications in sensors/actuators and hyperthermia[6]. Here, we present nanoparticles of $Gd_5(Si_xGe_{1-x})_4$ with x = 0.45, 0.55 and 0.60 resulted from ablating the

alloys with an Excimer KrF laser (248 nm) in a presence of an inert Ar gas. The collection of the product of this gas-phase synthesis performed with the substrate at 1 cm distance from the target allows a better collection of the nanoparticles. This procedure resulted in nanoparticles (NPs) with a narrow particle size distribution and well developed crystalline structure without additional phases, observed through TEM and XRD analysis. For x = 0.60 and 0.55 nanostructures, there is no change on their crystallographic structures when compared to the bulk counterpart when prepared as nanoparticles of 26 nm average diameter. On the other hand, the reduction of size below 30 nm, for the x = 0.45 NPs, lead to a reduction of 1.2% on the unit cell volume due to a structural change from a monoclinic to an orthorhombic one. Consequently, there is a shift on the Tc in 50 K with a second order magnetic transition associated. Synchrothron XRD measurements were performed and the *LeBail* calculations for the x = 0.45 nanostructure indicate a negative thermal expansion (NTE) around the magnetic transition temperature. The reduction of particle size for all produced composition lead to a broader working range temperature for the magnetocaloric effect, which increases the range for application in micro devices.

In summary, from the results at the macroscale, we have observed that magnetic dilution of Gd lead to changes in the crystallographic structure and, consequently, in the order of the system magnetic transition. By scaling down the particle size to the microscale, there is an increase on the amount of detected secondary deformed monoclinic phases with a second order magnetic transition. By dispersing the obtained micropowder into polymeric matrices, interface interactions generate pressure on the grains surface, reducing the MCE response from the M-phase. For electroactive PVDF, due to its piezoelectricity, there is a magnetoelectric coupling between matrix and filler that increases its ME-response for larger powders content due to the magnetic material magnetostriction. Finally, at the nanometric scale, there is the formation of an O(I) structure at room temperature for all produced compositions with reductions on unit cell volume and magnetocaloric response. Advanced characterization using Synchrotron measurements points to a conservation on the structural transitions at the nanometric scale, pointing to important effect: the negative thermal expansion. Initial analysis on the XRD patterns as a function of temperatures indicates the conservation of a structural transition in the particle size of $\sim$ 30 nm for the composition presenting a FOMT when produced as a bulk. Furthermore, the particle size reductions for all NPs are strongly related with the Si/Ge ratio where the unit cell volume reductions are proportional to the composition compressibility values. Interestingly, these observations are more evident for the nanoparticles produced by laser ablation processes, suggesting a similar mechanism on particle formation for $Gd_5(Si,Ge)_4$ compounds.

Resumo

Relatórios recentes sobre o consumo de energia em todo o mundo mostraram um aumento no uso de fontes renováveis com um incremento de emissões de combustíveis fósseis[1]. Foi avaliado em 2018 que $\sim$ 25-30% da eletricidade gasta é empregada em sistemas de refrigeração e este valor deve aumentar nos próximos anos devido ao aquecimento global[2,3,15]. Nesse sentido, o desenvolvimento de tecnologias alternativas de aquecimento/refrigeração - assim como a coleta de energia - é um dos principais desafios para as indústrias e, é claro, para a comunidade científica. Entre os substitutos mais promissores para sistemas convencionais de gás, estão os dispositivos termoelétricos, termoacústicos e baseados em efeitos magnetocalóricos que foram intensamente investigados para melhorar a eficiência durante a operação[4]. Cientistas de materiais voltaram sua atenção principalmente para compostos intermetálicos que podem exibir múltiplas ordenaçes ferroicas. As maiores respostas são observadas em materiais que apresentam transiçes de primeira ordem. Para estes sistemas, o forte acoplamento spin-rede conduz a grandes mudanças de volume durante a transição que contribuem para as variaçes dos parâmetros termodinâmicos. Um caminho de pesquisa recente tem sido combinar vários campos para induzir mais de uma resposta calórica - o chamado efeito multicalórico[5]. Os efeitos são classificados pela natureza do campo aplicado como: mecanocalórico devido a pressão ou tensão, eletrocalórica como resposta de um campo elétrico aplicado e magnetocalórica quando um campo magnético é aplicado. Entre os possíveis materiais, os compostos da família $Gd_5(Si,Ge)_4$ apresenta o efeito magnetocalórico gigante e uma grande resposta barocalórica[108**?**]. Por conta disso, este trabalho de PhD tem como principal interesse o efeito magnetocalórico (MCE) de compostos multifuncionais da família $Gd_5(Si,Ge)_4$ sob diferentes conformaćes. Uma avaliação das propriedades cristalográficas, morfológicas e magnéticas foi realizada nas amostras produzidas em três escalas dimensionais: *i)* substituição química em um material em *bulk*, *ii)* fragmentação na microescala e implementação em matrizes poliméricas e *iii)* nanoestruturação usando deposição por laser pulsado (PLD).

Para o sistema macrométrico, um estudo sobre as propriedades fundamentais dos compostos pseudo-binários $Gd_{5-x}La_xSi_{1.8}Ge_{2.2}$ com x = 1, 2, 3, 4 e 5 foi realizado por meio de difração de raios X e medidas magnéticas. Uma evolução de um tipo monoclínico do tipo $Gd_5Si_2Ge_2$ para uma estrutura tetragonal do tipo Zr_5Si_4 com a adição de

La foi observada, descobrindo que a fase tetragonal é estável para x $\geq$ 2. Uma expansão monotônica do volume de célula unitária com uma taxa de 28 Å^3/ La foi alcançada aumentando o conteúdo dos íons La não-magnéticos no sistema, influenciando significativamente o comportamento magnético geral. Por exemplo, T_C diminui em uma taxa de dT_C/dx = -47.8 K/La; e uma considerável redução de histerese foi observada como resultado da mudança na natureza da transição de fase de uma primeira para uma segunda ordem. Assim, estes resultados revelam o impacto de uma substituição não-magnética do La em ambas as propriedades magnéticas e cristalográficas desta família.

Visando aplicaçes práticas de materiais intermetálicos frágeis, uma microestrutura através do peneiramento das ligas pode reduzir os efeitos mecânicos do desgaste após vários ciclos. As caracterizações realizadas revelaram um aumento na detecção da fase monoclínica secundária, com uma transição magnética de primeira ordem a baixa temperatura. Após uma análise completa, os materiais magnéticos processados foram implementados em um termoplástico flexível. Assim, além do ganho nas propriedades mecânicas, há uma redução na degradação do filler e na oxidação durante a operação devido à camada plástica impermeável. O efeito da mistura magnetocalórica $Gd_5Si_{2.4}Ge_{1.6}$ com 3.4 μm de diâmetro médio em diferentes frações de peso em poli (metacrilato de metila) (PMMA). Filmes micrométricos com uma distribuição de grãos próximos à homogênea ao longo da superfície do polímero foram produzidos através de um método de fundição com solvente. Embora o PMMA não tenha influência na natureza magnética da fase principal das micropartículas, observa-se uma redução na quantidade de fase monoclínica secundária para todas as amostras compostas produzidas. Como consequência, observa-se um enfraquecimento do efeito das fases secundárias na resposta magnetocalórica do micropômero como resultado da pressão hidrostática decorrente da diferença entre os coeficientes de dilatação térmica da matriz e do material magnético.

O acoplamento entre ordens elétricas, magnéticas e elásticas em materiais multiferróicos é um campo emergente na ciência de materiais visando a aplicação como tecnologias de resfriamento e atuadores de estado sólido alternativos. Neste sentido, desenvolvemos uma investigação completa de um compósito multiferróico feito de pequenas quantidades de $Gd_5Si_{2.4}Ge_{1.6}$ micropartículas magnetocalóricas e magnetostritivas misturadas em um fluoreto de polivinilideno (PVDF) que é uma matriz piezo- e piroelétrico . Usando uma técnica simples de fundição de solvente, a quantidade de fases eletroativas no PVDF aumenta quando o conteúdo da carga aumenta de 2 para 12 frações de peso sem tratamentos adicionais. Este efeito contribui grandemente para o acoplamento magnetoelétrico (ME), com o coeficiente ME α_{ME} aumentando de 0.3 V/cm.Oe para 2.2 V/cm.Oe, aumentando a quantidade de material magnético. Além disso, as medidas magnéticas revelaram que o acoplamento ME influencia no efeito magnetocalórico com uma contribuição do polímero eletroativo, levando a um efeito multicalórico.

Desenvolvimentos recentes na produção de compostos magnetocalóricos com dimensão nanométrica reduzida através de técnicas de ablação a laser mostraram seu potencial para aplicações em sensores/atuadores e hipertermia[6]. Aqui, apresentamos nanopartículas de $Gd_5(Si,Ge)_4$ com x = 0.45, 0.55 e 0.60 resultado da ablação das ligas com um laser Excimer KrF (248 nm) na presença de um gás Ar inerte. A coleta do produto dessa síntese de fase gasosa realizada com o substrato a 1 cm de distância do alvo leva a um grande volume de amostra. Este procedimento resultou em nanopartículas (NPs) com uma distribuição de tamanho de partícula estreita e estrutura cristalina bem desenvolvida sem fases adicionais, como observado através de análise de TEM e XRD. Para x = 0.60 e 0.55 nanoestruturas, não há alteração em suas estruturas cristalográficas quando comparadas com a sua amostra em volume quando preparadas como nanopartículas com 26 nm de diâmetro médio. Por outro lado, a redução do tamanho abaixo de 30 nm, para os x = 0.45 NPs, leva a uma redução de 2.3 % no volume unitário celular. Consequentemente, há uma mudança no Tc em 50 K com uma transição magnética de segunda ordem associada.

Em resumo, a partir dos resultados na macroescala, observamos que a diluição magnética de Gd leva a alterações na estrutura cristalográfica e, consequentemente, na ordem da transição magnética do sistema. Reduzindo o tamanho da partícula para a microescala, há um aumento na quantidade de fases monoclínicas deformadas secundárias detectadas com uma transição magnética de segunda ordem. Ao dispersar o micropó obtido em matrizes poliméricas, interações de interface geram pressão na superfície dos grãos, reduzindo a resposta MCE da fase M. Para o PVDF eletroativo, devido a sua piezoeletricidade, existe um acoplamento magnetoelétrico entre a matriz e o preenchedor. Finalmente, na escala nanométrica, há a formação de uma estrutura O (I) à temperatura ambiente para todas as composições produzidas com reduções no volume da célula unitária e na resposta magnetocalórica. A caracterização avançada utilizando medidas síncrotron aponta para uma conservação nas transições estruturais em escala nanométrica, apontando para um importante e importante efeito: a expansão térmica negativa.

Contents

List of Figures

List of Tables

List of Abbreviation

Acronyms/Abbreviations

AMR - Active Magnetic Regenerator cycle

BCE - Barocaloric Effect

eCE - Elastocaloric Effect

FC - Field-Cooled Protocol

FFT - Fast Fourier Transform

FM - Ferromagnetic ordering

FOMT - First Order Magnetic Transition

FWHM - Full width at half maximum

GMCE - Giant Magnetocaloric Effect

GWP - Global Warming Potential

HR-TEM - High Resolution - Transmission Electronic Microscopy

MCE - Magnetocaloric Effect

MCM - Magnetocaloric material

MR - Magnetic Refrigeration

M - Tetragonal crystallographic structure

NPs - Nanoparticles

O(I) - Orthorhombic-I crystallographic structure

O(II) - Orthorhombic-II crytallographic tructure

ODP - Ozone Depletion Potential

OECD - Organization for Economic Co-operation and Development

PLD - Pulsed Laser Deposition

PM - Paramagnetic ordering

RBMR - Rotating Bed Magnetic Refrigerator

RCP - Refrigerant Cooling Power

RT - Room Temperature

SAED - Selected Area Electron Diffraction

SEM - Scanning Electronic Microscopy

SOMT - Second Order Magnetic Transition

tCE - Torsiocaloric Effect

TEM - Transmission Electronic Microscopy

T - Tetragonal crystallographic structure

XRD - X-ray Diffraction

ZFC - Zero-Fied-Cooled Protocol

Materials

CFC - Chlorofluorocarbon Halometane

GSG - $Gd_5(Si,Ge)_4$ family

HFC - Hydrochlorocarbon

HFO - Hydro-fluoro-olefins

PMN-PT - Pb-Mg-Nb/Pb-Ti-O ferroelectric substrate

PVDF - Poly(vinilidene) Fluorine

PZT - Pb[Zr_x Ti_{1-x}]O_3 with 0<x<1

RE - Rare Earth Elements

SMA - Shape memory alloys

Variables

α_{ij}	Cross-coupling thermodynamic coefficient
χ	Magnetic Susceptibility
ΔS_{iso}	Isothermal entropy change
ΔT_{ad}	Adiabatic temperature change
μ_B	Bohr Magnetron
μ_{eff}	Effective magnetic moment
μ_{sat}	Saturation magnetization
σ	Mechanical Stress
σ_{ij}	Cauchy stress tensor
θ_P	Paramagnetic Curie Temperature
B_{Landau}	B-parameter from Landau expansion and Banerjee criteria
C	Curie Constant
c_x	Specific heat under a constant field x
F	Free Gibbs Energy
Q	System Heat
S	Entropy
T	Temperature
T_C	Curie temperature
T_g	Glass temperature transition
U	Internal energy of a system
X_i	Conjugated thermodynamic quantity to x_i
x_i	Generalized force/field
E	Electric Field
H	Magnetic Field
M	Magnetization
P	Electric Polarization

Chapter 1

Thesis Outline

For several centuries, humanity has been pursuing ways to improve cooling systems for food conservation and beverage production, as shown on the timeline in Fig. 1.1. Until the 19^{th} century, the systems were mostly based on natural refrigeration using ice and salt solutions. Through history, there were four basic methods for this: ice harvesting, dating from 1000 B.C. in ancient China[7], conserving the ice from the winter to use at hottest seasons into storage pints covered by insulator materials (like grass, mud, clay, and leaves), through nocturnal evaporation cooling and using salt solutions[8]. Nocturnal cooling is based on the water heat loss by radiation during a clear night sky while evaporating, whereas salt solution techniques take advantage of the endothermic processes of water[9]. The first ice houses for food storage, called Yakhchal, were developed by the Persians for storing ice from winter underground in the arid desert[10]. Its use started around 400 B.C. with the architecture depicted in Fig. 1.1, where a cone-like roof up to 20 meters in height was built using a special mud called *sarooj* made of sand, clay, egg whites, lime, goat hair and ash. The Persian method became popular worldwide in the 1600s when the ice to fill the pits was transported from cold regions in the northern hemisphere[11].

Although these methods were highly profitable, the difficulties of the ice harvesting business boosted the search for alternative cooling systems. The first demonstration of artificial cold production using ether, performed by William Cullen in 1748, was the starting point for the later developments on vapour compression refrigerator systems[12]. The most important event for the advancement of refrigeration technology was the formulation of thermodynamic principles; in particular, the second law formulated by Carnot in 1824. Ten years later, Jacob Perkins patented the first practical refrigerator based on the cycle of ether compression and, for this reason, he is considered as the 'father of refrigeration'. With the advent of electricity at early 20^{th} century, the domestic refrigerators began to be produced on a large scale using hazardous and toxic refrigerant gases such as ammonia, dichloromethane and sulphur dioxide. To reduce the danger of domestic refrigerators, the halogens hydrocarbons - chlorofluorocarbon halometane (CFC) and dichlorodifluoromethane (Freon-R12) - started to be applied on

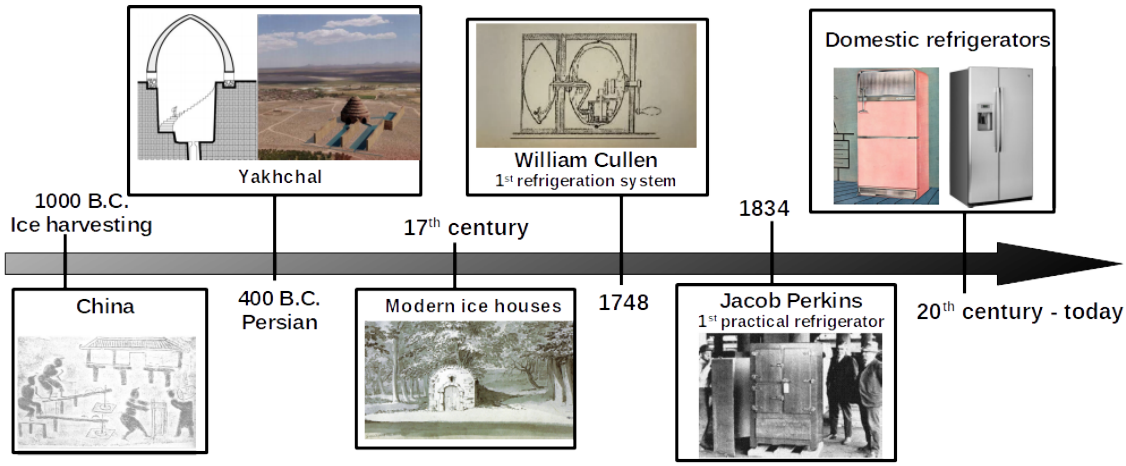

Figure 1.1: Timeline of the refrigeration's history starting from 1000 B.C. with ice harvesting in China[7]. Persians were the first to develop an ice storage house called Yakhchal ("yakh" means ice and "chal" means pit)[10] that became popular worldwide until the 17th century[11]. The first refrigeration system was patented by William Cullen in 1748 and only in 1834 was a practical refrigerator developed by Jacob Perkins[12]. With the advent of electricity the systems were updated to the known domestic refrigerators using vapour-compression technology.

this industry, highly contributing to the public acceptance and design optimization. A few decades later, it was found that these gases was harmful for the stratospheric ozone and the production of these gases were banned through the Montreal Protocol signed in 1987[13]. The alternative to overcome this issue was CFC replacement by hydrochlorocarbons (HFCs), which has 10% of the environmental impact of CFCs, for refrigerators and air conditioning designs. Although there are some substitute refrigerants with zero ozone depletion potential (ODP) and low global warming potential (GWP) - such as hydro-fluoro-olefins (HFO)[14] - the development of new cooling technologies are the best alternative to improve system efficiency.

Another issue for the large environmental impact of air conditioning and refrigeration is the energy consumption worldwide for food processing/storage, industrial applications and medical purposes (vaccines production/storage, blood banks, cryotherapies, etc)[2]. The energy generation to supply refrigeration systems contributes in 80% to atmosphere degradation while the direct emission of Freon, HFCs and CFCs are only 20%. A report of United Nations Enviroenment Programme from 2015 shows that about 25-30% of the worldwide electricity use goes to refrigeration, see Fig. 1.2(a)[15]. The demand for this sector is expected to increase due to global warming and population growth that will require more efficient cooling systems as well the use of renewable sources for power generation to supply it. According to the Statistical Review of World Energy from BP released in June of 2018, the primary energy consumption increased in 2.2% in 2017, being the largest growth since 2013[1]. Even though renewable power production grew 17% - more than the average values of the last 10 years - carbon emission rose 1.6% from energy utilization after 3 years with small or zero growth. The reason for this increase comes from the use of coal, mainly in India and China. Interest-

ingly, about 80% of contribution to this enlargement of energy consumption originates from countries under development, *i.e.*, non-OECD members, as can be seen on the chart in Fig. 1.2(b). As stated by Spencer Dale, the group chief economist of BP, the statistics from 2017 show a case of "two steps forward, one step back" in terms of the transition to long-term energy measures. Along with the pathway of renewable sources, the reduction on the environmental impact from refrigeration systems must be persecuted for more sustainable and efficient cooling devices.

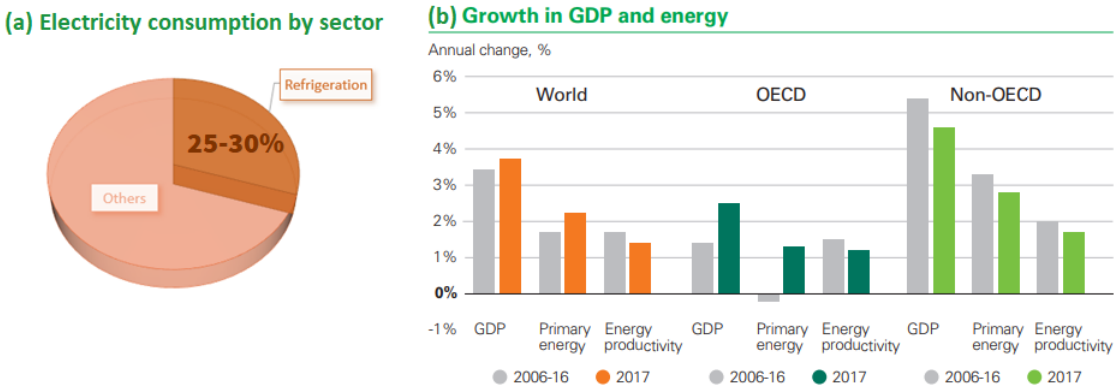

Figure 1.2: **(a)** Comparison of energy consumption worldwide where the refrigeration portion is 25-30%, adapted from Ref. 15. **(b)** The annual change trend of gross domestic product (GDP), energy consumption and production around the globe and for OECD and non-OECDs countries, obtained from Ref. 1, where the contribution for development nations are clearly larger than OECD ones.

In this framework, in order to prevent the use of hazardous and toxic gases, one of the approaches to overcome the traditional vapour compression systems is solid-state technology[16]. Solid-state physics have great potential to be applied in heat pumps, air conditioning, power generation and storage systems[17]. The search for materials with large caloric effects near room temperature for the development of environmentally friendly and more efficient systems is still a matter for industries and the scientific community. Recently, studies on multiferroic materials have shown that the combination of different applied fields (mechanical stress, electric and magnetic field) - the so-called multicaloric effect - can improve the efficiency of device operation, has been a novel field of interest for research[5]. Among the possible alternative systems, the thermoelectric, thermoacustic and magnetic based technologies are the most promising to compete with the conventional cooling machines[4]. In particular, the magnetocaloric effect (MCE) based system are the ones with the most extensive number of studies and experimental evaluations, both in materials evaluation and prototype developments.

The first evidence of heat generated by magnetic fields in magnetic materials dates from 1860 with the work of Thomson. Through a basic thermodynamic approach, he deduced that this effect occurs around the magnetic transition temperatures. Later in 1880, Warburg associated the heat dissipation of Iron by hysteresis cycles; however, with no experimental evidence since the Curie temperature (T_C) of the iron is well above room temperature[18]. It was only in 1917 that the first experimental observation

of the MCE was performed by Weiss and Piccard in Nickel[19]. The first demonstration of a magnetic refrigeration system based on the MCE was performed by Giauque and McDougall in 1933. Using the adiabatic magnetization/demagnetization of paramagnetic Gd-based salt in a liquid helium bath, they were able to reach temperatures below 1 K using a solenoid producing 0.8 T of magnetic field. However, due to the low temperatures of gadolinium sulfate, there were no possible practical applications with the known materials. In 1935, pure gadolinium obtained through electrolysis enabled the first studies on its properties revealing a T_C around 293 K, low specific heat, high thermal conductivity, adiabatic temperature changes (ΔT_{ad}) of $\sim$10 K and isothermal entropy variation (ΔS_{iso}) of $\sim$10 J/kg K with applied magnetic fields up to 5 T[20,21]. The practical applications were demonstrated with Brown's work showing that is possible to use the MCE to produce substantial cooling effect near room temperature[22]. Using metallic Gd and a magnetic field created by superconducting magnets of 7 T, Brown reduced the temperature of the system from 319 K to 272 K. For this reason, Gd is considered the reference material for magnetic refrigeration. However, due to its high cost and scarcity, the attention has been turned to its alloys and other intermetallic compounds in the search for higher responses at room temperature aiming practical applications[18,23]. Among the range of appliance on the MCE materials are energy harvesting/conversion[24], sensors/actuators, biomedical applications - like drug delivery and hyperthermia for cancer treatment[25], lab-on-a-chip and integrated systems[26].

The first report on a Giant Magnetocaloric Effect (GMCE) was published in 1996 on the FeRh alloy with a ΔT_{ad} of 8 K at 308 K for an applied magnetic field of 2.5 T; but, it was later shown that the effect is irreversible, which deviates from applications on MR[27]. A year later, Pecharsky and Gschneidner discovered a reversible GMCE in $Gd_5Si_2Ge_2$ compound around room temperature[28]. The authors have reported an entropy variation of $\sim$20 J/kg.K for an adiabatically applied magnetic field of 5 T around 292 K. This trademark was the responsible event to renew the scientific community interest on MR development and boosted the studies on $R_5(Si,Ge)_4$ (R = rare earth elements) compounds[29]. The following extensive investigations revealed that such intense MCE response is due to the FOMT that rises from the strong coupling between structural and magnetic behaviour on the $Gd_5(Si,Ge)_4$ family compounds[30]. During the system transition from a ferro- to a paramagnetic state, there is a transformation in structure that leads to an increase in the unit cell volume that has great contribution on the MCE response. This important feature is also responsible for the observation of other exotic effects like a giant magnetoresistance[31] and colossal magnetostriction - that is about 10 times higher than observed on commercial Terfenol-D[29]. The change in structure is related to the connection/ruptures between the Si and Ge atoms on the unit cell. For this reason, the $Gd_5(Si,Ge)_4$ family compounds are extremely sensitive to chemical composition, pressure, temperature, applied magnetic field and, from recent reports, particle size[6,32–34]. Given these interesting and exotic features, it is possible to use multiple fields to induce caloric effects and tune the properties ac-

cording to the desired application, which is a new avenue for multicaloric materials[5]. It is well known that GMCE manifests on materials presenting a first order magnetic transition (FOMT) where the transition is discontinuous in a short temperature range and associated hysteresis which limit the magnetic refrigeration (MR) performance. On the other hand, second order magnetic transition (SOMT) materials present a broader working range temperature for the MCE with the net hysteresis but lower ΔS_{iso} and ΔT_{ad}. For engineering purposes, the magnetic material must fulfil a series of properties to improve efficiency, including: no thermal or magnetic hysteresis, broader working temperature, mechanical stability to increase the device life-time and low manufacturing costs for commercial viability[35,36]. Currently, together with the $Gd_5(Si,Ge)_4$ family compounds, $La(Fe,Si)_{13}$ and its hydrides[37], magnetic shape memory alloys (MSMA)[**?**] and high entropy alloys (HEAs)[38], more specifically the MnCoFePAs[39] are the top candidates presenting FOMT and, consequently, GMCE for practical applications on MR at room temperature[17]. Due to the high cost of rare-earth elements, MnCoFePAs and $La(Fe,Si)_{13}$ have received higher interest targeting commercial viability of magnetocaloric technology.

In parallel with the search for the best magnetic refrigerant, MR prototype development has encountered new challenges for device operation optimization. Recently, Franco *et al.* listed over 100 MR prototypes since Brown's first demonstration[17] and a recent report pointed to the main companies in the MR market[40] that promise a reduction of 40-50% on energy consumption. Among the requirements for efficiency enhancement, it is possible to mention higher rates of heat exchanger during operation, reduction of the intensity of required applied field for the MCE and chemical and mechanical stability to sustain long-time device operation[35]. Once MR technology requires a fluid (oil, water, ethanol solutions, etc) as a heat exchanger, the magnetic material can oxidise which diminishes the MCE response. Besides that, since most of the alloys are brittle, after hundreds of thousands of cycles, the sequential expansion/compression of the system volume due to the FOMT can lead to wear and, consequently, reduce the device lifetime. Some alternatives have been followed to overcome some of the mentioned drawbacks, such as microstructural designing by introducing porosity[41], chemical doping[42], implementation on polymeric matrices[43] and particle size reduction[44].

For instance, the substitution of Gd by low amounts of elements like Sc and Pb can enhance the spin-lattice coupling and, thus, promote the FOMT which enlarges the MCE response[45,46]. Mudryk *et al.* have shown through first principle calculations that the preferential occupation of the doping element is responsible for the change in the magnetostructural transition that can be used to tune the properties of the $Gd_5(Si,Ge)_4$ family compounds[47]. Polymer-bonded powder of magnetocaloric materials has already shown its potential to enhance heat transfer in 10% over the $LaFe_{11.6}Si_{1.4}$ bulk compound[43]. This procedure also enhances the durability and flexibility of the system when compared to the lifetime of the massive material[48]. When the combination is

performed using electroactive polymers, new product effects can arise from the interactions between the magnetic filler and matrix interfaces, called the magnetoelectric effect (ME)[49]. The ME can be used as power converter, as already demonstrated by Mechanical Engineering group of Texas University through the implementation of different concentrations of crushed $Gd_5Si_2Ge_2$ alloy onto piezoelectric poly(vinilidene fluoride) (PVDF). The electrical testing on the produced device has revealed an energy generation 1725 times higher than observed on pure PVDF on the system with 4 wt.% of filler[50]. Although the ME arises from the magnetostriction of $Gd_5(Si,Ge)_4$ compound, no evaluation on the ME coefficients were performed by the authors, putting into question how the amount of magnetic filler contributes to increase the power density of converted energy. The particle size can also have influence in the polymer-filler interface interactions once the micro/nanostructuring will affect the material magnetostrictive response[51]. Indeed, the reduction of dimensionality to the micro- and nanoscales can lead to the observation of novel effects and, in the case of the MCE, can lead to a shift on the magnetic transition order from a first to a second one, leading to a gain in the working range temperature[44]. However, it can diminish the intensity of the required applied magnetic field to promote the magnetostructural transition, as shown by Moore *et al.* through the fragmentation of Gd_5Ge_4 alloy into pieces with $\sim$100 μm. As concluded by the authors, this effect is due to the reduction of magnetic ions per particle, since it lowers strain fields on the system[52]. Further reports on particle size reduction of the $Gd_5(Si,Ge)_4$ family compounds have used the ball milling technique reaching samples with average diameter of 0.5-10 μm[33,53,54], DC/RF Magnetron sputtering for thin film production[55] and laser ablation techniques for the synthesis of nanoparticles[6,56]. The last has been revealed as a method to produce samples with better quality crystalline features, low levels of oxidation and narrow particle size distribution. Femtosecond laser ablation in a vacuum chamber have produced granular thin films of $Gd_5Si_{1.3}Ge_{2.3}$ with particle size of $\sim$80 nm where the MCE evaluation revealed a reduction of 33% in comparison with the bulk counterpart, with ΔS_{ad} $\sim$8.9 J/kg.K for an applied field of 5 T[6]. Through X-ray diffraction analysis, a colossal magnetostriction of $\Delta a/a$ of 1.2% was detected; however, the formation of secondary Gd_5Ge_3 and Gd_5Si_4 phases were also found on the film. In another direction, Tarasenka *et al.* were able to produce nanoparticles of 25-30 nm using Nd:Yag nanosecond laser in sequential ablations of Gd, Si and Ge targets separately in colloidal solutions of water[56]. Although they have performed structural and magnetic characterization on the produced nanoparticles, no evaluations on the MCE were performed. This work opens the possibility of using nanosecond pulsed lasers for the production of nanostructures of $Gd_5(Si,Ge)_4$ alloys which are less expensive and more accessible then femtosecond lasers. Surprisingly, few works have been dedicated to the study of this important and complex family compounds due to the obstacle of finding the best technique to obtain single-phase samples which could help answer fundamental questions, such as: *i)* the critical size for the observation of the magnetostructural transition; *ii)* break of symmetry from the miniaturization; *iii)*

atomic stabilization of the material; *iv)* intrinsic surface effects; *v)* kinetics effects on the transition, and so on[35].

Nowadays, nanotechnology is among the promising pathways to improve current devices and for the development of innovative appliances ranging from daily life products to health care and environmental issues[57,58]. Promoting better conditions for human existence and increasing efficiency of existing technologies can reduce energy and resource consumption worldwide. For instance, functionalized nanostructures can be utilized for drug delivery and to kill cancer cells by hyperthermia. These non-invasive methods are bnaspirational substitutes for the traditional treatments involving long periods of radiation and major surgeries in cancer patients[59]. In this matter, it is possible to mention the Lab-on-a-chip (LOC) platform merges nanotechnology and microfluidics as an integrated system that can allow complete biological analysis using small amounts of sample, causing efficient medical diagnosis and patient treatment[60]. Currently, the advance in nanoscience are evident from the reduction of device sizes, like mobile phones and computers, with a great gain on efficiency that clearly have altered human behaviour and relationships. Most importantly, the use of nanotechnology can be the main path to convert climate changes and global warming consequences - since Earth is already warning us about its depletion[3,23]. Such crucial features of nanoscience arise from the new physical/chemical properties observed in materials at reduced scales. A clear example has been shown by ZnO nanoparticles that can be applied as food additives due to the importance of this element in the human body[61]. In 2015, the Nanotechnology Consumer Products Inventory (CPI) reported that over 72 edible products available on the market contain manufactured nanostructures[62], the effects of which have not yet been evaluated for the human body[61]. For the reasons here presented, the understanding of systems at reduced nanoscale from a fundamental point of view is essential for the advancement of these important technologies.

In this work, based on the motivation presented above, the introduction on the alternative solid-state technologies with a more specific approach on the MR and a state of the art on the $Gd_5(Si,Ge)_4$ family compounds will be presented in Chapter 2. The theoretical foundations and experimental techniques used in this work will be presented in Chapters 3 and 4, respectively. Chapter 5 will present the investigation of the effect of substitution of Gd by non-active La on the $Gd_5Si_{1.8}Ge_{2.2}$ composition to understand how large concentrations affect its GMCE. Chapter 6 is dedicated to the characterization of $Gd_5Si_{2.4}Ge_{1.6}$ micrometric powders obtained by sieving for introduction to a flexible thermoplastic polymer for the evaluation on the effects on the MCE behaviour of the powder. This same micropowder was used to produce a multiferroic composite by blending with piezoelectric poly(vinylidene) fluorine (PVDF), presented in Chapter 7, where a magnetoelectric coupling is evaluated and there has been found active influence in the composites MCE. In Chapter 8, the effect of nanostructuring $Gd_5(Si_x,Ge_{1-x})_4$ with x = 0.45, 0.55 and 0.60 using nanosecond Pulsed Laser Deposition (PLD) is studied through Synchrotron X-ray Diffraction, High Resolution Transmission Electronic Mi-

croscopy and Magnetic measurements. A general discussion and future prospects of the work achieved on this project will be discussed in Chapter 9.

Chapter 2

Solid-state Cooling Systems and an Overview of the $Gd_5(Si,Ge)_4$ Family Compounds

Global warming and population growth have increased the demand on energy production and consumption worldwide, which correspond to an addressed issue on environmental sustainability due to the reduction in natural resources[3,23]. The use of clean energy sources for power generation to be applied in cooling, heating, transport and other industries is the best approach to ensure basic human needs are in the net future[63]. Climate change will increase the need to improve refrigeration and air conditioning systems in a warming future with alternatives and more efficient technologies to maintain quality of life. One of the pathways is the use of devices based on solid materials that can reduce ozone depletion from hazardous gases used in traditional vapour systems[64]. The advancement of this technology can also be used to energy storage/harvesting, biomedical applications and smart sensors with higher efficiency[17]. Given this, the present Chapter will give a brief overview on the alternative systems to then focus on magnetic based technology and materials for a further detailed review on the $Gd_5(Si,Ge)_4$ family compounds - which is the core of this work.

2.1 Caloric materials for alternative cooling systems

The study of solid-state based technologies has been a challenge in materials science for the reduction of environmental impact from refrigeration and pump systems worldwide. These new devices are based on caloric materials that present reversible thermal variations by the application of an external field adiabatically, leading to temperature changes (ΔT_S), or isothermally, with an associated change in entropy (ΔS_T)[65]. The materials are classified as mechanocaloric, electrocaloric and/or magnetocaloric depending on the nature of the applied field that will lead to inductions on the strain,

polarization and magnetization, respectively. Electrocaloric and magnetocaloric effects have similar mechanisms where the electric dipoles/magnetic moments orientation along the applied electric/magnetic field isothermally, for example, will lead to a reduction in the ensemble entropy and, since $\Delta Q = \Delta S/T$, the material release heat. The opposite will occur when the applied field is removed and the polarization-depolarization/magnetization-demagnetization processes can be combined in a cycle for refrigeration purposes, as will be expanded in the next section. A more detailed description on the magnetocaloric effect is given in Chapter 3.

The mechanism involved in the mechanocaloric effect is similar to the compression/expansion of gases and can be divided in subcategories depending on the type of induced strain variation, as summarized on Table 2.1. The classification is based on the Cauchy stress tensor non-zero components, illustrated in Fig. 2.1, which will depend on the direction of deformation: *i)* elastocaloric (eCE) is a thermal response along one direction (only one $\sigma_{ij} \neq 0$ for $i = j$); *ii)* barocaloric (BCE) is a response to hydrostatic pressure ($\sigma_{ii} = p$ and $\sigma_{ij} = 0$ for $i \neq j$) and *iii)* torsiocaloric (tCE) is the effect of a torsion along a fixed n-axis driven by a shear stress ($\sigma_{ij} = 0$ for $i = j$ and $\sigma_{ij} = 0$ for i and $j \neq$ n)[66]. However, for practical purposes, the mechanocaloric effect is generically called "thermal effect" of "thermoelastic effect".

Field	Variable	Classification
Magnetic	Magnetization	Magnetocaloric
Electric	Polarization	Electrocaloric
Stress Field:	Strain	Mechanocaloric:
Uniaxial stress		Elastocaloric
Isostatic stress		Barocaloric
Pure shear stress		Torsiocaloric

Table 2.1: Summary of the caloric effect classification, based on Ref. 66.

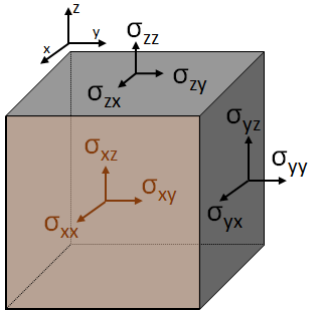

Figure 2.1: Illustration of the Cauchy stress tensor.

Recently, it was found that a single crystal of Cu-Zn-Al alloy presents superelastic eCE[67] and the magnetic shape memory alloy (SMA) of Ni-Mn-In shows a giant BCE[68]. These findings opened a pathway for mechanocaloric-based cooling systems. The major advantage of this underdevelopment technology is the easiness of applying several MPa of stress over high electric and magnetic fields is the major advantage of these technology that is under development. Much effort has been made for the improvement of these systems since the first built elastocaloric prototype by a German group in 2015[69]. Using Ni-Ti micro ribbons and loading pressures at the order of 10^3 MPa, they were able to reduce the heat source temperature in $\sim$ 3.5 K after 60 cooling cycles. The main limitation factors for the uniaxial stress are the material fatigue and the mechanical work due to hysteresis denigrating the process efficiency. More recently, Sharar *et al.* reported the largest temperature drop in a heat source of $\sim$ 16 K

by applying uniaxial pressure in a Ni-Ti wires setup[70]. Even though these prototypes shows the technology potential, the number of cycles that typical materials can undergo are around 10^6 with the maximum of strain variation between 1-10%. As stated by Sehitoglu, "the research on elastocaloric effects coupled with mechanical response in SMAs is still in its infancy"[71].

Concerning the electrocaloric effect, the attention has been turned to this alternative after the report of an adiabatic temperature change ΔT_S of 12 K in a 350 nm thin film of piezoelectric Pb(Zr,Ti)O_3[72]. The materials presenting higher electrocaloric responses and, for this reason, the best candidates for practical applications are thin films of ceramics and electroactive polymers, such as: Pb[Sc_xTa_{1-x}]O_3 (PST), (1-x)[Pb($Mn_{1/3}Nb_{2/3}$)O_{3-x}PbTiO_3] (PMN-PT), polyvinylidene fluorine/ trifluoroethylene (PVDF-TrFE) and its co-polymers[73]. Since bulk and monocrystals present low dielectric strength and electromechanical breakdown, the thin films are advantageous once they can stand longer with the application of larger electrical fields changes. A complete list with a comparison between the different materials' electrocaloric responses is given in Ref. 73. A few prototypes were proposed in the last years; however, due to the low temperature change (0.5-1.5 K) and the difference between cold and heat source temperatures of a few K, there is still much research needed to improve its efficiency[73]. Indeed, the full understanding on the mechanism of the electrocaloric effect is still lacking and several models have been proposed aiming prototype developments[74]. For this reason, electrocaloric cooling based devices were proposed so far for cryogenic refrigeration and micro-cooling electric circuits[69,74]. In another direction, thermoelectric technology, where the electrical field is activated by the application of a temperature gradient (*Seebeck effect*[75]), is the most evolved option with great potential of implementation for electronic gadgets and energy harvesting[4]. However, the low efficiency associated with the high cost of thermoelectric devices using BiTe thin films and PbTe based dots is the main obstacle for a large scale production.

Nevertheless, the ongoing search for the best caloric materials is an important task for the advance of all the mentioned alternative technologies for refrigeration, heat pumps and air conditioning. A large caloric effect occurs at the edge of phase transitions and is usually stronger for materials that undergo a first order transition that is highly temperature dependent. The same material can present substantial caloric responses for different field natures. For this reason, giant magnetocaloric and electrocaloric materials are expected to have large mechanocaloric effect because they are often strongly structurally coupled[5]. Therewith, multicaloric materials allow use of more than one field, that can endorse the access to phase transitions with lower field intensities and broader working temperatures. Some examples are given in the diagram in Fig. 2.2. For instance, Heuser alloys like Ni-Mn-Co-Ga can have the elastocaloric refrigerant capacity increased 20% by applying magnetic fields of 1 T[76]. The combination of magnetic and mechanical fields are more feasible than combining with electrical fields. However, it is possible to control the magnetic properties by using elec-

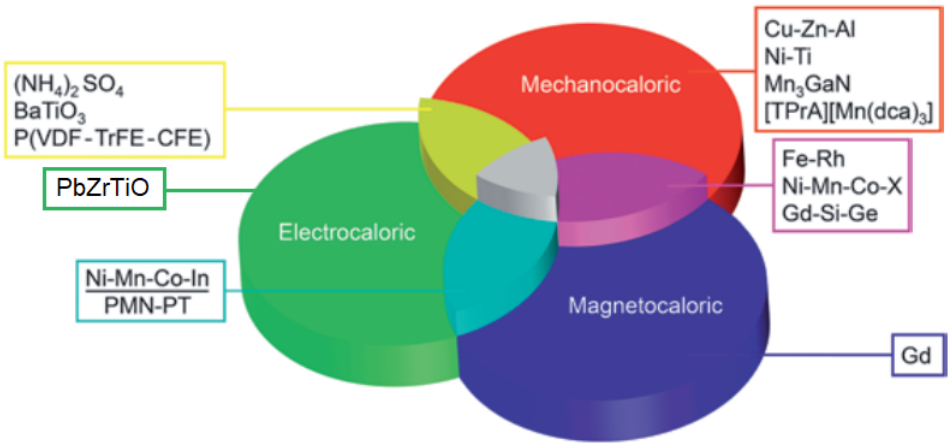

Figure 2.2: Diagram of multicaloric materials related to each one. Materials with large caloric effects near room temperature were selected and, as well, at the intersections the system presenting both effects. Image obtained from Ref. 5

trical fields in multiferroic systems, like the combination of Ni-Mn-Co-In with ferroelectric substrate of Pb-Mg-Nb/Pb-Ti-O (PMN-PT) also shown in Fig. 2.2. Some approaches have been followed in order to combine materials presenting different caloric properties, like through the blending with organic polymers[24], multilayers films[77] and particle size reduction[6]. In this sense, the exploitation of multicaloric systems is a field still in development with great promise for the community[78].

For this work, the magnetocaloric effect will be the focus from now on. The magnetocaloric based technology is in a distinct situation which is well established and tested, but there is much to be done in order to overcome the conventional cooling systems.

2.2 Magnetic Refrigeration: thermodynamic cycles, prototypes and materials

Several cooling/heating cycles with different thermodynamic process have been proposed for magnetic refrigeration since the first demonstration by Giauque and MacDougall in 1933. They achieved the temperature of 250 mK by using paramagnetic salts based on the method proposed by Giauque in 1929[79,80]. The cycles are based on the second law of thermodynamics consisting of different combinations of isothermal, adiabatic and isofield processes - where the applied magnetic field is kept constant - with the aim to achieve maximum efficiency. The mechanism is analogous to vapour compression systems where the application/removal of a magnetic field acts as the compression/expansion on refrigerant gases. In the case of magnetic materials, the spin alignment when applying a magnetic field adiabatically leads to reduction of magnetic entropy (S_M) in the material. Thus, in order to conserve the total entropy of the system, the lattice entropy (S_L) should increase, consequently increasing the temperature[17]. There are two basic processes to observe the MCE: the first when the magnetic field is

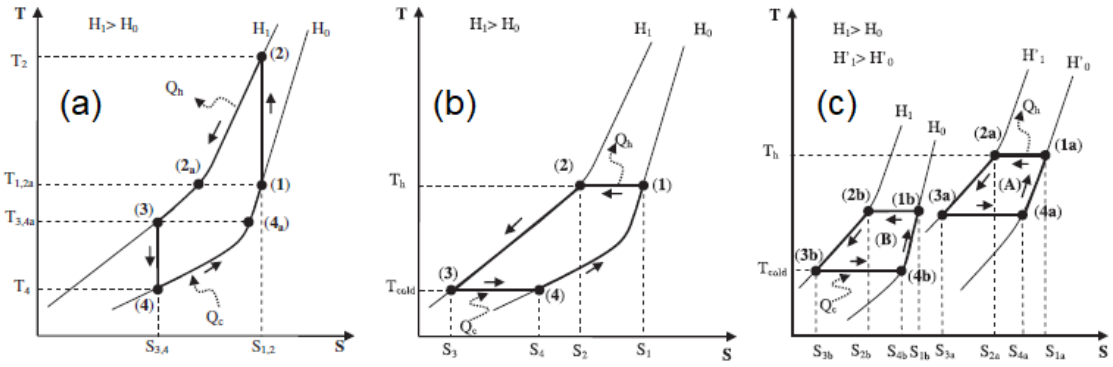

Figure 2.3: Temperature-Entropy (T-S) diagrams for **(a)** Brayton, **(b)** Ericsson and **(c)** cascade regenerative magnetic cycles. The images were extracted from Ref. 36

applied adiabatically, as mentioned above, and the second when applying a magnetic field isothermally allowing the material to exchange heat with a thermal reservoir, once $\Delta S_{iso} = \Delta Q/T$. In that way, the physical quantities which characterized the effect are the temperature change (ΔT_{ad}) and the entropy change (ΔS_{iso}). In particular, since magnetic materials are mainly solids, a fluid is required for the heat transfer between cold and hot sources. A more detailed description of the theoretical approaches for the MCE evaluation is given on Chapter 3.

The reference cycle is the Carnot one, which is a combination of the already mentioned isothermal and adiabatic processes, with the highest ranges and heat transfer associated. However, the requirement of variable magnetic fields during the hole cycle is a drawback to practical applications. The working range temperature is also limited by the lattice contributions during adiabatic magnetization/demagnetization process. These issues can be overcome by considering regenerative cycles with isofield processes such as Brayton and Ericsson ones, with the T-S diagram shown in Fig. 2.3(a) and (b). As in conventional vapour based systems, the use of regeneration does not restrict the working temperature which enables it optimization for room temperature devices. In a Brayton cycle, two adiabatic and two isofield process are considered. The magnetic material is heat up from T_1 to T_2 through adiabatic magnetization (1-2); under the applied magnetic field H_1, the heat is transferred through the fluid to hot source (Q_H) and the system decreases it temperature to T_{2a}. A regenerative (2_a-3) process lowers the temperature to T_3 and the removal of magnetic field at (3-4) reduces even more the material temperature to T_4. At this stage, the transfer fluid absorbs heat from the cold source (Q_C) increasing its temperature (4-4_a), thus, reaching the initial temperature T_1 by means of other regenerative (4_a-1) process.

In a similar way, the Ericsson cycle, shown in Fig. 2.3(b), also has two isofield processes combined with two isothermal steps. The material will release and absorb heat from hot and cold sources, respectively, through the isothermal application in (1-2) and removal in (3-4) of the magnetic field. In this case, the regeneration process occurs at (2-3) and (4-1) stages of the cycle. Both cycles can be designed with the movable

parts being the magnetic materials with a steady field that can be originated from a permanent magnet, for example. Furthermore, as already pointed on the description of MCE, the maximum effect occurs at the transition temperature. The MCE is higher for materials that undergo a FOMT with a narrow transition that constrains the working range temperature for practical purposes. A possible solution to enlarge the span temperature for MR is by combining materials with different at the vicinity of each other critical temperature. A combination of two Ericsson cycles A and B are shown on the diagram in Fig. 2.3(c) where $T_C^A > T_C^B$. As can be noted, the heat absorbed from the cold source by material B is transferred to A and then is released to the hot source. In this way, the total work of the cycle can be enhanced by the addition of more materials with different 's.

It is worth pointing out that, since the materials are at the solid state, the same fluid exchanger can be used for each cycle which is one of the main advantages of magnetic refrigeration. The magnetic material can also work as a regenerator itself for the heat transfer flow when the applied magnetic field is kept constant on the active magnetic regenerator cycle (AMR)[21]. First demonstrated by Brown, the AMR was the starting point for the development of magnetic refrigeration near room temperature[81]. In this cycle, the losses of irreversible processes on the heat transfer between steps can be reduced and, for this reason, it is considered the most efficient for room temperature MR[82]. A schematic of the AMR cycle is shown in Fig. 2.4(a)-(d), which is basically composed of a magnet (1), a porous bed of MCM working as a regenerator (2) and a system to perform the flow of the transfer fluid through the MCM (3). Two adiabatic and two isofield processes, in a Brayton cycle - leading to changes on the MCE temperature - occurs simultaneously with the heat transfer to the fluid. In (a) MCE is adiabatically magnetized which increases the fluid transfer temperature; then, (b) the field is held constant and the MCM cools down by the fluid flow from cold to hot source. The opposite way works almost the same wherein the adiabatic demagnetization in (c) reduces the MCM temperature even more, and the fluid is transferred from the hot to the cold source with a null applied magnetic field in (d). Using this continuous operation device, Brown was able to achieve an 80 K temperature span using Gd plates and a solution 80% water and 20% ethanol under alternative applied magnetic fields of 70 kOe[83]. At the same year, Steyert proposed an AMR cycle using a rotative system, shown in Fig. 2.4(e), where a permanent magnet is applied instead of a superconducting magnet as a field source[84]. He was able to achieve a temperature span of 14 K with a cycle frequency of 1 Hz, also using pure Gd.

Several studies were performed in order to improve the solid-state cooling technology but, its revival was only after the discovery of GMCE at room temperature in $Gd_5Si_2Ge_2$ alloy in the late 1990s. The first demonstration of long period operation of an AMR based refrigerator was performed by the scientists of Ames Laboratory and Astronautic Corporation of America in 1998 where the prototype worked for 18 months with minor maintenance[88]. However, the highest temperature spans were

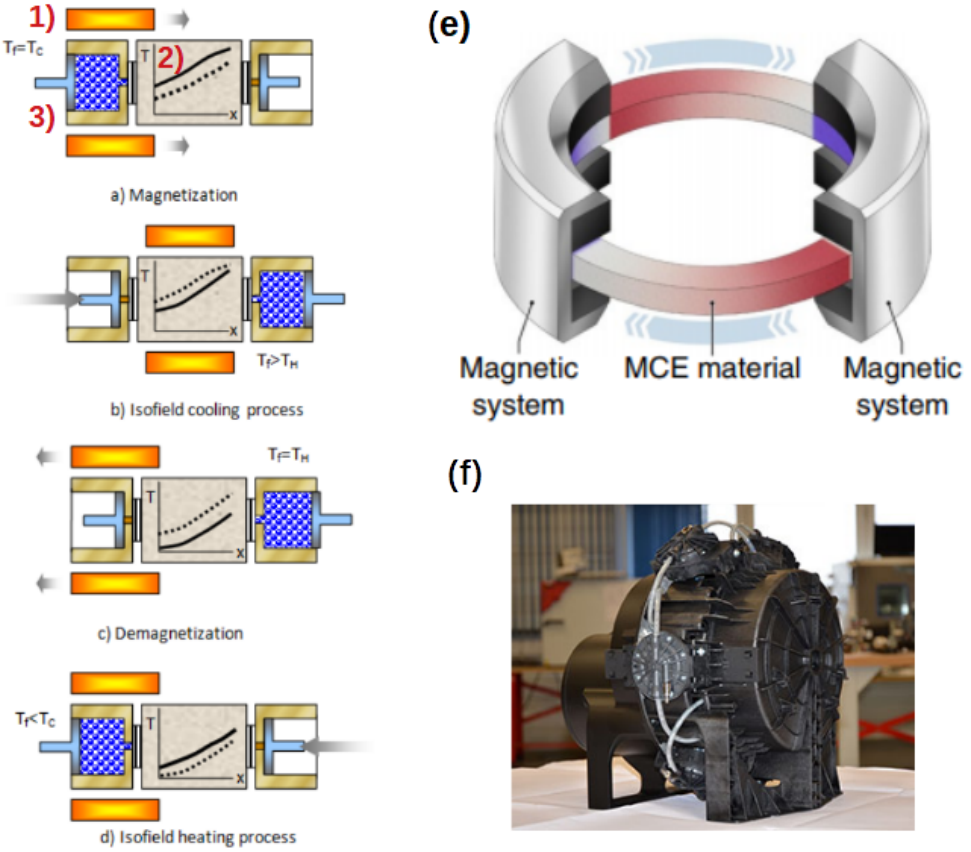

Figure 2.4: Schematic of an active magnetic regenerative (AMR) extracted from Ref. 85 containing a 1) superconducting magnet, 2) MCM as regenerator and 3) a system for the transfer fluid flow through the regenerator. AMR cycle has four steps: **(a)** adiabatic magnetization increasing the MCM temperature releasing heat to the transfer fluid; **(b)** field is held constant and fluid flows to cold reservoir. MCM temperature is later reduced by an **(c)** adiabatic demagnetization and the heat transfer fluid passes from the cold to hot source with no applied magnetic field. **(e)** A rotating bed magnetic refrigerator (RBMR) based to improve the cycle efficiency using permanent magnets that was demonstrated in 2001, extracted from Ref. 86. **(f)** The first commercial magnetic refrigerator developed by Cooltech Applications with cooling capacities between 200-700 W in 2016, the image was obtained from Ref. 87.

only achieved with the cost of reducing the Carnot efficiency and cooling power (CP) of the system[81]. The researchers from Ames Laboratory observed that, in order to improve the system performance, cycle frequencies higher than 1 Hz should be implemented on the machine - which was operating at 0.16 Hz (6 s per cycle). To achieve this order of frequency, they have applied the design proposed by Steryert that is now called rotating bed magnetic refrigerator (RBMR), shown in Fig. 2.4(e). With this geometry, the MCM is the movable part and the heat transfer fluid flows between each section of magnetized/demagnetized regions. In 2001, the demonstration of RBMR feasibility was performed with a prototype containing 160 g of Gd spheres under an 15 kOe of applied magnetic field using a NdFeB permanent magnets and steel flux concentration poles. The apparatus could operates from 0.5 up to 4 Hz of cycle frequency and with different fluid flows. They have also performed tests using Gd layers, $Gd_{94}Er_6$ spheres and $La(Fe,Si)_{13}$ hydrides particles as fillers for the bed regenerative

component. Although it worked over 1500 h, the fluid system was the main problem to improve the device design. The tests results showed that the machine performance could be improve by using layers with different 's in a cascade system. This is due to the loss on MCE response as the working temperature shifts from during the cycles. Rowe and Tura have demonstrated that a three-layered MCM bed composed of Gd, Gd-Tb and Gd-Er crushed particles could produce a 50 K of temperature span for applied magnetic fields of 2 T in a reciprocating AMR design[1] [89]. By comparing with single and double-layer beds, the authors have concluded that a multicomponent system performance will only depend on the type of MCM; however, it would not exceed for single phase ones. A major step on magnetic refrigeration availability to the market was a demonstration of a wine cooler at the International Consumer Electronics Show (CES) in 2015 developed by Haier, Astronautics Corporation of America, and BASF[90]. At the same year, Cooltech Applications presented a medical fridge that saved 40% of consumed energy with reduced noise when compared to standard systems. The first prototype with the promise of a commercial magnetic refrigerator, however, was launched also by Cooltech Applications in 2016, based on a rotary system using 165 g of Gd and four NdFeB magnets with the design presented in Fig. 2.4(f)[87,91]. Besides Cooltech Applications from France, the key companies on the MR market are Cambridge (UK), Astronautics Corporation America (US), Whirlpool Corporation (US), Qindau Haier (China), BASF (Germany), among others according to a late report from QY Market Insights[40]. Although these companies have shown the prospects of MR systems, they have not become commercially available yet.

Recently, Franco *et al.* listed over 50 patents on MR and 100 prototypes presented chronologically in Ref. 17. Among the variety of setups - with static/movable magnets and/or MCM bed - they operate using basically pure Gd, Gd-Tb, $Gd_5Si_2Ge_2$, Mn-Fe-P, $La(Fe,Si)_{13}$ (also the hydrides and borides) and manganites as the magnetic refrigerants and water, oil, ethanol solutions or He gas as fluid exchanger. Even though the higher temperature spans are achieved with high frequencies and applied magnetic fields (which can be originated from Nd-Fe-B permanent magnets or superconducting magnets), the material processing also has a great influence on the final product. For instance, table-like MCE where the ΔS_{ad} and ΔT_{iso} are constant during the working temperature range presenting higher cooling power. Most importantly, aiming for large scale production for domestic use, materials with low associated cost and higher response under the influence of minor magnetic field intensities are required.

Most of the studies concerning MCE have been around rare earth metals and their alloys and using the magnetocaloric potential of Gd as reference. Gadolinium metal has magnetic transition temperature around 292 K, where the MCE is maximum, and achieve ΔS_{iso} of approximately 10 J/kg.K upon a magnetic field variation from 0 to 5 T. These remarkable discoveries were made by Pecharsky and Gschneidner with the observation of the GMCE in $Gd_5(Si_2Ge_2)$ in 1997[28]. With the magnetic temperature

[1] Using a superconducting magnet.

transition around 276 K, this alloy when subjected to a magnetic field variation from 0 to 5 T reach 20 J/kg.K, much large than the observed in Gd. Since these results, several researchers turned their attention to the studies on $R_5(Si_xGe_{1-x})_4$ (where R is a lanthanide), with x $\leq$ 0.5, family of alloys in order to obtain materials with the properties necessary to implement in MR, more details about these properties will be explained in the next section. Other materials have also been targeted for the MCE study, like transition metal based compounds[92,93], amorphous materials[94,95], Heusler alloys[96], manganites[97], among others[17]. As can be noted in Fig. 2.5, the materials presenting larger entropy changes are MnFe(As,P) - which is toxic -, $La(Fe,Si)_{13}$·H, Fe-Rh, Heusler alloys and $RE_5(Si,Ge)_4$ (RE = rare earth). Around 90-95% of current rare earth metals come from China which increases the production costs. It is worth to point out the importance on the applied magnetic field for the operation of MR due to the variable prices of Nd that could be a drawback for commercial production[23].

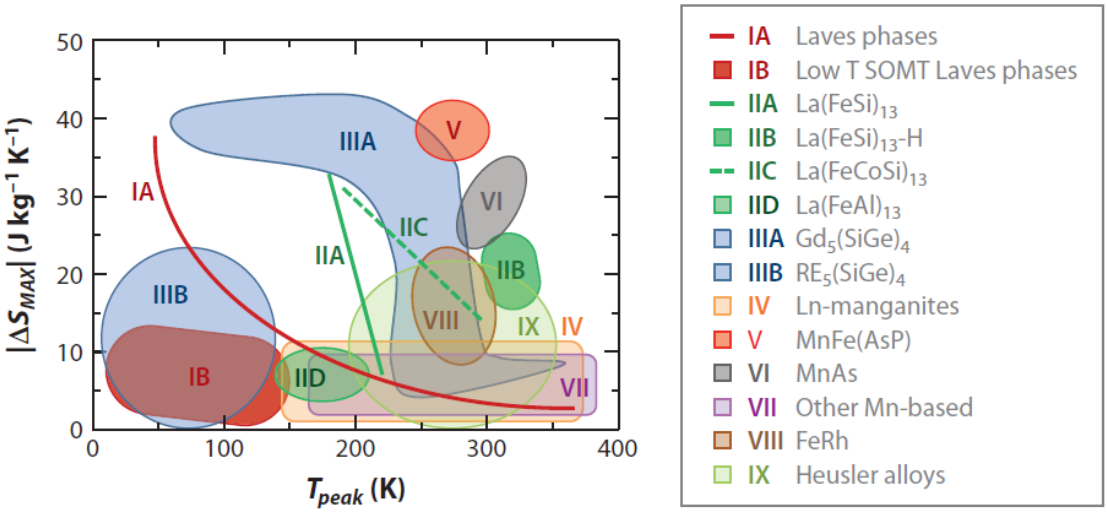

Figure 2.5: Values of entropy magnetic change for most important magnetocaloric materials. The images were extracted from Ref. 98

For the present work, the studies will be focused mainly on the magnetocaloric effect of intermetallic $Gd_5(Si,Ge)_4$ multifunctional material. It is well known that large responses are observed on materials presenting a first order transition; however, the character of the transitions are discontinuous in a short temperature range with associated hysteresis losses, which is a limitation for device operation performance.

2.3 The $Gd_5(Si,Ge)_4$ family compounds

The initial studies on the R_5M_4 family were performed by Smith *et al.* in 1966 for M = Si or Ge and R = rare earth series (with the exception of Pm, Eu and Yb)[99]. Through single-crystal structural characterization, they were able to predict quite well the space groups and lattice parameters of the produced compositions. A year later, Holtzberg

and co-workers reported for the first time an evaluation of crystallographic and magnetic properties of the $Gd_5(Si_xGe_1 - x)_4$ series[100]. In this work, the authors found that values at the Si-rich region were higher than for pure Gd and an antiferromagnetic ordering presented at low temperatures for Ge-rich stoichiometries. In spite of these fascinating observations, the question on this high went unsolved for almost 30 years. It was only in 1997 with the discovery of a GMCE in $Gd_5Si_2Ge_2$, that the scientific community turned its the attention to this pseudo-binary family. The magnetic entropy of $Gd_5Si_2Ge_2$ is at least 30% higher than that observed in pure Gd. Since then, several strategies were followed in order to evaluate and increase the MCE properties of the $Gd_5(Si,Ge)_4$ family compounds for the development of new technologies[101]. Although is not among the top materials for MR, it can be used in a large range of applications, such as: sensors[102], micro-cooling devices[6], energy conversion[24] and medical treatments[103]. This is due to the important properties discovered through extended research like an unusual Hall effect[104], giant magnetoresistance[30] and colossal magnetostriction CMS despite a rich crystallographic and magnetic phase diagram[32]. Thorough studies performed so far on these alloys have revealed that its important features are consequences of its extreme sensitivity to variation of external (temperature, magnetic field, pressure) and internal (stoichiometry and doping) parameters[105].

The $Gd_5(Si_xGe_{1-x})_4$ family compounds can crystallize in three distinct structures: Orthorhombic-I [O(I)] or Sm_5Si_4-like (Pnma space group), Monoclinic ($P112_1/a$ space group)(M) and Orthorhombic II (O(II)) or Sm_5Ge_4-like (also Pnma space group)[105,106]. These three structures are basically formed by stacks of slabs, constituted by two polyhedrons with sub nanometre height (along the b-axis) and infinite width (a and c-axis). The first pseudo-cube, shown in Fig. 2.6(a), is an arrangement of Gd atoms in a body cubic centred structure with Si and Ge positioned in each face of the cube. While the second one, in Fig. 2.6, the Si/Ge dimmers stand along the c-axis at the centre of the pseudo-cube of Gd atoms. The Si and Ge can be disposed in two positions: T1 (interslab), responsible for the connection between slabs, and T2 (intraslab) position, which establish the connection between pseudo-cubes. Projections of the formed blocks are shown in Fig. 2.6(c) and (d) with the T1 bonds along the b-axis. It can be noted from Fig. 2.6(e-g) that the major difference between the three structures is the number of covalent bonds formed between the atoms at T1 position: **O(II)** does not have T1-T1 bonds; **M** only has half of T1-T1 bonds; **O(I)** has all T1-T1 bonds.

Therefore, the formation and rupture of the T1-T1 bonds is the main factor defining the crystallographic structure of these gadolinium silicon germanides. An empirical relation to predict the structure of $R_5(Si,Ge)_4$ was obtained by Pecharsky *et al.* that will depend on the ratio between the rare earth (r_R) and Si/Ge (r_M) atomic radii, with $r_M = x \cdot r_{Si} + (1 - x) \cdot r_{Ge}$[107]. In particular, for Gd atoms at room temperature, the system will adopt an O(I) structure for r_R/r_T in the [1.362-1.338] range; and, for M and O(II) the values will be in the [1.334-1.327] and [1.322-1.307] range, respectively. It is worth mentioning that this relation fails for La, Pr and Nd elements due to their

anomalous behaviour when compared to the heavy elements[107].

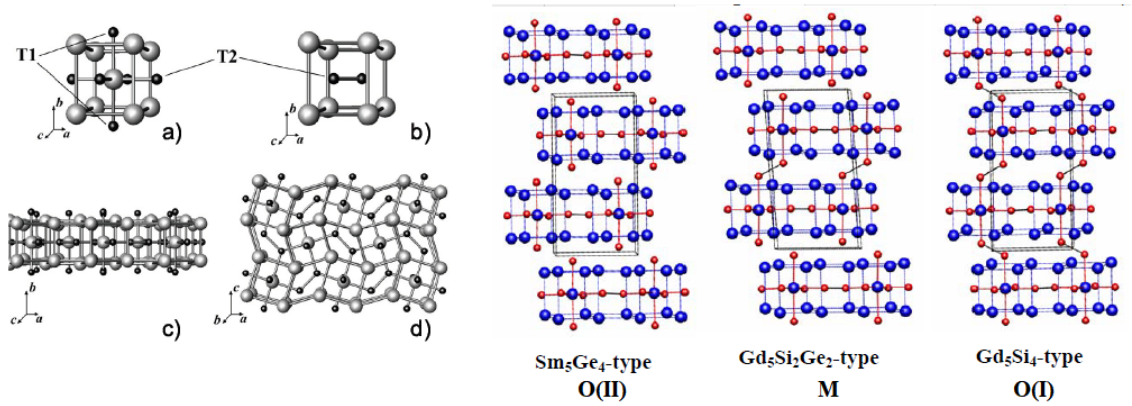

Figure 2.6: The building blocks of $Gd_5(Si,Ge)_4$ family compounds consist of trigonal prism **(a)** and cubic **(b)** pseudo-cubes connected interslab and intraslab by T1 and T2 connections, respectively, of Si and Ge atoms forming the projections shown in **(c)** and **(d)**. The number of formed T1-T1 covalent bonds will differentiate the three possible structures adopted by this family where for Sm_5Ge_4-type [O(II)] there is no formation of the bonds; distorted $Gd_5Si_2Ge_2$-type with half of the bonds; and, Gd_5Si_4-type [O(I)] with the formation of all Si-Ge bonds. (The images were extracted from Refs. 108,109)

The strong relation between the crystallographic structure and magnetic ordering on the $Gd_5(Si_xGe_{1-x})_4$ family compounds can be seen on the phase diagram shown in Fig. 2.6(a). Ferromagnetic (FM) states are associated with O(I) structures while paramagnetic (PM) and antiferromagnetic (AFM) orderings are associated with M and O(II) structures. For the x$\geq$0.30, the system presents FM to AFM ordering change with a structural transition from an O(I) to O(II) structure that can be magnetically induced[110]. For instance, the structural [FM,O(I)]$\rightarrow$[AFM,O(II)] transition on the Gd_5Ge_4 composition only occurs for applied magnetic fields higher than 11 kOe[111]. At the intermediate region (0.41$\leq$x$\leq$0.51), the system undergoes a first order magnetic transition (FOMT) from a [FM,O(I)] to [PM,M] state at the 250-300 K temperature range, that can also be magnetically induced. For this reason, it is possible to tune the transition temperature through the application of magnetic fields. As for the Si-rich compositions, x$\geq$0.56, a SOMT occurs at 's that exceed the observed for pure Gd, as already mentioned. This is due to the increase of exchange interactions as Si content increases from the reduction on the interslab T1-T1 dimers and Gd-Gd distances, as can be seen in Fig. 2.7(b) and (c)[112]. Nowadays, it is well accepted that the FM character of this family compounds is given by the indirect RKKY interactions between 4f orbitals of Gd and from the superexchange Gd-Si/Ge-Gd interactions - stronger at the Si-rich region[32]. The Si(Ge)/Si(Ge) dimmers are formed when the distance is below 3.50Å along the b-axis, which only occurs for M and O(I) structure. In particular, due to the distortion of M-phase, only half of these bonds are formed, as shown in Fig. 2.6(b). Furthermore, the regions at 0.30<x<0.41 and 0.51< x <0.55 are mixture phase compositions. Indeed, Pecharsky had already pointed the difficulties stabilizing single M-phase on $Gd_5Si_2Ge_2$ polycrystalline samples at the edge of the M+O(I) mixture region. The sample homogenization

can be achieved by careful heat treatments and appropriate quenching[113].

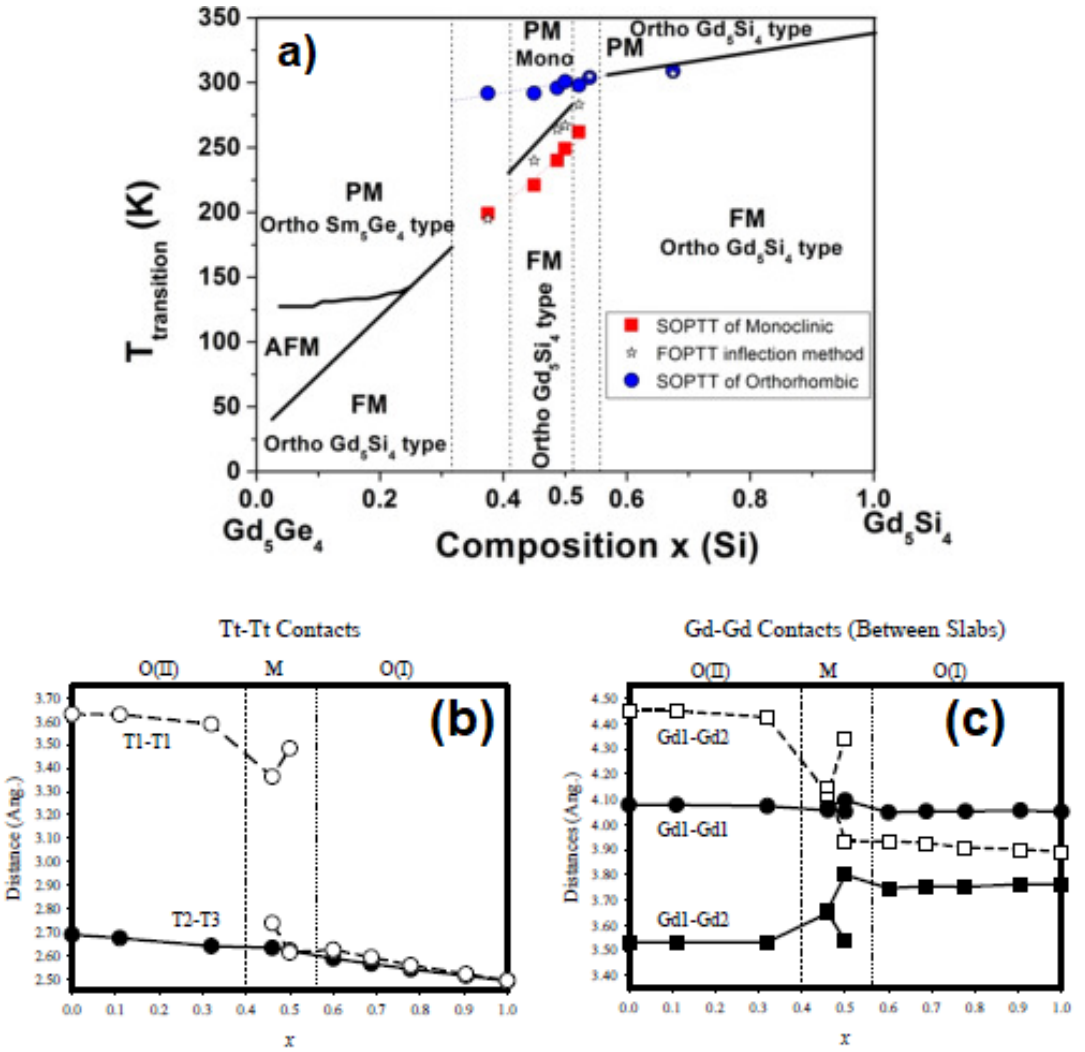

Figure 2.7: **(a)** T-x phase-diagram of $Gd_5(Si_xGe_{1-x})_4$ family compounds with the first and second order magnetic transitions temperatures - FOMT and SOMT. (Extracted from Ref. 114.). The increase in the transition temperature as Si content (x) increases is due to the reduction between **(b)** interslab (T1-T1) and intraslab (T2-T3) dimmers that reduces **(c)** Gd-Gd contacts at the structures, thus increasing the exchange interactions (the graphs were obtained from Ref. 112).

Despite the aforementioned magnetic field induced transitions, the hydrostatic pressure has also great influence on the $Gd_5(Si,Ge)_4$ family compounds. In particular, for Gd_5Ge_4 it was found through magnetization data that a hydrostatic pressure of 8 kbar can induce a [FM,O(I)] state at low temperature in 80% of the system volume[110]. This is also observed for $Gd_5Si_{1.8}Ge_{2.2}$, where the Curie temperature varies with a dT_C/dP of +0.3 K/kbar[115]. In this case, a hydrostatic pressure of 20 kbar would be enough to shift to RT. Through in situ X-ray diffraction, Mudryk *et al.* have shown that above 21.5 kbar, the M-phase is completely converted to O(I)-phase at the $Gd_5Si_2Ge_2$ compound[116]. This effect is reflected in the MCE behaviour that vanishes for applied hydrostatic pressure above 6 kbar, as can be seen on the entropy change curves for

$Gd_5Si_2Ge_2$ polycrystalline sample (with annealing treatment at 1300 ^oC) depicted in Fig. 2.8(a)[117]. Under null applied pressure, the curve presents a sharp profile that becomes broader towards higher temperatures as a direct consequence of the interatomic distances at the unit cell, inducing an O(I) structure with a SOMT. Such findings reveal that the $Gd_5(Si,Ge)_4$ family can be used as a multicaloric material and, therefore, improve the production and absorption of heat through multiple fields.

These are just a few examples of the extreme sensitivity of $Gd_5(Si,Ge)_4$ family compounds to internal and external parameters. Understanding this mechanism is of great importance from a fundamental standpoint in order to enhance the material features in practical applications. Several models were proposed to describe the thermodynamic origin on the magnetostructural transition on these alloys. Through first principal calculations using a local spin density approximation, Paudyal and co-workers were the pioneer on predicting the MCE of $Gd_5Si_2Ge_2$ through of thermomagnetic models[118]. With the crystallographic parameters obtained experimentally and non local exchange correlation functions, they were able to construct the free energy (ΔF) temperature dependence of the competing phases [M and O(I)], obtaining the structural transition temperature (T_S) of 265 K which is close to the experimental value of 275 K. The O(I)$\rightarrow$M structural change will occur when $\Delta F_{O(I)} = \Delta F_M$, *i.e.*, the system will be arranged in an O(I) structure until the M phase becomes energetically favoured, displayed in Fig. 2.8(b)[119]. As can be noted, the FM-PM transition of M-phase occurs around 200 K, well below T_S, that can be tuned by the application of magnetic field which will enhance the MCE response, corroborating with experimental results[28,120,121]. In order to obtain larger MCE and features related to structural transition like magnetostriction, the phase with lower should be close of T_S. Pecharsky *et al.* showed that below 2 T of applied magnetic field, the structural entropy change (ΔS_{str}) corresponds to more than 50% of the magnetic one (ΔS_M) for Gd_5Ge_4, $Gd_5Si_2Ge_2$ and close compositions[122]. This is due to the significant change in the unit cell volume when a covalent bond breaks, on the M to O(I) crystallographic phase transition and, consequently, changing the macroscopic dimensions[123].

2.4 Chemical substitution effects on the $Gd_5(Si,Ge)_4$ compounds

Chemical doping can tune the magnetic properties of intermetallic materials by increasing/decreasing the transition temperatures[124–126], enhancing the magnetostructural coupling[42,46] and reducing hysteresis losses[127]. It can also improve ductility of intermetallic compounds by substitution of brittle atoms, like Germanium, to more malleable ones, like Boron and Iron[128]. The robust structures adopted by the $Gd_5(Si,Ge)_4$ family of compounds allow substitutions by a large number of elements, with important consequences for their physical properties[29,42,126]. For instance, rare earth substitu-

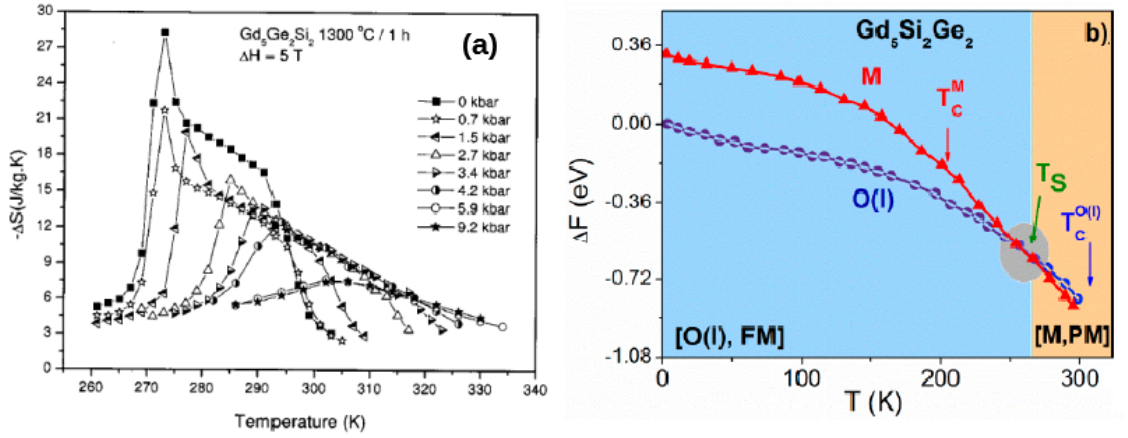

Figure 2.8: **(a)** The GMCE of $Gd_5Si_2Ge_2$ compound is also affect under the influence of pressure leading to a dissappearence of the FOMT above 6 kbar, as shown on the study on Ref. 117. This is due to the competition between the phases, where the M structure is energetically favoured around 265 K - theoretical obtained from first principle calculations on Ref. 119.

tions lead to chemical pressure, magnetic dilution and site-preference occupation effects[42,126,129]. Low amounts of La in the Gd_5Ge_4 compound do not interfere in the magnetostructural transition, as already mentioned above. First-principle calculations, have shown that La^{3+} occupies the R2 site on the O(I)-Gd_5Ge_4 structure, which does not have much influence on the ferromagnetism, as it does not interfere with the main ferromagnetic R1-T3-T3-R1 chains formed in these compounds. However, more than 20% of La becomes critical for the $Gd_{5-x}La_xSi_4$ family, leading to an enhancement on the structure symmetry as x increases[130]. The authors observed that a structure change from O(I) (for x = 1) to tetragonal (for x = 2) led into an abrupt reduction of T_C in 90 K. In contrast, this same amount of La on the $Tb_5Si_2Ge_2$ system led into a transition from M to T structure with an increase of the T_C[42]. This enlargement brings a gain on the collinear alignment of the Tb ions due to the La preferential occupation on the R2 site (localized at the slab edges). Further La contents cause drastic losses on the $Tb_5Si_2Ge_2$ ferromagnetic behaviour reflected by a weakening and consequent elimination of a Griffiths-like phase and a spin reorientation transition. A recent study on the $Gd_{5-x}Sc_xSi_{1.8}Ge_{2.2}$ revealed an increase in T_C for the FOMT from 243 K to 266 K followed by a reduction in the hysteresis for $x \leq 0.2$[46]. Higher amounts of non-magnetic Sc, however, shifts the transition from a FOMT to a SOMT with a reduction on the MCE response for $x > 0.2$. The authors have attributed such behaviour to dilution effects where the introduction of Sc leads to internal pressures above critical for the parent compound, leading to a change in the magnetic ordering nature.

It is pertinent that in this family of compounds, atomic structure plays a vital role in the magnetic properties and is responsible for their exotic features. Many studies report the properties of this pseudo-binary family by combining different R elements and Si:Ge ratio[105,126,131]. For instance, when R is a light rare earth element, the tetragonal (T) structure is the most stable, where all the Si(Ge)-Si(Ge) are bonded without slab

formation. The distinction between these formed structures can be observed in Fig. 2.9; the packing of the cubes at the M structure are along the b-axis [the same for O(I) and O(II)] while T structure packing occurs along the c-axis[29]. Typically T systems present FM ordering at low temperatures, however, without exhibiting any coupled structural transition[131].

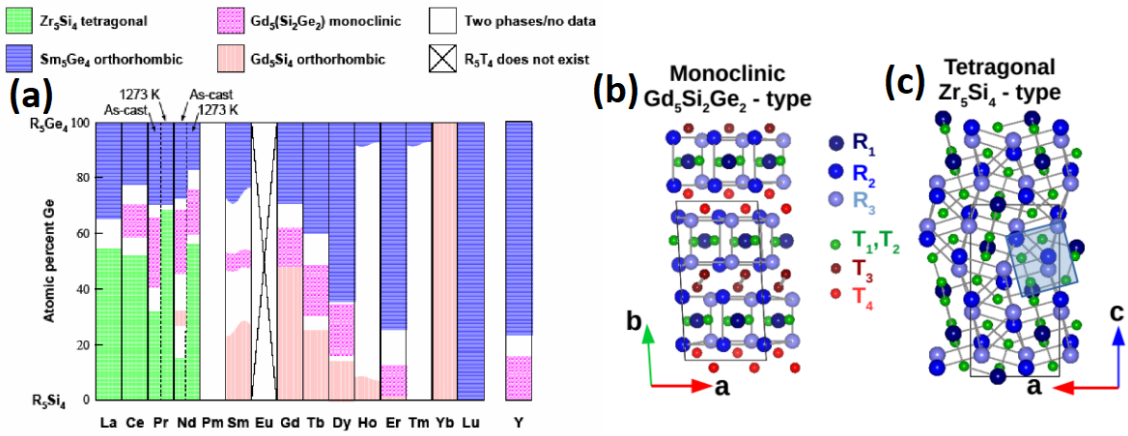

Figure 2.9: **(a)** Scheme on the adopted structures by $R_5(Si,Ge)_4$ compounds with their indicated structures and mixture regions in white, extracted from Ref. 132. The distinction between **(b)** monoclinic (M) $Gd_5Si_2Ge_2$-type ($P112_{1/a}$ space group) and **(c)** tetragonal (T) Zr_5Si_4-type ($P4_12_12$ space group) crystallographic structures adopted by $R_5(Si,Ge)_4$ family compounds. The distance between Si/Ge atoms are the same on the T structure followed by a shift on the pseudo-blocks alignment from the b-axis for M unit cell to the c-axis for T one. The images in **(b)** and **(c)** were produced using Vesta software 133.

2.5 The path to micro/nanostructuring the $Gd_5(Si,Ge)_4$ compounds

The MCE response of systems at micro/nanoscale, despite being related in their bulk composition, will also depend on their morphology, particle size distribution, anisotropy and interparticle interactions[17]. Although a loss in the saturation magnetization with the reduction of particle size is often observed, the transition gradually becomes smoother, enlarging the working range temperature and the refrigerant cooling power (RCP)[134]. Few reports are dedicated to the study of $Gd_5(Si,Ge)_4$ family compounds at low dimensionality. The fragmentation of Gd_5Ge_4, due to the reduction in the number of magnetic domains per particle, can reduce the hysteresis losses on the system[52]. On the micrometric scale, the ball milling technique allows the production of $Gd_5(Si,Ge)_4$ polycrystalline samples where the particle size can be controlled by increasing the milling time[33,54]. Pires *et al.* showed that $Gd_5Si_{1.3}Ge_{2.7}$ composition reduces its grain size from 6.0 μm to 3.4 μm is increased the milling process from 30 min to 150 min[54]. A direct consequence of highest periods of process promotes the formation of O(I) phase with a SOMT that lead to a 35% reduction on the MCE when compared to the bulk counterpart. For Gd_5Si_4 stoichiometry, the nanometric scale was achieved by milling

the grounded ingot for 4320 min (72 hours); however, with larger amounts of undesired Gd_5Si_3 structure phase, sample amorphization and high levels of oxidation[135]. Although Fe contamination from the balls used during sample preparation was detected, the produced Gd_5Si_4 have already showed its potential to be used as a contrast agent for magnetic resonance imaging (MRI)[136] and as high frequency microwave absorption systems when implemented in silicon-based polymers[137].

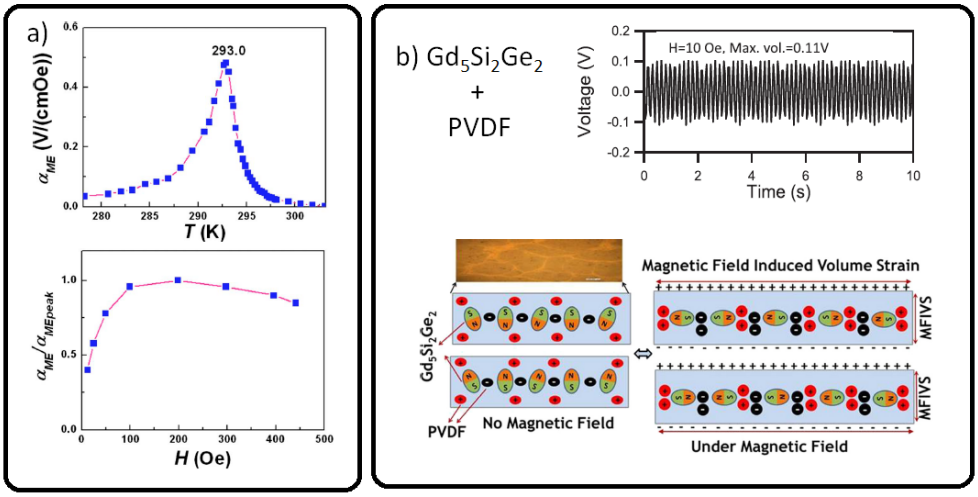

Figure 2.10: The magnetoelectric coupling (in green) is observed in multiphase systems composed of piezoelectric and magnetostrictive materials like $Gd_5Si_2Ge_2$ and PVDF in **(b)**. The strain change of $Gd_5Si_2Ge_2$ under an applied magnetic field induces the an electric polarization on the piezoelectric polymer that generates an output of 0.11 V, that is 4 times higher than the observed for pure PVDF, as detailed on Ref. 24.

The possibilities of applications in energy conversion has already been shown by Ozaydin *et al.* by incorporating low amounts ($<$10%) of $Gd_5Si_2Ge_2$ micropowder in PVDF[24]. Since PVDF is a piezoelectric polymer, its pure film can convert stress into energy with 3.25 mW/cm^{3}Oe of power density while Gd_5Si_2Ge2 has null conversion power alone. However, the combination of these two materials improves the power density to 14.3 mW/cm^3 with 4 weight fraction (wt.%) of filler. The authors concluded that such enhancement comes from a magnetic field induced strain generated by the expansion of $Gd_5Si_2Ge_2$ particles when being magnetised, generating extra electrical polarization from internal strains, which is the mechanism of ME-coupling on composites. Several approaches have been followed to improve the production of PVDF polymers in order to enhance the formation of it piezoelectric features. A more recent study, performed by Harstad *et al.*, revealed that less than 5% volume fraction of Gd_5Si_4 nanoparticles in PVDF improve the formation of the piezoelectric phase and, consequently, the energy conversion efficiency[138]. However, with no evaluation on the ME-effect in this produced type of composite.

Concerning the reduction to the nanometric scale, Sambandam *et al.* reported the first attempt to produce $Gd_5Si_2Ge_2$ thin films by RF magnetron sputtering but the silicon nitride did not prevent the film degradation and the trial was unsuccessful[55]. In 201

Hadimani *et al.* demonstrated that femtosecond pulsed laser deposition allows the production of Gd_5Si_4 granular thin films with 150 nm of average particle size[139]. Although the deposited Pt-layer deposited on top of the film prevented the sample oxidation, the main crystalline phase formation of Gd_5Si_3 phase was a handicap for the MCE properties. A year later, the IFIMUP group in collaboration with Hadimani *et al.* obtained $Gd_5Si_{1.3}Ge_{2.7}$ thin film with ∼790 nm of thickness using the femtosecond pulsed laser ablation technique[6], but still with low amounts of the desired phase and granular surface. Through magnetic measurements, a decrease in the ΔS_{max} value is observed; however, with broader working range temperature and reduction of magnetic hysteresis losses when compared to the bulk counterpart[6]. More recently, a group from Belarus were able to produce $Gd_5Si_2Ge_2$ nanoparticles through laser ablation in liquids using a Nd:Yag nanosecond laser with pulse durations of 8 ns[56]. A particle size of 25 nm was achieved by ablating separately the Gd, Si and Ge pure reagents in different times (40, 15 and 15 min) to then perform a sequential ablation on the colloidal solutions, achieving the desired stoichiometry that was confirmed through magnetic results. However, no evaluation on the MCE and MS behaviours were performed by the authors. These observations reveal that nanosecond pulsed lasers can also be used to produce $Gd_5(Si,Ge)_4$ crystal structures at the nanometric scale.

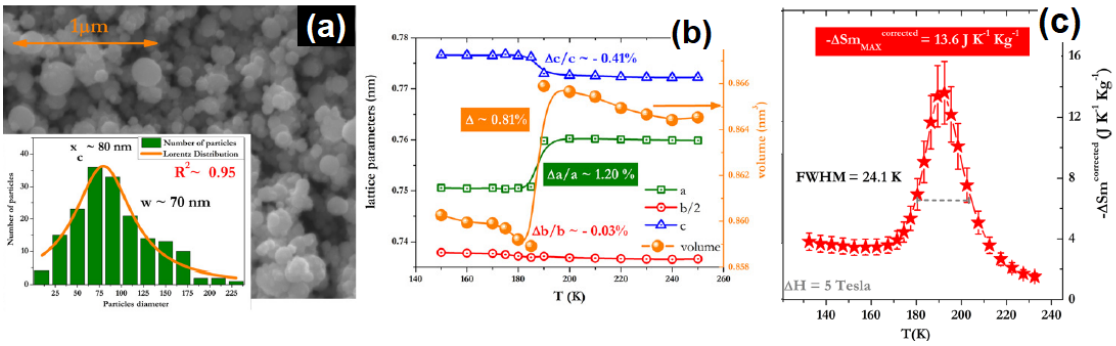

Figure 2.11: Results obtained by Hadimani in collaboration with IFIMUP for $Gd_5Si_{1.3}Ge_{2.7}$ granular thin film produced by fs PLD from Ref. 6. **(a)** SEM images revealed that the grains constituting the film present an average diameter of 70 nm and **(b)** Synchrotron XRD measurements carried out by swiping temperature have shown a magnetostriction along the a-axis of 1.20% (or 1200 ppm) at the structural transition around 190 K. **(c)** The maximum of entropy change for the thin film of 8.81 J/kg.K is lower than obtained for the bulk counterpart (∼43 J/kg.K); however, with a broader working temperature range that lead to an enhanced RCP values, shown in the inset. **(d)** By considering only the amount of O(I)-phase on the magnetization curves, the corrected maximum of this phase enlarges to 13.6 J/kg.K.

Chapter 3

Theoretical Foundations

This Chapter is reserved to present a theoretical framework on the basis of magnetism in solid materials and the thermodynamic approaches on the magnetocaloric and generalized caloric effects that will be important for the results analysis of this work.

3.1 Brief introduction of magnetism

The evidences on the knowledge of magnetism dates from 600 B.C. at ancient Greek schools with magnetites and lodestone[140]. Since the 12^{th} century, these materials were used as a compass on Western Europe. However, it was only after five centuries that scientific investigations on these systems were performed with contributions from important scientists like Gilbert, Gauss, Coulomb and Oersted[141]. The latter mentioned was the first to suggest the connection between magnetism and electricity. Further experimental evidences from Faraday and Ampere were fundamental for the theoretical foundations of electromagnetism developed by Maxwell that integrates the electroweak forces[142]. The Maxwell's equations were essential for the later Hertz findings that light are electromagnetic waves, which had great contributions to the advent of quantum mechanics. Regarding the magnetism in Condensed Matter, the mechanism is described on the basis of theory of relativity and quantum mechanics which is still a great matter of interest from a fundamental point of view nowadays[142].

In solid-state materials, the magnetism originates at the atomic level and it magnetic moment ($\vec{\mu}$) have two contributions: **1)** from the electrons intrinsic spins ($\vec{\mu_S}$) and **2)** from their orbital angular moment ($\vec{\mu_L}$)[141], as illustrated in Fig. 3.1. The $\vec{\mu_S}$ magnitude is defined as:

$$\vec{\mu_S} = -g_S \mu_B \frac{\vec{S}}{\hbar} = \gamma_S \vec{S} \tag{3.1}$$

where $g_S = 2$, $\gamma_S = -e/m_e$ is the spin gyromagnetic factor and $\mu_B = e\hbar/2m_e$ the Bohr magnetron with the value of 9.274$\times$10^{-24} A.m^2, in SI units. Similarly, by definition, μ_L is:

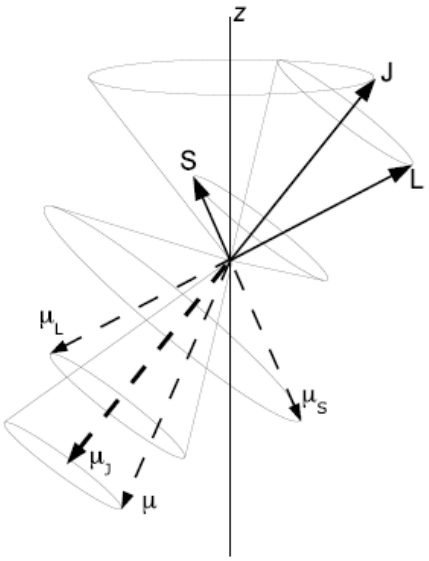

Figure 3.1: Illustration of an electron total angular momentum $\vec{J}$, given by the sum of orbital $\vec{L}$ and spin $\vec{S}$ angular momenta with their associated magnetic moments. Although the total magnetic moment ($\vec{\mu}$) has two components along the $\vec{J}$ direction, only the parallel one contributes to the magnetic energy. Image extracted from Ref. 143.

$$\vec{\mu_L} = -g_L \mu_B \frac{\vec{L}}{\hbar} = \gamma_L \vec{L} \tag{3.2}$$

with $g_L = 1$ and $\gamma_L = -e/2m_e$ being the orbital gyromagnetic factor. In the same way, taking the total angular moment $\vec{J} = \vec{S} + \vec{L}$, the total magnetic moment :

$$\vec{\mu_J} = -g_J \mu_B \frac{\vec{J}}{\hbar} = \gamma_J \vec{J} \tag{3.3}$$

where g_J is the Landé factor to be defined.

Considering the Zeeman Hamiltonian for an electron under an uniform applied magnetic field, the total magnetic moment $\vec{\mu}$ is then given as[143]:

$$\vec{\mu} = \vec{\mu_S} + \vec{\mu_L} = -\frac{\mu_B}{\hbar}(g_S \vec{S} + g_L \vec{L}) \tag{3.4}$$

The magnetic moment precess along the total angular momentum $\vec{J}$ direction; however, the contribution to the magnetic energy is given only by the parallel component (see Fig. 3.1). Thus, multiplying both sides of the equation above by the unitary vector $\hat{J} = \frac{\vec{J}}{J}$, we obtain:

$$\vec{\mu} \cdot \hat{J} = \mu_J = -\frac{\mu_B}{\hbar}\left(\frac{\vec{S} \cdot \vec{J}}{J} + \frac{\vec{L} \cdot \vec{J}}{J}\right) \tag{3.5}$$

Since $\vec{J} = \vec{S} + \vec{L}$,

$$\vec{S}^2 = (\vec{J} - \vec{L}) \cdot (\vec{J} - \vec{L}) = \vec{J}^2 + \vec{L}^2 - 2\vec{L} \cdot \vec{J} \tag{3.6}$$

and

$$\vec{L}^2 = (\vec{J} - \vec{S}) \cdot (\vec{J} - \vec{S}) = \vec{J}^2 + \vec{S}^2 - 2\vec{S} \cdot \vec{J} \tag{3.7}$$

Hence, substituting these relations in 3.1, we have:

$$\mu = -\frac{\mu_B}{2\vec{J}^2\hbar}(3\vec{J}^2 - \vec{L}^2 + \vec{S}^2) \tag{3.8}$$

Comparing it with Eq. 3.1, the Landé factor is then:

$$g_J = \frac{3\vec{J}^2 - \vec{L}^2 + \vec{S}^2}{2\vec{J}^2} \tag{3.9}$$

The eigenvalues of the square angular moments are $j(j+1)$, $l(l+1)$ and $s(s+1)$; thus, the above equation is written as[143]:

$$g_j = 1 + \frac{j(j+i) - l(l+1) + s(s+1)}{2j(j+1)} \tag{3.10}$$

Furthermore, the magnetization of a solid material with volume V is the sum of all μ contributions, defined as follows[143]:

$$M = \frac{\sum_i \mu_i}{V} \tag{3.11}$$

Experimentally, M is measured as A/m (SI) or emu/cm^3 (CGS); however, in this work, the mass magnetization in emu/g is also used, for practical reasons.

Another important quantity that can be experimentally obtained for a material under an applied magnetic field with intensity H is the material magnetic susceptibility (χ), that is defined as:

$$\chi = \lim_{H \to 0} \frac{\partial M}{\partial H}. \tag{3.12}$$

Furthermore, the response of a solid material to H will depend on the interactions between the different magnetic moments that can lead to the observation of different rearrangements; however, for the present work, three of them will be relevant and are listed below[141,143]:

- **Diamagnetism (DM):** is a weak and non-cooperative arrangement. Under the influence of an applied magnetic field, the magnetic moments align along the opposite direction in order to repeal induced fields inside the system. This type of ordering presents negative magnetic susceptibility and is intrinsic of all materials and the magnetic moment values are constant in temperature;
- **Paramagnetism (PM):** is a non-cooperative ordering where, in the presence of an

applied magnetic field, the alignment of the magnetic moments - that are initially randomly oriented - occurs along the field direction up to the saturation (M_S). If the field is held constant and the temperature is increased, the thermal vibrations reduce the magnetization value towards zero. For this arrangement, the magnetic susceptibility is given by the Curie law:

$$\chi = \frac{C}{T} \tag{3.13}$$

where, C is the Curie constant, defined as:

$$C = \frac{N\mu_0\mu_{eff}^2}{3k_B} \tag{3.14}$$

with N being the number of magnetic active ions, μ_0 the vacuum permeability, k_B the Boltzmann constant. The paramagnetic effective moment μ_{eff} is given in terms of the total angular moment J and the Landé g-factor, as follows:

$$\mu_{eff}^2 = g^2 J(J+1)\mu_B^2 \tag{3.15}$$

Commonly, the inverse susceptibility (or reciprocal magnetic susceptibility) as a function of temperature is used to classify different magnetic arrangement. In the case of paramagnetism, this quantity has a linear trend, as can be seen in Fig. 3.2;

- **Ferromagnetism (FM):** distinctly from the above mentioned, this arrangement is cooperative: the magnetic behaviour will depend on the atoms magnetic moments of the neighbours. It is characterized by two basic parameters: *1)* the Curie temperature (T_C) - that is the critical point where the material transits from a ferromagnetic to a paramagnetic state. This transition can be classified as a first order, whit an associated latent heat due to the structural transformations, ore as second order with a more smooth change on the magnetization values[144]. The distinction between these cases will be treated on Section 3.1.2. Furthermore, below T_C, the material presents a spontaneous magnetization that increases, reaching *2)* the saturation magnetization as the applied magnetic field increases, as can be seen in Fig. 3.2. Due to the magnetic moments interactions, an internal magnetic field is generated inside the system that allows the ensemble to reach saturation for small applied magnetic fields. As the temperature increases, the volumetric magnetization reduces until zero values at T_C and the magnetic susceptibility is given by the Curie-Weiss law:

$$\chi = \frac{C}{T - \theta_P} \tag{3.16}$$

where θ_P is the paramagnetic Curie temperature. The reciprocal magnetic susceptibility follows a linear trend and $T > \theta_P > 0$[143].

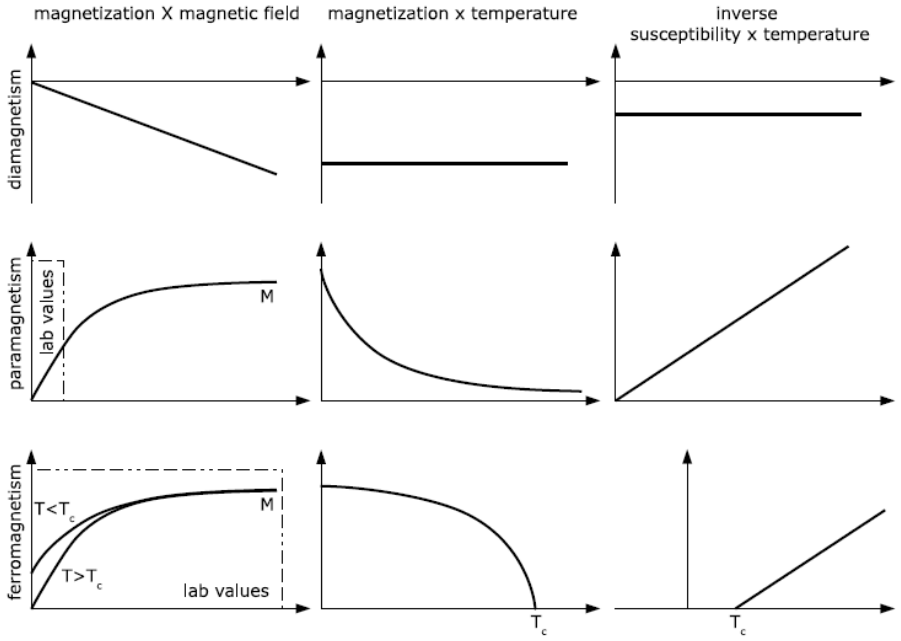

Figure 3.2: Qualitative illustration on the magnetic arrangements of solid materials. The magnetic moments behaviour is given as a function of applied magnetic field and temperature and the inverse susceptibility trend as a function of the temperature. Schemes extracted from Ref. 143.

3.1.1 The magnetic susceptibility in multiple-phase materials

For the production of intermetallic alloys with the standard techniques, the quality of the reactants elements and the experimental parameters are determinant to obtain single-phase samples. In particular, for the case of $R_5(Si,Ge)_4$ compounds, the fast cooling after melting for the alloying led to the formation of secondary $R_1(Si,Ge)_1$ and $R_5(Si,Ge)_3$ phases[145]. For compositions with similar amounts of Si and Ge, the formation of a single-phase sample with the expected monoclinic phase also requires a systematic control on the parameters during synthesis[42]. As a matter of fact, even miniaturization techniques can lead to products with more than one crystallographic phase, as observed for $Gd_5Si_{1.3}Ge_{2.7}$ nanoparticles with $\sim$80 nm[6]. However, the presence of different phases can be detected through magnetic measurements and can be used to confirm crystallographic results.

In these systems, the magnetic moments are localized with long-range RKKY-type exchange interactions. At the paramagnetic state, there is only non-cooperative interactions which allows to write the total magnetization of a material by summing up each phase contribution: $M_T = \sum_i x_i M_i$. Considering the Curie constant (C_i) and the paramagnetic Curie temperature (θ_P^i) of each crystallographic phase amount (x_i), the magnetic susceptibility can be written as[113,143]:

$$\chi = \frac{x_1 C_1}{T - \theta_P^1} + \frac{x_2 C_2}{T - \theta_P^2} + \cdots + \frac{x_n C_n}{T - \theta_P^n} = \sum_{i=1}^{n} \frac{x_i C_i}{T - \theta_p^i}. \tag{3.17}$$

Since, by definition, the linear region of the reciprocal magnetic susceptibility is given at the $H \rightarrow 0$[143], the calculations using the above equation should be performed on magnetization values obtained for small applied fields. The free parameters for the calculations are x_i, C_i and θ_P. However, with the constraint $\sum_i x_i = 1$. The Curie constant also gives the values of paramagnetic effective moment of each phase by using Eq. 3.14. Indeed, μ_{eff} values are essential for the confirmation of the method once it values should be close for the expected on the active magnetic ions. As for θ_P, since we are not dealing with an ideal system, it should at least be close to T_C.

3.1.2 Phase transitions

The order of a magnetic transition for the present work will be evaluated via Arrott plot using the Banerjee criteria[146]. According to Ehrenfest[147], the order of a phase transition can be determined by analysing the free Gibbs energy $F(T,p)$. If the first derivatives, $(\partial F/\partial T)_p = -S$ and $(\partial F/\partial p)_T = V$, are discontinuous the transition is classified as the first order. For magnetic materials, the description is given by the Landau theory that is build in two principles: *1)* the free energy (*F*) should be analytical and *2)* follows the Hamiltonian symmetry[143]. Considering a ferromagnetic system under an applied magnetic field *H*, *F* can be expanded in a potential series of magnetization *M* around the critical temperature (T_C) as follows:

$$F(M) = -HM + F_0 + \alpha(T)M^2 + bM^4 + ... \tag{3.18}$$

where F_0 and *b* are constant and α(T) will depend on temperature. At the vicinity of T_C, $\alpha(T)$ can be written as $\alpha(T - T_C)$, where $\alpha > 1$ and null in T_C. Using the equilibrium conditions for the free energy minimization for magnetization:

$$2aM + 4bM^3 = H \tag{3.19}$$

At the transition, the above equation is reduced to:

$$\frac{H}{M} = BM^2 \tag{3.20}$$

where the $B = 4b$ is the parameter that will allow the order determination according to Banerjee criteria[146]. Thermodynamic analysis reveal that for FOMT, B must be negative and H/M *versus* M^2 curve should have a decreasing behaviour. The distinction between a FOMT and SOMT Arrott plot curves can be seen in Fig. 3.3. The pros and cons of each material will be exposed by comparing practical results reported in MR prototypes.

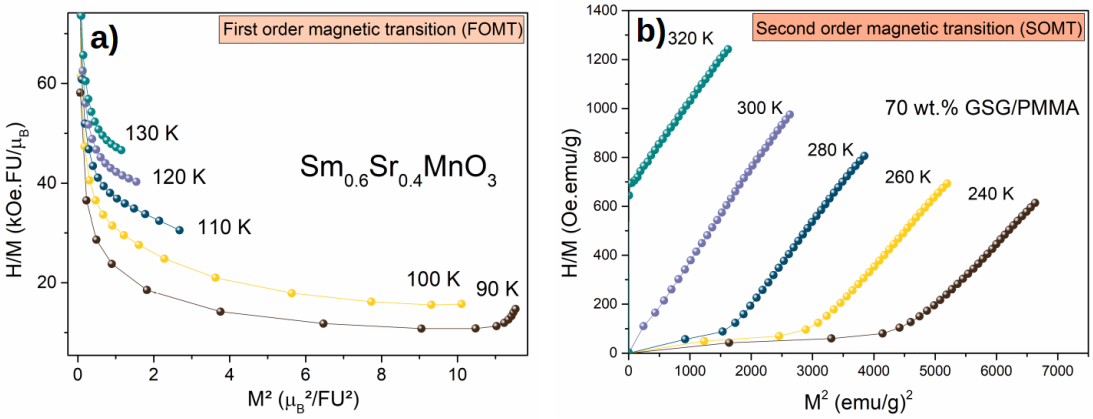

Figure 3.3: Arrott plot curves for **(a)** the bulk of $Sm_{0.6}Sr_{0.4}MnO_3$ with a negative slope (obtained from Ref. 44) and, consequently FOMT; the positive slope is observed for $Gd_5Si_{2.4}Ge_{1.6}$ composite with a SOMT that will be discussed at the results of this work.

3.2 The Magnetocaloric Effect

The magnetocaloric effect (MCE) was first observed by Weiss and Piccard in Ni[19], the process is analogous to the exchange heat when a fluid is in influence of pressure. However, in magnetic materials the thermal variations are generated by the spin-lattice coupling. As previous mentioned, materials with large caloric potentials (ΔS_{iso} and ΔT_{ad}) present a strong coupling between magnetic and electric states. The total entropy of a magnetic material for a certain temperature and magnetic field will have contributions from the phonons of crystal lattice vibrations (S_L), magnetic states of the sub-lattice (S_M) and from the free electrons (S_E) of the system:

$$S_T(T,H) = S_M(T,H) + S_L(T) + S_E(T) \tag{3.21}$$

For the purposes of ΔS_{iso} calculations, the electronic entropy contribution can be neglected and the MCE will be described in terms of the interplay between lattice and magnetic excitations. A refrigeration cycle combining isothermal and adiabatic process are illustrated in Fig. 3.4(a)-(d). When the magnetic field is applied adiabatically, there is a reduction on the magnetic entropy of the material (S_M). Thus, in order to conserve the total entropy of the system, the lattice entropy (S_L) should increase, consequently, leading to a ΔT_{ad}[98]. At this stage, a fluid (such as water or ethanol) can be used to remove heat from the material in an adiabatic process once $\Delta S_{iso} = \Delta Q/T$, Fig. 3.4(b). By reducing the magnetic field intensity adiabatically to null, the temperature of material decreases [Fig. 3.4(c)] and later absorbing heat from the exchanger fluid [Fig. 3.4(d)].

From a practical point of view, the magnetocaloric potential in adiabatic process ΔT_{ad} can be directly measured using a thermometer or indirectly from specific heat measurements. However, for isothermal process, ΔS_{iso} can only be indirectly determined using magnetization or specific heat measurements. Both quantities can be observed from a magnetic entropy diagram as a function of temperature with and with-

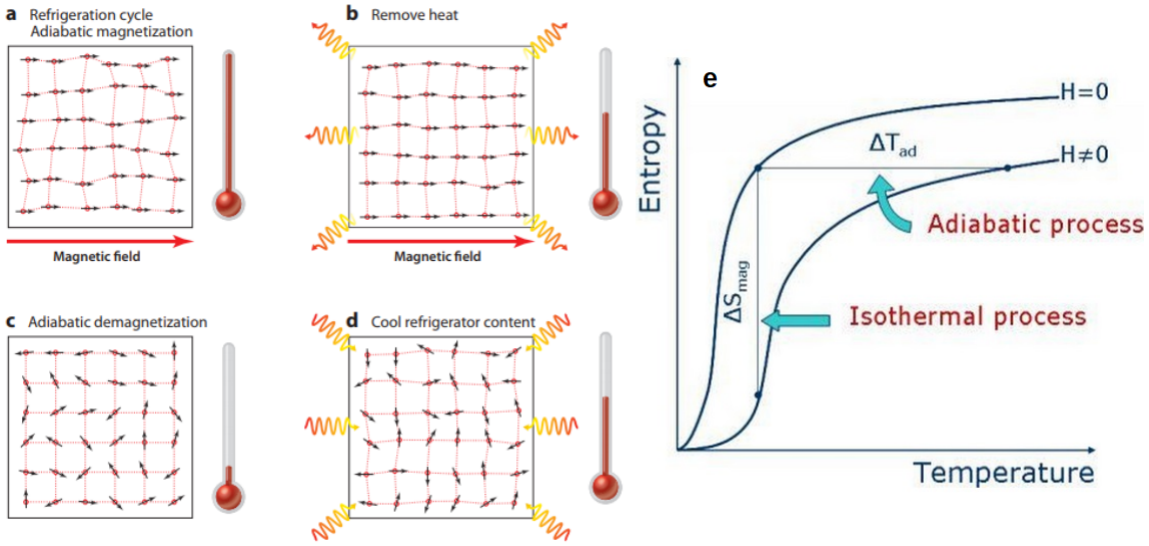

Figure 3.4: Illustration of a refrigeration cycle where **(a)** the magnetic field is applied adiabatically, increasing the material temperature. The heat is removed by using a heat exchanger fluid **(b)** and the material temperature reduces when the magnetic field is completely removed **(c)**. After that, the material will absorb heat from the heat source/exchanger fluid **(d)**. The images were extracted from Ref. 98.**(e)** Magnetic entropy diagram as a function of temperature for a magnetic material with and without applied field. It is possible to observe the magnetocaloric quantities for adiabatic (ΔT_{ad}) and isothermal (ΔS_{iso}) processes. The images were extracted from Ref. 148.

out magnetic field, as shown in Fig. 3.4. The lattice and electronic contributions for entropy can be neglected for the systems in this work. In that way, the total entropy variation of the systems will be equivalent to the magnetic entropy change[149]. For the present work, the MCE quantities will be obtained from magnetization as a magnetic field function for different temperatures.

For a qualitative determination of ΔS_{iso}, we can use the thermodynamic Maxwell relation below that take into account the applied magnetic field (H) and the temperature (T)[21]:

$$\left(\frac{\partial S(T,H)}{\partial H}\right)_T = \left(\frac{\partial M(T,H)}{\partial T}\right)_H \tag{3.22}$$

Integrating this relation from an initial magnetic field H_0 to the final one H_F, we obtain:

$$\Delta S_{iso}(T)_{\Delta H} = \int_{H_0}^{H_F} dS(T,H)_T = \int_{H_0}^{H_F} \left[\frac{\partial M}{\partial T}\right]_H dH \tag{3.23}$$

It is worth pointing out that ΔS_{iso} depends on the temperature derivative of magnetization and, for this reason, MCE is maximum around the transition temperature. Simple FM and PM materials, in a presence of a constant magnetic field, have their magnetization value decreased by increasing temperature. Given that, $(\partial M/\partial T)$ has a negative value and also ΔS_{iso}, consequently, as can be seen in Fig. 3.4. Materials with FOMT present a discontinuity in $(\partial M/\partial T)$ and a more careful attention is required for both ex-

perimental measurements and calculations[143]. In cases of non-equilibrium conditions, like large irreversibility on the isothermal curves, overestimated values can be obtained and the use of different modelling methods like Landau and mean field theory should be used for corrections[150]. On the other hand, for compounds with a SOMT, Eq. 3.2 can be used without problems, once $(\partial M/\partial T)$ is continuous[21].

Hence, isothermal magnetization measurements as a function of applied magnetic field it is possible to calculate the MCE. Considering that each curve at a temperature T is measured in a magnetic field that variates by $\Delta H = H_F - H_0$ in a constant step δH, it is possible to integrate numerically Eq. 3.2 using a trapezoidal rule:

$$\Delta S_{iso}(T) = \frac{\delta H}{2\delta T}\left(\delta M_0 + 2\sum_{i=2}^{n-1}\delta M_k + \delta M_n\right) \tag{3.24}$$

wherein $\delta T = T_{i+1} - T_i$ is the temperature difference between the two isothermal under consideration and *n* is the number of points for each curve. All the quantities in Eq. 3.2 are represented in Fig. 3.5.

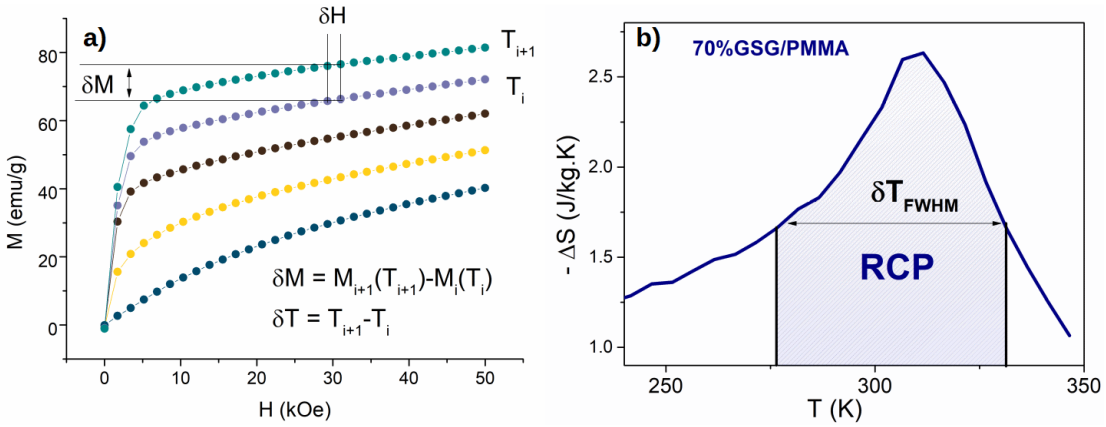

Figure 3.5: **(a)** A set of isothermal curves and an indication of the quantities used to calculate MCE potential ΔS from the Eq. 3.2. **(b)** The resulted $-\Delta S(T)$ curve for the composite produced in this work (Chapter 6) is shown with the determined full width at half maximum (FWHM) used for the RCP calculation.

An important factor to determine the material efficiency on heat transfer, is the refrigerant cooling power (RCP). It is a quantity defined as the refrigeration power per unit of volume, and is determined through the integration at the full width at half maximum (FWHM) of $\Delta S_{iso}(T)$ curve as follows[21]:

$$RC = \int_{\delta T_{FWHM}} \Delta S_{iso}(T)dT \tag{3.25}$$

Fig. 3.2(b) illustrates the Eq. 3.25 for a composite sample with a SOMT prepared in this work. As can be noted, broader working ranges temperatures can compensate reductions on the maximum of entropy changes on the RCP values that can be advantageous for MR applications at room temperature. For engineering purposes, the magnetic material must fulfil a series of properties in order to be used as cooling material, such as

(i) Curie temperature near working temperature, (ii) no thermal or magnetic hysteresis, (iii) broader working temperature, (iv) low manufacturing costs for commercial viability, etc[21,151].

3.3 Generalized thermodynamic for caloric effects

The theory on the multicaloric effect in multiferroic materials was first demonstrated by M. Vopson in 2012 that have later published a generalized analytical thermodynamic description in 2013[152,153]. Since then, several theoretical models and experimental results have been published focused on a better understand on the behaviour of ferroic orderings in multiferroic materials[66,77,85,154–156]. The thermodynamic parameters of caloric effects in a solid-state system is given by the adiabatic temperature and isotherm entropy changes under the application of a field X_i. For this, we should write the internal energy in terms of the entropy and its conjugated quantity x_i, $U = U(S,[X_i])$ given by the first thermodynamic law:

$$dU = TdS + \sum_{i}^{n} x_i dX_i, \tag{3.26}$$

with the extensive variable x_i defined as:

$$x_i = \left(\frac{\partial U}{\partial X_i}\right)_{S,X_j \neq X_i}. \tag{3.27}$$

The general term X_i represents the applied forces such as mechanical stress (σ), magnetic field (H), electric field (E), etc. While x_i corresponds to the generalized variables associated to this forces like strain (x), magnetization (M), polarization (P), and so on. The first term of Eq. 3.3 represents the exchanged heat by the system $Q = TdS$ that will be use to obtain the relation for adiabatic temperature change of multicaloric materials. According to Vopson, free Gibbs energy (F) is the most suitable potential to describe the caloric effect once relates temperature and external field/forces that are more accessible, from an experimental point of view[153]. Using the Legendre transformation $F(T,[x_i]) \equiv U(S,[x_i]) - ST - \sum X_i x_i$, the differential form of F is than:

$$dF = -SdT - \sum_{i}^{n} X_i dx_i \tag{3.28}$$

where, the entropy and generalized extensive variable term can be written as follows:

$$S = -\left(\frac{\partial F}{\partial T}\right)_{x_j, j\neq i} \tag{3.29}$$

$$X_i = -\left(\frac{\partial F}{\partial x_i}\right)_{T, x_j, j\neq i}. \tag{3.30}$$

From the combination of (1.4) and (1.5) derivative forms, we obtain the generalized Maxwell relations:

$$\left(\frac{\partial S}{\partial x_i}\right)_{T, x_{j,j\neq i}} = \left(\frac{\partial X_i}{\partial T}\right)_{x_j} \tag{3.31}$$

$$\left(\frac{\partial X_j}{\partial x_i}\right)_{T, x_{j,j\neq i}} = \left(\frac{\partial X_i}{\partial x_j}\right)_{T, x_i} \tag{3.32}$$

The relation 3.31 is the starting point to indirectly determine the isotherm entropy change in terms of the experimentally accessible parameters. For example, by measuring the polarization generated by electric fields in different temperatures, $(\partial P/\partial T)_E$ can be determined[157]. However, to directly achieve the caloric effect, we must define the specific heat of the system under a constant field:

$$c_x = T\left(\frac{\partial S}{\partial T}\right)_x. \tag{3.33}$$

Assuming $S = S(T,[x_i])$ and using the Maxwell relation 3.31, the total differential equation can be written as follows:

$$dS = \left(\frac{\partial S}{\partial T}\right)_{x_i} dT + \sum_i^n \left(\frac{\partial S}{\partial x_i}\right)_{x_{j\neq i}} dx_i \tag{3.34}$$

$$dS = \frac{c_x}{T} dT + \sum_i^n \left(\frac{\partial X_i}{\partial T}\right)_{x_i} dx_i. \tag{3.35}$$

Thus, if the field is applied adiabatically, $dQ = TdS = 0$, or isothermally the term dT is zero. Applying these conditions to Eq. 3.3, the adiabatic temperature (ΔT_{ad}) and isothermal entropy (ΔS_{iso}) changes, that characterize a caloric process, will have the generalized integration forms:

$$\Delta T_{ad} = -\frac{T}{c_x} \sum_i^n \int_{x_0}^{x_f} \left(\frac{\partial X_i}{\partial T}\right)_{x_i} dx_i \tag{3.36}$$

$$\Delta S_{iso} = \sum_i^n \int_{x_0}^{x_f} \left(\frac{\partial X_i}{\partial T}\right)_{x_i} dx_i \tag{3.37}$$

In materials presenting simultaneous primary ferroic ordered states, the cross-coupling effects, like magnetoelectric effect where the interplay between magnetic and electric orderings occurs, as illustrated in Fig. 3.3. For this, we must assume a linear coupling between intensive and extensive variables X_i and x_i, respectively, where the coefficient can be defined as:

$$\left(\frac{\partial X_j}{x_i}\right)_{T,x_{j\neq i}} = \left(\frac{\partial X_i}{\partial x_j}\right)_{T,x_{i\neq j}} = \alpha_{ij} = \alpha_{ji} = \alpha. \tag{3.38}$$

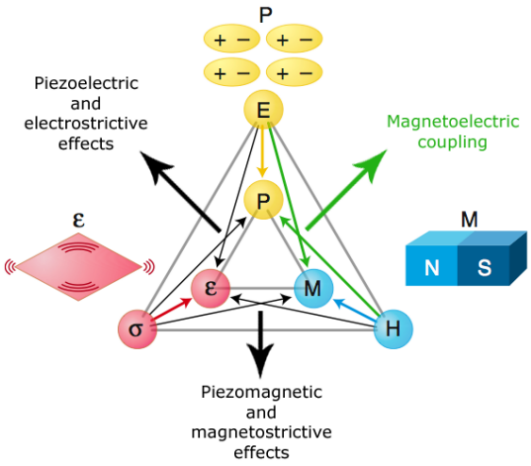

Figure 3.6: **(a)** Primary ferroic orders: *i)* ferroelectric with the polarization (P) as a response of an electrical field, *ii)* ferromagnetism with the magnetization (M) driven by a magnetic field (H) and *iii)* ferroelastic with a strain variation (ϵ) due to a mechanical stress (σ) - Illustration extracted from Ref. 158

This particular feature of multiferroics is the reason for the interest on applying them on solid-state caloric effect since it can present multiple responses to only one applied field. As pointed by Vopson on the response to a rebuttal, these coupled effect and entropy change are undisputed effects[159]. For instance, an applied magnetic field can induce an electric polarization at the material and vice versa. According to Eq. 3.3, an applied field x_j will modify not only it conjugated parameter X_j but also lead to an induced field x_i as: $dX_j = \alpha_{ji} dx_i$. For such cases, we can separate the components in Eq. 3.36 and 3.37 to take into account the contributions from coupled effects:

$$\Delta T_{ad} = -\frac{T}{c_x}\left[\sum_{i;i\neq j}\int_{x_i}\left(\frac{\partial X_i}{\partial T}\right)_{x_j} dx_i + \int_{x_j}\left(\frac{\partial X_j}{\partial T}\right)_{x_i} dx_j\right] \tag{3.39}$$

$$\Delta S_{iso} = \sum_{i,i\neq j}\int_{x_i}\left(\frac{\partial X_i}{\partial T}\right)_{x_j} dx_i + \int_{x_i}\left(\frac{\partial X_j}{\partial T}\right)_{x_i} dx_j \tag{3.40}$$

In a linear approximation, the generalized susceptibility is defined as $(\partial X_i/\partial x_i) = \chi_i$; thus, combining it with the cross-coupling coefficient in Eq. 3.3, we have:

$$dx_i = \frac{\alpha_{ij}}{\chi_i} dx_j. \tag{3.41}$$

Including Eq. 3.3 in 3.40 and 3.39 relations, the multicaloric effect can be written in terms of cross-coupling coefficients and susceptibilities as follows:

$$\Delta T_{ad} = -\frac{T}{c_x} \sum_{i;i\neq j} \int_{x_j} \left[\frac{\alpha_{ij}}{\chi_i} \left(\frac{\partial X_i}{\partial T} \right)_{x_j} + \left(\frac{\partial X_j}{\partial T} \right)_{x_i} \right] dx_j \tag{3.42}$$

$$\Delta S_{iso} = \sum_{i;i\neq j} \int_{x_j} \left[\frac{\alpha_{ij}}{\chi_i} \left(\frac{\partial X_i}{\partial T} \right)_{x_j} + \left(\frac{\partial X_j}{\partial T} \right)_{x_i} \right] dx_j \tag{3.43}$$

These relations reveal that the interplay between the primary ordered phases in a multiferroic material plays an important role on the multicaloric effect[153]. However, a fully comprehension on the mechanism behind such feature is still under development. As a matter of fact, there has been a significant interest in this research topic on scientific community in the last couple of years[5,86,155].

Chapter 4

Experimental Techniques

The experimental approaches for the studies of this work will be given in this Chapter that is divided into two Sections: the first for bulk, micro- and nanoparticles samples production and the second to approach the characterization techniques for the samples features evaluation.

4.1 Sample preparation

4.1.1 Bulk synthesis: arc melting technique

The arc melting technique is commonly used for the production of intermetallic materials due to its simplicity and effectiveness. For the present work, several bulk samples were prepared using standard arc-melting furnaces at Centro de Materiais da Universidade do Porto (CEMUP), Instituto de Física da Universidade Federal Fluminense (IF-UFF) and the Departamento of Eletrônica Quântica at UNICAMP - Brazil. Particularly, for the $Gd_5(Si,Ge)_4$ family compounds some precautions are to avoid oxidation and secondary phases formation, as will be exposed.

The used systems in this work are basically composed by a water cooled Copper plate and a Tungsten tip connected with a high power supply isolated in a high vacuum chamber, as in Fig. 4.1. The samples are prepared inside the Copper plate cavities, the so called crucibles. For this, the amount of each constituent element are accurately weighted for the production of ingots with 3 g of the desire stoichiometry with 5:4 ratio of R:(Si+Ge). After cleaning the starting metals, they are inserted at the crucibles by choosing the volatile ones at the bottom to avoid losses during the melting. Among all the reactants, Gd is the more problematic due to it high reactivity with oxygen. Because of this, additionally to the high vacuum pump ($\sim 10^{-8}$ mbar) and three or four purges with Ar gas ($\sim$0.5 bar), a Ti ingot (with almost the same weight as the produced sample) is used to absorb the remnant O_2 at the chamber during synthesis.

The absence of oxygen in the chamber is important for a meticulous control of the arc during process. For the discharge, an Ar atmosphere of $\sim$1 bar is required with the

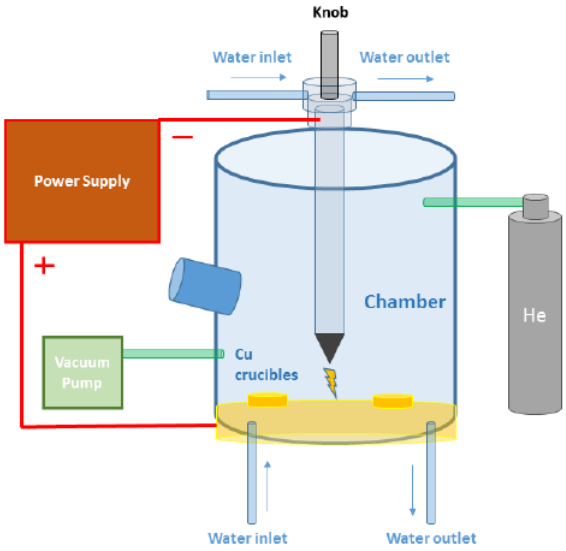

Figure 4.1: Generic scheme of an arc melting furnace with a water-cooled Copper vessel, a Tungsten tip connected in a high power source controlled by the knob. In one of the crucibles, a Ti ingot is used to absorb the remnant O_2 in the chamber.

Tungsten tip at a ∼2 cm distance from the Copper plate. Typically, the applied current intensity ranges from 80 to 100 A and the temperature inside the chamber can reach ∼ 2000-3000 ^{o}C. The tip is then first put on top of the Ti ingot for a few seconds to stabilize the arc and reduce the amount of O_2. When the arc is well stated, it can be approximated to the metals and a single button is formed. It is important to check if the water flow is passing through the Cu crucibles to avoid overheating the system and sample weight losses. With temperatures around 10-15 ^{o} C, the formed buttons are cooled down in a non-homogeneous way. The ingots need to be melted three times, by turning the side after each round in order to ensure a good homogeneity degree. At the end of this process, the obtained bulk of $Gd_5(Si,Ge)_4$ compounds are crystallized and the weight losses should be less than 3% to ensure the correct stoichiometry. Furthermore, for the crystallographic and magnetic characterization, a small piece of the ingot is cut off and grounded as will be further exposed.

4.1.2 Composites synthesis: solvent casting technique

Polymer composite samples were prepared via solvent casting technique by Dr. Nathalie Barroca using $Gd_5Si_{2.4}Ge_{1.6}$ microparticles[160]. For this, the chosen composition was first produced by arc-melting with the method aforementioned. No heat treatment was performed on the obtained as-cast ingot (bulk sample). The bulk was then grounded and sifted through several filters with hole sizes from 50 μm to 5 μm to obtain a thinner powder and to ensure a homogeneous dispersion on the polymer solution. As will be further shown through SEM images, in Chapter 6, the obtained powder is composed by particles with average sizes of 3.4 μm. The composite solutions were prepared

by dissolving poly(methyl methacrylate) (PMMA) in dichloromethane (DCM) (Sigma, 270997-1L) at 40^{o}C until complete dissolution in order to obtain a 10% PMMA solution, (1)$\longrightarrow$(2) steps in Fig. 4.2. Afterwards, composite solutions with GSG weight fractions of 10, 30, 50 and 70% were obtained by simply dispersing the GSG microparticles in the PMMA solution, (3)$\longrightarrow$(4) steps. The composite solutions were then solvent cast in order to obtain a polymer film after the evaporation and drying of the used solvent, step (6)$\longrightarrow$(7). A similar process was used to produce the polyvinylidene fluoride (PVDF) composites. However, for the PVDF (Alfa Aesar, 44080) powder dissolution dimethylformamide (DMF) (Sigma, 227056-1L) was used and the final solution was obtained with 30 wt.% with 1 ml. After include 2 wt.% and 12 wt.% of $Gd_5Si_{2.4}Ge_{1.6}$ micropowders, the solution was solvent cast and dried at 40 ^{o}C in order to improve the formation of the piezoelectric phase[161].

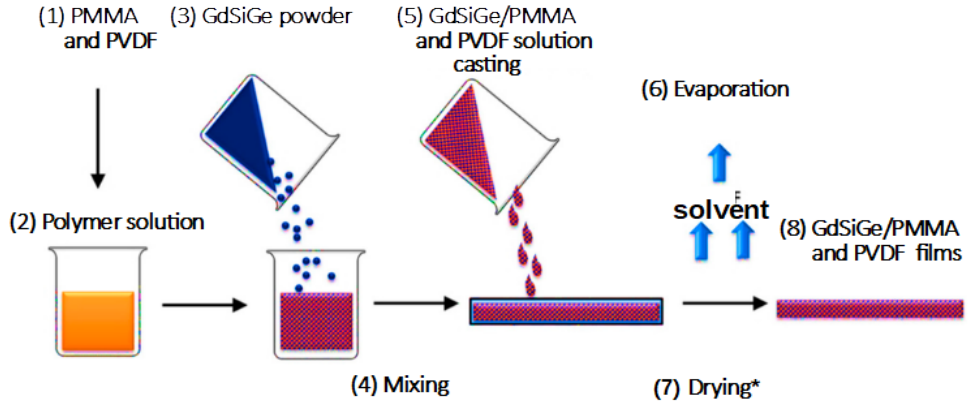

Figure 4.2: Illustration on the steps for the production of GSG/PMMA and PVDF composite samples. First, the polymer dissolution in solvent (DMC for PMMA and DMF for PVDF) followed by the mixture and solvent casting the resulted solution. For the drying and evaporation of PVDF, the solution was kept at 40^{o}C in order to improve the piezoelectric phase formation.(Adapted from Ref. 160.)

4.1.3 Nanoparticles synthesis: Pulsed Laser Deposition (PLD)

Pulsed laser ablation techniques has been widely used for the production of complex materials at reduced dimensions such as thin films, multilayers systems, nanostructures, colloidal solutions. Since 1960's the research on these products focus on several studies aiming a variety of technological applications[162]; among them, it is possible to mention biomedical applications, sensing/actuators, superconducting films, microelectronics[163,164]. Although it popularization occurred in the late 80's with the growth of superconducting high T_C oxides[165], the simplicity for setup implementation without the requirement of chemical products are some of the attractive features of this technique in material science research. One of the main advantages of using pulsed laser deposition (PLD) relies on the stoichiometry transfer from target to the deposited ablation product, allowing the growth of complex materials[162].

The PLD setup consists basically in a laser beam, with high energy density, that is focused onto the target inside a vacuum chamber, as shown on the scheme in Fig. 4.3(a). If the beam energy exceeds the material ablation threshold, it will locally heat the target leading to the melting, vaporization, ions ejection forming the plasma and it further expansion, as explained in Fig. 4.3(a) for some laser features. Conventional lasers can have pulse durations within intervals of a few femtoseconds up to 25 nanoseconds that will be dominate on the laser-target interaction. Ultrafast lasers are more efficient for plasma formation since a pulse duration of a femtosecond beam is shorter than the electron to ion energy transfer time giving no time for the laser-induced plasma interaction. Zeng *et al.* have experimentally verified the plasma dynamics in Si target by ablating with fs Ti:Sapphire femtosecond laser and a quadruplet Nd:YAG laser with 100 fs and 3 ns pulse width, respectively, and the same energy of 220 μJ per pulse[166]. The laser-generated shock wave propagation after 10 ns for both laser shots are shown in Fig. 4.3(b)-(c). As can be noted, fs laser induced plasma expands perpendicularly to target surface while for the ns laser, it will expands spherically. Additionally, for the ns beam, a fraction of it energy is absorbed by the induced plasma leading to large temperatures as compared with fs pulse laser, where there is no induced plasma-laser interactions. The typical characteristic thermalisation time of materials is around ps and, for that reason, the depth diffusion will be lower for short pulse widths with a minimal surface damage and fully energy absorption[166]. The difference on the formed craters for fs and ns can be seen in Fig. 4.3(d) and (e) where the penetration depth is clearly higher for the last one.

After plasma formation, the chamber conditions will rule the vapour dynamic and, consequently, the product of this ablation. For instance, in ultra-high vacuum (UHV) the plasma will travel longer distances, as can be seen in Fig. 4.3(f) for Al target in vacuum where the spatial distribution of material expands freely. The UHV ($\sim 10^{-9}$ Torr) condition are used for thin film deposition and the substrate is positioned far from target, typically 2-10 cm[169]. It is also possible to use reactive gases for the growth of complex oxides thin films; as a matter of fact, the gas flux influences the deposition rate of material. For instance, hematite growth by ablation of pure Fe with an KrF excimer laser can have the deposition rate improved from 0.095 nm/s to 0.168 nm/s by increasing the O_2 pressure in the chamber from 50 mTorr to 25 mTorr[170]. Furthermore, from the snapshots in Fig. 4.3(f), is clear that the background Ar gas compresses the vapour dissappearence small and mid-size clusters at the front part of the plume (range 1-1.5 μm)[168]. By using a low pressure gas (0.2-10 Torr) of inert gas, the atoms mean free path is short and the nanoparticles are formed before reaching the substrate through: *i)* nucleation of at least three atoms or molecules that will be the core for *ii)* the atoms condensation at the nuclei surface, clustering it and leading to particle formation. Further nuclei and molecules random collisions, can increase the surface energy exchange leading to *iii)* coagulation of small particles that can saturate and, if the chamber temperature is too high, the *iv)* grains agglomeration can occurs. A way

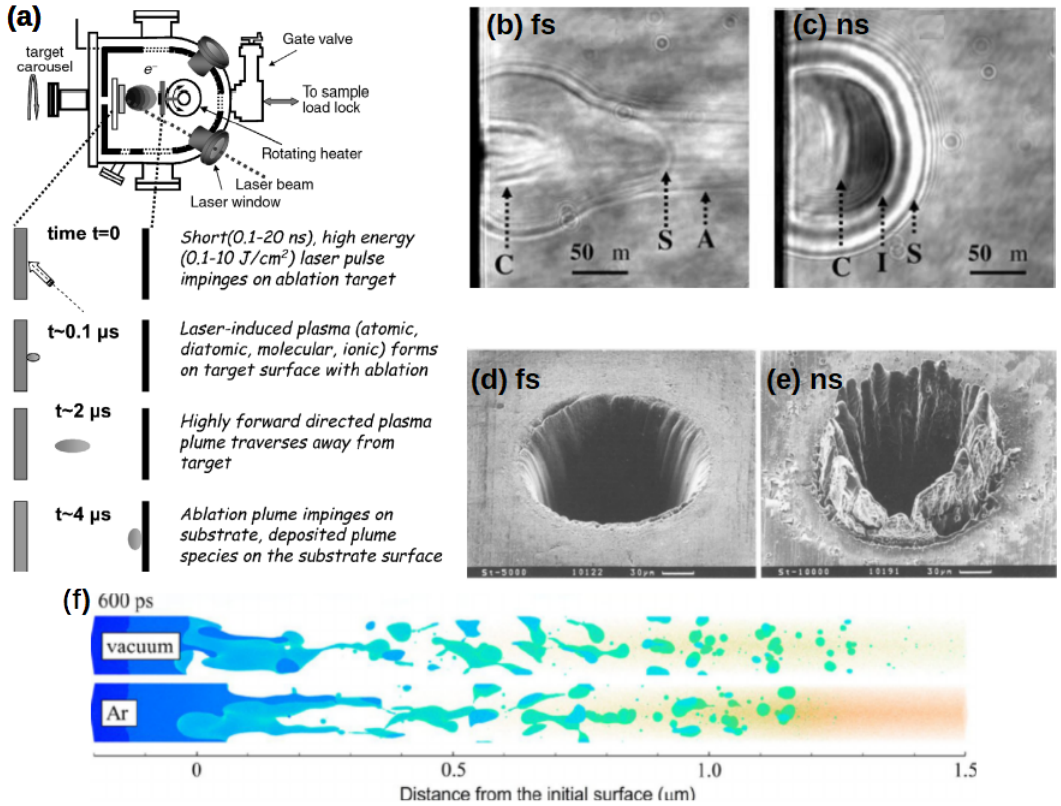

Figure 4.3: **(a)** Standard setup of PLD with the temporal plume evolution for fluencies ranging from 0.1-10 J/cm^2. Spatial plasma evolution obtained after 10 ns of ablation in Si target for a **(b)** femtosecond Ti:Sapphire and a **(c)** nanosecond Nd:YAG lasers with 220 μJ of energy where the label **S** is the shock front, **I** and **C** represents the ionization and contact front, respectively, and **A** is the air breakdown plasma. The different formed craters in steel surface after being ablated by a Ti:Sapphire laser with **(d)** 250 fs and **(e)** 3.3 ns pulses durations. **(f)** Simulated atomic configuration of Al target irradiated by a 100 fs laser pulse at 0.2 J/cm^2 fluency in vacuum and at 1 atm of Ar atmosphere after 600 ps. The images were extracted, respectively from Ref. 162, 167, 166, 168.

to reduce the probability of agglomeration is an accurate gas flux control inside the chamber and target rotation to avoid melted pools formation.

Aforementioned, fs pulsed laser deposition in vacuum already showed as a good technique to obtain $Gd_5(Si,Ge)_4$ nanogranular films without oxidation issues; however, is an expensive and unreproducible method where the sample surface is not continuous. For that reason, the aim of the present work is to demonstrate that a ns PLD can also be used for the production of this pseudo-family compounds nanostructures. A Nd:Yag PLD system at Physics Centre of Minho University, see Fig. 4.4(a), was chosen for this task. A complete setup description can be seen in Ref. 171 and some modifications were held for sample production optimization. The first adaptation was performed on the target holder; usually, the target is a disk with 2.54 cm of diameter with top and down polished surfaces that is glued to the holder with silver ink. In our case, the targets were produced using the arc-melting technique (see Section 4.1.1) where the as-cast ingot have $\sim$1.2 cm of diameter and, since $Gd_5(Si,Ge)_4$ alloys are brittle, polishing both sides can critically damage the target. To facilitate the target assembly, a holder of

2.54 cm with an aperture of 0.8 cm for the beam shot was produced, shown in Fig. 4.4(b). The ingot is simply fixed with the screws and just one side of the ingot ought to be polished. In order to collect the nanoparticles, the substrate should be as close as possible from ablated target. It is worth to point out that this procedure can also reduce the agglomeration during synthesis. However, the minimum target-substrate distance allowed by the setup is 3 cm that is not enough for sample collection. To solve this issue, an extension for substrate holder was build as shown in Fig. 4.4(c).

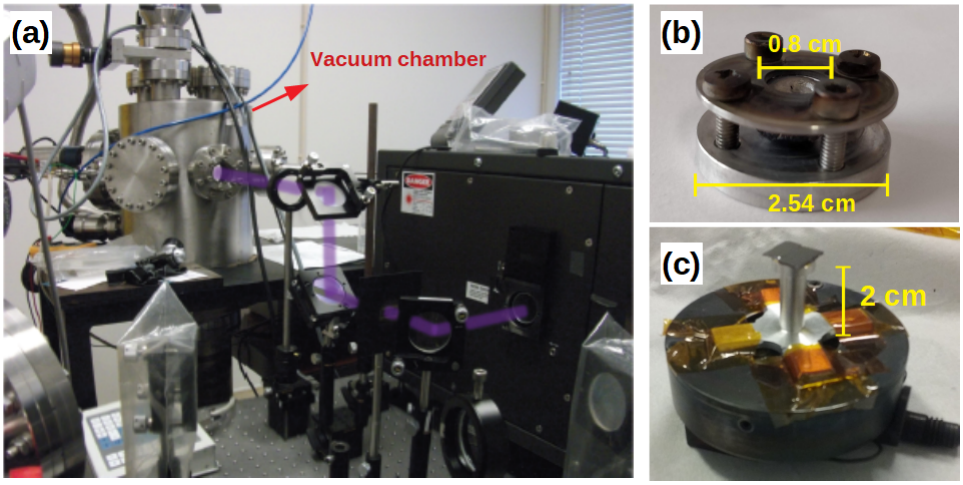

Figure 4.4: **(a)** PLD setup from Physics Centre at Minho University (removed from Ref. 171) and the modified parts for synthesis optimization: **(b)** target holder for the as-cast ingots produced by arc-melting and **(c)** an extension for the substrate holder for approximation to the formed plasma.

Using these setup modifications, we were able to obtain $Gd_5(Si_xGe_{1-x})_4$ nanoparticles with x = 0.45, 0.55 and 0.60 by using a Lambda Physik LPXpro 210 pulsed excimer KrF laser with 248 nm of wavelength, pulse duration of 20 ns with a repetition of 10 Hz and a maximum energy of 550 mJ. Previous to laser incidence in the target surface, the chamber was pumped using an Alcatel ADP80 turbomolecular with a rotational speed of 27000 rpm for 1 hour an a half reaching a high pressure of $\sim 10^{-10}$ Torr. The system was then purged using Argon gas in order to remove remnant O_2, due to the high oxidation of Gd^{3+}. The target was then cleaned by focusing the beam with 200 mJ and 10 Hz onto it surface in rotation for two complete cycles under Ar atmosphere at 1 Torr of pressure. After the cleaning, substrate was positioned at 30 mm distance from the target to avoid agglomeration and droplet formation. For technical and simplicity reasons, two types of substrates were used: 1) carbon coated grids (Ted Pela, inc.) for 15 min for HR-TEM imaging and 2) Si (001) substrate with 2 hours of deposition for crystallographic and magnetic measurements. It is worth to point out that the long hours for the Si NP collection is due to the low rate deposition of material ($\sim$4-8$\times 10^{-3}$ mg/min) since there is losses to the chamber and pump system.

4.2 Characterization techniques

4.2.1 Transmission Electron Microscopy (TEM)

Electron microscopy is a powerful tool vastly applied in nanoscience and nanotechnology field since is the technique with major image resolution in comparison with optical microscopies. The maximum magnification of an optical microscope is around 1000 times, corresponding to resolution of 0.2 μm, while robust TEM instruments have atomic resolution[172]. This is due to the shortest wavelengths for the electrons that can couple with sample electrons and the results of this collision will carry the sample information allowing image construction with such resolution. All the particles and radiation generated from electron-matter interaction are depicted in Fig. 4.5 with the respective informations regarding the sample properties interest. Particularly for TEM imaging, the transmitted electrons are collected, thus enabling the construction of a 3D image and also gives information of internal chemical composition, crystallographic structure and orientation.

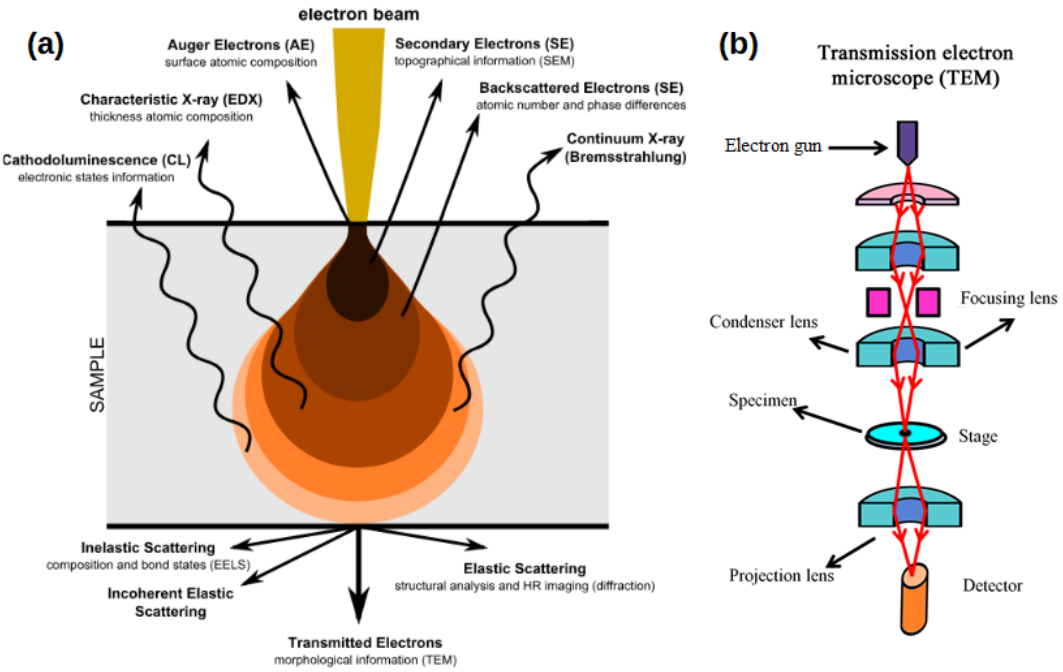

Figure 4.5: **(a)** Illustration of particles generated from electron-matter interaction and their respective information useful for electron microscopes, extracted from Ref. 173; **(b)** Transmission electron microscope standard scheme with the arrows indicating the object image construction, adapted from Ref. 174

The TEM system consists in an electron gun that generates high energy electron beam in a high vacuum column ($\sim 10^{-7}$ Torr) where beam passes through a set of lens and the sample, as shown in Fig. 4.5(b), to then reach the detector. The beam wavelength (λ) is established by the applied potential difference (U) for electron acceleration and the theoretical maximum resolution (d) can be simply calculated as[144]:

$$d = \frac{\lambda}{2\beta} = \frac{0.6nm}{\beta\sqrt{U}} \tag{4.1}$$

where β is the numerical aperture. For a tension of 100 kV, the expected resolution is at the sub-atomic scale; however, due to instrumental limitation, in practice is around 0.2 nm[172]. In modern microscopes, only the electron gun is an electrostatic lens, the further are magnetic lens. The source of resolution loss comes from aberrations originated at the objective lens such as threefold astigmatism, coma and spherical aberration. In high-resolution TEM (HR-TEM) systems, several components are added for image correction on the objective lens, allowing image construction with resolution below 1 Å. For the present work, the morphological characterization of the NP deposited onto carbon grid were carried out using a JEOL 2100F-200KV at LABNANO-CBPF. The image analysis were performed using the open software *Image J*.

4.2.2 Scanning Electron Microscopy (SEM)

The SEM setup system is very similar to TEM, as can be seen in Fig. 4.6(a), however the detector is above the sample once the image is constructed using secondary electrons, backscattered electrons, characteristic X-rays and cathodoluminescence. Distinctly, the micrographs produced by this technique are 2-dimensional an can achieve resolutions of 1 nm. For this surface interactions, the sample ought to be a good electric conductor. For that reason, the sample is prepared on top of Carbon tape to avoid charge accumulation and interferences with the beam source. As can be seen in Fig. 4.6(b) and (c), in SEM micrographs the particles surfaces are well defined however, without information about the internal structure as shown in TEM images where the crystallographic character of the NP are clearly observed.

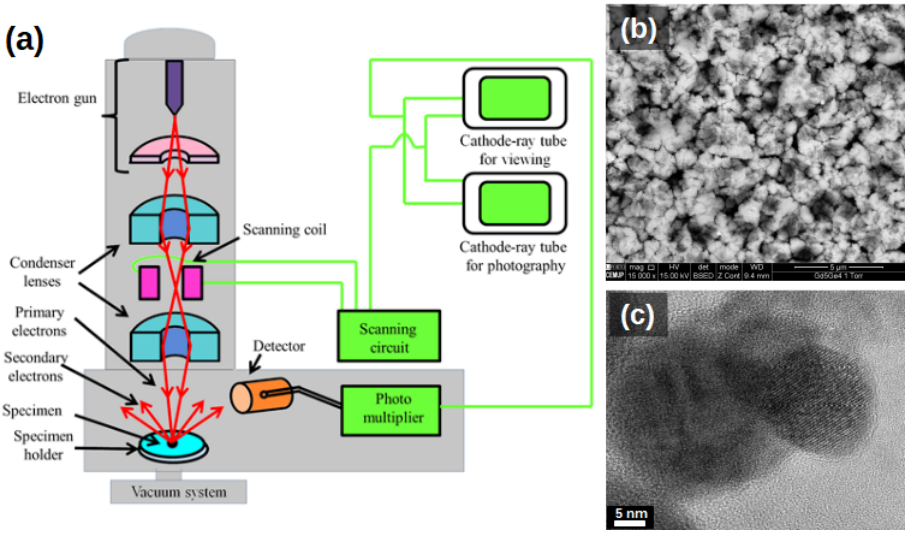

Figure 4.6: **(a)**Simplified scheme for SEM extracted from Ref. 174. The difference between images of **(b)** SEM and **(c)** TEM obtained for Gd_5Ge_4 and $Gd_5Si_{1.8}Ge_{2.2}$ nanoparticles, respectively.

Furthermore, for the polymeric composite samples, SEM imaging were performed at Centro de Materiais da Universidade do Porto (CEMUP) in a Philips-FEI/Quanta 400.

4.2.3 X-ray Diffraction (XRD) techniques

One of the major tools for characterization of crystalline materials is the X-Ray Diffraction technique, that is based on the Bragg's law and is vastly discussed in the literature[144,175–177]. The typical interatomic distances in solids are at the same order of the X-ray wavelength ($\sim$0.1-100 Å); which allows it diffraction after being elastically scattered by a crystal net. From an ondulatory point of view, the electromagnetic wave is instantaneously absorbed and reissued by the matter electron, working as an X-ray emission centre, that will directly influence at the diffracted beam intensity[144]. Thus, the interactions between electrons at the material will change the optical path of the X-ray photons without changing the incident photon phase. For a constructive interference among the coherently reflected beams, the optical difference path between incident and reissued wave with an angle θ is given as:

$$2d_{hkl}sen(\theta) = \lambda \tag{4.2}$$

where *hkl* are the Miller index that defines the family planes in a Bravais lattice and, for that reason, $2d_{hkl}$ represents the parallel interplanar distances of these planes. Although the reflected beams are specular, only for certain θ values that the reflections from all the parallel planes will sum up in phase to form an intense diffracted planes, forming the so called characteristic material peak. Additionally, since electrons are the emission centre, the relative intensity of the diffracted peaks will be given by the atom light scattering power that composes the sample of interest.

The experimental setup for X-ray Diffraction is basically composed by a source (Cu, Fe, Mo, Ag, etc) and a detector positioned after the sample. During the measurement, source and detectors are moving in θ while the sample is hold at the spot and, for this reason, the resulted X-ray pattern is given as a function of 2θ angle, as can be seen in Fig. 4.7(a). Indeed, several elements are required to set the optical system; however, it will not be given in this work and more technical details concerning equipment setup can be found in Ref. 175. For this work, a Rigaku Smartlab Diffraction with a Cu-Kα radiation (λ = 1.54059 Å), 45 kV and 200 mA and a D/Tex Ultra detector was used for bulk and composite samples crystallographic characterization in a Bragg Brentano geometry at IFIMUP. The data collection was performed in the range between $20^\circ \leq 2\theta \leq 80^\circ$ with the sample fixed at the support during measurement, in a 0.02° steps per degree.

Notwithstanding, the resolution of Cu-Kα radiation is not enough to obtain a good pattern for the nanoparticles produced by PLD. The main factors are (i) particle size and (ii) amount of produced material. The High Resolution Synchrotron X-ray Diffraction was chosen to unveil the crystallographic properties of $Gd_5(Si,Ge)_4$ NPs. The syn-

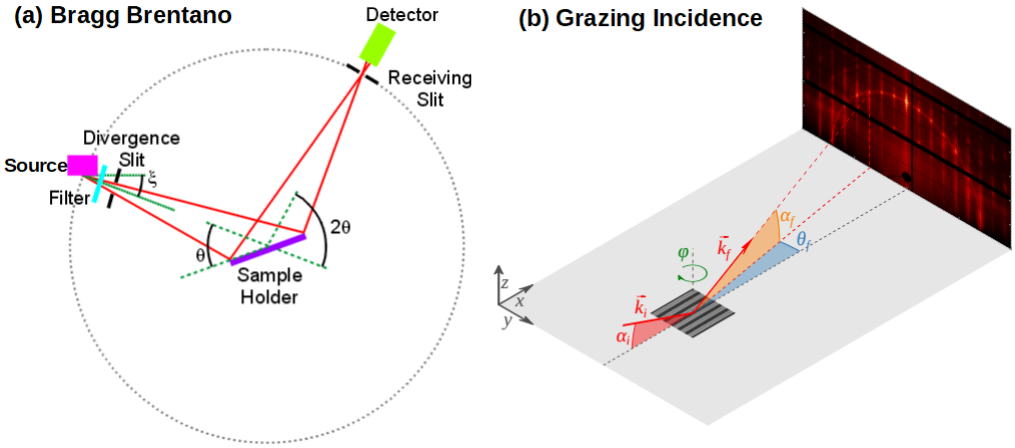

Figure 4.7: **(a)** Diagram of Bragg Brentano geometry where a divergent beam is focussed at the sample with a θ angle and the detector will be rotated by 2θ angle along the goniometer circle (dotted-circle). **(b)** Geometry of Grazing Incidence Diffraction where a monochromatic X-ray light reaches the sample with a wave vector $\vec{k_i}$ at a grazing incidence angle α_i. The beam is elastically scattered with $\vec{k_f}$ and exit angle α_f and azimuthal angle θ_f, creating the diffraction pattern at the linear detector surface. The schemes were extracted from Ref. 178,179, respectively.

chrotron radiation is generated by accelerated charged particles in a curvilinear particle accelerator that are selected by energy range to several sections depending on the desired application. Due to a complex optical system, that includes high power slits, transfocator and different monochromators, the resulted beam is highly collimated with a very small wavelengths. For this reason, a high brilliance of the beam is achieved - typically 10^8 times larger than conventional X-ray tubes - which reduce the exposure time of smaller samples with higher resolution when compared to standard laboratory systems. The principles of this technique are the same as usual XRD setup previously mentioned; however, the measurements are performed using the Grazing Incidence Diffraction geometry shown in Fig. 4.7(b) where transmitted and scattered beams are measured.

For this work, the measurement were performed at European Synchrotron Radiation Facility (ESRF), at Grenoble, France. Inaugurated in 1994, is the more powerful synchrotron third generation light source worldwide. Our measurements were carried out at beamline ID31 with a wavelength λ = 0.177 Å and 70 keV of energy to cover the 2-7 Q-range for the samples using the setup shown in Fig. 4.8. The sample detector (Pilatus3 X CdTe 2M) distance was 1.05 m and the beam spot on the sample was of 2x2 μm. The powder to be measured was put onto Kapton tape - with low signal - and introduced on the sample holder with the system inside of a glove bag under Ar atmosphere to avoid condensation during temperature decrease. The cryostat has three connections: *i)* thermocouple for temperature control, *ii)* He flow for the closed system and *iii)* vacuum system using a diffusion pump. A magnet was also present on the setup; however, few measurements were performed with the applied magnetic field due to the lack of time. Data treatment were realized at the facility using the internal python programs for integration and normalization of the patterns.

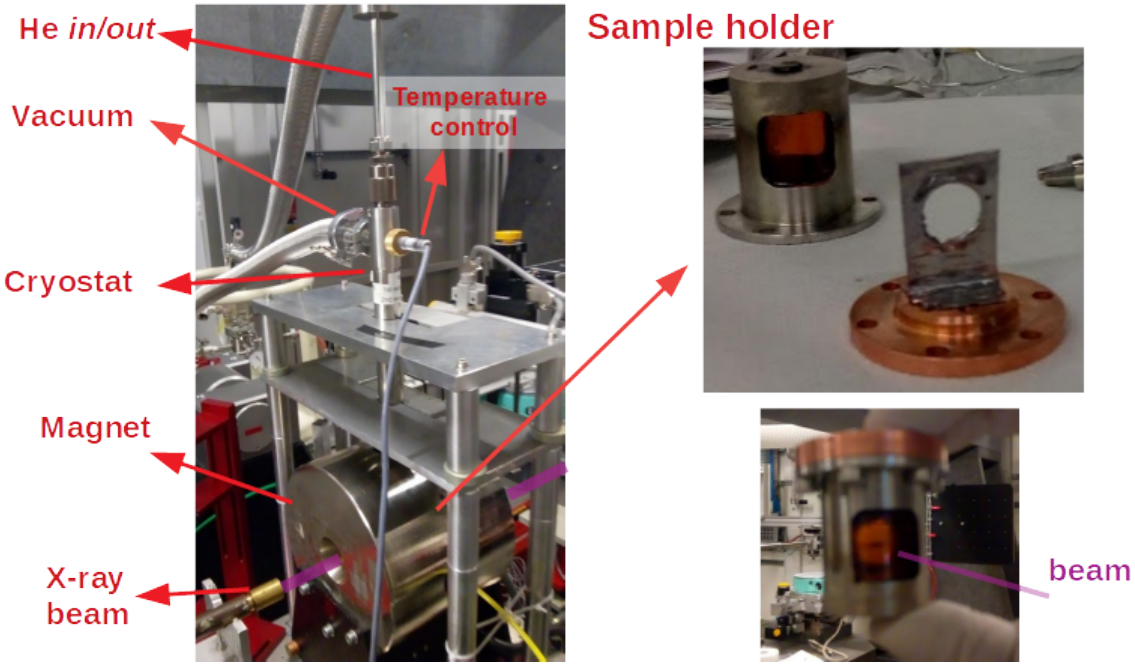

Figure 4.8: The setup used for the GIXD measurements of the nanostructures at ESRF.

For some samples, a quantitative analysis from calculations using the *Fullprof Software* was not achieved and is a work in progress. This software allows several types of calculations ranging from crystallographic to magnetic analysis using X-ray or neutron diffraction. For the present work, we have applied two different methods: *LeBail* and *Rietveld*[180]. The first one, take into account only the structure, *i.e.*, the symmetry space group and lattice parameters which gives only qualitative information of crystallographic features. In this case, for a sample with multiple phases, it is not possible to determine the amount of each crystallographic structure because *LeBail* method considers all the possible diffracted planes at the structure. However, it can be used to achieve a good *Rietveld* method where the atomic positions are pondered for the calculation and, thus, selecting the diffracted planes related to the electric density of the structure. For both cases, a Pseudo-Voigt curve was considered and a full information concerning the crystallographic structure, atomic positions and angle is achieved.

4.2.4 Superconducting Quantum Interference Device (SQUID) Magnetometer

The superconducting quantum interference device (SQUID) is the detector element of a magnetic properties measurement system (MPMS) that operates using the extraction method, with a complete description in Ref. 181. The MPMS technique is based on the Faraday induction law where the variable magnetic flux induces an electromotive force at the detector. It consist on a superconducting coils that generates the magnetic field inside of a cryogenic bath where the sample can move vertically. Depending on the setup, the induced magnetic field by a DC current, can vary from 5.5 T up to 7

T. Beyond that, a temperature control, extraction and acquisition systems are required for equipment operation. The Josephson junction in each coil, is the responsible for the high sensitivity of SQUID (10^{-10}A.m^2)[181] and is composed by two superconductor layers separated by an insulator material. With this geometry, when the sample is moved around the centred position induces a voltage variation inside the junction with the period of a magnetic flux quanta of $\hbar$/2e (10^{-14} T.m^2)[182].

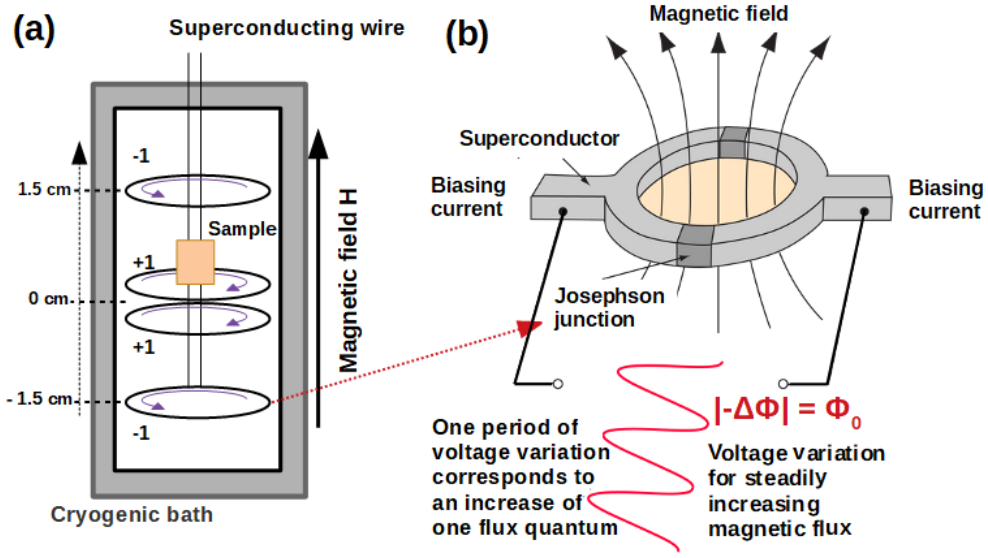

Figure 4.9: **(a)** Scheme of a SQUID magnetometer where the sample moves along the superconducting wires that generates the applied magnetic field along the vertical direction squid. The sample movement generates a magnetic flux that is detected by a **(b)** Josephson junction that has a high sensitivity to voltage variation, extracted from Ref. 183.

The main magnetization measurements performed at SQUID are as a function of the temperature with different protocols [M(T)] and hysteresis cycles [M(H)]. Usually, a zero field cooling protocol is first carried where the sample is cool down to 5 K - or below it, depending on the setup -, the magnetic field is applied and the magnetization values are measured while the chamber is heated up. The field cooling protocol can be executed by decreasing (FCC) or increasing temperature (FCW) with the applied magnetic field. It is worth to point out that the ZFC and FCC protocols are commonly used for nanostructures since the irreversibility can give information concerning superparamagnetic and spin glass behaviours[184]. Regarding the evaluation of MCE, several isothermal curves are obtained with the same number of points for $-\Delta S$ calculation (see Section 3.2) and, for samples with thermal irreversibility, the material is heated above the Curie temperature between each curve[185]. For the present work, the measurements were carried out using a 5.5 T SQUID at IFIMUP and Laboratório de Magnetismo e Baixas Temperaturas (LMBT-Unicamp). In collaboration with LABNANO from Centro Brasileiro de Pesquisas Físicas (CBPF), a 7 T SQUID was also used for measure the NPs produced by PLD.

4.2.5 Fourier-Transform Infrared Spectroscopy (FTIR)

FTIR curves were obtained at the Laboratory of Multi-users (LAMULT) at UNICAMP using a Jasco Deutschland (Model FT/IR-6100 type A) at the absorption mode with a 2 cm^{-1} resolution for phase analysis of PVDF composites[186]. Samples with 2x2 mm dimensions were positioned inside the chamber and a Ni atmosphere was used for the calibration curve.

4.2.6 Magnetoelectric coupling: experimental setup

Magnetoelectric (ME) coupling occurs in multiferroic materials where a magnetization is induced by the application of an electrical field and, in the same way, a polarization can be induced through an applied magnetic field. It can occur in single-phase or multicomponent systems, usually composed of piezoelectric and magnetostrictive phases. More traditionally, ME-coupling is evaluated by measuring the output voltage generated by an alternate applied magnetic field. However, due to the requirement of high amplitudes of AC fields (H_{AC}), a DC magnetic field (H_{DC}) is applied to couple with H_{AC} generating a pseudo-piezo-magnetic linear response. As a response, the multicomponent system will present an output voltage (V) from the piezoelectric phase, that is more accessible experimentally. The electrical field generated by an AC field the ME-coefficient is mathematically described as follows:

$$\alpha_{ME} = \left(\frac{\partial E}{\partial H}\right). \tag{4.3}$$

Considering the setup scheme in Fig. 4.10, an AC magnetic field (H_{AC}) applied across the sample plane with thickness t; thus, the electric field is than $E = V/t$ and the ME-coefficient can be obtained experimentally using:

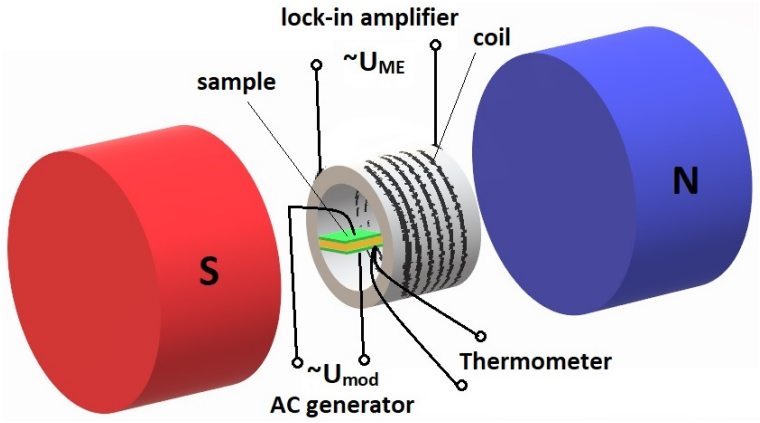

Figure 4.10: Scheme of experimental setup used for evaluation of ME-coupling on multiferroic composites.

$$\alpha_{ME} = \frac{V}{t.H_{AC}}. \tag{4.4}$$

For this work, measurements were carried out by Dr. A. Amirov on a custom designed setup, with the scheme shown in Fig in a 77-350 K temperature range at Amirkhanov Institute in Russia[187]. The ME signal was measured by a lock-in amplifier (Stanford research system, Model SR830) and AC magnetic field was generated by internal waveform generator of SR830. The amplitude of AC magnetic field was $\sim$10 Oe and DC magnetic field was applied in 0-18 kOe range with $H_{AC}||H_{DC}$. ME coefficient was measured in mode, where the applied bias magnetic field H_{DC} is parallel to the direction of ME voltage ($H_{DC} \parallel$ U) and perpendicular to the plane of sample. The samples used for magnetoelectric measurements have the shape of thin rectangle plates with sizes of 0.26$\times$4$\times$7 mm and 0.17$\times$4$\times$3 mm, for 2 wt.% and 12 wt.% composites.

Chapter 5

Dilution effects on the $(Gd,La)_5(Si,Ge)_4$ family

"The extraordinary responsiveness to relatively weak external stimuli makes Gd_5Ge_4 and related compounds a phenomenal playground for condensed matter science."

Y. Mudryk et al., PRL **105**, 066401 (2010).

The first alternative approach to reduce cost on the $Gd_5(Si,Ge)_4$ family compounds aiming practical applications will be presented on this Chapter by substituting Gd per La element. A deep study of the crystallographic, magnetic and magnetocaloric properties was performed on samples produced with different levels of La non-magnetic ion.

The great features on the $Gd_5(Si,Ge)_4$ family compounds rises from the strong coupling between atomic structure and magnetic behaviour. Such effects rely on the extreme sensibility of these materials to internal (Si:Ge ratio) and external (temperature, magnetic field) parameters[29,30,42,47,105,188], as explained in Chapter 2. The role of the magnetic active ions on the structure can be evaluated through doping with non-magnetic ions. In the present case, this will be performed by the introduction of La[42,47,130]. Although La doping has already been studied in this family of compounds, a thorough evaluation of La replacement on the $Gd_5Si_2Ge_2$-type structure in Gd compound is still lacking.

5.1 Crystallographic characterization

The crystallographic structure of $Gd_{5-x}La_xSi_{1.8}Ge_{2.2}$ samples were identified through XRD analysis by means of *LeBail* refinements and the results for all samples are shown in Appendix A. It is known that the parent compound, $Gd_5Si_{1.8}Ge_{2.2}$ (x = 0) crystallizes

in a monoclinic (M) $Gd_5Si_2Ge_2$-type ($P112_{1/a}$ space group) structure with a distorted γ angle of 93.18^o[30]. With the introduction of one La atom to it structure, *i.e.*, x = 1 sample, additional peaks are observed that belongs to the tetragonal (T) Zr_5Si_4-type ($P4_12_12$ space group) structure[42], as indicated in the inset in Fig.5.1(a). These results are expected since, as previous mentioned, for light rare-earth elements, namely La, Ce, Pr and Nd, R_5M_4 compounds crystallizes in a T structure at the Si-rich region[29]. A similar mixture of M and T structure was observed by Yang, *et al.* for the $Nd_5Si_2Ge_2$ alloy as-arc-melted[189]. The authors were able to stabilize the T phase of the sample by a heat-treatment at 1273 K for one week. In a similar way, for the $Gd_5Si_2Ge_2$ composition, the majority of M structure is obtained after an annealing at 1373 K for 100 min[113]. Due to the close similarity to $Gd_5Si_2Ge_2$ compounds, the same annealing procedure was performed on the $Gd_4La_1Si_{1.8}Ge_{2.2}$ sample and the XRD analysis has returned no improvement on phase stabilization. In that way, this sample is indeed a mixture of M and T phase; and, these results supported through the *LeBail* refinements presented on the Appendix A.

The structural change for higher La contents can be observed from the XRD patterns shown in Fig.5.1(a) where the peaks associated with the M phase vanish for x $\geq$ 2 samples. A similar result was obtained by Elbicki *et al.*[130] for Gd_5Si_4-La_5Si_4 system that undergoes from an O(I) to a T structure when the La content is higher then 20 % *i.e.*, x = 1. In fact, this critical concentration for a monoclinic to tetragonal phase transition was also observed by Belo *et al.*[42] for the $Tb_{5-x}La_xSi_2Ge_2$ family compounds. It is worth to point out that to improve the calculated patterns through *LeBail* method, the formation of R_1M_1 (1:1) phase with an orthorhombic symmetry ($O_{1:1}$) was considered. The formation of spurious 1:1 and 5:3 phases is commonly observed in these compounds and is due to an eutectic-like decomposition during the synthesis process[42,145]. Although the analysis have estimated that the amount of 1:1 phase on the samples are less than 15%, the wide overlapped indexed peaks for the considered structures lead to uncertainty on the phase amounts estimation using the *LeBail* refinement[190]. For this reason, the results from magnetization analysis will be used to provide a more precise estimation on the phase fractions.

As it can be noted in the inset of Fig. 5.1(b), the shifts on peaks towards lower angles is associated with an increase on the crystal lattice parameters as La is introduced into the M $Gd_5Si_{1.8}Ge_{2.2}$ compound. The evolution on the lattice parameters in Fig.5.1 reveal that the main contribution for increasing unit cell volume is given along the symmetry axis for the T structure, as observed in similar substituted systems[42,126,129,191]. The increasing rate of $\sim$28 Å$^3/La$ for the present system corroborates well with the one found by Yang *et al.*[192] for the Gd_5Ge_4-La_5Ge_4 alloys. This rate is bigger when La substitutes Tb on the $Tb_5Si_2Ge_2$ compound, being around 33 Å$^3/x$ in the T phase region[42]. These differences can be attributed to the bigger ratio between La and Tb ionic radius (r_{La}/r_{Tb} =1.114) in comparison to the La and Gd (r_{La}/r_{Gd} =1.083)[193]. The same behaviour is observed in similar substituted systems,

such as $(Gd,Y)_5(Si,Ge)_4$ [126], $(Gd,Ho)_5Si_4$ [191] and $(Gd,Pr)_5Si_4$ [129]. Nevertheless, the improvement on the structure symmetry is reflected on the decrease of the distorted γ angle of the M phase from 93.14^o to 92.07^o, from x = 0 to 1. These conclusions on the crystallographic properties will be directly related with the magnetic results, as will be shown in the next section.

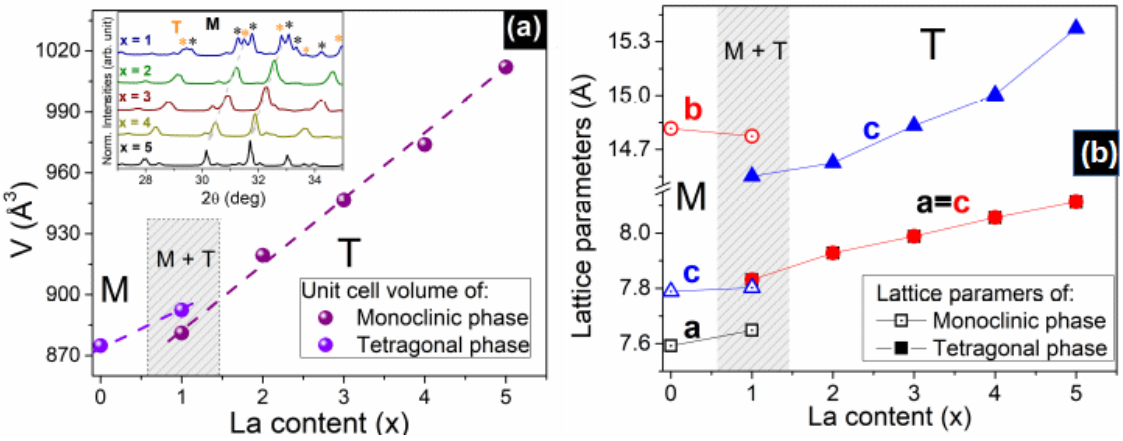

Figure 5.1: (colour line) **(a)** Increasing of the unit cell volume (V) as a function of La content, emphasizing the monoclinic and tetragonal phase mixture for 0< x <2 region. *Inset:* X-ray diffraction patterns around the main peaks obtained for $Gd_{5-x}La_xSi_{1.8}Ge_{2.2}$ samples. It is possible to observe the disappearance on the monoclinic phase as the La content x increases. **(b)** Lattice parameters as a function of x for the main phases; the change in symmetry can be noted from the initial decrease along the b-axis of the M phase for x = 1 sample that becomes the c-axis of the T phase for x >1.

5.2 Phase diagram and Magnetocaloric Effect

Introduction of non-magnetic La atoms on the $Gd_5Si_{1.8}Ge_{2.2}$ leads into drastic changes on the crystal structure and, consequently, on it magnetic behaviour. Aiming to evaluate the magnetic dilution effect on the produced samples, Field Cooling (FC) magnetization measurements under applied magnetic field of 10 Oe were obtained as depicted in Fig.5.2(a). Since the end member $La_5Si_{1.8}Ge_{2.2}$ do not present magnetic ordering [105], it curve is not presented. The coexistence of M and T phases for x = 1 sample, as obtained through XRD analysis, are revealed on the magnetic measurements with the appearance of two plateaus on the FC curve. This results in two minimum on the temperature derivative of magnetization (dM/dT) curves at 175 K and 235 K, see inset of Fig.5.2(a). The lower temperature will be attributed to the FM-PM transition of the T phase, denoted as T_C^T, that presents a higher unit cell volume which decreases the magnetic exchange interactions between the Si/Ge dimers [29] and the higher one to the M phase, indicated as T_C^M in Fig.5.2(a). Further analysis on the magnetic susceptibility data will corroborate with these conclusions. Distinctly, for x = 2, in addition to the T_C at 146 K, there is an anomaly around 75 K that can be attributed to a metamagnetic transition of the 1:1 phase, since it was found to be greater than 10% from XRD analysis. Distinctly, the dM/dT curve for x = 3 and 4 samples present a single minimum at 107 K

and 32 K, respectively, revealing that 1:1 phase formation do not affect the compounds magnetic ordering.

Beyond the decrease on T_C as La content increases, the dilution effects are clearly detected through M vs H isotherms obtained at 5 K for all samples, portrayed in Fig.5.2(b). This data was used to obtain the saturation magnetization by means of the linear fit on the M vs 1/H plots and the results are summarized on Table5.1. Although there is a slight increase on μ_{sat} from x = 1 to x = 4 sample, the mean value of 7.73 μ_B are in agreement with the expected for Gd^{3+} [42]. For x = 5, a close to null magnetization response at 5 K confirms the absence of a magnetic ordering at the temperature range of the equipment (5K - 350 K).

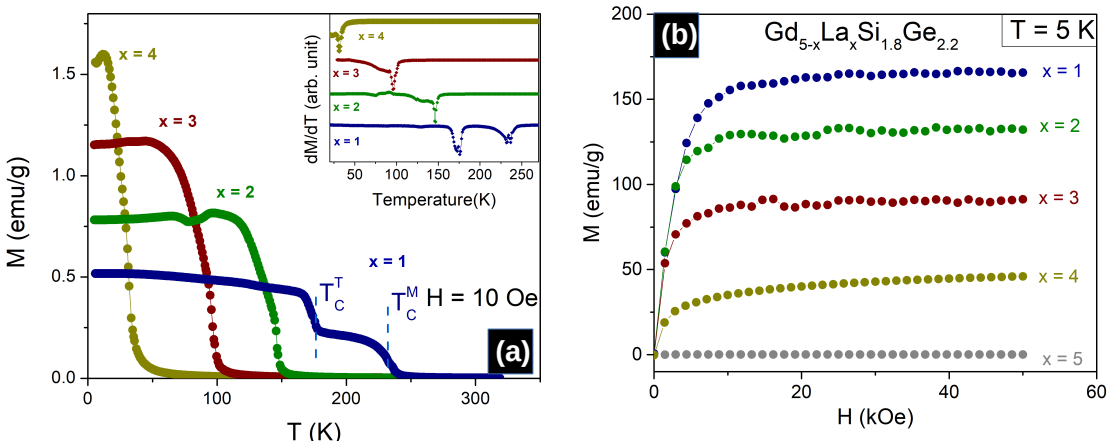

Figure 5.2: **(a)** Magnetization curves obtained at the FC regime with an applied magnetic field of 10 Oe for x = 1, 2, 3 and 4 samples and their temperature derivative of magnetization in the inset. **(b)** Magnetic field dependence on magnetization obtained at 5 K for all produced samples.

Although XRD analysis revealed a mixture of M and T phases for x = 1 sample, *LeBail* refinement does not allow a precise estimation of each phase amount. Given this, due to the relation between crystal structure and magnetic ordering on the R_5T_4 family, the existence of secondary phases is also revealed by magnetic measurements [189,194]. With this in mind, the reciprocal magnetic susceptibility (χ^{-1}) will be used to infer the magnetic contribution of each phase present in the samples. The extensive nature of magnetization allows to write the magnetic susceptibility as [143,194]:

$$\chi(T) = \frac{\alpha C_M}{T - \theta_P^M} + \frac{\beta C_T}{T - \theta_P^T} + \frac{\gamma C_{1:1}}{T - \theta_P^{1:1}} \tag{5.1}$$

where θ_P is the paramagnetic Curie temperature, C the Curie constant, the labels M, T and 1:1 corresponding to the monoclinic, tetragonal and 1:1 ratio of these phases, respectively [143]. The phase fraction of each phase is given by the α, β and γ variables, where $\alpha + \beta + \gamma = 1$. For the samples with x$\geq$2, γ was considered to be null and the best calculated curves are presented on the SID. The curve fittings were performed considering J = 7/2 for Gd^{3+} and the unit cell volume from Fig. 5.1(a), as initial values

for the C parameter. The best fitting to the reciprocal magnetic susceptibility and the resulting amount of each phases for the x = 1 sample is presented in Fig.5.3(b). The estimated phase fraction of 72.3% of M phase and 26.6% of T phase for $Gd_4La_1Si_{1.8}Ge_{2.2}$ sample, is in fine agreement with the XRD analysis. As for x = 2 sample, the presence of R_1T_1 phase was found to be 13.2% and the T_N value of 50.8 K confirms that is responsible for the anomaly at 75 K the magnetization curve in Fig.5.1(b)[195]. For x = 3 and 4 samples, the calculation on the amount of 1:1 phase are 9.2% and 2.5%, which are in good agreement with the obtained through *LeBail* refinements. The calculated paramagnetic effective moment (μ_{eff}) per Gd^{3+}, summarized in Table 1, are below the expected value of 7.94μ_B for Gd^{3+} that can be due to the presence of secondary 1:1 phase. A similar conclusion can be made for the saturation magnetization values. For x = 4 composition, particularly, the weakening of the magnetic response combined with the low magnetic applied field of 10 Oe lead to a negligible and inconclusive value of μ_{eff}. The end-member, x = 5 sample, is a full paramagnetic material; however, due to the low applied magnetic field combined with the signal close to the SQUID sensibility limit of 10^{-6} emu, the fitting was not possible to be performed.

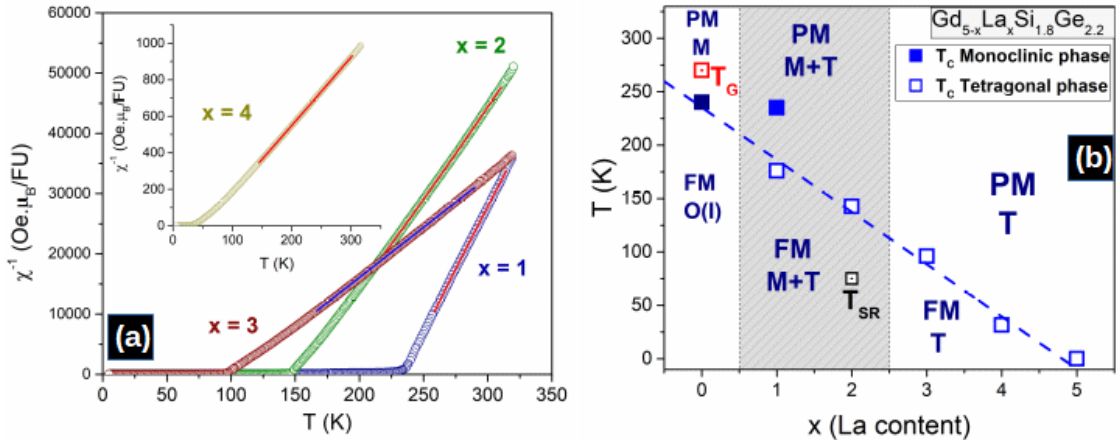

Figure 5.3: **(a)** Reciprocal magnetic susceptibility for $Gd_3La_2Si_{1.8}Ge_{2.2}$ and $Gd_4La_1Si_{1.8}Ge_{2.2}$ samples and the best fitting obtained from equation 5.2. **(b)** La content x-temperature phase diagram for magnetic and structural phases. T_C: magnetic critical temperature; T_G: Griffiths temperature.

Through the results above presented, it is possible to construct a crystallographic and magnetic composition temperature (x-T) phase diagram of the $Gd_{5-x}La_xSi_{1.8}Ge_{2.2}$ system. The proposed phase diagram is depicted on Fig.5.3(b). At room temperature all the compositions analysed in this work are PM with two distinct crystal phases: M and T structures. The parent compound $Gd_5Si_{1.8}Ge_{2.2}$ (x = 0) presents a first order transition that undergoes from a [O(I),FM]→[M,PM], their indicated values on the x-T phase diagram was obtained from Ref. 188. Additionally, due to the strong magnetic correlation, it presents a Griffiths-like behaviour as highlighted on Fig.5.3. With the addition of 20% of La content, such behaviour is vanish. A similar behaviour was observed for La substitution on $Tb_5Si_2Ge_2$ compound[42], where the magnetic comportment suffer a significant change when the La content is higher then 20%, *i.e.*, x = 1. At this region

Table 5.1: Magnetic parameters obtained through analysis of $Gd_{5-x}La_xSi_{1.8}Ge_{2.2}$ family compounds.

x	Phase	Amount (% mass)	T_C (K)	θ_P (K)	μ_{eff}/Gd^{3+} (μ_B)	μ_{sat}/Gd^{3+} (μ_B)
1	M	72.3	235	235	7.48	
1	T	26.5	175	213	6.99	7.26
1	$O_{1:1}$	0.20	-	43.2	8.00	
2	T	86.4	146	147	7.78	7.53
2	$O_{1:1}$	13.2	75	50.8	8.71	
3	T	90.8	107	103	7.92	7.44
3	$O_{1:1}$	9.20	-	52.5	8.25	
4	T	97.5	31.5	42.0	7.82	7.60
4	$O_{1:1}$	2.50	-	53.1	8.10	
5	T	95.2	0	0	0	0
5	$O_{1:1}$	7.20	0	0	0	0

of concentration, the suppression of the strong magnetocrystalline anisotropy (MCA) leads to the annihilation of the Griffiths-like phase and the spin reorientation. This is due to the absence of electrons on the f-band of La^{3+}, responsible for the strong MCA. In fact, Pereira *et al.* have shown that the short-range magnetic correlation is restricted to $R_5(Si,Ge)_4$ family (R = Gd, Tb, Dy and Ho) with M and O(II) structural phases[188], in agreement with these findings.

Furthermore, the decreasing on T_C for the present family compounds has a rate of dT_C/dx = -47.8 K/La. However, it is not as drastic as on the Gd_5Si_4 system that presents a rate of -85 K/La in a range of $0 \leq x \leq 2$ of La content[130]. This higher sensitivity arises from the smaller T_1-T_1 distances on the O(I) structure adopted by the compound. Another contribution originates from the decrease of 90 K in T_C during the structural transition between x = 0.5 and 1 compositions, not observed for the present samples. Although x = 1 is also a critical concentration for the $Tb_{5-x}La_xSi_2Ge_2$ alloys, there is a maximum on the T_C value when the system changes from a M to a T structure[42]. The authors attributed this behaviour to the increase of the collinear alignment of Tb^{3+} ions with La substitution. Because of this, the rate of decrease on T_C for this system is lower than the observed for the $(Gd,La)_5Si_{1.8}Ge_{2.2}$ family. Such feature is associated with a combination of i) the dilution of Gd magnetic sites and ii) the increase on the unit cell volume[42,130].

For materials that undergo a SOMT, the evolution on the MCE can be performed by calculating the isothermal magnetic entropy change using the integrated Maxwell relation $\Delta S(T) = \int_{H_0}^{H_F} (\partial M(T,H)/\partial T) dH$, as explained in Section 3.2[149]. This procedure can be performed since there is no discontinuity on the transition and, therefore, $\partial M/\partial T$ is finite at the transition temperature. Fig.5.4(c) shows the obtained $-\Delta S(T)$ curves for all the produced samples within an applied magnetic field of 5 T and they

follow a λ-shape which is typical of SOMT materials[134,194]. It is worth to point out that, due to the high value of applied magnetic field of 5 T, the effects of the spurious 1:1 phase can be neglected for this analysis.

For x = 1, due to the phase mixture, the ΔS curve presents two maximum values, $\sim$4.4 J/kg.K from the O(I) phase and $\sim$4.0 J/kg.K from the T, as denoted in Fig. 5.4(c). The overlap of two ΔS curves lead to the so-called table-like MCE that enhances the working range temperature, which is an important consequence for MR applications, particularly in a cascade system[36,196]. Since that type of system consists in a sequence of cycles with magnetic materials with different T_C's around the operating temperature, a compound presenting more than one magnetic transition can reduce the amount of material for the operation. As for further La content, namely x = 2, the increase on ΔS_{max} to $\sim$5.2 J/kg.K for x = 2 can be due to a thermal compensation for the decreasing on T_C[194]. The subsequent reduction on the maximum values for x = 3 and 4 samples is mainly a consequence of the loss in magnetization when Gd is removed from the structure. Although the $-\Delta S_{max}$ values are expected to enhance by decreasing T_C[194], the observed reduction for the present system is a direct effect of Gd^{3+} dilution on the unit cell of $Gd_{5-x}La_xSi_{1.8}Ge_{2.2}$.

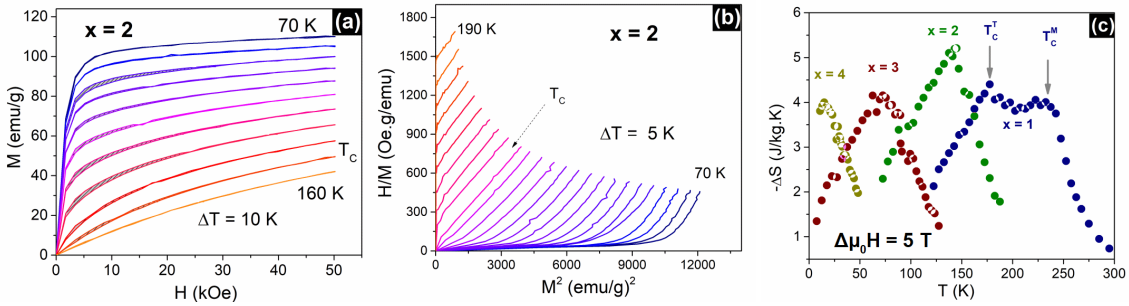

Figure 5.4: **(a)** Isothermal magnetization curves for the $Gd_4La_1Si_{1.8}Ge_{2.2}$ composition, measured from 120 K to 310 K with a step of 10 K, **(b)** the corresponding Arrott plot and **(c)** the calculated $DeltaS(T)$ curves.

5.3 Partial Conclusions

In the present work, the evaluation of Gd dilution effects was presented through a crystallographic and magnetic study on the $Gd_{5-x}La_xSi_{1.8}Ge_{2.2}$ compounds with x = 1, 2, 3, 4 and 5. It was found that, for the sample with lower La content, there is a mixture of monoclinic and tetragonal phases, identified through X-ray Diffraction analysis and confirmed using magnetic data. Furthermore, the results revealed that these fundamental properties can be controlled through La substitution. Namely, increasing non-magnetic atoms content lead to magnetic ordering temperatures reduction combined with the suppression of the magneto-structural transition and the Griffiths-like behaviour. Such effects are directly related with the La dilution concentration limit in the monoclinic structure, after which the tetragonal configuration is thought to be favoured. The structural

transition also lead to a change on the nature of the magnetic transition order, as confirmed through Arrott plot curves. As a consequence, an enlargement on the working temperature for the magnetocaloric effect is observed, which is of great importance for magnetic refrigeration applications. These findings show that Gd atom plays a key role on the modifying the structure of $Gd_5Si_{1.8}Ge_{2.2}$. It is worth to point out that lower doping levels ($0<x<1$) on the chosen composition of this work should be further investigated since substitutions of Gd by non-magnetic active ions can be a tool for tuning the properties of the $Gd_5(Si,Ge)_4$ pseudo-binary compound.

Chapter 6

Flexible Composites of $Gd_5(Si,Ge)_4$ Compounds in Polymeric Matrices

"Cost reduction is desirable, as is limiting the use of elements that can be extracted only from very few places in the world, because these strategic materials can endanger the ultimate success of any new technology if the geopolitical situation changes."

V. Franco *et al.*, Annu. Rev. Mater. Res. **42**, 305 (2012).

This Chapter is reserved for presenting the effect of blending $Gd_5Si_{2.4}Ge_{1.6}$ in flexible poly(methyl methacrylate) (PMMA) obtained through a simple solvent casting technique (described in Chapter 4). The characterization of the produced powders will be first presented in Section 6.2 and the structural, magnetic and magnetocaloric impact of blending different concentrations the into PMMA polymer are given in Sections 6.3 and 6.4, respectively.

6.1 Introduction

In the last decades there was an increase in research on polymer-based composites for implementation in several industries such as transport, military, aerospace[197], biomedical[198] and textile[199]. The interest in polymeric materials rises for practical applications due to the low manufacturing cost associated with gain in mechanical strength and elasticity[200]. Represented on the chart in Fig.6.1(b), the combination of metallic and ceramic materials reduces the polymer Young's modulus - parameter that quantifies the stress per unit area of a solid material - with a slight reduction in associated costs. That

is one of the main reasons for its use in automotive and aerospace technology where resistance to extreme conditions is required.

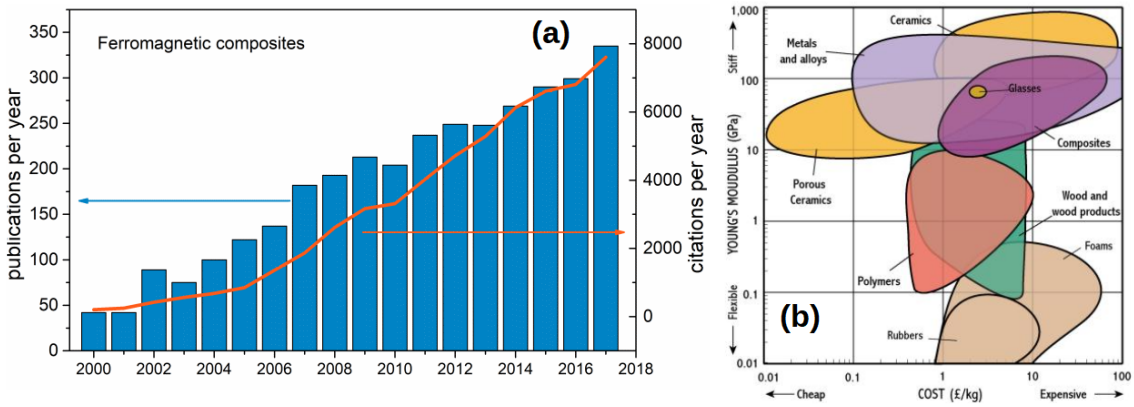

Figure 6.1: The increasing interest in ferromagnetic composites by the scientific community can be seen through the volume rise of publications and citations per year on this subject. *(Source: Web of Science on 16/05/2018).* A chart on the Young's modulus with the associated cost is shown, and it was extracted from Ref. 201.

In particular, for elastomer polymers - with low Young's modulus and viscoelasticity - the combination with magnetic microparticles allows the tuning of their properties with applied magnetic/electric fields, temperature, pressure, etc[202]. These smart materials, so-called magnetoactive elastomers (MAEs) or magnetorheological elastomers (MREs), are mainly based on iron nano/microparticles with silicon-based polymers and synthetic rubbers where their magnetic response can be adjusted and optimized through synthesis[202]. For instance, an improvement of 30% on mechanical features can be reached by applying a constant magnetic field during polymerization due to dipole interparticle interactions[203]. They have attracted much attention as a new generation of soft actuators/sensors and active dumpers[204]. Several models have been proposed for understanding the mechanisms of soft magnetic elastomers (SMEs) to improve device engineering in this matter[205,206]. An interest effect, unpredicted by theory, is that when SMEs are under uniform applied magnetic fields, the system expands towards the field direction when it was expected to compress. Stolbov *et al.*, using a 2D model have shown that, in order to reduce the magnetostatic energy, the particles on the matrix tend to align in a chain fashion through long-range interparticle interactions to achieve the equilibrium deformation[205]. The authors denoted these interactions as magnetodipolar striction which opened a pathway for understanding SMEs behaviour and to improve device engineering in this matter[205,206].

Concerning Gd-based composites, which is the main interest of this work, the use of functionalized iron oxide composites for high efficiency water purification and photocatalysis should be highlighted[207,208]. For optical purposes, Cai et al. have successfully produced and tested a scintillating composite using Gd_2O_3 nanocrystals copolymerized in polyvinyl toluene (PVT) for applications in gamma and X-ray spectroscopy[209]. Due to the large band gap of Gd, the production of photons at the visible spectra is

enhanced via photoelectric effects, improving the energy resolution for gamma radiation detection by 11%. More recently, Bora and co-workers demonstrated the potential of applying Gd_5Si_4 milled powder blended with the elastomer polydimethylsiloxane (PDMS) on microwave absorption in the Ku-band[137]. Furthermore, for MCE studies in polymer-bonded devices, most research is performed using low weights of polymer, with the reinforcement of magnetic materials as an application focus[43]. Imamura *et al.* evaluated the effect of compacting and sintering $Gd_{5.09}Si_{2.03}Ge_{1.88}$ powder with low amounts ($\sim$15%) into a camphorsulfonic acid doped polyaniline (PANI-CSA) conductive polymer[48]. Although there was a reduction of $\sim$22% on the Refrigerant Cooling Power (RCP) values, the gain on the mechanical properties had no influence on the magnetic nature of the powder. However, the study was performed using a base-powder with particle size around 40 μm and the compacting process was performed manually, which led to the observation of distinct behaviour for composites produced with the same amount of constituent materials.

PMMA is a suitable polymer for making flexible magnetocaloric composites due to its high durability, high resistance to scratches and very low water absorbency ($\sim$3%)[210–212]. Considered the hardest thermoplastic, PMMA presents a thermal stability in a wide range of temperature going from 200 K to 400 K which is of great importance for refrigeration purposes[213]. Although the reported values for thermal conductivity of PMMA were produced through different process, between 0.17-0.25 W/mK, the addition of a filler with high thermal conductivity can compensate the typical energy loss during a cycle[214]. In this context, the present Chapter aims to evaluate the behaviour of blending different weight fractions of smaller $Gd_5Si_{2.4}Ge_{1.6}$ powder ($\sim$3.4 μm) in transparent and resistant PMMA.

6.2 $Gd_5Si_{2.4}Ge_{1.6}$ (GSG) powders characterization

For better comprehension of the structural and magnetic behaviour of the produced composites, an evaluation of the sieved powders structural and magnetic properties needs to be performed firstly. The as-cast ingot of GSG was ground in agate mortar and sieved using a sequence of three sieves with hole sizes of: *i)* 50 μm, named as powder 1; *ii)* 10 μm, powder 2; and *iii)* 5 μm, powder 3. As can be seen on their SEM micrographs in Fig.6.2, the particles present an irregular shape and a broad Log-normal distribution[215]. Although the mean grain size for all powders are bellow their respective sieves, the presence of bigger particles is due to the fact that the grain needs to have only one of the dimension with 50, 10 or 5 μm to pass through the holes. Similar particle size of $Gd_5(Si,Ge)_4$ family compound was achieved through ball milling technique by Pires *et al.*[54] and Hunagund *et al.*[135].

The XRD patterns obtained for all ground powders are presented in Fig.6.3(a) and the reduction on particle size becomes evident from the peaks broadening[54,134,135].

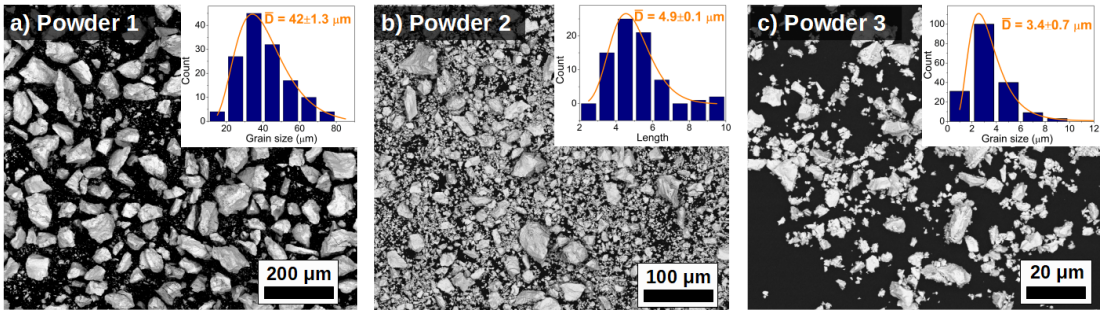

Figure 6.2: SEM images obtained for the sieved powders with their respective Log-normal distribution and average particle size in the *inset.*

From *Rietveld* refinements it was found the formation of expected O(I) structure, M-phase and eutectic R_5M_3-phase (that will be simply denoted as 5:3), commonly formed due to the fast crystallization after melting[113]. Misra *et al.* have shown that at the Si-rich region of $Gd_5(Si,Ge)_4$ family compounds, Ge preferentially occupies the interslab T1 positions at the O(I) structure and these values were considered for the calculations[112]. As for the M-phase, the Si/Ge sites were initially considered to be fully occupied[1] and, after the refinement, the same preferential occupation of Ge atoms were found at T1 sites with a short distance between the dimers with the atomic positions as displayed on the Appendix B. The structural parameters returned from calculations are summarized on Table 6.1 where the full width at half maximum of Pseudo-Voigt curve are larger for the smaller grains, as pointed by XRD data[44,134,135]. As highlighted in Fig.6.3(a), the correspondent peaks intensities for M phase becomes larger for powders with 4.9 and 3.4 μm particle size, indicating the increase on this phase amount with decreasing particle size. Such observation is confirmed through crystallographic analysis, with the smaller micrometric particles (powders 2 and 3) presenting the presence of more than 20% of M-phase. With the selection of particles by the strainers, the deformations at the grain boundaries become more evident and lead to the detection of larger amounts of the distorted monoclinic phase[216]. Indeed, the presence of eutectic phase increases for Gd_5Si_4 compound when the particle size reduces from 700 to 80 nm through ball milling with a broadening on the XRD peaks[135]. As for the enlargement of secondary R_5M_4 phases, such behaviour was observed for milled $Gd_5Si_{1.3}Ge_{2.7}$ and $Tb_5Si_2Ge_2$ followed by a reduction on the unit cell volume of the main phase[54]. In our case, by sieving the GSG powders and reducing the particle size from 42 to 3.4 μm, there is a slight increase on the unit cell volume of the main O(I) phase while M and 5:3 phases remains unchanged, as can be noted on Table6.1. With the selection of smaller particles by the strainers, the defects at the grain boundaries become more evident and can be leading to the detection of larger amounts of the distorted monoclinic phase[216]. In another words, there are a self-segregation of the crystallographic structures on the $Gd_5Si_{2.4}Ge_{1.6}$ compound since there is no thermal effects involved on

[1]Since they share the atomic positions, Si was considered to occupy 60% and Ge 40%.

the chosen technique for grain separation[113,217].

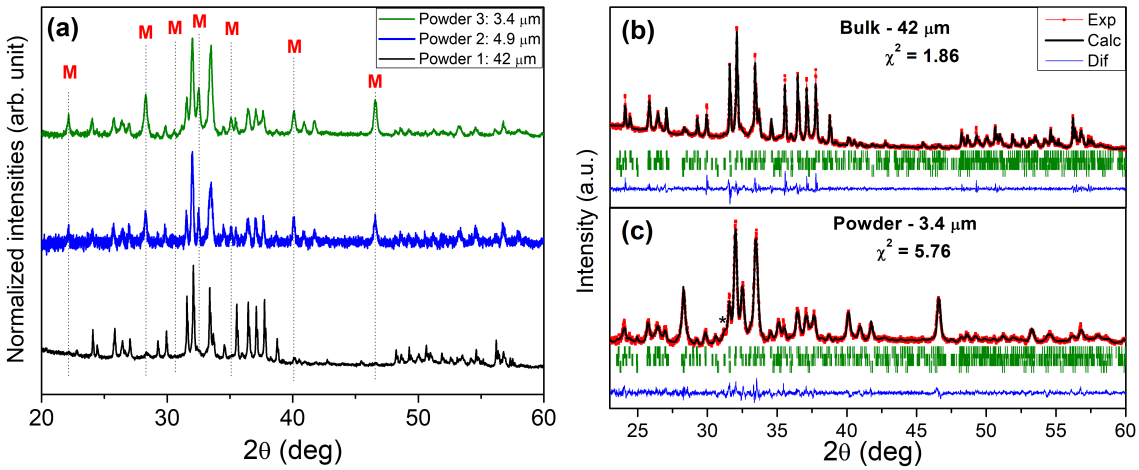

Figure 6.3: **(a)** XRD patterns for all powder samples with the indicative of corresponding peaks of the M phase. Examples of the *Rietveld* calculations are presented for powder 2 **(b)** and 3 **(c)** samples with the indicative Bragg positions for O(I), M and 5:3 phases, respectively.

Temperature dependence on the magnetization for an applied magnetic field of 0.1 T in Fig. 6.4(a) shows that all powder samples transition from a FM to PM state at 308 K, as previously reported for this composition[112,217]. With the selection of particles with mean size of 4.9 μm and 3.4 μm of the $Gd_5Si_{2.4}Ge_{1.6}$ compound, the transition becomes smoother due to surface effects[54,218]. Although there is no shift on T_C, as usually observed in magnetic materials at the micro/nanoscale[44,54,219], the appearance of a thermal hysteresis ranging from 200 to 300 K is due to the transition of M-phase[113]. Another evidence on the presence of this phase, is a small lump at the dM/dT curve presented in the inset of Fig.6.4(a), confirming the XRD analysis. $Gd_5(Si,Ge)_4$ compositions that crystallize in M structure will present a FOMT changing from an O(I) at low temperatures, as already mentioned[217]. Similar to the procedure used on the previous chapter, the χ^{-1} method proposed by Belo *et al*[113], can also be used to quantifies the amount of different phases on the $Gd_5(Si,Ge)_4$ family compounds. The calculations were performed considering the returned values of the unit cell volume from the XRD analysis and the ordering temperature of 254 K and 308 K for the M and O(I) phase, respectively, as initial values on the modified Curie-Weiss law for the fitting of the χ^{-1} curves. To improve the calculations, several constraints were established in order to avoid returned values with no physical meaning, such as θ_P and C being positive values and the sum on the amount of all proportional parameters being equal to 1. All the returned values are summarized on Table6.2 where it is possible to observe the increase of both M and O(I) phase for the smaller particles in values close to the obtained through XRD analysis. Although T_C does not suffer any change, the paramagnetic Curie temperature θ_P for the O(I) phase increases for the powders 2 and 3 while decreases for M-phase, due to the increase on the larger amount of such phase. As previously mentioned, the contribution of secondary phases becomes more

Table 6.1: Returned lattice parameters, Pseudo-Voigt profile curve U, V, W and goodness of *Rietveld* fitted patterns for $Gd_5Si_{2.4}Ge_{1.6}$ powders. (Note: the U,V,W values correspond to the main O(I) phase).

Phase	**Powder 1** 42 μm	**Powder 2** 4.9 μm	**Powder 3** 3.4 μm
Fraction	93.4(2)%	77.3(5)%	76.2(2)%
O(I) Pnma	a = 7.50(0) Å b = 14.8(1) Å c = 7.79(1) Å V = 865(1) Å^3	a = 7.52(1) Å b = 14.7(1) Å c = 7.79(1) Å V = 865(1) Å^3	a = 7.54(1) Å b = 14.8(1) Å c = 7.80(1) Å V = 869(1) Å^3
Fraction	6.51(6)%	21.4(9)%	23.4(2)%
M $P112_1/a$	a = 7.51(3) Å b = 14.6(1) Å c = 7.84(1) Å γ = 93.1(4)^o V = 860(1) Å^3	a = 7.51(1) Å b = 14.7(1) Å c = 7.75(0) Å γ = 93.3(3)^o V = 854(0) Å^3	a = 7.50(1) Å b = 14.7(1) Å c = 7.78(0) Å γ = 93.2(8)^o V = 858(1) Å^3
Fraction	0.12(3)%	1.32(5)%	0.44(2)%
5:3 $P6_3/mcm$	a = 8.73(1) Å b = 8.73(1) Å c = 6.29(6) Å V = 415(4) Å^3	a = 8.74(4) Å b = 8.74(4) Å c = 6.29(4) Å V = 416(3) Å^3	a = 8.76(2) Å b = 8.76(2) Å c = 6.30(0) Å V = 418(2) Å^3
U	0.00022	0.00042	0.00403
V	-0.00010	-0.00091	-0.00212
W	0.00135	0.00262	0.00351
N^o of Parameters	51	50	46
Rp	5.21	4.55	3.99
Rwp	7.11	5.88	5.32
Rexp	2.84	3.14	1.55
χ^2	6.27	3.52	11.8

evident for smaller particles, since the surface/volume ratio becomes bigger at reduced scale[33,54,218]. Concerning the 5:3 phase, it content also increases as particle size is reduced to microscale and the returned θ_P and μ_{eff} are in agreement with the obtained by Roger *et al.*[195]. Nevertheless, the μ_{eff} mean value for the powders of $\sim$7.70μ_B are within the errors for the expected value of 7.94 μ_B, considering that all the formed phases present 5 Gd^{3+} active ions[143].

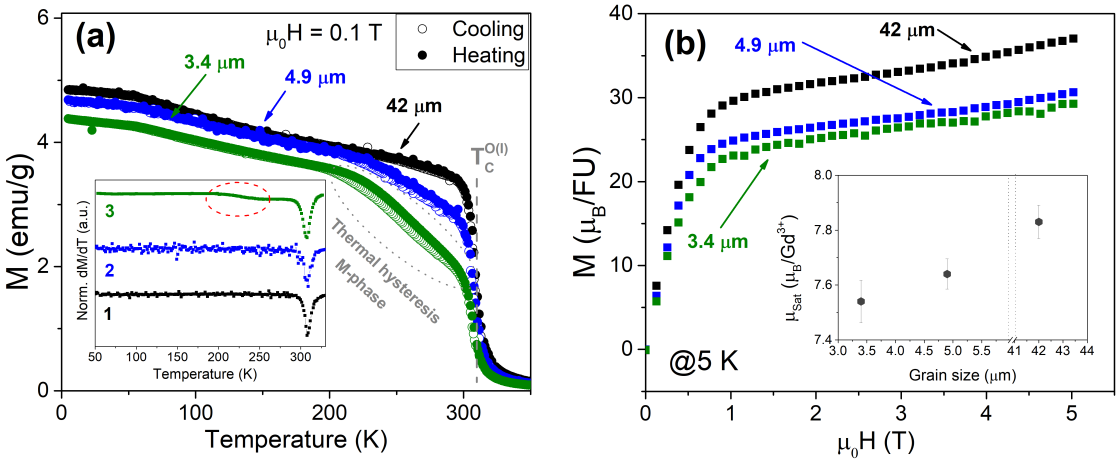

Figure 6.4: **(a)** Temperature dependence under an applied magnetic field of 0.1 T for GSG sifted powders with 42, 4.9 and 3.4 μm of mean size with the dM/dT curves in the inset. The thermal hysteresis becomes more evident for the smaller grains, confirming the increase on the amount of M-phase. **(b)** Magnetization isothermal curve at 5 K with the respective saturation magnetization in the inset.

The loss on saturation magnetization is due to the reduction of particle size to micrometer scale can be observed through the curves presented in Fig.6.4(b). The contribution on each phase for these values were performed considering the amount returned from the reciprocal susceptibility analysis, as exposed on Table6.2. For 42 μm powder, the saturation magnetization (μ_{sat}) of 7.40(6) μ_B/Gd^{3+} are in fine agreement with the observed for $Gd_5(Si,Ge)_4$ bulk samples with O(I) structure (Si-rich region)[113,217]. As for 4.9 and 3.4 μm grains, there is a reduction on these values due to the large content of 5:3 phase, that decrement the saturation due to it AFM ordering - the T_N of this phase is report to be 75 K[195].

Furthermore, the MCE of powders were evaluated through isothermal magnetization curves obtained at the [214,350] K temperature range and the calculated $-\Delta S(T)$ curves are presented in Fig.6.5. Particularly, for powder 2 sample with 4.9 μm, the data was taken from 300-350 K only for comparison reasons since it will not be used for composite preparation. Our main interest relies on the difference between the larger and smaller grains. As pointed out by Gschneidner and Pecharsky, the formation of multiple phases on $Gd_5(Si,Ge)_4$ family compounds can decrement the MCE response[121]. Indeed, for single O(I) phase $Gd_5Si_{2.5}Ge_{1.5}$ bulk, a maximum entropy change (ΔS_M^{max}) of $\sim$9.5 J/kg.K[220] and, since powder 1 can be considered as bulk due to the particle size of 42 μm, the reduction to ΔS_{max} of 6.9 J/kg.K, is expected. Furthermore, the abrupt decrease on the maximum of entropy change (ΔS_{max}) to $\sim$3.0 J/kg.K from 42

Table 6.2: Magnetic parameters of $Gd_5Si_{2.4}Ge_{1.6}$ sifted powders obtained through the reciprocal magnetic susceptibility fitting and magnetization at low temperature.

Sample	Phase	T_C (K)	θ_P (K)	μ_{eff} (μ_B/FU)	μ_{sat} (μ_B/FU)
Powder 1 42 μm	O(I) - 91.2%	308(5)	304(7)	7.84(5)	7.83(6)
	M - 5.44%	254(5)	302(9)	7.66(4)	
	5:3 - 3.36%	-	164(3)	8.13(5)	
Powder 2 4.9 μm	O(I) - 78.2%	308(5)	309(6)	7.60(4)	7.64(6)
	M - 12.5%	254(5)	294(3)	7.71(5)	
	5:3 - 9.30%	-	165(2)	8.05(7)	
Powder 3 3.4 μm	O(I) - 76.2%	308(5)	310(4)	7.92(5)	7.00(8)
	M - 22.4%	254(5)	293(3)	7.54(8)	
	5:3 - 1.37%	-	186(4)	8.16(6)	

to 3.4 μm powder is followed by a change on the curve profile. There is a lift on the powder ΔS curve from 230 to 300 K due to the larger contribution of M-phase as the particle size reduces, similar to observed for $Gd_4La_1Si_{1.8}Ge_{2.2}$ bulk presented on the previous chapter. This is due to the presence of multiple phase transition, that lead to a table-like MCE which is also a matter of interest for application, since it can increase the temperature span during device operation[17,21]. Although it is not possible to assure a similar behaviour for 4.9 μm powder, the thermal hysteresis on the M-T curves are an indication that it could occur. Furthermore, Fig.6.5(c) and (d) reveals that the presence of M-phase does not affect the order on the magnetic transition of both 42 μm and 3.4 μm powder: second order magnetic transition. These results will be used for further comparisons with the PMMA and PVDF composites.

6.3 $Gd_5Si_{2.4}Ge_{1.6}$/PMMA composite characterization

6.3.1 Morphological and crystallographic analysis

The thinner powder, with the properties described above, were used to produce reinforced and flexible $Gd_5Si_{2.4}Ge_{1.6}$/PMMA composites with 10%, 30%, 50% and 70% weight fractions (wt.%) of filler concentrations. SEM images were performed in order to verify the particles distribution along the polymeric matrix volume, some images are depicted in Fig.6.6. As can be noted, which concerns magnetic composites, the interconnection between matrix and grains have great matter on the system behaviour. For instance, porosity is beneficial for heat transfer during AMR cooling cycles[17,151] and the mechanical gain with flexible polymers can enlarge the range of application for brittle materials[70,221]. Fig.6.6(b)-(d) shows the cross-section of freeze-fractured composites, where it is possible to notice that the polymer structure grows around the particles, revealing the bonding between particle and PMMA interface. The amplifications on these images does not allow inference the porosity level of the samples; however, it is possible

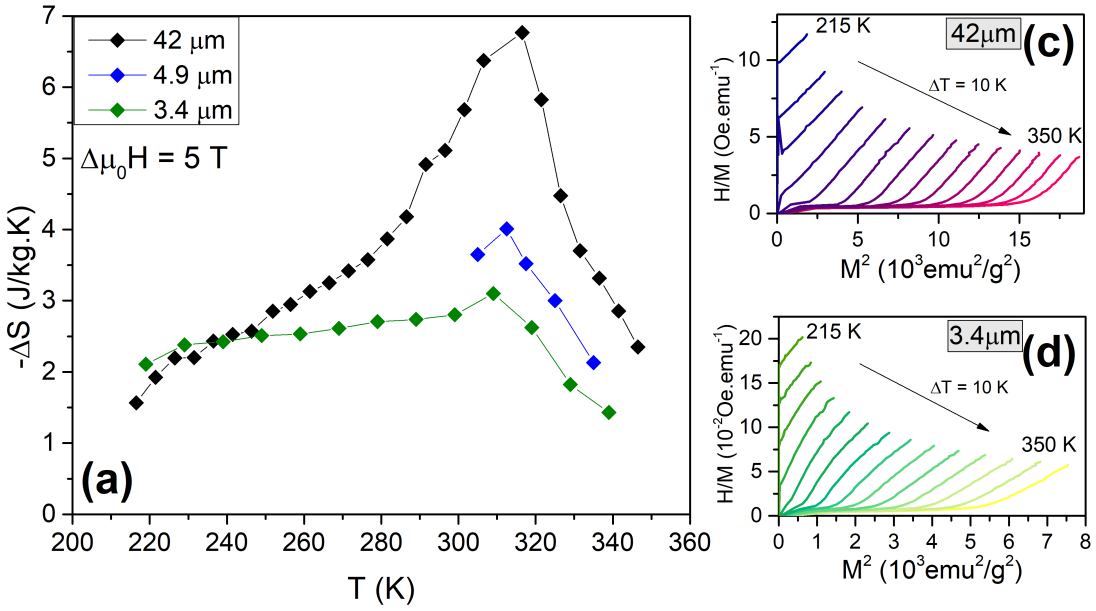

Figure 6.5: **(a)** Entropy change curves as a function of temperature and for $Gd_5Si_{2.4}Ge_{1.6}$ sieved powders with 42, 4.9 and 3.4 μm of grain size where the lift observed for the smaller one can be due to surface effects of deformed M-phase. The Arrott plot for **(b)** 42 μm and **(c)** 3.4 μm show that the reduction of particle size does not affect the magnetic transition order.

to notice a few gaps around the grains that suggest higher porosity. These observations will reflect on the crystallographic and magnetic behaviour of the produced composites due to the extreme sensitivity of powder M-phase on the grains boundaries[32]. For comparison purposes, a pure PMMA sample was prepared by following the same procedure and a film with $\sim$15 μm of thickness was obtained. With the addition of 10 wt.% GSG microparticles, the composite thickness increases exponentially to $\sim$36 μm, depicted in Fig.6.6(e), and nearly reaches saturation for denser composites showing a maximum thickness of $\sim$42 μm. The particles agglomerate at the bottom of the composite due to gravity, see Fig.6.6(f), which leads to stress on the PMMA surface and an increase on the curvature. This particle segregation is the responsible for a non-regular surface of the films, as can be noted for 50 wt.% in Fig.6.6(c). It is known that particles with mean size ranging from 2-5 μm cannot be perfectly dispersed onto polymeric matrices even with sonication, stirring and other conventional techniques[222]. This evidence is another advantage for application in cooling systems since the thermal contact of the device can be selected at one side and being isolated by the polymer layer at the other[223].

The chosen solvent casting technique for the composite production is a simple chemical route that can enlarge the possibility of producing samples with different geometries and designs since it will depend on the used mould. Two examples of composites obtained through this technique are depicted in Fig.6.7(a) and (b). It is also possible to notice that the composites surface becomes visually tough and darker as the GSG weight fraction in PMMA increases. The XRD patterns for the free grains and composite

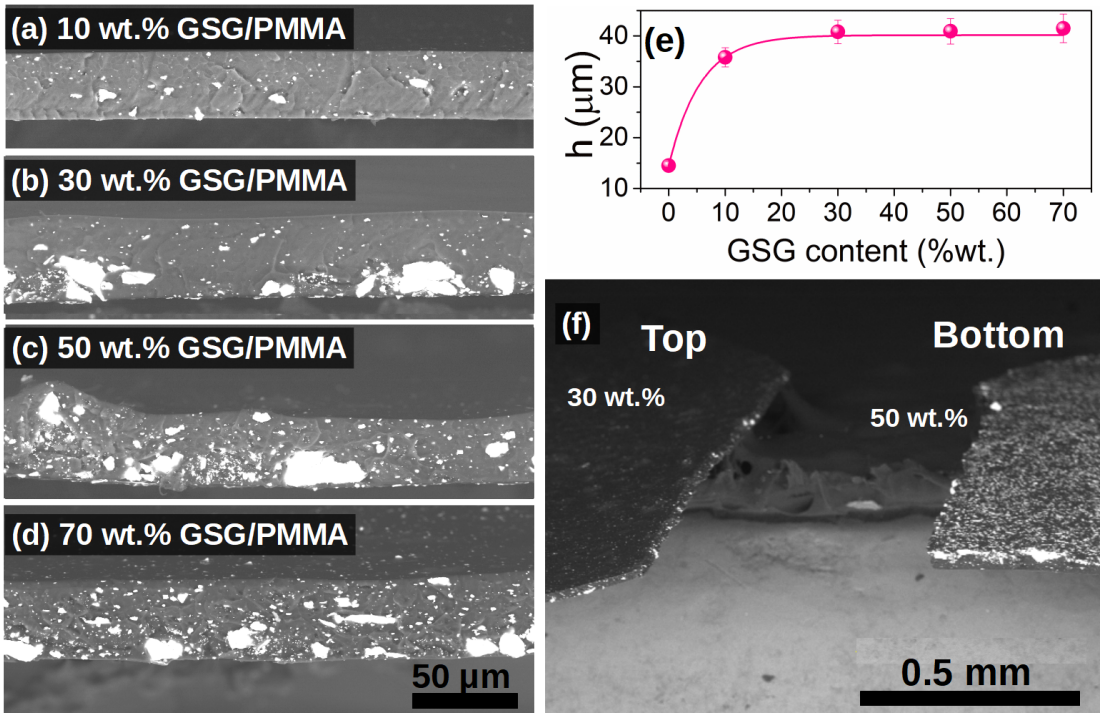

Figure 6.6: Cross-section SEM images of the PMMA + $Gd_5Si_{2.4}Ge_{1.6}$ composites with **(a)** 10 wt.%, **(b)** 30 wt.%, **(c)** 50 wt.% and **(d)** 70 wt.%. The increase on density becomes clear and leads to an exponential enlargement on the films thickness as shown in **(e)**. A visual from the particle agglomeration at the bottom of surface PMMA films in **(f)** during the casting.

samples obtained at room temperature, shown in Fig.6.7(b), reveal a shift on the peaks positions towards higher angles, indicating a reduction on the unit cell volume. Besides that, there is a reduction on the intensity of diffracted peaks from secondary M-phase, suggesting that the presence of PMMA is affecting the micropowder crystallographic features. In order to confirm these, *Rietveld* calculations were performed by considering the returned lattice parameters and atomic positions from the powder with 3.4 μm as initial values. Since PMMA is amorphous, there is a large background on the pattern leading to a decrease on *Rietveld* refinement quality; however, the results summarized on Table6.3 are in fine agreement with previous reports[112,217]. The best fitted curves are presented on the Appendix B.

The introduction of magnetocaloric powder on the polymeric matrix leads to a rapid increase on the phase fraction of O(I)-phase from 76.2% for the free powder to ∼88.9% in average for the composite samples, as can be seen in Fig.6.8(a) with the values summarized in Table6.3. Consequently, the detection of M-phase reduces from ∼22% of the free powder to amounts around ∼10.0% for the reinforced system due to the applied pressure on the surface by PMMA. This is reflected on the relative unit cell volume reduction ($\Delta V/V_0$) of these phases with the increase of GSG content, shown in Fig.6.8(b). The normalized unit cell was obtained considering the O(I), M and 5:3 phase fractions summarized on Table6.3, that follows the same behaviour as the individual phases. This is mainly due to the extreme sensitivity of $Gd_5(Si,Ge)_4$ family

Table 6.3: Returned lattice parameters, Pseudo-Voigt profile curve U, V, W values and goodness of fit for $Gd_5Si_{2.4}Ge_{1.6}$/PMMA composites *Rietveld* refinements. (Note: the U,V,W values correspond to the main O(I)-phase).

Phase	10 wt.%	30 wt.%	50 wt.%	70 wt.%
Fraction	88.3(5)%	88.9(1)%	88.3(5)%	90.0(3)%
	a = 7.488(1) Å	a = 7.469(1) Å	a = 7.458(5) Å	a = 7.435(2) Å
O(I)	b = 14.73(1) Å	b = 14.69(1) Å	b = 14.69(1) Å	b = 14.69(3) Å
Pnma	c = 7.764(5) Å	c = 7.733(0) Å	c = 7.733(4) Å	c = 7.769(2) Å
	V = 856.2(1) $Å^3$	V = 849.8(9) $Å^3$	V = 847.4(9) $Å^3$	V = 846.5(3) $Å^3$
Fraction	9.84(7)%	10.2(4)%	10.0(7)%	9.32(5)%
	a = 7.508(1) Å	a = 7.486(2) Å	a = 7.445(2) Å	a = 7.455(1) Å
M	b = 14.69(2) Å	b = 14.67(2) Å	b = 14.65(2) Å	b = 14.62(0) Å
$P112_1/a$	c = 7.743(1) Å	c = 7.720(2) Å	c = 7.764(2) Å	c = 7.760(1) Å
	γ = 93.09(1)^o	γ = 93.27(1)^o	γ = 93.03(7)^o	γ = 92.9(2)^o
	V = 852.8(1) $Å^3$	V = 846.4(2) $Å^3$	V = 845.5(3) $Å^3$	V = 844.547(3) $Å^3$
Fraction	1.90(7)%	0.84(4)%	1.71(8)%	0.73(4)%
	a = 8.733(4) Å	a = 8.726(4) Å	a = 8.672(2) Å	a = 8.665(2) Å
5:3	b = 8.733(4) Å	b = 8.726(4) Å	b = 8.672(2) Å	b = 8.665(2) Å
$P6_3$/mcm	c = 6.272(4) Å	c = 6.279(4) Å	c = 6.255(2) Å	c = 6.326(6) Å
	V = 414.3(4) $Å^3$	V = 414.1(3) $Å^3$	V = 407.4(2) $Å^3$	V = 411.4(3) $Å^3$
U	0.00403	0.03307	0.02927	0.00225
V	-0.00212	-0.02093	-0.01955	-0.00164
W	0.00351	0.00601	0.00551	0.00315
N^o of Parameters	51	50	43	42
Rp	6.14	5.11	6.05	2.98
Rwp	7.80	7.31	8.29	4.18
Rexp	6.04	2.38	2.52	2.36
χ^2	1.67	9.45	10.8	3.16

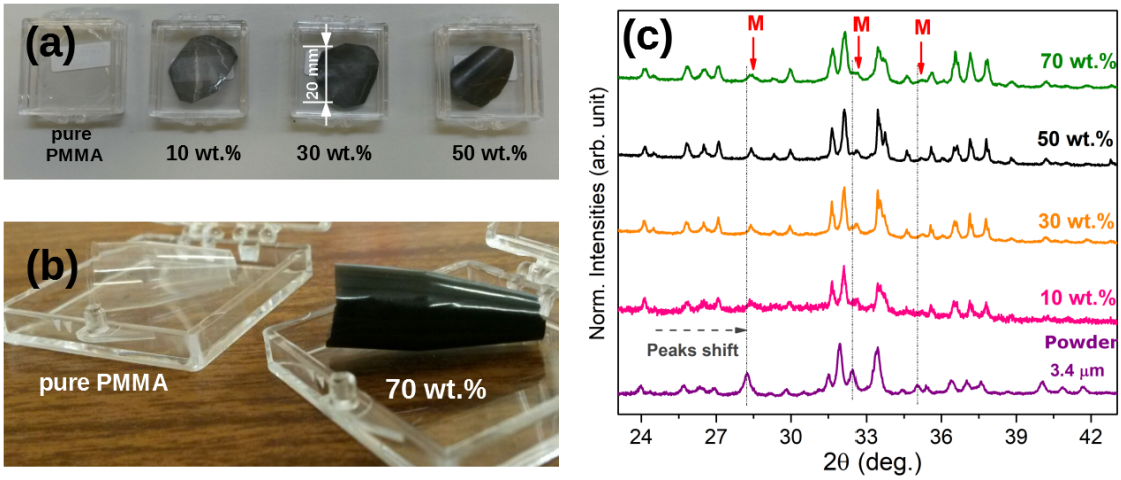

Figure 6.7: Examples of designs for PMMA/GSG composites obtained through solvent-cast technique in **(a)** and **(b)**. X-ray diffraction patterns for the composites with different concentrations and for 3.4μm powder of $Gd_5Si_{2.4}Ge_{1.6}$**(c)**.

compounds to external parameters, where the PMMA surface in contact with the grains is working as a pressure cell[32]. Through *in situ* XRD measurements, Mudryk *et al.* have shown that an applied pressure of 2 GPa is required to induce a transition from the M to O(I) structure of $Gd_5Si_2Ge_2$ polycrystal[116]. The authors have obtained the isothermal compressibility (κ_T) of 3 TPa^{-1} and 6 TPa^{-1} for M and O(I) phases, respectively. Considering these values and using the experimental relative reduction on the unit cell volume, it is possible to estimate the applied pressure on each structural phase of the grains through the thermodynamic relation: $\kappa_T = -(1/V)(dV/dP)_T$. The calculated values are presented in Fig.6.8(b), which shows that the thermoplastic walls force along the M-phase at grain boundaries are above the critical value for a polycrystalline sample. This might be the reason for an uncompleted conversion of M into O(I) phase by the matrix. As a matter of fact, since the present composition has higher Si/Ge ratio than $Gd_5Si_2Ge_2$ stoichiometry, these estimations can be overestimated. A more accurate approach to calculate the real values for the present samples would be using *in situ* XRD measurements, as performed by Mudryk and co-authors[116]. This is possible using the home-made cryogenic setup on the IFIMUP Smartalb Diffractometer that will be discussed on the future perspectives of this work.

6.3.2 Magnetic results

The normalized M-T curves for the $Gd_5Si_{2.4}Ge_{1.6}$ in the form of bulk, powder and flexible composite obtained at cooling and heating between 5 and 350 K with an applied magnetic field of 0.1 T are shown in Fig. 6.9(a). An amplification with the magnetization curves on cooling is given in the inset for better visualization. There is a slight lift on the magnetization curves for the composite samples at the thermal hysteresis temperature range that lead to a reduction on the bump at the derivative curves in Fig. 6.9(b). As

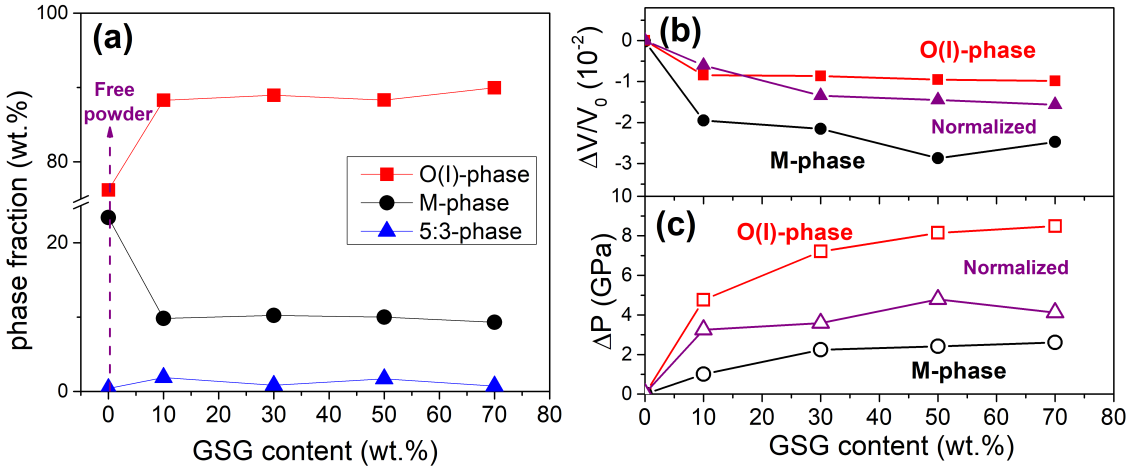

Figure 6.8: **(a)** Phase fraction of O(I), M and 5:3 phases considered for the Rietveld calculations of all samples (powder and composites), revealing that the introduction of GSG micropowder onto PMMA matrix, lead to an enhancement of O(I) phase fraction and, consequently, reducing the detection of M-phase. **(b)** The relative unit cell volume as a function of GSG filler content, where V_0 corresponds to the free powder results. The respective hydrostatic pressure applied by PMMA walls in **(c)** was calculated considering the compressibility values of: $\kappa_{O(I)}$ = 3 TPa^{-1} and κ_M = 6 TPa^{-1} from Ref. 116.

for the O(I) phase temperature transition, there is no shift on T_C due to the presence of non-magnetic PMMA matrix. This is clear for 10 wt.% composite sample due to the quality of the curve measurement while for the higher filler content systems, since the data were acquire on the DC mode of SQUID, the signal noise on the curves does not turn it clear. Given this observation, it is possible to assume that the implementation of GSG micropowder in PMMA matrix is only affecting the M-phase. Such effect come from the higher sensitivity of the M structure over O(I) to applied magnetic field, hydrostatic pressure and particle size[29,117]. Besides that, there is a small difference between heating and cooling curves at 5 K which is maximum for 30 wt.% composite ($\Delta M_{5K} < 0.4\mu_B/FU$) by considering the weight fraction of magnetic material, that is not observed for the powder and can be a consequence of thermal dissipation and internal strain effects of multiphase GSG/PMMA system[205,221,224].

As performed in the previous section, the magnetic results will also be useful to infer the phase-fractions of GSG grains when immersed on non-magnetic PMMA. The χ^{-1} method was applied for all composites samples following the same procedure as for the powders. In particular, for 10 wt.% composite, the diamagnetic contribution from the matrix were removed for accuracy on the results. The best calculated curves are presented in Fig.6.10(a) for all samples and the returned values are summarized on Table6.4. In comparison with the XRD results, there is no significant change on the values obtained through χ^{-1} method, since they are within the error, as can be seen in Fig.6.10(b). Most notably, the magnetic analysis seems to detect a slightly higher content of M-phase than XRD calculations which might be related to it higher sensitivity of χ^{-1} method. These findings corroborate with the assumption that PMMA polymeric matrix works as a pressure cell on the grains surface and, thus, weakens the effects

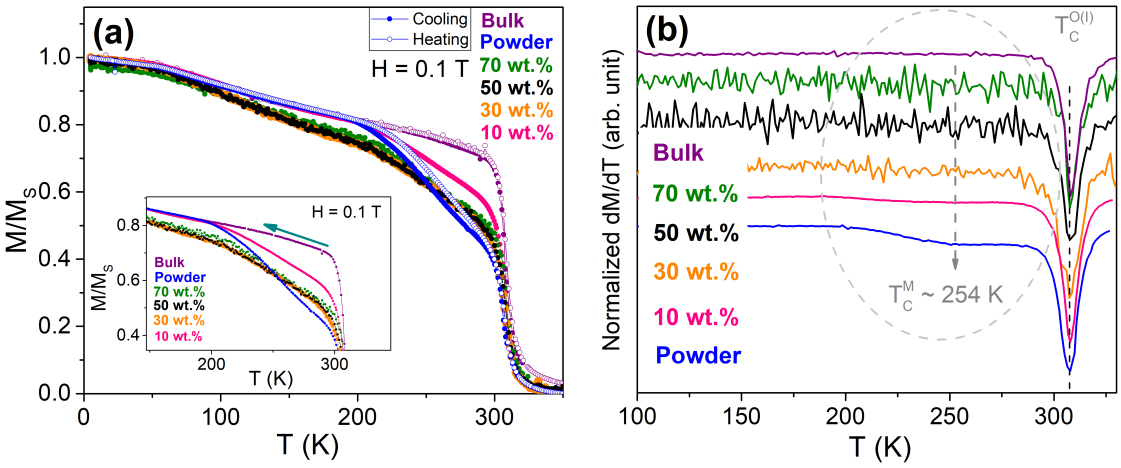

Figure 6.9: **(a)**Temperature dependence on the magnetization with an applied magnetic field of 0.1 T and it **(b)** temperature derivative curves (dM/dT) for $Gd_5Si_{2.4}Ge_{1.6}$ as bulk, powder and the composites with 10, 30, 50 and 70 % weight fraction of PMMA.

of secondary M-phase. Indeed, further evaluation on the MCE results will also reveal the strong influence of the non-magnetic thermoplastic on the magnetocaloric powder. Furthermore, the μ_{eff} value for this phase is below the expected 7.94μ_B and will have consequences on the MCE features of GSG magnetic material[117]. Furthermore, θ_P and μ_{eff} are in fine agreement with the obtained for pure powder and the theoretically expected[113,195]. Although there is a reduction on μ_{eff} values, they are still close to theoretically expected 7.94μ_B for Gd^{3+} ions[113]. Therewith, the presence of PMMA does not affect the intrinsic magnetic features of the 3.4 μm powder. In another words, the polymeric matrix is acting as an external agent on the grains in form of hydrostatic pressure that have been shown to have great influence on the M-phase[29,108,116].

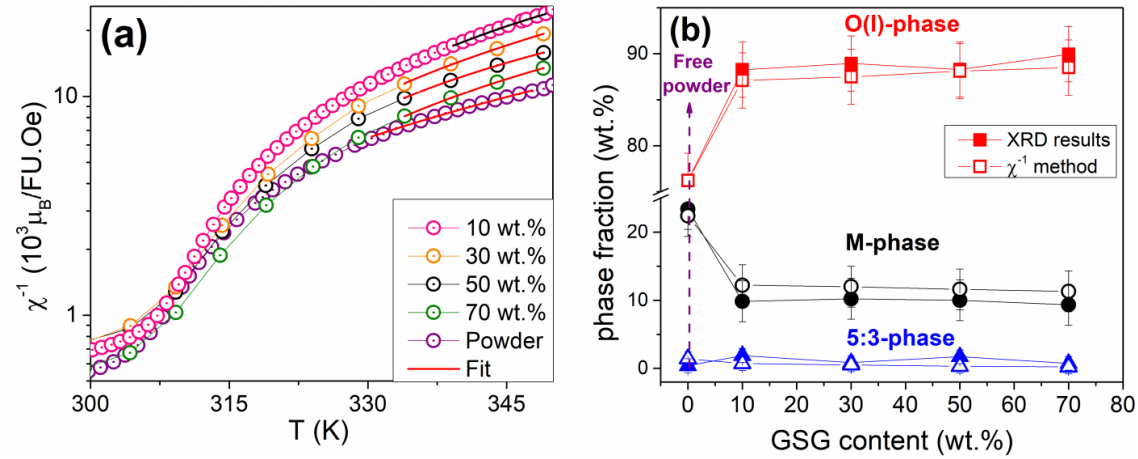

Figure 6.10: **(a)** The best fitted curves for the reciprocal magnetic susceptibility using Eq. 3.1.1 were used to obtain the phase fraction of each crystallographic phase in **(b)** to validate the results obtained from XRD *Rietveld* calculations.

Nevertheless, magnetization data at 5 K for the bulk, powder and composite sam-

Table 6.4: Results obtained from the Curie-Weiss law: the amount of O(I), M and 5:3 phases is shown and their respective calculated values of paramagnetic temperature (θ_P), diamagnetic contribution of PMMA (χ_0), the effective moment (μ_{eff}). Important magnetic parameters are also placed: the magnetization at 5 K and 5 T for the composite samples (*i.e.*, taking into account the weight of filler and polymer), the saturation magnetization (μ_{sat}) obtained considering the grains weight fraction and the irreversibility between cooling and heat magnetization curves at 5 K.

Sample	**Phase**	θ_P (K)	μ_{eff} (μ_B/Gd^{3+})	M(5K,5T) (μ_B/FU)	μ_{sat} (μ_B/Gd^{3+})	ΔM_{5K} (μ_B/Gd^{3+})
	88.5% O(I)	310(3)	7.92(2)			
70wt.%	11.3% M	291(4)	7.45(7)	21.5(4)	6.13	0.12(2)
	0.20% 5:3	186(5)	8.03(2)			
	88.1% O(I)	310(5)	7.94(2)			
50wt.%	11.6% M	296(6)	7.51(5)	15.1(5)	6.03(2)	0.30(3)
	0.30% 5:3	186(5)	8.20(3)			
	87.5% O(I)	308(3)	7.93(4)			
30wt.%	12.0% M	289(5)	7.59(3)	5.23(1)	6.03(3)	0.37(2)
	0.50% 5:3	183(3)	8.03(6)			
	87.1% O(I)	308(5)	7.89(6)			
10wt.%	12.2% M	294(5)	7.91(4)	3.04(1)	6.07(3)	0.29(1)
	0.70% 5:3	184(6)	8.09(3)			

ples were acquired for rating their saturation magnetization (μ_{sat}) values, which will be important for the MCE studies. Considering the contribution from all the system components, *i.e.*, $m_{GSG} + m_{PMMA}$, shown in Fig.6.11(a), the magnetization values at 5 K with an applied magnetic field of 5 T [M(5K,5T)] reduces as the amount of non-magnetic PMMA material enlarges, as expected[221]. As can be noted, the saturation is reached at lower intensities of magnetic field for the composite samples with lower filler contents and it starts to behave as the free powder with increasing the amount of magnetic material. Such behaviour can raise from interparticle short range interactions with associated low level of deformation, as observed in soft magnetic elastomers, can also contribute to this fast magnetization on the composite samples[202,205]. Although there are a small loss on the saturation magnetization (μ_{sat}), they are still within the error which corroborates with previous assumptions that the presence of a non magnetic polymer does not affect the nature of magnetocaloric material.

6.4 Magnetocaloric Effect (MCE) evaluation

Following the same procedure of previous Chapter, the MCE evaluations were performed through magnetization isothermal measurements obtained from 215 K to 350 K by increasing and decreasing the applied magnetic field up to 5 T. It is worth to point out that, due to the magnetic irreversibility, the samples were warmed up to 330 K between each isothermal measurement[21]. For 10 wt.% GSG/PMMA sample, due to

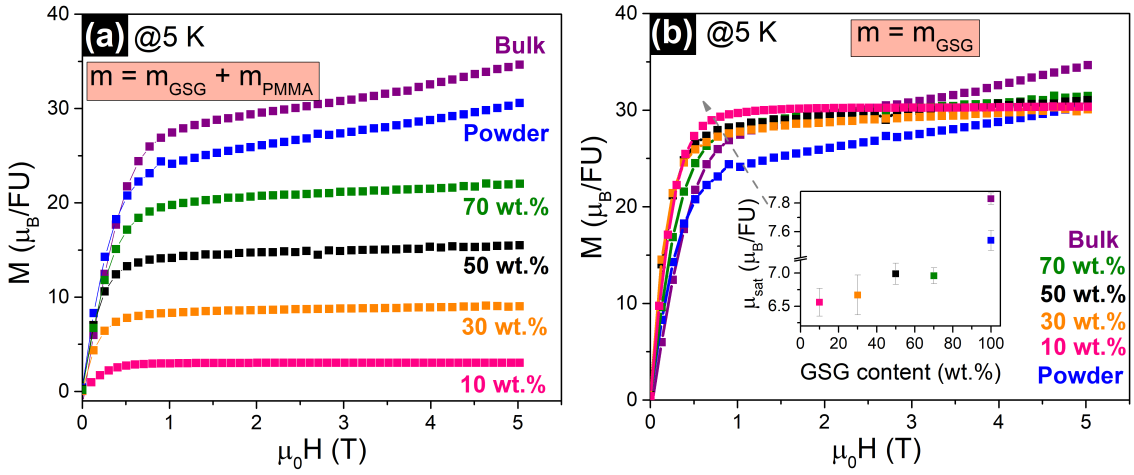

Figure 6.11: Field dependence on the magnetization at 5 K considering for bulk (42 μm), powder (3.4 μm) the weight of the hole sample and molar mass from 5:3-phase in **(a)** and taking into account only the amount of magnetic material in **(b)**. The curves in **(a)** give the magnetization at 5 K and 5 T (M_{5K}^{5T})for the composites while **(b)** represents the saturation magnetization (μ_{sat}) of the system, depicted in the inset.

the low signal from magnetic material, a diamagnetic contribution from sample holder and polymeric matrix were subtracted from magnetization curves on the [215-270]K temperature range. Therefore, through the magnetization map M(T,H), see Fig.6.12, the magnetocaloric potential ΔS was calculated by using the integrated Maxwell relation[21] in Chapter 3. The Arrott plot curves are also presented in Fig.6.12 revealing that the insulator matrix of PMMA does not change the SOMT nature of GSG powder. In this case, the magnetic and temperature dependence of the entropy is continuous and, therefore, no corrections around the critical points are required for the integration using Eq. 3.2[21,44,54,218].

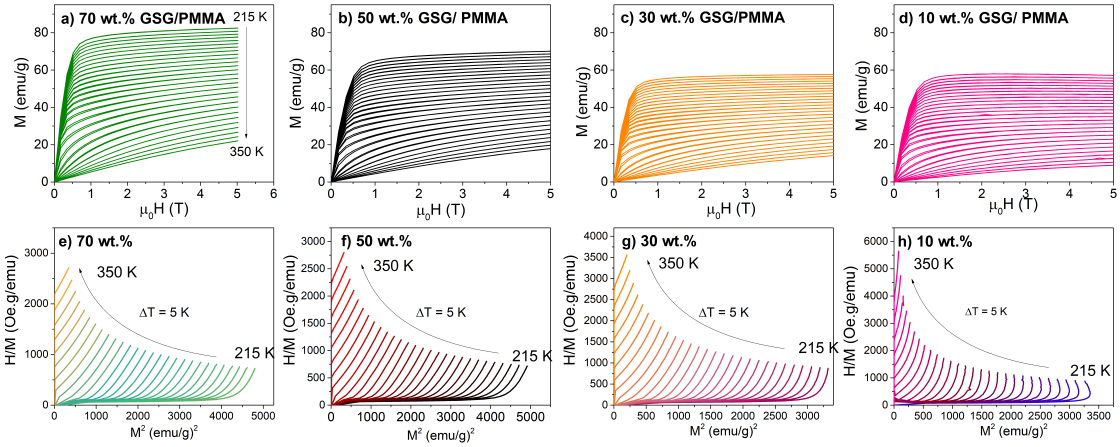

Figure 6.12: M(T,H) map for and Arrott plot curves for **(a-b)** 10 wt.%, **(c-d)** 30 wt.%, **(d-e)** 50 wt.% and **(e-f)** 70wt.% composites used for the phase transition order determination and evaluation on the samples MCE properties.

For the calculations, first it was considered only the contribution from magnetic material, *i.e.*, the weight fraction of GSG, resulting at the maps shown in Fig.6.12. There is

Table 6.5: Magnetocaloric properties for all the synthesized samples obtained for an applied magnetic field of 5 T calculated considering the sample weight and volume. The RCP values were calculated considering the *full width at half maximum* (FWHM)[21].

Sample	ΔS_M^{max} (J/kg.K)	ΔS_V^{max} (J/kg.K)	δT_{FWHM} (K)	RCP_{FWHM} (J/kg)
Bulk	6.04	50.4	23.4	69.4
Powder	3.09	23.2	23.8	33.1
PMMA + 70wt.%	2.64	12.5	26.4	26.2
PMMA + 50wt.%	1.14	10.4	25.2	10.6
PMMA + 30wt.%	0.46	5.35	25.2	4.50
PMMA + 10wt.%	0.99	1.84	24.7	8.84

a reduction on the saturation magnetization as filler content decreases with the diamagnetic contribution from PMMA being more evident for 10 wt.% sample, as mentioned above. The obtained $\Delta S_M(T)$ curves in mass for powder and composite samples are depicted in Fig. 6.13 for $\Delta\mu_0 H = 5T$. For practical purposes, the $\Delta S_M(T,H)$ calculated for all produced samples are given on the Appendix B. The $\Delta S_M(T,H)$ curves for the composites follow a λ-shape, typical of SOMT, and its maximum values raise as the applied magnetic field increases[113]. Concerning application goals, the volumetric entropy change ΔS_V is rather informative for device engineering than the mass one[221]. The magnetic material density (ρ) was considered to be 7.45 g/cm^3, in agreement with reported by Gschneidner and Pecharsky[105]. As for the composite samples, the density was obtained through a carefully measurement on the film area and considering the thickness obtained by SEM cross-section imaging, the results are shown in the inset of Fig.6.13(b) calculated using:

$$\rho_T = \frac{m_T}{\frac{m_{GSG}}{\rho_{GSG}} + \frac{m_{PMMA}}{\rho_{PMMA}}}. \tag{6.1}$$

.

The systems with 10 and 30 wt.% of magnetic material are below the expected and might be the reason for loss on ΔS_M^{max} since perfect homogeneous distribution along the film volume cannot be assured during[225]. A close composition $Gd_5Si_{2.5}Ge_{1.5}$ have been reported to present a maximum entropy of 70.7 mJ/cm^{3}K at 313 K[226]. Taking into account the formation of secondary M-phase and eutectic 5:3 phase, the obtained value of $\sim$50 mJ/cm^{3}K for 42 μm are close to the expected[220]. For the smaller grains, it drastically decreases to $\sim$25 mJ/cm^{3}K with the same profile as shown in Fig.6.13(a). Although the effect of M-phase is blocked by the polymeric matrix, the presence of non-magnetic material leads to losses on the system magnetocaloric response. However, the values of 5-10 mJ/cm^{3}K are in the range for applications in micro-cooling devices for pump systems[223].

Regarding the ΔS_W and ΔS_V curves features, the lump from 220 to 300 K is not observed for the GSG powder when is blended with PMMA thermoplastic. As already

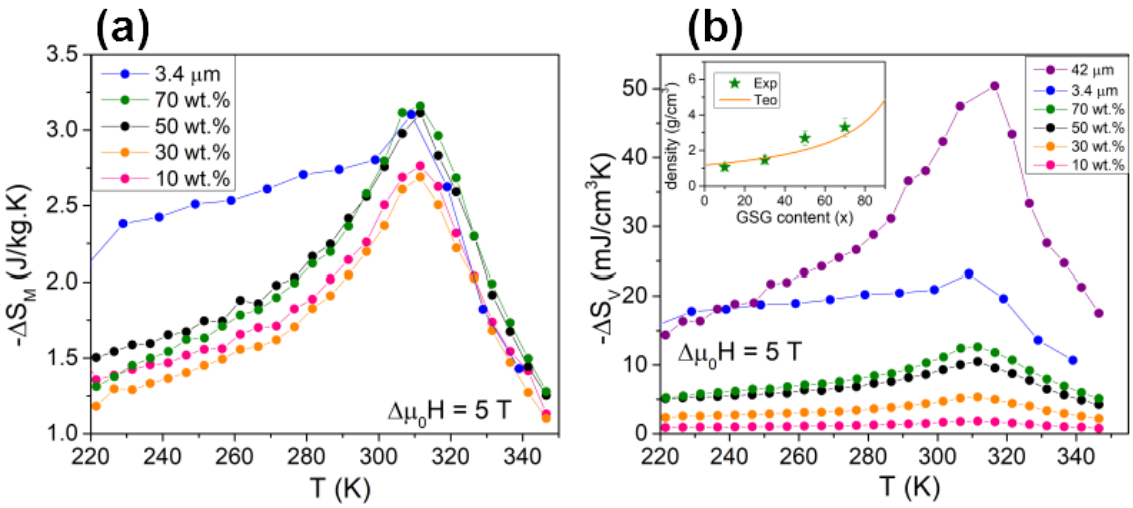

Figure 6.13: Temperature dependence of the entropy change (ΔS) obtained for all the samples using Eq.1.4 for an applied field of 5 T in **(a)** mass and **(b)** volumetric. The inset shows density as a function of GSG content considering the theoretical values ρ_{PMMA} = 1.19 g/cm^3 and ρ_{GSG} = 7.45 g/cm^3 reported in Ref.[101] and[220], respectively. As can be noted, the effect of secondary M-phase - the lump at Δ_S curve - is not observed for the composites.

exposed, the particles are confined on the polymeric matrix that can be acting as a pressure cell on the grain boundaries. It is known that $Gd_5(Si,Ge)_4$ is highly sensitive to internal and external stimuli[32]. The thermal expansion of the filler, monoclinic $Gd_5Si_2Ge_2$ stoichiometry presents an anomalous behaviour on it volumetric thermal expansion (γ) that reaches a maximum $\sim 1.46 \times 10^{-2}$ for a single-crystal[227], being the mechanism responsible for the GMCE on this material. Carvalho *et al.* have already shown that by applying a hydrostatic pressure of 0.1 GPa reduces the ΔS_{max} of $Gd_5Si_2Ge_2$ compound in $\sim$23% and eventually vanishes after 0.6 GPa due to a suppression of the FOMT[117]. Given this, we can assume that during heating, the thermal expansion of the M-phase changing to an O(I) by the sliding of the pseudo-blocks on the crystal structure is limited by PMMA surface around the grains - since the polymer present a lower thermal expansion[213]. Besides that, it would be interesting to perform studies on temperature cycling of the microcaloric samples to observe if the polymer deformation is reversible, which could allow the structural change on the magnetic material. Since there are particles with a broad particle size distribution and PMMA thermal expansion is anisotropic, there is no simple solution to describe the mechanism behind this effect to estimate the applied pressure from the matrix to the grains edges. For this reason, we can only assume that is above the 0.6 GPa observed on M $Gd_5Si_2Ge_2$ single crystals. Nonetheless, these findings reveal the interplay between mechanical and magnetocaloric properties that can be used to tune the best material features to produce multifunctional devices.

6.5 Partial Conclusions

The results presented in this Chapter show that solvent casting is a suitable technique for the implementation of 10, 30, 50 and 70 weight fraction of 3.4μm $Gd_5Si_{2.4}Ge_{1.6}$ particles in non-magnetic PMMA. The micropowder was obtained through sieving and the reduction of particle size intensified the effect of deformity on the grain boundaries, leading to a detection of $\sim$30% M-phase from magnetic analysis for the resulting powder. Although there is no change in the magnetic nature of the microparticles when blended with the thermoplastic, there is the appearance of small irreversibility at low temperature that can be a result of internal strain of the grains. However, the saturation magnetization at 5 K reveal that the magnetic response of the composite are ruled to the particle density. This is reflected on the MCE results where the interface GSG/PMMA interaction seems to weaken the contribution from secondary M-phase on the ΔS curves. Further investigations on thermal and mechanical properties are required for a full understanding in the mechanism of GSG/PMMA composites during thermal cycles. Furthermore, these observations indicate that the system can allow several applications such as energy harvesting, microfluidic system and magnetic refrigeration[78,102,138,221].

Chapter 7

Multiferroic $Gd_5(Si,Ge)_4$ Polyvinylidene fluoride composites

"A truly synergistic symbiotic relationship between he materials designer and the bench engineer/scientist is critical if significant advances are to occur in magnetic refrigeration"

Gschneidner & Pecharsky, *Int. J. of Refrigeration* **31**, 945 (2008).

The $Gd_5Si_{2.4}Ge_{1.6}$ 3.4 μm powder characterized in the previous Chapter was also used to produce a multiferroic composite by blending it with a piezoelectric polyvinylidene fluoride (PVDF) polymer. To understand the interplay between magnetocaloric and ferroelectric features of composite constituents, an evaluation of the magnetoelectric coupling and magnetocaloric properties was performed after a meticulous structural and morphological characterization using XRD, SEM, AFM and FTIR analyses.

7.1 Introduction

The requirements for device reduction with high performance associated has been a great challenge for application in several fields such as computational, biomedical, sensors/actuators, energy harvesting/generation/storing, among others[228,229]. In particular, for electronic designs, the control on the electric and magnetic fields generated during operation is desired for improving its efficiency[49]. An approach to overcome this issue is through the magnetoelectric (ME) effect where magnetization (or polarization) can be driven by applying an electric field (or magnetic field). First observed in antiferromagnetic Cr_2O_3 single crystals in 1960, the ME-effect had gained a great interest of the scientific community[230]. However, the low magnitude of ME-coupling

coefficients observed in a restricted number of known multiferroic systems and the occurrence at cryogenic temperatures led to a loss on the interest on this subject. It was further shown that ME response on single phase systems are constrained by the product of electric and magnetic susceptibilities tensors[231]. The lack of knowledge on theoretical concepts behind the mechanism on multiferroic systems and the limitations of experimental techniques at the time largely contributed to the recession on ME-effect research[49]. Multiferroic materials are single-phase systems presenting at least two of the following primary ferroic ordered phases: ferromagnetic, ferroelectric, ferroelastic or the more recently included, ferrotoroidicity - that until the date was only observed for antiferromagnetic compounds[232]. It was already demonstrated by Melvin Vopson in 2013 that multiferroic materials fill the requirements to present giant multicaloric effects being the most promising for alternative solid-state cooling systems[153]. Indeed, they can be used as an "all-in-one" solid-state system for the development of a multifunctional device capable of memory storage, logic operations, thermal activation, energy conversion, and so on[187]. This fact rises from the degrees of freedom in the material - spin, charge, orbit, lattice - that lead to cross-coupling effects such as piezoelectric, magnetostrictive and, the main interest of the present Chapter, magnetoelectric coupling, illustrated in Fig.7.1.

It was only in 2001 that the ME-effect gained the proper attention after Ryu *et. al.* reported a large ME coefficient for epoxy bonded Pb(Zr,Ti)O_3(PZT)/Terfenol-D ceramic disks[233]. PZT is a piezoelectric ceramic and Terfenol-D a high magnetostrictive material that does not present the ME-effect when is free and the ME-coupling is a product effect on the composite[49]. In the case of composites, the synergy between components increases the number of free parameters to tune the ME-coupling on multiphase systems such as shape, composition, connectivity, microstructure, and so on[49]. Most commonly, the composites are classified by the connectivity type that have a strong relation with the elastic coupling: *i)* 0-3 type consist of magnetic particles immersed in a piezoelectric matrix; *ii)* 1-3 type are cylinder composites based of magnetic fibers/tubes/wires embedded in piezo-matrix; and *iii)* 2-2 type which are the laminated composites consisting of alternating magnetostrictive and piezoelectric layers. The first studies on ME composites were concentrated on laminated systems due to the reduced of chemical reaction between the constituents observed on particulate composites. It has been shown that the interfacial bonding between piezoelectric and magnetostrictive phases is strongly related with the ME-coupling. The initial study on PZT/Terfenol-D demonstrated a ME-coefficient 36 times higher than the one observed for particulate composites[233]. Several compositions and geometries have been proposed to optimize ME properties. So far, the material presenting the highest piezomagnetic coefficient is the amorphous Metglas (Fe-based) that, with a magnetic susceptibility in the order of $\sim 10^3$, can enhance ME-coupling when implemented with a magnetostrictive component. For instance, a colossal ME-coefficient was reported in 2006 by Zhai *et. al.* in a Metglas/PVDF bulk composite, with the largest value when compared to other systems[234].

As depicted in Fig.7.1(b), Metglas is the most attractive magnetostrictive material due to the unique properties of fast magnetization/demagnetization, low saturation and high permeability[64].

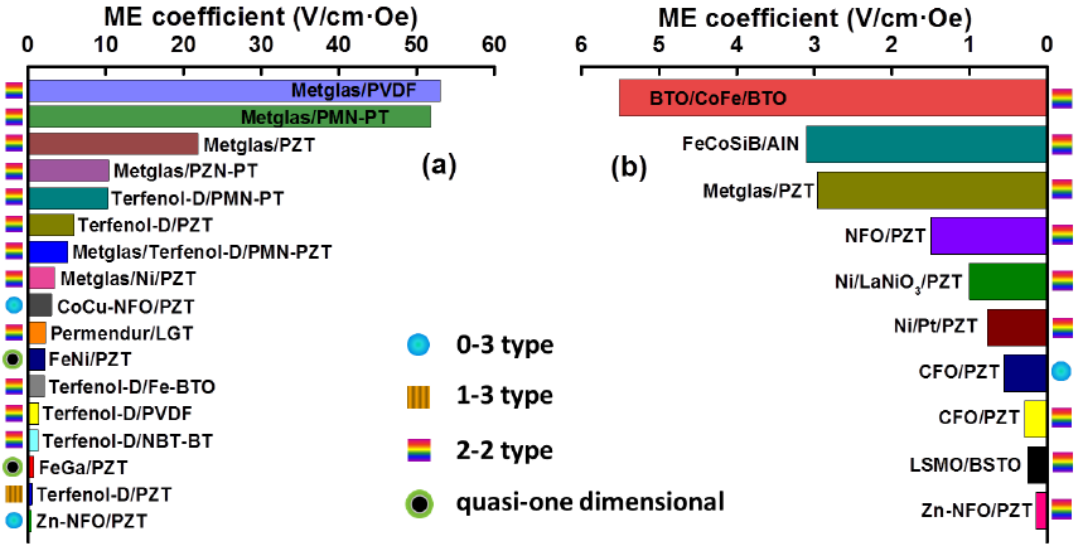

Figure 7.1: ME-coefficients reported for **(a)** bulk and **(b)** film-based composite systems with the indicative connectivity type: 0-3 being the particulate composed of piezoelectric and magnetic grains; 1-3 type for fibre composites; 2-2 type that are the layered composites with piezoelectric and magnetostrictive layers; and quasi-one dimensional systems. Extracted from Ref. 64.

It is possible to enlarge the applications of magnetic materials by incorporation in polymeric matrices, as exposed in Chapter 2. In particular, PVDF is the most promising polymer for developments on sensing/actuating devices and energy harvesting due to its piezo- and pyroelectric properties[235]. Although there are few reports dedicated in pyroelectric composites, Lu *et al.* have already proven the enhancement on the ME-effect by mediations of polymer ferroelectric relaxation and MCE of Gd[236]. The T_C of Gd is around 293 K that corresponds to the pyroelectric peak of PVDF-TrFE copolymer and, consequently, to the maximum on the ME-coefficient. Through a phenomenological approach, the authors have shown that the adiabatic temperature change of MCE material, thermally mediates the ME-coupling due to the PVDF pyroelectric character. PVDF is a semi-crystalline plastic formed by C-H-F chains with arrangements mainly observed in three different crystalline structures: α-, β- and γ-phase. Its pyroelectricity rises from the β-phase relaxation during the melt of amorphous phases (around 220 K) and at the glass transition of crystalline phases (around 330 K)[237]. The β- and γ-phase are the electroactive (EA) phases where the first presents a highest dipole moment per unit cell and is the main interest for application purposes[238]. Several approaches have been reported targeting the enhancement of polarized β-phase formation such as mechanical stretching, thermal treatment, electrospinning and by the addition of magnetic fillers[239–241]. El Achaby *et al.* were able to achieve a pure β-phase of PVDF by adding 0.1 wt.% of graphene oxide due to the strong interaction between the -C=O group of

the filler and the CF_2 polymeric chains[242]. Through adsorption energy calculations, Yu *et. al.* have shown that the oxide graphene surface favours the nucleation of β- electroactive phase around the graphene nanostructure after sonication the mixture with PVDF[243]. Although the mechanisms behind the increase in the nucleation of β-phase are dependent of electronegativity, morphology and content of the material, they are basically due to interface interactions[240].

As already mentioned, low amounts of $Gd_5(Si,Ge)_4$ magnetic material can enhance the formation of such phase as observed by Harstad and Ozaydin *et al.*[24,138]. The mentioned studies have also shown an improvement on the energy conversion of PVDF; however, with no evaluation on the composites magnetoelectric properties. In that sense, we will present in this Chapter a thorough study on low amounts (2 and 12 wt%) of $Gd_5Si_{2.4}Ge_{1.6}$ micropowders immersed in PVDF matrix for the evaluation of their magnetoelectric and magnetocaloric effects.

7.2 Morphological and structural characterization

PVDF is a polymorphic polymer with Young's modulus in the order of GPa for microfilms produced through solvent casting[244] and, for this reason, the samples will present a tougher surface than that obtained for the PMMA composites, presented in the previous Chapter. Fig.7.2(a) shows the SEM micrograph on the surface of pure PVDF that reveals a dense and continuous layer with low amounts of defects[245]. The composite top view in Fig.7.2(b) and (c), shows a drastic change on the PVDF morphology when 2 wt.% of 3.4 μm GSG powders are introduced to the matrix where the grains limit becomes evident and the surface apparently has a higher level of porosity, with a profile typical of electroactives β- and γ-phases formation[237,246]. It is worth to point out that the scratches along sample surface is due to the manipulation during preparation for SEM imaging[225]. Furthermore, the increase on particle density becomes clear from 2 wt.% to 12 wt.% sample, in Fig. 7.2(b) and (c)[247]. Cross-section imaging on freeze-fractured films, shown in Fig.7.2(d)-(f), showing that the particles are distributed along the PVDF volume. The thickness was found to be around 200 μm with no significant variation due to the low amount of magnetic filler. The fracture profile is in agreement with previous reports on PVDF films produced through the solvent casting technique[240]. There are also a couple of vacancies indicating that the polymer crystals grow around the particles, as observed for oxide graphene[244].

Aiming to access the interface interactions between the grain and polymeric chain, AFM measurements were carried out on the sample with 12 wt.% of filler content due to the higher probability of detect a particle. Fig.7.3(a) shows the obtained 3D map for a selected area of 25x25 μm^2 with a continuous view of the polymer surface, i.e., the magnetic particles are covered by PVDF. An important observation on the GSG/PMMA composite samples, studied in the previous Chapter, is that the particles tend to ag-

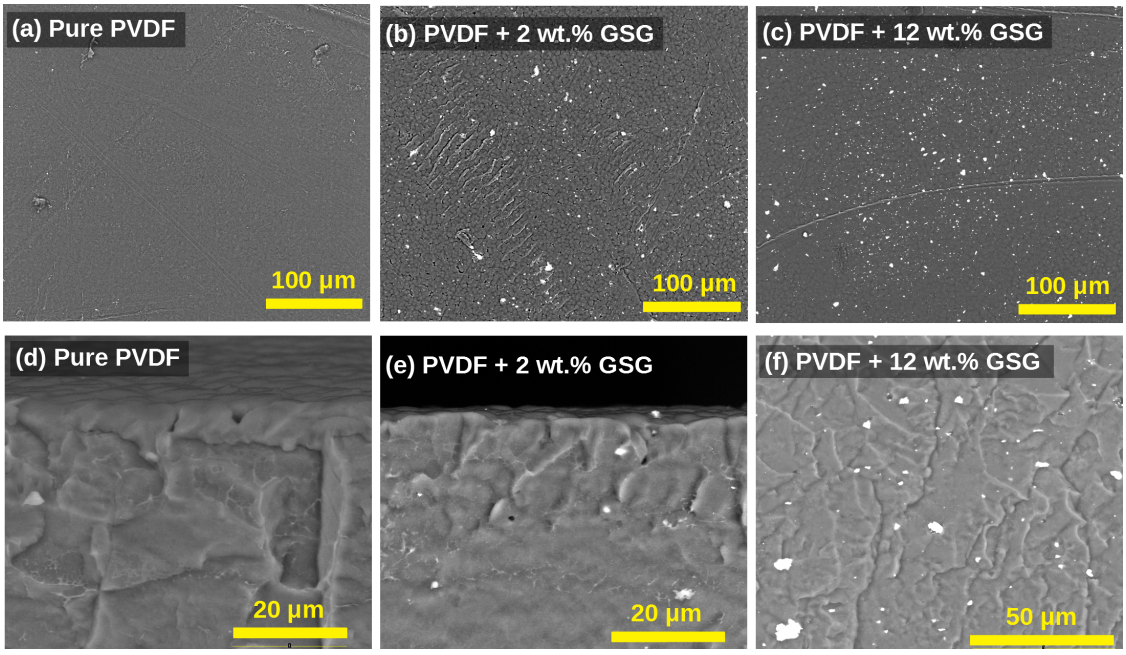

Figure 7.2: Top view (a)-(c) and cross-section (d)-(f) SEM images for pure PVDF and GSG/PVDF composite samples with 2 and 12 wt.% concentration. The distinct surface morphology with the addition of filler is clear from the surface micrographs while the fracture profile seems to not be affected by the presence of a 3.4μm magnetic material.

glomerate at the bottom of the film. For this reason, imaging the other system face was performed to confirm that all the particles are completely hidden by polymeric chains, shown in Fig.7.3(b). The larger structures present diameters around 7-8 μm, indicating that the polymer layer surrounding the micropowders must be around 2-3 μm of thickness. Indeed, the thinner regions at the valleys present diameters of 1-4 μm that represent the granular structures observed through SEM imaging.

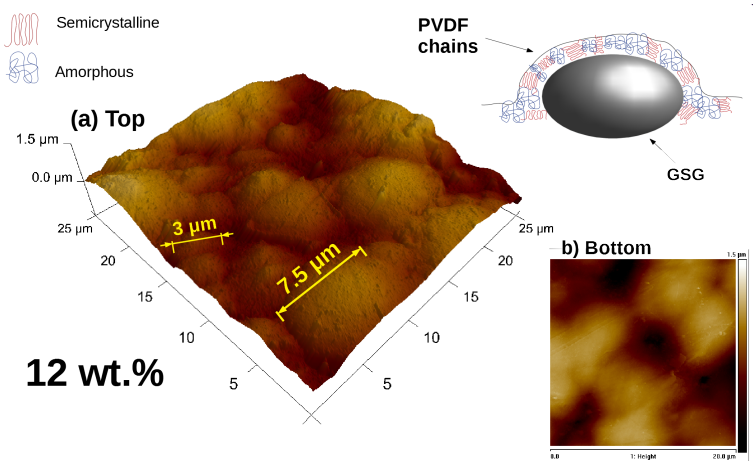

Figure 7.3: Atomic force microscopy for 12 wt.% composite obtained at both sides **(a)** top and **(b)** bottom revealing that PVDF chains nucleates around the magnetic grains.

Since PVDF is a semi-crystalline and polymorphic polymer[247] where, during the cast, the C-H-F atoms crystallizes usually in three structures[248]: α and γ with mono-

clinic symmetry ($P2_1/c$ space group), β with an orthorhombic symmetry ($Cm2m$ space group)[249]. In Fig. 7.4, a view on the unit cell of these phases is shown where the α structure has the lower symmetry being non-polar, since none of the monomers are aligned along the same directions. Distinctly, the β conformation is the most symmetric one composed of sequential H_2C-CF_2 chains in a zigzag fashion being the phase with highest dipole moment. The γ-phase is a rotation in 180^o on the alternative chains of α-phase that favour the alignment of fluoride group and, for this reason, this phase is also electroactive[249]. The corresponding Bragg peak positions for all phases are displayed on the XRD patterns inn Fig.7.4, where pure PVDF presents two main peaks around 19 and 20^o indicating the formation of γ- and β-phase[250]. As for the composites with 2 and 12 wt.% of magnetic filler, in addition to the EA peaks, the small lump around 27^o on the XRD patterns indicated the α-phase formation on these systems. This observation might be the reason for a different features observed on SEM micrographs, presented in Fig.7.2. The formation of all three phases in PVDF produced through solvent casting without any further treatment are in agreement with previous reports[161,247,248,251]

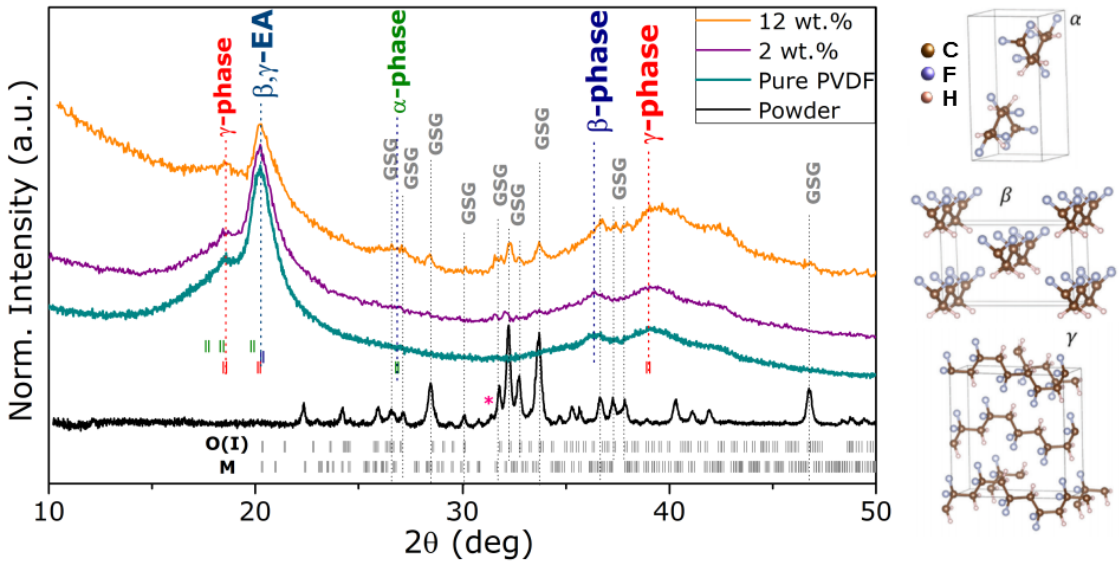

Figure 7.4: XRD patterns obtained at room temperature for $Gd_5Si_{2.4}Ge_{1.6}$ powder and the produced GSG/PVDF composites with the Bragg positions of O(I) and M phases of magnetic materials and for the polymer crystallographic α, β and γ-phase. A view on the unit cell view for the different PVDF crystalline phases is shown and was extracted from Ref. 249

Although XRD results confirm the crystallization of PVDF in α and β-phases, the amount of each formed structure needs to be determined. It is well accepted that the quantification of these phases can be performed through the absorption peaks at the FTIR spectra[252–254]. According to Cai *et al.*, who performed a thorough study on FTIR absorption results in several reports in PVDF films, there are three classifications for the observed peaks: (1) common peaks for α-, β- and γ-phases; (2) exclusive peaks for each phase and (3) dual peaks appearing for two different phases. For α-phase, the

exclusive peaks are localized at 763, 795 and 854 cm^{-1}, as indicated in Fig.7.5. The β and γ-phases have their exclusive vibration bands at 124 and 1275 cm^{-1}, respectively and is observed for all produced PVDF films. For the wavelength range of 837-841 cm^{-1}, the β and γ absorbance of IR is stronger, denoted as 839*-EA in Fig.7.5. For the α structure, the stronger absorbance is at 763 cm^{-1} and the peak intensity will be used for determination of the relative amount of EA-phases using the following relation[255]:

$$F_{EA} = \frac{I_{EA}}{(K_{840}/K_{763})I_{763} + I_{EA}}, \tag{7.1}$$

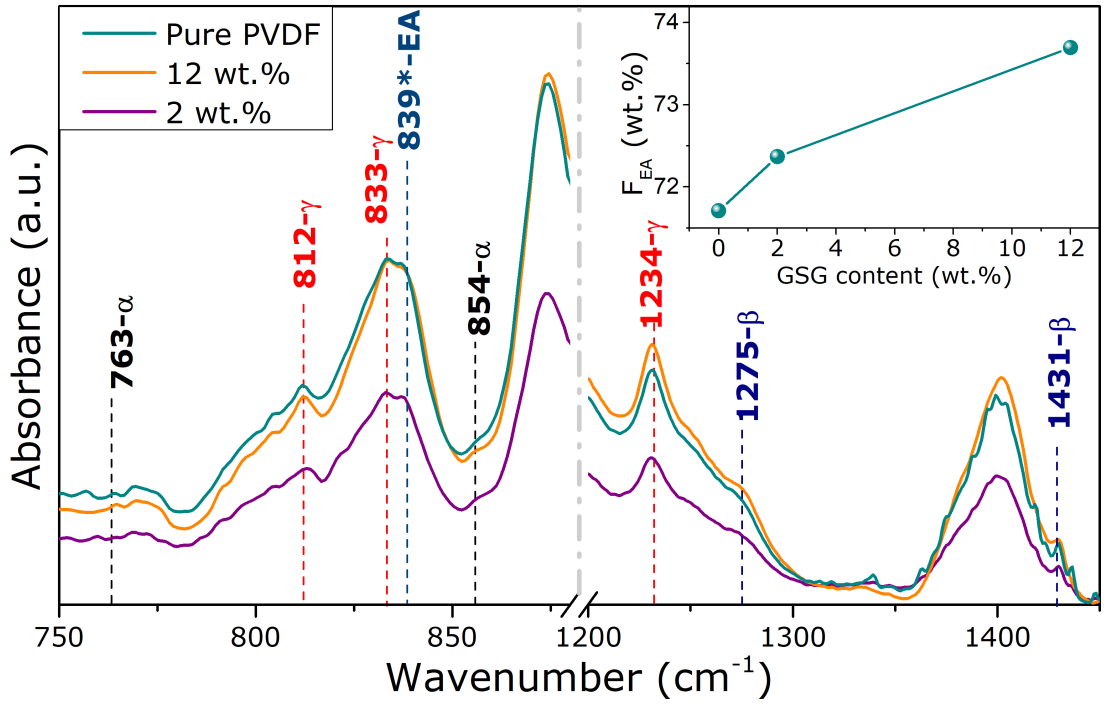

Figure 7.5: FTIR absorption curves for PVDF and composite samples with the indicated exclusive modes vibration for α-, β- and γ-phases. The quantification of the EA-phases (β and γ) for all samples, obtained using Eq. 7.2, is depicted on the inset.

where I_{EA} and I_{763} are the absorbance intensity of each phase. The constants K_{840} and K_{763} are related to the absorption coefficients associated with each wavenumber with values of 7.7$\times$10^{-4} cm^{2}mol^{-1} and 6.1$\times$10^{-4} cm^{2}mol^{-1}, respectively[255]. The formation of α-phase is kinetically more favourable during melting and commonly formed when DMF or acetone is used[256]. Nevertheless, the amount of EA-phases from 2 to 12 wt.% ferroelectric films suffers a slightly increase from 72 to 74%. Considering that typically, the amount of amorphous PVDF material range from 40-50%, the real fraction of EA-phase for 2 and 12 wt.% systems will be ranging from 36-45%[138,240,252,255,257,258]. Such observations will be important for the evaluation on the ME coupling of the produced systems, which is still lacking in literature.

7.3 Magnetic and magnetocaloric properties

Magnetization as a function of temperature (M-T) for low applied magnetic field obtained to evaluate the effect on the magnetic features for magnetocaloric $Gd_5Si_{2.4}Ge_{1.6}$ powder with the piezoelectric PVDF polymer composite samples are shown in Fig. 7.6. The FM-PM transition occurs at 308 K (obtained from the temperature derivative of $M(T)$ - not shown) being in agreement with previous reports on this composition[112,217]. There is no shift on T_C for the 2 wt.% and 12 wt.% composites, as observed for other blended systems, revealing no influence from the ferroelectric character of PVDF on the filler intrinsic magnetic features[24,138,221]. The thermal hysteresis between cooling and heating M-T curves for the powder, depicted on the inset of Fig. 7.6, is an evidence of the presence of monoclinic phase, confirming the crystallographic analysis[32]. As already mentioned, the magnetic ordering of $Gd_5(Si,Ge)_4$ family compounds is strongly coupled with the crystallographic structure and, for this reason, the XRD results should be included on the magnetic analysis[113,124].

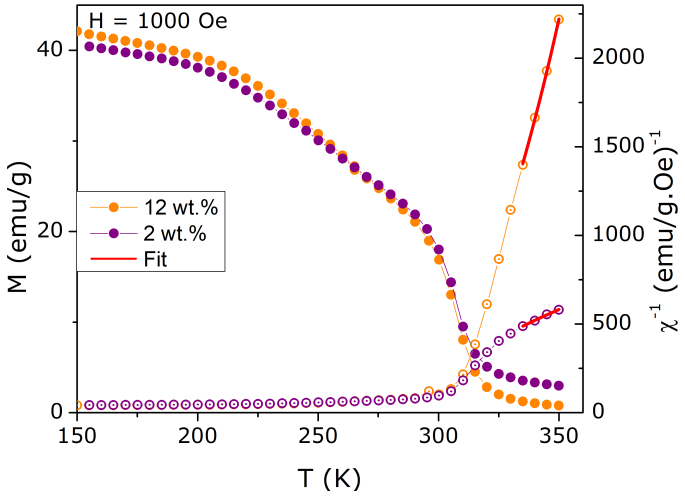

Figure 7.6: Reciprocal magnetic susceptibility as a function of temperature with the corresponding fits at high temperature, far above the Curie temperature, considering a Curie-Weiss law with an extra term from the diamagnetic contribution of the PVDF matrix.

Due to the presence of multiple phases on the magnetic material, the amount of each phase was obtained through magnetic results using Eq. 3.1.1. For the calculations, the procedure was performed considering the initial values from M-T curves and *Rietveld* refinements - as detailed in Ref. 113. In particular, for composite samples, the χ_0 values were subtracted from magnetization curves taking into account the weight fraction of magnetic material. The best fittings to the data are presented in Fig. 7.6 and the corresponding free parameters are listed on table 7.1. Although there are oscillations on the phases fractions of M and 5:3 phases, the returned values from χ^{-1} method are in good agreement with XRD analysis for all samples[44,113]. The θ_P values for the main phases suffer a slight reduction from powder to 2 wt.% composite that can

be related to the grains dilution along the polymeric chain. It is worth pointing out that the glass transition temperature (T_g) for the amorphous phase of PVDF is around 233 K, where the matrix deformations during melting can be affecting the system magnetic response[205]. Besides, although PVDF is not a magnetic material, the β-phase presents a net non-zero dipole moment which can interact with the embedded particles that can be the responsible for the associated errors of the fit parameters[239]. These findings are consistent with the ME-effect evaluation where the interplay between elastic features of powder (magnetostriction) and PVDF (piezoelectric) lead to the observation of high ME-coefficient values. Furthermore, the paramagnetic effective moment (μ_{eff}) values - obtained through the relation $C = \mu_{eff}^2/3k_B$ - for all phases are within the error for the theoretical expected for Gd^{3+} for the 5:4 phases and for reported values on 5:3 binary phase[113,143,195].

The isothermal magnetization data were collected for the evaluation of magnetocaloric effect, as presented in Fig.7.7(a) and (d). The curves obtained at 5 K were used to achieve the saturation magnetization through the extrapolation of M versus 1/H curves, with the results depicted on Table 7.1. Using the Banerjee criterion[146] through the Arrott plots in Fig. 7.7(d) and (e), we could extract the Landau B coefficient (B_{Landau}), presented in Table 7.1. The determined B_{Landau} coefficients present a positive value, i.e., the Arrott plot curves have a crescent profile, which ratifies the second order transition for all of the prepared samples: powder and composites. Following the same procedure of previous Chapters, the M(T,H) map is the starting point to obtain the magnetic entropy change of the material. To achieve this quantity, the Maxwell-relation presented in Section 3.2 was used for the calculation considering different applied magnetic fields from 0.5 to 5.0 T. The results are shown in Fig.7.7(c) and (f) for 12 and 2 wt.% composite samples revealing a distinct behaviour for each system. First, lets focus on the sample with lower magnetic content: the curve is well behaved for low applied magnetic fields and, above 1.0 T, there is a significant noise at the 200-300 K temperature range that rises the low signal of the sample. As for the 12 wt.% composite, there is a clear lump at the 200-270 K temperature range, that can be directly related with the presence of electroactive phases on the polymeric matrix.

To compare the MCE behaviour of free GSG micropowder and multiferroic composites, the $\Delta S_W(T)$ curves obtained considering the weight fraction of magnetic material for a field variation are shown in Fig. 7.8(a). The maximum values (ΔS_W^{max}) range from 2.88 to 3.10 J/kg.K from powder to 2 wt.% composite, indicating no effect of PVDF matrix on the second order FM-PM transition at 308 K. However, the ΔS_W curve profile suffers a drastic change on the [230-295]K temperature range: for the powder, there is a lump due to the thermal hysteresis of M-phase; 12 wt.% composite shows a deviation from the powder curve at 265 K and 2 wt.% curve has a linear grow above 230 K. This difference shows that indeed there is a coupling between ferroelectric character of PVDF and MCE behaviour of GSG, which will have direct influence on the ME-coupling, as will be further shown. The glass transition of amorphous α-phase occurs around 230

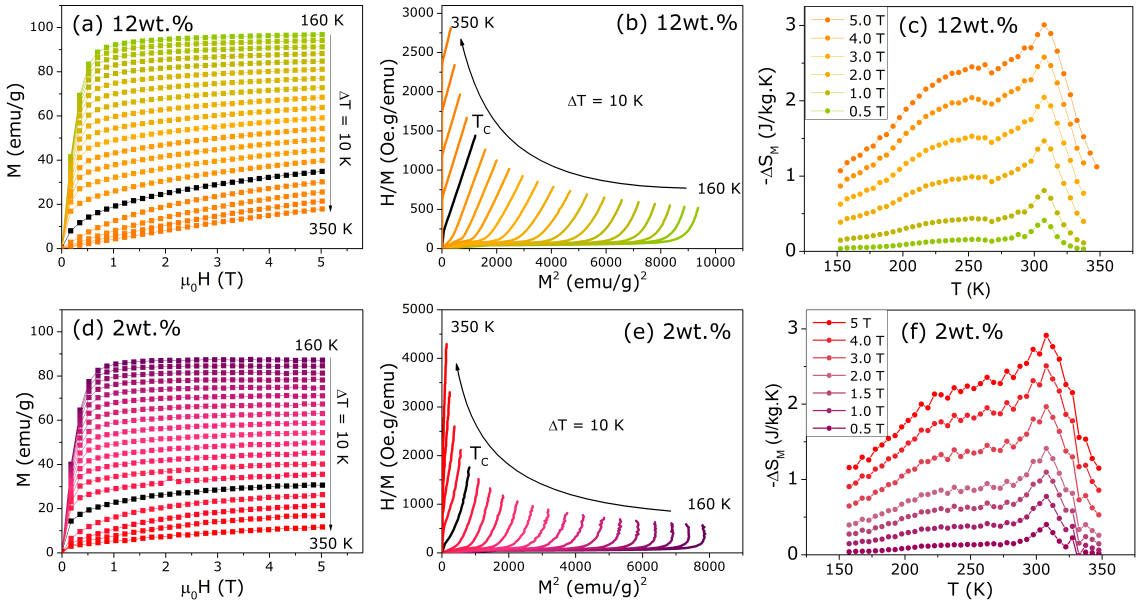

Figure 7.7: Magnetization isotherms curves for **(a)** 2 wt.% GSG, **(b)**12 wt.% GSG composites and **(c)** for the powder, labelled as 100 wt.% GSG, where is possible to notice an increase on the magnetization values as the amount of magnetic materials increases that will be reflected on the magnetocaloric properties.

K, leading to a relaxation of the semicrystalline chains with a small associated pyroelectric effect that vanishes around 275 K[236]. At this range, the 12 wt.% composite ΔS_W curve presents a slope while for the 2 wt.% system, due to the low amount of magnetic material, such behaviour is almost null.

Nevertheless, targeting engineering applications, the most effective unit for the change on entropy is the volumetric one ΔS_V [220], depicted in Fig.7.8. The ΔS_V^{max} values drastically decrease from ∼24 mJ/cm^{3}K to ∼6.62 mJ/cm^{3}K and 0.10 mJ/cm^{3}K when the amount of magnetic material is 2 and 12 wt.%, respectively. These values correspond to 27.7% and 4.2% of ΔS_V^{max} of free powder for the lower and higher weight fraction composite. This might be an indicator that the synthesis method does not allow a perfectly uniform dispersion of the filler, which is difficult to avoid during casting[225]. These evidences affect the ME-coupling of produced samples, as will be shown below.

7.4 Magnetoelectric effect (ME)

As explained above, the ME-effect in composite samples consisting of piezoelectric and magnetostrictive phases, in our case PVDF and GSG, occurs by a induced strain from the alignment of magnetic moments along the applied magnetic field. First, the ME-coefficient α_{ME} was measured at RT (∼ 293 K) as a function of the frequency of modulated AC magnetic field H_{AC} with zero applied bias magnetic field H_{DC} for the composite samples, shown in Fig.7.9. The resonance-induced ME occurs around 53 kHz and 71 kHz for 12 wt.% and 2 wt.% composites, respectively, revealing the cou-

Table 7.1: Suitable parameters extracted from the magnetic results for $Gd_5Si_{2.4}Ge_{1.6}$ (GSG) powder and GSG/PVDF composites: Curie temperature (T_C), paramagnetic Curie temperature (θ_P) and effective moment (μ_{eff}), saturation magnetization obtained at 5 K (μ_{sat}), χ_0 extracted from the susceptibility fittings and the Landau coefficients **A** and **B** returned from the Arrott plot curves.

	Phase	Fraction	θ_P (K)	μ_{eff} (μ_B/Gd^{3+})	μ_{5K} (μ_B/Gd^{3+})	χ_0 $(10^{-4}$emu/g.T)	B_{Landau} $(10^{-2}$T.FU$^3/\mu_B^3)$
2 wt.%	O(I)	76.2%	293(4)	7.92(2)	6.87(1)	-1.01(4)	6.31(3)
	M	23.6%	276(3)	7.43(6)			
	5:3	2.00%	184(9)	8.13(5)			
12 wt.%	O(I)	76.0%	305(9)	7.92(2)	6.91(1)	-1.04(5)	2.00(1)
	M	16.3%	287(8)	7.51(7)			
	5:3	7.70%	187(6)	8.11(2)			
Powder 3.4 μm (100%)	O(I)	76.2%	310(4)	7.92(5)	7.00(9)	-	1.39(3)
	M	22.4%	293(3)	7.58(7)			
	5:3	1.37%	186(4)	8.16(6)			

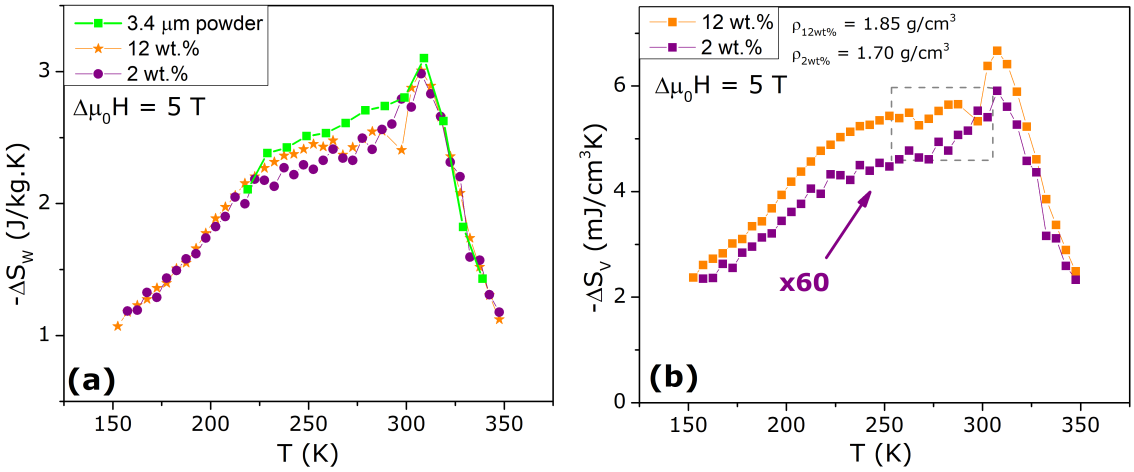

Figure 7.8: Magnetic entropy change curves obtained from the isotherms measurements for the powder and composite samples showing that the maximum value increases linearly with the GSG content, following the same behaviour as the saturation magnetization (μ_{sat}).

pling on the systems. A small anomaly is observed at 15 kHz for the composite with higher filler content that can be related with non-linear effects associated with low frequencies. As demonstrated by Laletin *et. al.*, such behaviour arises from a non-uniform distribution of the mechanical stress across the sample generated by the interface interactions of the system phases[259]. This might be due to the irregular shape of GSG grains and broad particle size distribution that can lead to anisotropic relaxation on the piezoelectric phase[260].

The cross-coupling effect, is higher around the phase transition and, for this reason, the temperature dependence of α_{ME} was obtained at different H_{DC} bias magnetic field, depicted in Fig.7.10 for both composite samples. As highlighted for both GSG/PVDF systems, the maximum ME-coefficient occurs at $\sim$ 305 K that is close to T_C - as obtained from M-T curves presented in the previous section. The α_{ME} value for 12 wt.%

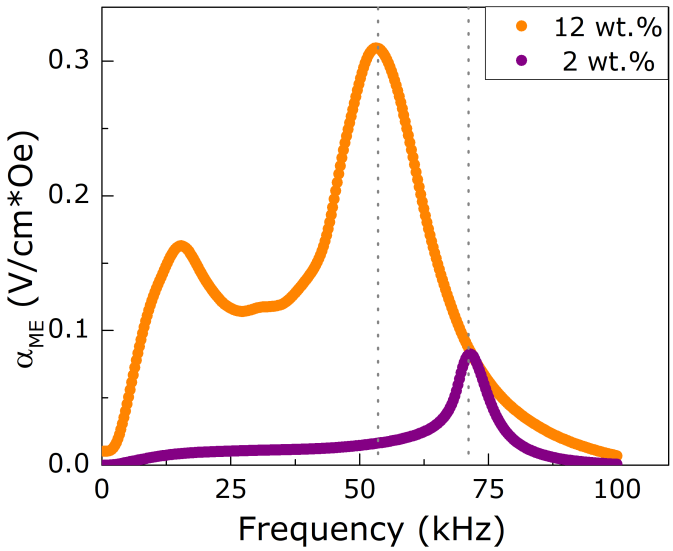

Figure 7.9: Magnetoelectric coefficient as a function of AC magnetic field frequency with a null DC bias field obtained at room temperature ($\sim$ 293 K) for 2 wt.% and 12 wt.% GSG/PVDF composite samples. Double peak for 12 wt.% composite is due to non-linear interactions at low applied fields.

system is about 7$\times$ higher than for the samples with lowest magnetostrictive amount phase. For a bias magnetic field of 0.5 T, the $\alpha_{ME}(T)$ curve reaches a maximum of 2.2 V/cm.Oe and 0.3 V/cm.Oe for 12 and 2 wt.%, respectively. These results are comparable with traditional magnetoelectric thin films, being only below the reported 3 V/cm.Oe for Metglas/PZT as shown on the chart in Fig.7.1 [64]. Considering systems with the 0-3 type connectivity, which is our case, the obtained coefficients are only comparable with PZT-based composites[64,229], revealing the great coupling on the present GSG/PVDF composite. As H_{DC} increases, the coefficient intensities suffers a slight decrease. This is because ME-coupling is driven by the magnetostriction of GSG that is reaching saturation at 0.5 T; thus, reducing the mechanical strain on the piezoelectric phase[261].

In Fig.7.11(a), around the transition temperature of GSG, the α_{ME}^{304K} increases for applied DC fields up to 0.5 T and reduces as H_{DC} intensity is raised. According to Lu *et al.*'s observations on Gd/PVDF-TrFE composites, this behaviour is an evidence of contributions to ME-coupling from MCE and pyroelectricity from the components of the composites. Due to the temperature change induced by the MCE of GSG grains, the output voltage of PVDF will be enhanced due to its pyroelectric character[236]. This can be measured through a thermally stimulated discharge current technique that could not be performed for this work. A study performed by Stavrakas *et al.* revealed that the inclusion of 1 wt.% of graphene on the PVDF matrix reduces the nanocomposite pyroelectric response. Through fitting on TSDC curves, they concluded that this loss is due the internal polarization fields generated by the addition of graphene. For the present case, the coupling between GSG grains and PVDF matrix has already show its contribution to MCE through the distinct behaviour for composites between 200-270 K

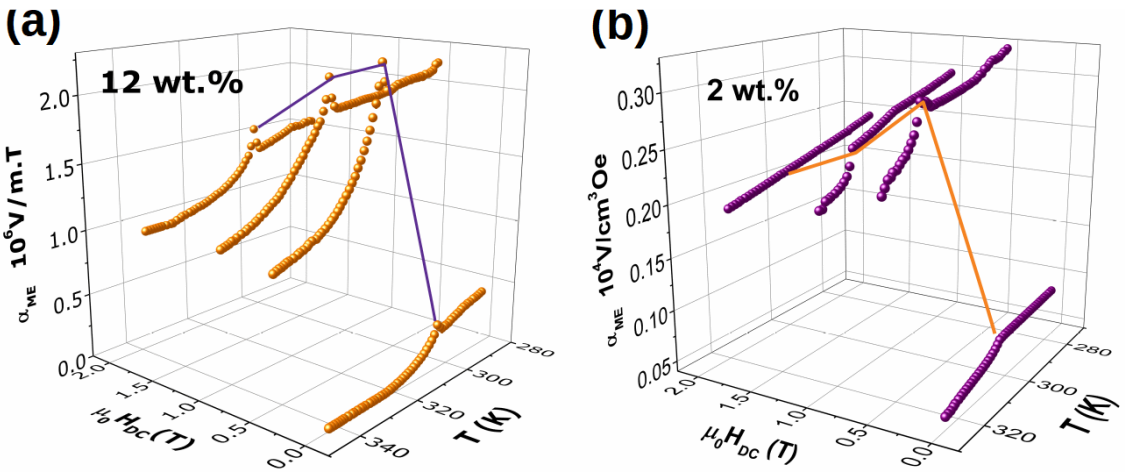

Figure 7.10: Magnetoelectric coefficient for different DC magnetic fields as a function of temperature for GSG/PVDF composites. The maximum of α_{ME} occurs around 305 K, which is close to FM-PM transition, as observed in the magnetic analysis.

temperature change as can be seen from the curves are presented in Fig.7.11(c).

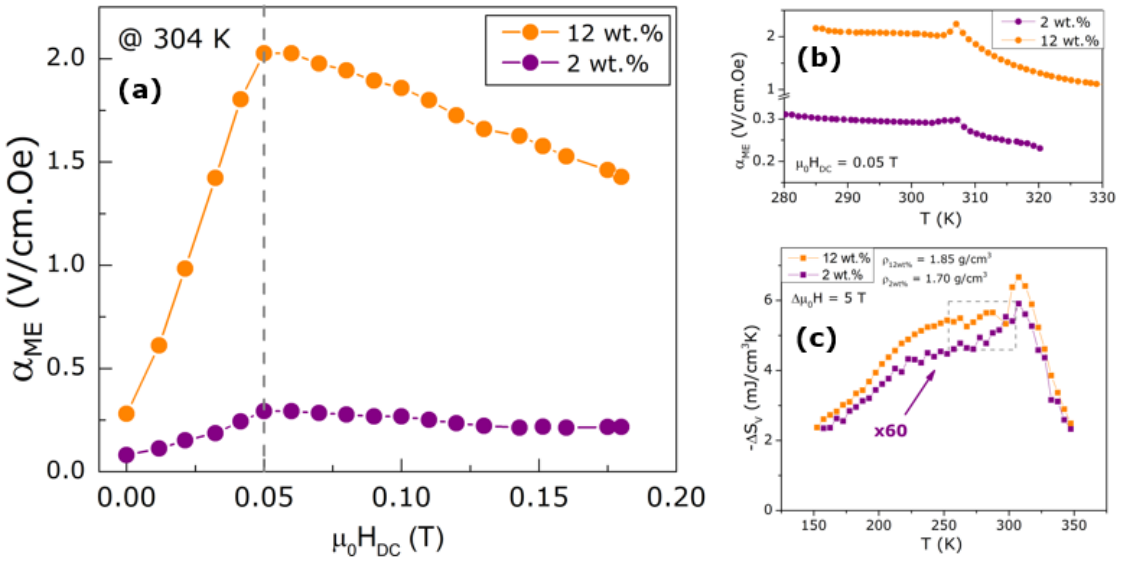

Figure 7.11: **(a)** ME voltage coefficient α_{ME} as a function of DC bias magnetic field obtained at 304 K, corresponding to the maximum observed on the temperature dependence presented above. **(b)** The temperature dependence of ME-coefficient under an applied field of 0.05 T that contributed to the entropy change curves of produced composites in **(c)**

7.5 Multicaloric Effect

As pointed by Vopson, systems presenting two primary ferroic orders simultaneously, the multiferroic materials, are the main candidates to present giant magnetocaloric effects[153]. The search for materials presenting multicaloric effects is a new topic of

research aiming to find the best system to fulfil the imposed requirements for practical applications. Among the conditions, the material must present low heat capacity, large ME-coupling coefficient and low magnetic/electric hysteresis. For the present case, the α_{ME} of 2.2 V/cm.Oe obtained for 12 wt.% composite is large when compared to other 0-3 type composites reported on literature which is affecting the MCE response of the system[229]. In this way, the cross-coupling effect should be taken into account for the isothermal entropy change of the system under the influence of an applied magnetic field. The alignment of magnetic particles along the polymeric matrix will induce an electric polarization (P_{ind}) and, consequently, an internal electrical field (E_{ind}). If we assume a linear ME-effect, the induced field on the material is:

$$dE_{ind} = \frac{\alpha_{ME}}{\epsilon_0 \chi^e} dH \tag{7.2}$$

with ϵ_0 being the vacuum permittivity and χ^e the electrical susceptibility[153]. In this way, the total entropy change of the multicomponent system when a magnetic field is applied derived from the generalized Maxwell relations in Ref. 153 is given as follows:

$$\Delta S_{total} = \int_{\Delta H} \left(\frac{\partial M}{\partial T}\right)_{E_{ind}} dH + \int_{\Delta H} \frac{\alpha_{ME}}{\epsilon_0 \chi^e} \left(\frac{\partial P_{ind}}{\partial T}\right)_H dH. \tag{7.3}$$

The curves presented on Fig.7.8 were indirectly obtained through the temperature derivative term of equation (5); thus, rearranging this relation for the calculated ΔS_W, we have:

$$\Delta S_W = \Delta S_{total} - \int_{\Delta H} \frac{\alpha_{ME}}{\epsilon_0 \chi^e} \left(\frac{\partial P_{ind}}{\partial T}\right)_H dH. \tag{7.4}$$

The derivative term represents the pyroelectric effect that, in the present system, rises from the PVDF electroactive phase relaxation[153,262]. Hence, the polymer ferroelectricity character is contributing negatively to the magnetic entropy change which justifies the deviation from the powder curve observed around 270 K for 12 wt.% composite. In this sense, in order to completely understand the mechanism behind the coupling between magnetic and electric phase orders on the multicomponent system, an evaluation on the induced polarization in the samples should be performed. It would be possible to experimentally access the coupling effect by using the modified setup proposed by Vopson consisting of a thermal bath where electrical and magnetic fields could be applied with an accurate measurement of the sample temperature[187]. Nevertheless, these results reveal that the cross-coupling effects play a role on the MCE behaviour of GSG/PVDF composites which can be used to tune its features for future applications[48,153,239].

7.6 Partial Conclusions

This work presents a thorough investigation on structural, morphological, magnetoelectric and magnetocaloric properties of low amounts of $Gd_5Si_{2.4}Ge_{1.6}$ micropowder immersed into a piezoelectric PVDF semi-crystalline polymer. Through XRD and FTIR analysis, higher weight fraction of magnetic filler have shown to improve crystallization of electroactive phases formation on the polymers. The intermetallic grains act as a centre of nucleation for the more symmetric β- and γ-phases of PVDF due to interface interactions. Although the increase of EA-phases was found to be only 2%, the ME-coefficient suffers a drastic reduction of 85% from 12 wt.% to 2 wt.% composite samples. The field dependency of ME-coupling has shown a thermally mediated effect rising from magnetocaloric and pyroelectricity of the system constituents. From magnetic analysis, the interplay between ferroelectric and ferromagnetic behaviour is translated by the oscillations on the paramagnetic Curie temperatures. However, while the nature of the second order magnetic transition of the powder is not affected by the piezoelectric matrix, the adiabatic entropy change reveals the contribution of PVDF pyroelectricity at the 220-350 K. This temperature range corresponds to the secondary M-phase thermal hysteresis on the micropowder surface, which demonstrates the origin of ME-coupling on the interfacial interactions between PVDF chains and grain boundaries. The results presented here open a pathway for the advancement of novel and multifunctional devices.

Chapter 8

$Gd_5(Si,Ge)_4$ nanoparticles produced by Pulsed Laser Deposition

"The thermodynamic stability of rare earth silicides and germanides is much greater compared with the appropriate compounds of 3d transition metals."

G. M. Lukashenko, *et al.* J. of Alloys and Compounds **179**, 299 (1992).

This chapter will present an alternative approach to produce $Gd_5(Si,Ge)_4$ nanostructures using a more accessible nanosecond Pulsed Laser Deposition (PLD) technique, described in Subsection 4.1.3. The best obtained set of samples with three distinct compositions of this family compounds will be investigated through morphological, crystallographic and magnetic characterization for evaluation on the MCE presented at this reduced scale.

8.1 Introduction

As presented in Chapter 2, the family $R_5(Si,Ge)_4$ has well known properties in the bulk form and few reports dedicated to the study of its properties at micro/nanoscale. There was a first attempt of produce $Gd_5Si_2Ge_2$ thin films by RF magnetron sputtering but the silicon nitride did not prevent the film degradation and the trial was unsuccessful[55]. Recent work at IFIMUP in collaboration with Hadimani *et al.*, successfully obtained a $Gd_5Si_{1.3}Ge_{2.7}$ granular thin film with $\sim$790 nm of thickness using the femtosecond pulsed laser ablation technique[6], but still with low amounts of desired phase and granular surface. The thin film thermal expansion around the magnetic transition tempera-

ture of 12×10^3 ppm is, however, 10 times larger than the observed in $Co_{1-x}Fe_x$ thin films, showing its potential[263]. Regarding the MCE, the nanogranular thin film showed a broader working range temperature and reduction of magnetic hysteresis losses than the compared with the bulk counterpart[6]; however, with lower ΔS_{max} values. For this reason, it is necessary to find a balance between the decrease of ΔS_{max} and the increase of working temperature range, which is broader for second-order transitions, in order to apply it in magnetic refrigeration. For instance, a 22% increase on the effective RCP values is observed for $MnNi_{0.8}Fe_{0.2}$ compound when the bulk is fragmented into grains with 20-40 μm particle size due to the wider working range temperature, in spite of the lower $-\Delta S_{max}$[264]. This reduction on the intensity of MCE response is commonly observed in magnetocaloric materials at reduced micro and nanoscales that can be related with losses on saturation magnetization[134], surface effects[218], change in symmetry[265], anisotropy contributions[266], shift from a FOMT to a SOMT[267] and so on. For instance, 200 nm diameter nanotubes and nanoparticles with 45 nm mean size of valence mixed manganites of $Sm_{0.6}Sr_{0.4}MnO_3$, with the morphology presented in Fig. 8.1(a)-(c), present a distinct MCE behaviour when compared to their bulk counterpart, shown in Fig. 8.1(c)-(d)[44]. The wider entropy change curve for the nanoparticle is a direct consequence of the magnetic transition order change from a first to second one, while the M-shape of $-\Delta S(T)$ for the nanotubes is due to the more pronounced superparamagnetic behaviour since it walls are composed by smaller nanoparticles with 25 nm.

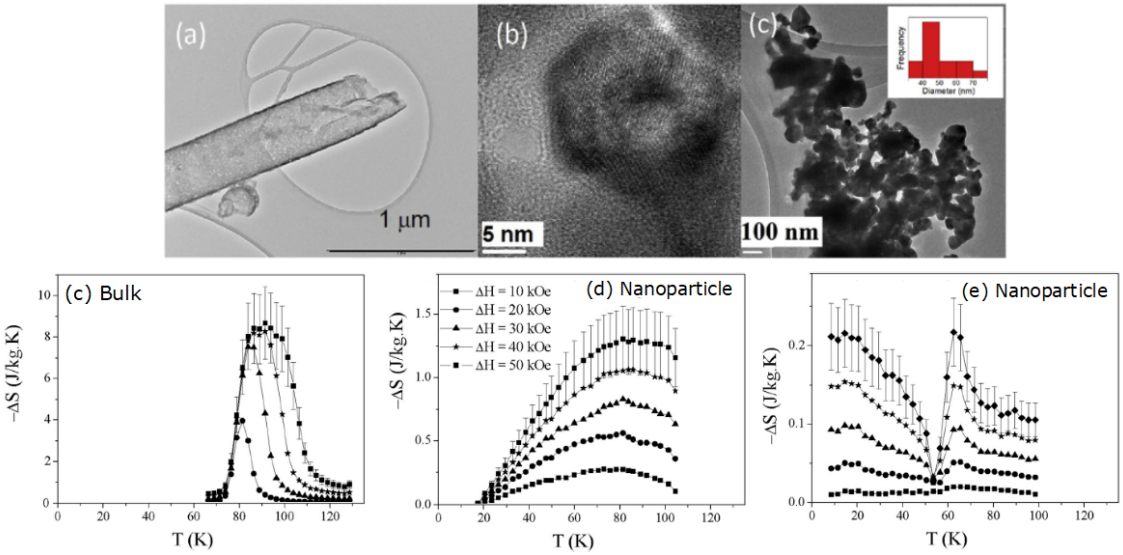

Figure 8.1: TEM images of $Sm_{0.6}Sr_{0.4}MnO_3$ in the form of (a) nanotube, with a high resolution visualization in **(b)** of the particles that constitutes the nanotube walls and **(c)** nanoparticles with 45 nm mean size. The entropy change curves for **(c)** the bulk counterpart, **(d)** nanoparticle and **(e)** nanotube revealing the influence of morphology on the MCE response of FM materials. The images were extracted from Ref. 44.

It is very well known that when the particle size is reduced to micro/nanometric scale, the surface/volume grain ratio is bigger than that observed in the bulk counterpart

and the effect of surface is more evident. In particular, magnetic materials at nanometric scale can display curious and intriguing behaviors, such as spin glass, superparamagnetism, large coercivities, changes in saturation magnetization and in Curie temperature[268–271]. Interestingly, nanostructuring processes can lead to a negative thermal expansion (NTE), like the observed for CuO nanocrystals with 5 nm of average diameter[272]. The large NTE of -1.1$\times 10^{-4}$ K^{-1} (10 times larger than observed for renowned ZrW_2O_8 compound[273]) below $T_N \sim$67 K rises from it strong magneto-lattice coupling that is boosted by the reduction of particle size to the nanometric scale. However, to the date, a complete understand on the mechanism of this effect at low dimensionality was not demonstrated.

Furthermore, a laser with a femtosecond pulse has already been proven as good technique for the production of $Gd_5Si_{1.3}Ge_{2.7}$ granular film with particle size of 80 nm[6]. However, as previously mentioned, it is an expensive and irreproducible method. More recently, Tarasenka *et al.*[56] were able to produce $Gd_5Si_2Ge_2$ NPs using a nanosecond Nd:YAG pulsed laser ablation in liquids. They have sequentially ablated the starting targets in a cell filled with ethanol in a double-pulse configuration corresponding to a wavelength of 1064 nm, obtained nanostructures with particle size ranging from 60-30 nm. Although they were able to perform magnetic measurements, an evaluation on the systems MCE properties was not performed. However, this work demonstrate that ns pulsed laser techniques can also allow the production of $Gd_5(Si,Ge)_4$ material at the nanoscale with good crystalline and magnetic features. In this sense, we have produced $Gd_5(Si_xGe_{1-x})_4$ nanoparticles with x = 0.45, 0.55 and 0.60 via a nanosecond *Pulsed Laser Deposition* in Ar atmosphere to evaluate their morphological, crystallographic, magnetic and magnetocaloric properties.

8.2 Experimental results

8.2.1 Morphological and structural characterization

Similar to the composite samples prepared in Chapters 6 and 7, the bulk targets ought to be first analysed in order to ensure a good quality of their deposition products. In the present work, the $Gd_5(Si_xGe_{1-x})_4$ with x = 0.45, 0.55 and 0.60 compounds were chosen for the nanoparticles production. Although they are compositions with similar Si:Ge ratio, their crystallographic structures are distinct due to a symmetry change that occurs close to the x = 0.5 composition on the phase-diagram. For x = 0.45 target, a Monoclinic (M) $Gd_5Si_2Ge_2$-type structure phase with a distorted angle γ = 93.13^o was obtained, thus, being the sample with lower symmetry. On the other hand, x = 0.60 compounds crystallizes in an Orthorhombic-I [O(I)] Gd_5Si_4-type structure; while x = 0.55 will present a mixture of both M and O(I) phase. These results are in good agreement with Ref. 217 and the obtained parameters after *Rietveld* refinement with the *Fullprof software* are presented in the Appendix C. The aforementioned gain in

structural symmetry is also reflected on the reduction of distorted γ angle from 93.13^o for x = 0.45 to 92.96^o for x = 0.55 bulk sample. An evolution of this change in structure can be seen in Fig. 8.2 from the disappearance of some planes associated to the M phase, like (-132) plane, and the enhancement of diffracted peaks for higher 2θ angles at the x = 0.60 pattern[217]. Furthermore, since Si covalent radius is smaller than Ge one and there is a change from a $P112_1/a$ to a Pnma space group, there is a decrease on the unit cell volume from 874.9 Å^3 to 864.1 Å^3 for x = 0.45 and 0.60, respectively. This reduction lead to the shift of some peaks towards higher angles. Among them, the most notable are (042) and (301) planes that correspond to the a- and $b-$axis, respectively - highlighted in Fig. 8.2. These evidence are supported by *Rietveld* refinements and the suitable parameters are summarizes on Table C.1 on the Appendix C, in agreement with the literature[105,217]. These observations will be important for further analysis of the produced NPs.

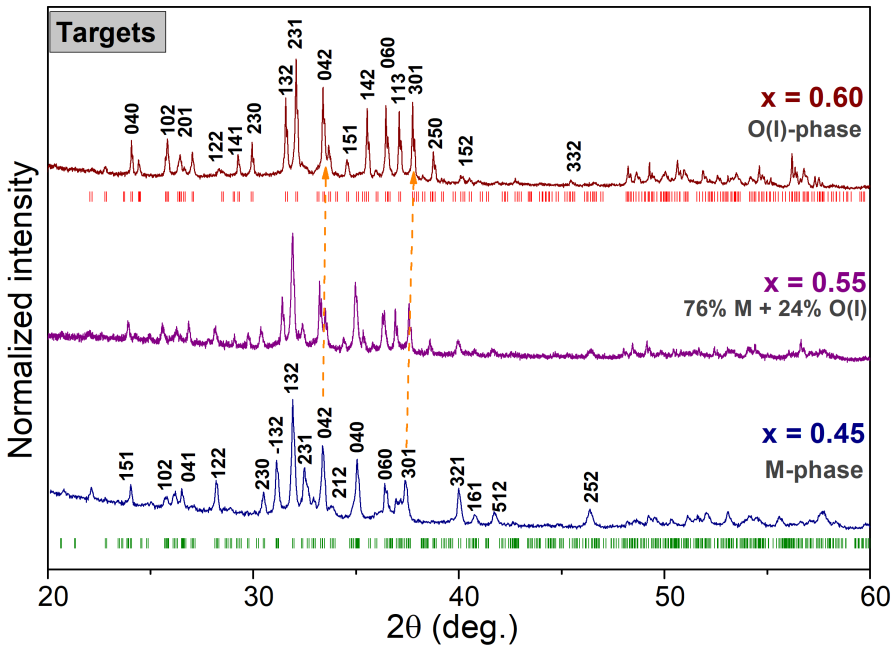

Figure 8.2: XRD patterns for the bulk targets of $Gd_5(Si_xGe_{1-x})_4$ with: x = 0.45, that crystallizes in a monoclinic ($P112_1/a$ space group) phase; x = 0.55, with a mixture of M and orthorhombic-I ($Pnma$ space group); and, for x = 0.60 in an O(I) structure. The Bragg positions and respective Miller indices for some peaks are indicated for the end compositions target samples, obtained through *Rietveld* refinements.

Subsequently to the bulk structural characterization, the targets were ablated using Argon gas flux in a way that the chamber was kept at a constant pressure of 1 Torr, following the procedure given in Chapter 4[219,274]. For evaluation on the morphological features of produced NPs, the samples were collected using Carbon grade substrate to perform measurements using HR-TEM, presented in Fig. 8.3(a)-(c). The morphology of the three compositions deposition products present a semi-spherical configuration with a low level of agglomeration with structures at the nanometric scale. For x = 0.45 and 0.55, the particle size distribution is narrow when compared with

previous reports on $Gd_5(Si,Ge)_4$ produced NPs through ablation[6,56]. This might be related to the chosen inert gas since the successfully reported nanostructures in this family were previously produced only under vacuum and water. Several experimental parameters can affect the growth formation of nanostructures besides the chamber atmosphere, such as: pulse duration and energy, distance between substrate and targets, etc[274]. To completely understand the mechanism behind $Gd_5(Si,Ge)_4$ NPs formation using nanosecond PLD, a systematic study should be performed by changing the deposition parameters to evaluate the distinction between produced structures[219]. Moreover, the x = 0.60 sample image - shown in Fig. 8.3(c) - reveal an absence of statistic and a broad log-normal distribution where the particle size are higher than 100 nm, forming the so-called droplets. The amplification in Fig. 8.3(f) (and the FFT on the) indicates that these products present a crystallographic ordering. For this reason, we will assume that 15 min of deposition was not enough for the collection of substantial NPs, depleting this initial evaluation and further results will help to confirm the features of this particular composition.

Furthermore, for x = 0.45 the average particle size is $\sim$27$\pm$0.9 nm, as obtained through a log-normal fitting shown at the of Fig. 8.3(a)[219]. Similarly, x = 0.55 sample, present a mean size of $\sim$26$\pm$0.9 nm. This slight reduction can be related to the reduced unit cell volume for this stoichiometry in comparison with x = 0.45 one. The confirmation on the crystallographic features of the NPs were initially obtained through Selected Area Diffraction (SAED) analysis, shown on the of Fig. 8.3(a) and (b) for x = 0.45 and 0.55 NPs, respectively. The obtained ring pattern corresponds to a polycrystalline nanoscructure, similar to previous results obtained for Gd-Si-Ge NPs produced using laser assisted technique on water[56]. Through a comparison between the peaks on the resulted profile using a standard image analysis software and the XRD targets pattern, all the produced NPs present an O(I) structure. The associated planes are shown in Fig. 8.3(a) and (b) and correspond to the peaks marked with (*) at the patterns in Fig. 8.2. Among all the adopted crystal structures of $Gd_5(Si,Ge)_4$ family compounds, the O(I) is the more stable and symmetric one[105,106,217]. Therefore, due to an intrinsic pressure on the particle surface, the atom ensembles will tend to be arranged in the lower energy state[34]. Besides, an amplification at one NP, see the of Fig. 8.3(a), reveals the crystallographic features on the produced NPs with a clear observation of the interplanar spacing (d_{hkl})[219]. By measuring the d_{hkl} distances at the NPs amplifications and comparing with the XRD bulk pattern of the O(I) structure, the following values are obtained: d_{hkl} = 2.78 Å for x = 0.45 NPs which corresponds to the (051) plane; d_{hkl} = 2.77 Å for x = 0.55 which also coincides with the (051) O(I)-structure plane; and x = 0.60, d_{hkl} = 2.68 Å related to the (042) diffracted plane. The observed direction for all compositions are parallel to the a-axis which might indicate the NPs have similar formation mechanisms[274]. Once the SAED image was not possible to acquire for x = 0.60 sample due to the low statistic of specimen, a fast Fourier transform (FFT) pattern is shown on the inset of Fig. 8.3(c). These observations reveal that the PLD technique

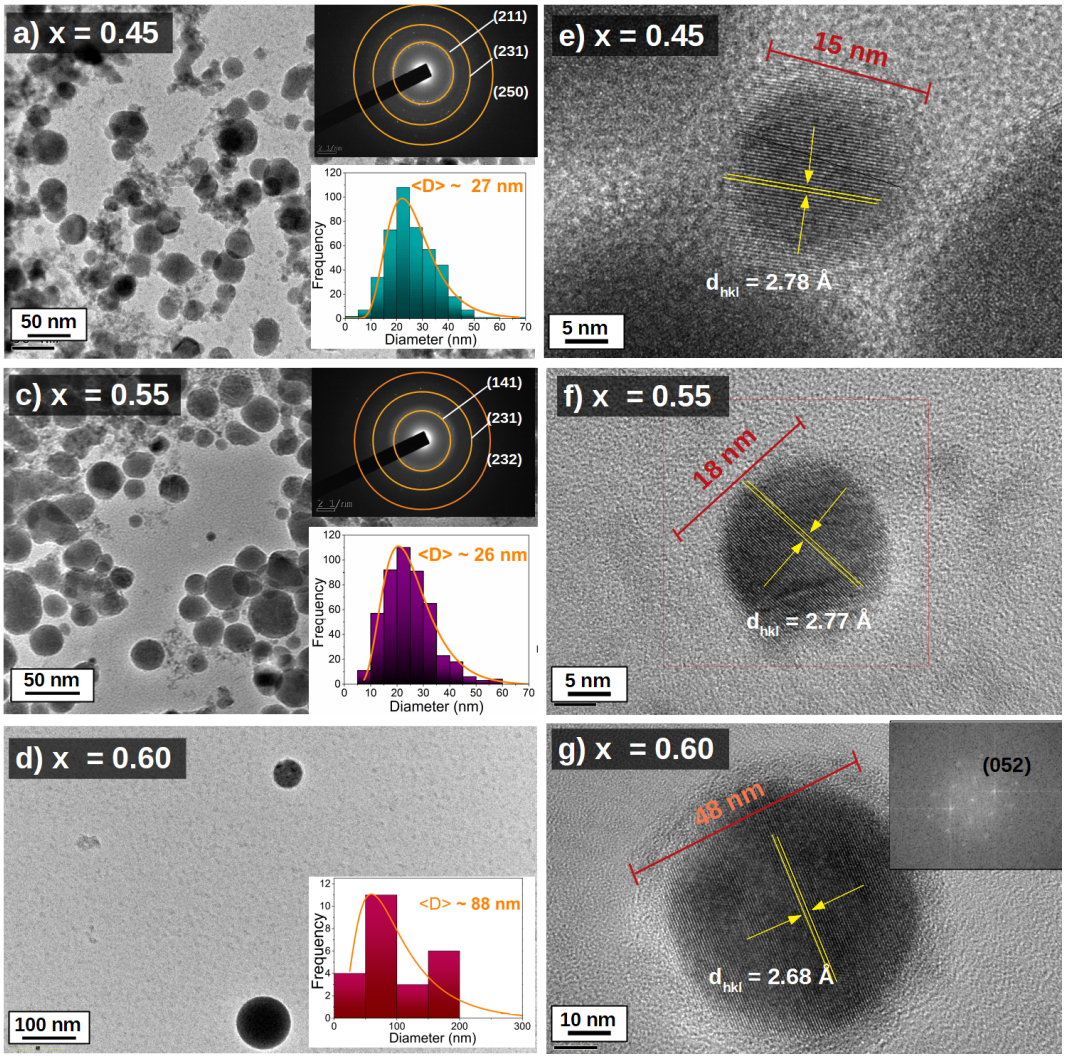

Figure 8.3: HR-TEM images for the $Gd_5(Si_xGe_{1-x})_4$ collected nanoparticles with **(a)** x = 0.45, **(b)** 0.55 and **(b)** 0.60 with their respective SAED (when possible) and log-normal particle size distribution on the . It is possible to observe the interplanar distances in a high magnification on the amplification presented on the right side - from (d) to (f) - of each micrograph. In particular, since x = 0.60 composition have presented lower amount of products, *fast Fourier transform* (FFT) are presented on the to confirm the crystalline nature.

allows the growth of $Gd_5(Si_xGe_{1-x})_4$ NPs in a narrow range of Si:Ge ratio with good crystallographic and morphological features.

8.2.2 Synchrotron measurements

Given this initial characterization, we were able to attain Synchrotron XRD measurements at ESRF on the ID-31 beamline for x = 0.45 sample, with the setup presented on Subsectio n4.2.3. This stoichiometry was chosen for the reason that, due to the higher amount of Ge on x = 0.45 sample, there is more possibility on the observation of a structural transition and/or NTE. A comparison between bulk and NP pattern of x = 0.45 composition is shown in Fig. 8.4 which reveals a few differences on it peaks profile.

An important point to stress is that the measurements were performed with the powder inserted on a Kapton tape that is amorphous and contributed for a large background on the resulted pattern. This lead to a reduction in the peak intensities for intermediate and higher d spacing values (or low Q) , where the Kapton signal was found to be higher. For the analysis, a removal of the Kapton signal lead to an increase on the noise and, consequently, deprecating *LeBail* calculations quality. This is because the main peaks of O(I) structure (Gd_5Si_4-type structure) relies on the 2.4-3.1 Å d-range. For this reason, the calculations were performed using the raw data at room temperature, presented in Appendix C, where we obtained the following lattice parameters: a = 7.596 Å, b = 14.58 Å, c = 7.907 Å. For the bulk targets, as mentioned above, it was identified that x = 0.45 target crystallizes in a monoclinic ($Gd_5Si_2Ge_2$-type structure) with a = 7.594 Å, b = 14.82 Å, c = 7.788 Å and distorted angle γ = 93.13^o.

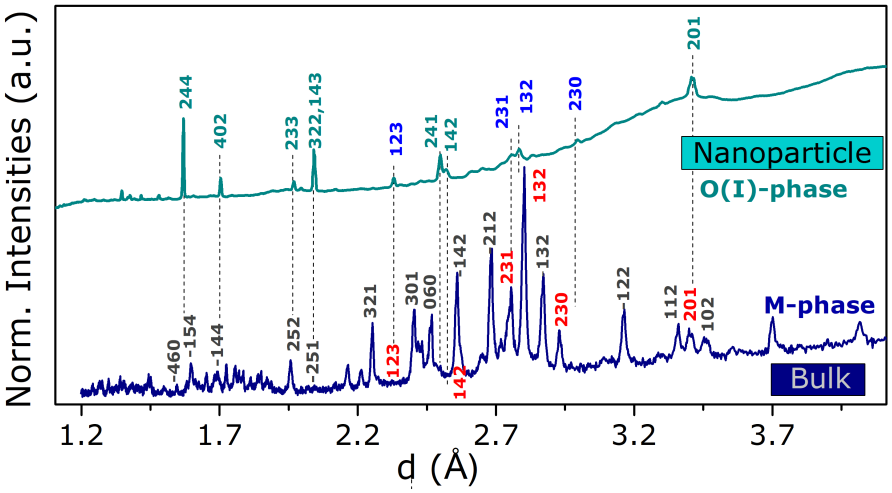

Figure 8.4: XRD patterns as a d-spacing function for x = 0.45 composition obtained at room temperature through standard diffractometer for the bulk and by synchrotron radiation for the nanoparticle sample. The planes highlighted with (*) correspond to the planes observed through SAED images presented above.

Most notably, the relative reduction of the lattice parameter b from bulk to nanoparticle is $\Delta b/b\sim$ 1.64%. It should be mentioned that the constituents pseudo-blocks of $Gd_5(Si,Ge)_4$ crystallographic structures are connected by the Si-Ge dimers along the b-axis. Thus, for the x = 0.45 NPs, an enhancement on the exchange interactions of the atoms for structures below 30 nm is expected as will be exposed on the magnetic results[106]. This lattice parameter variation consequently led to a $\Delta V/V\sim$1.21% that is smaller than the $\sim$1.81% observed for x = 0.325 granular thin film[6]. The authors have attributed this effect to an intrinsic pressure rising from the nanostructures surface. Indeed $Gd_5(Si_xGe_{1-x})_4$ compounds with higher Si content present a lower unit cell volume where, for the conformation on a nanoparticle, it will present less variation. In another words, by considering the pressure effects, the compressibility κ reduces as x increases[32,115,117]. If we consider the compressibility of 1.82 Mbar^{-1} for x = 0.45 bulk compound from Ref. 115, the corresponding hydrostatic pressure for the observed volume reduction on the nanoparticles should be around 6 kbar. These results are in good

agreement with the findings obtained by Hadimani and co-authors for x = 0.325 composition with particle size around 80 nm[6,34]. To the date, this change in symmetry at room temperature for nanostructures of this family compounds was not reported[6,33,34,54–56]. This behaviour has great impact on the magnetic behaviour of these materials, as will be presented below. For this reason, the magnetic results will be used to confirm the exposed findings.

In addition, diffraction patterns were acquired by decreasing and increasing temperature in the 20-320 K range with an exposure time of 10 s. In order to avoid non-equilibrium conditions, a temperature sweeping rate of $\sim$ 2 K/min and the data integration were performed using the software from ESRF facility. For the analysis, the patterns with better quality were selected and normalized using the *Powder 3D software* by excluding the low Q regions to avoid contributions from the Kapton tape used for the measurements. A colour mapping on the resulted patterns obtained by increasing temperature - where the setup control was better - within the 100-320 K temperature range is presented in Fig. 8.5(a). From this image, it is possible to notice two distinct regions with significant change on the peaks positions: **Region I** with a discontinuity between 210 K and 240 K and **Region II** where, above 120 K, there is the increase of some diffracted planes. The lower temperature change can be related with the small lump observe on the magnetization measurements suggesting a SPM ordering below 100 nm. As for the Region II, the shift indicates that the structural transformation from an M to an O(I) phase can occur when the particle size is reduced to 27 nm.

The reduction in the peak intensities when compared to the bulk patterns is due to the large contribution on the background from the sample holder. By removing the Kapton contribution, it was possible to perform initial *LeBail* calculations using *Fullprof software* to have an overview on the unit cell volume change-over temperature. Around the magnetic transition temperature, as shown in Fig. 8.5(b), as the temperature increases, the peak position shifts towards higher angles indicating an increase in the unit cell volume. At this region, the calculations were performed considering only the presence of an O(I) structure and the results are given in Fig. 8.5(c). The unit cell volume follows the expected behaviour from 210 K to 270 K, where it enlarges due to thermal variation. Above 270 K, however, there is an anomaly and the volume is reduced until reaching T_C of 290 K with a variation of 34.8 ppm/K. As for the patterns obtained at 230-270 K, the volume change corresponds to 352 ppm/K by considering only an O(I) structure. This result is still incomplete, it should be taken into account the presence of M-phases below 270 K; however, a good quality of refinement was not achieved yet and this is currently a work in progress. In order to confirm these evidence, *Rietveld* calculations ought to be performed - which is a work in progress.

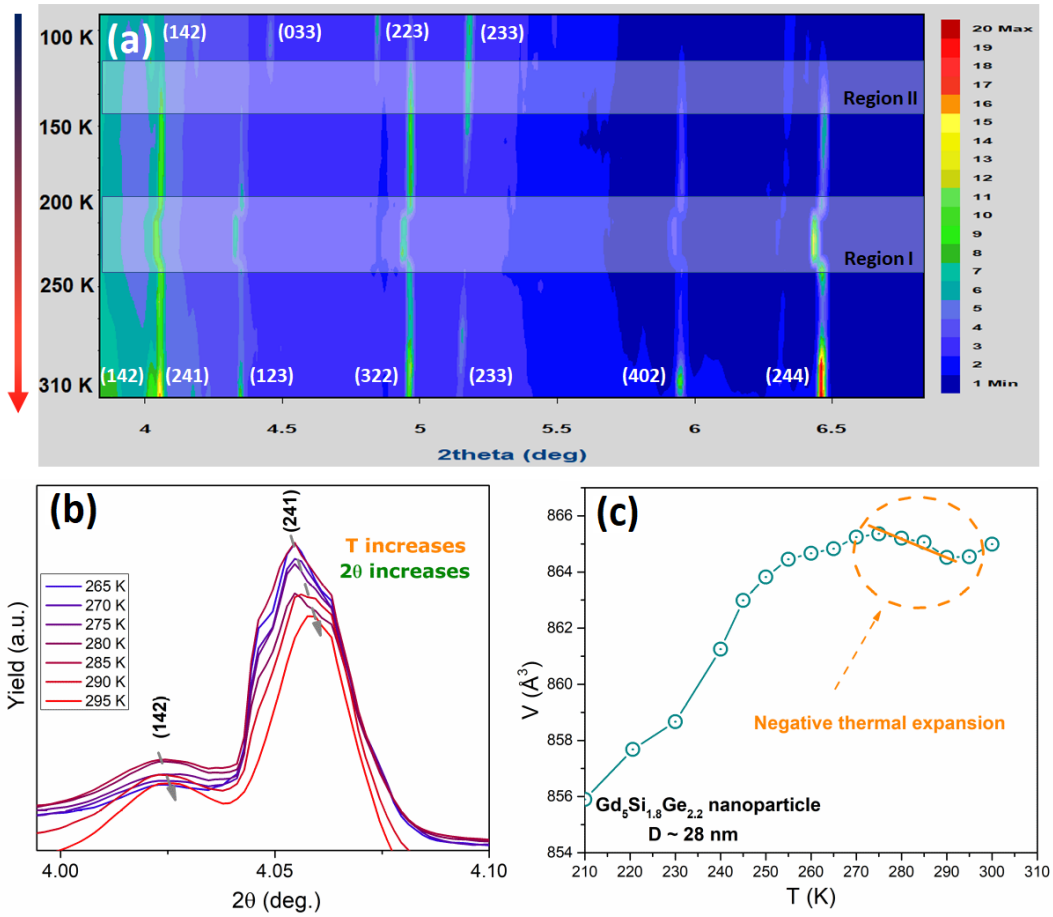

Figure 8.5: **(a)** Countorplot of Synchrothron XRD patterns in the 310-100 K temperature range obtained for $Gd_5Si_{1.8}Ge_{2.2}$ nanoparticles produced by ns PLD, two possible transitions are observed and highlighted as **region I**, with a discontinuity, and **region II** that can correspond to a structural change. **(b)** The patterns in the 265-295 K temperature range and **(c)** initial *LeBail* calculation results indicate a negative thermal expansion.

8.2.3 Magnetic and Magnetocaloric Properties

Following the same protocol as crystallographic characterization, the bulk target magnetic results will be first analysed since they will be important to understand the behaviour of $Gd_5(Si,Ge)_4$ nanostructures. The temperature dependence of magnetization under 1000 Oe of applied magnetic field for all samples are depicted in Fig. 8.6(a). For the NPs, in particular, the displayed measurements were carried out by increasing the temperature from 5 K to 350 K using a zero field cooling protocol. From the of Fig. 8.6(a), it is shown that x = 0.45 target present a thermal hysteresis between 150-250 K that is due to a FOMT wherein the sample shows a [O(I),FM]→[M,PM] magnetostructural transition[30]. In addition, there is a small lump around 290 K that corresponds to the SOMT of the O(I)-phase[106]. As for the x = 0.45 NP, a single FM → PM transition is observed at 290 K, which confirms that indeed the system crystallizes in a O(I) structure, corroborating with XRD and TEM analyses. For x = 0.55 target composition, however, two associated ordering temperatures are observed: 1) around 245 K from the

M-phase and 2) around 300 K that correspond to O(I)-phase, as can be seen on the inset of Fig. 8.6(a), respectively. While the produced NPs of this composition present a single T_C at 300 K, which corroborates with the structural analysis where the identified crystal structure is also O(I). A small lump around 70 K for ZFC curve of x = 0.60 NPs can be due to a low temperature spin reorientation of Gd[275], as observed by Hadimani *et al.* on the $Gd_5Si_{1.3}Ge_{2.7}$ nanoparticles produced by femtosecond laser ablation[6], and will affect the magnetization of the sample. As for x = 0.60, the O(I) structure is preserved when the particle size is reduced to diameters of 88 nm and, for that reason, the T_C remains at 310 K. This particular observation follows the understanding of the studies since on ball-milled Gd_5Si_4-type structures with this range of diameter does not present a critical change on it magnetic behaviour[135]. Nevertheless, the low temperature transition (below 10 K) can indicate that the system presents a SPM behaviour; however, for the present work, it was not possible to measure the magnetization below 5 K.

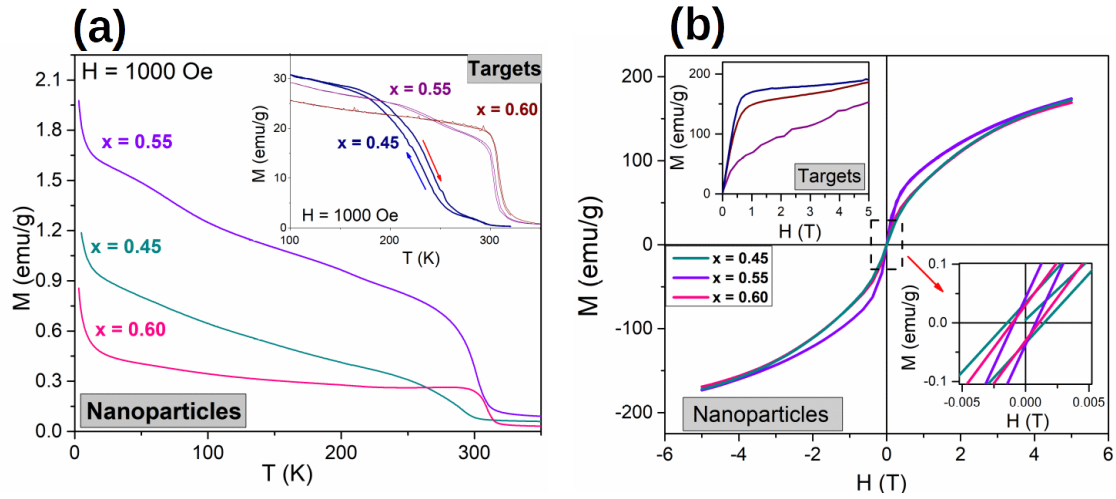

Figure 8.6: **(a)** Temperature dependence on the magnetization curves obtained under an applied magnetic field of 1000 Oe for x = 0.45, 0.55 and 0.60 compositions as NPs and as targets on the . **(b)** Hysteresis curves obtained at 5 K for NPs and targets (left) where, besides the reduction on μ_{sat}, there is a change on the curve profile that can indicate a SPM behaviour.

Fig. 8.6(b) shows the hysteresis curves measured at 5 K where is possible to observe that for all samples, the saturation is not reached with the applied magnetic field of 5 T. This can be related to the presence of amorphous phases on the sample that will have a PM contribution on the system magnetization[139]. For this reason, the μ_{sat} were obtained through the linear fitting on the M-1/H curves[143], and their values are summarized in Table 8.1. The reduction in μ_{sat} from the macro to nanoscale can be a result of intra and interparticle interactions, anisotropy and surface effects[17,35]. As a matter of fact, the increase on system anisotropy can be seen from the amplification around zero applied field, shown on the right side of Fig. 8.6(b), with the presence of coercive field and reminiscence magnetization[134]. Besides that, the drastic change on the hysteresis curve profiles in Fig. 8.6(b) reveal the possible SPM behaviour of all

produced NPs[184]. In order to confirm these findings, magnetization curves below 5 K or AC susceptibility measurements should be performed[184]. For this reason, we will assume that the system is FM on the temperature of interest for further investigations on the MCE properties.

As mentioned previously, the change on magnetic transition order is often observed for ferromagnetic materials when is reduced to the nanometric scale[6,17,35]. A broadening on the magnetic transition for the nanostructure is commonly observed for ferromagnetic materials at the nanometric scale generated rising from surface anisotropy increase and particle size distribution[44,276,277]. This occurs because there is a grain size distribution for the produced particles, the FM-PM transition temperature will also be a distribution if we consider that the easy magnetization for this materials will depend on the shape and size, i.e., anisotropy[274]. In order to confirm this effect, isotherm magnetization measurements were carried out by increasing and decreasing the applied magnetic field up to 50 kOe for the bulk targets, shown in Fig. 8.7(a)-(c), and for the nanoparticles, in Fig. 8.7(d)-(f). The data were obtained for temperatures above 200 K since the interest for practical applications of the MCE relies mostly around room temperature. In particular, x = 0.45 target presents magnetic irreversibility for the curves around T_C, namely from 230 K to 260 K, that is a signature of a FOMT[121,143,217]. When particle size is reduced to $\sim$27 nm, this metamagnetic transition is vanished, indicating a change to a SOMT. A similar behaviour is observed for the x = 0.55 and 0.60 compositions with the irreversibility disappearance is followed by a reduction on the magnetization values. These observations are confirmed through the Arrott plot (AP) curves, shown in Fig. 8.7(g)-(i), revealing a positive slope for the nanostructures, in agreement with the Banerjee's criteria[143]. The B parameter values obtained from the fit at T_C using the Landau expansion (see Subsection 3.1.2) obtained for all samples are summarized on Table 8.1. This change in the magnetic transition order is often observed on nanostructured systems, due to an increase on the system anisotropy derived from the larger contributions of the surface[134,274]. Consequently, the effect of the SOMT will affect the magnetocaloric effect (MCE) for the nanostructures.

The magnetic entropy change estimation can be conveniently performed using the discrete integrated Maxwell relation: $\Delta S = \sum_i \delta M_i/\delta T_i \times \delta H$[44,143] with the results from Fig. 8.7. The curves calculated for all samples, target and nanostructures, are shown in Fig. 8.8. In particular, for the x = 0.45 target with a FOMT, Δ_S can be obtained using the Maxwell relation because the applied magnetic field of 5 T is strong enough to complete the transition[121,150]. However, the temperature rate of 10 K/min and the presence of eutectic 5:3 phases, there is a considerable reduction from the reported $-\Delta S_{max}$ from $\sim$20.3 J/kg.K to 8.15 J/kg.K[121]. Furthermore, for x = 0.55 and 0.60 bulk targets, due to the higher T_C, there is a reduction on the maximum entropy change and, consequently, on the RCP values [shown in Fig. 8.8(b)], in agreement with previous reports[278]. The nanostructures follow the same compositional trend to the ΔS_{max} values with a larger working range temperature. In Fig. 8.8(c), the tempera-

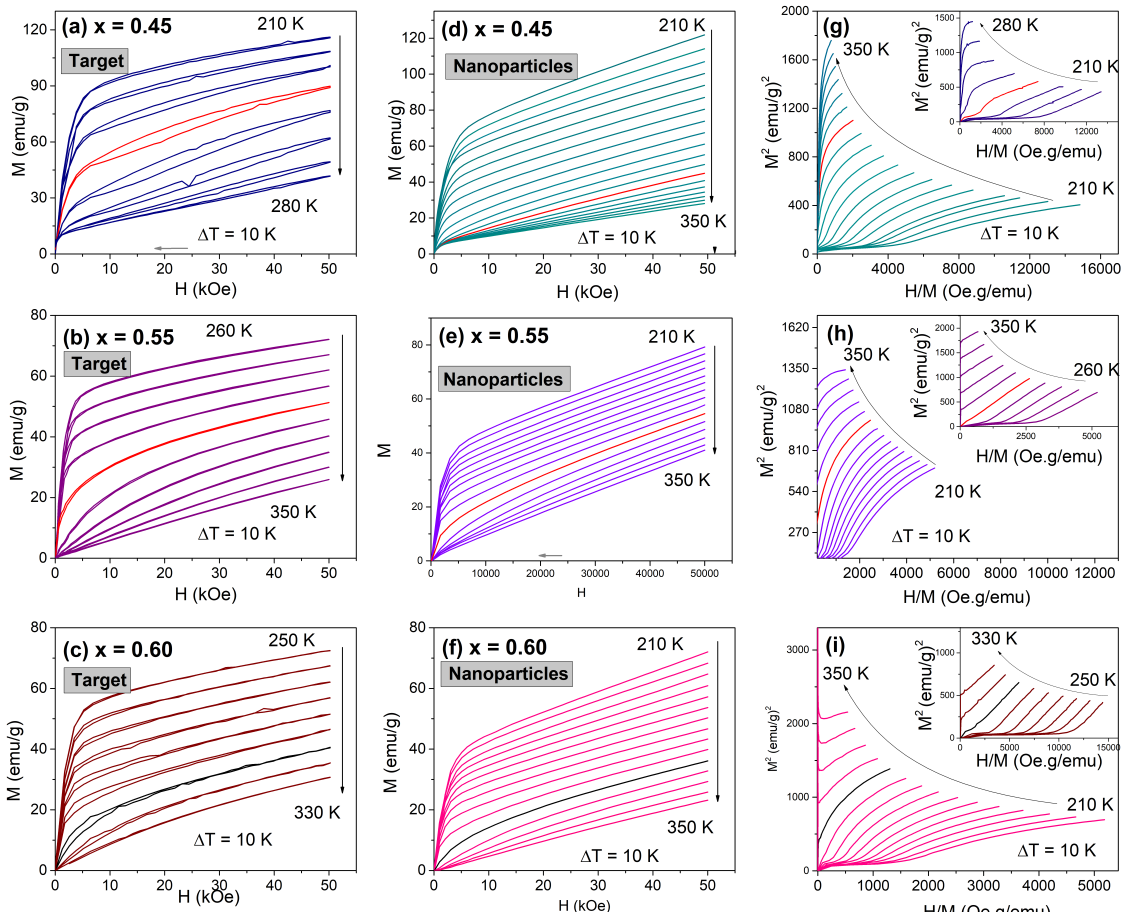

Figure 8.7: Isotherm magnetization curves for the targets and nanoparticles of $Gd_5(Si_xGe_{1-x})_4$ with the labelled compositions. A loss on the saturation magnetization and absence of hysteresis for the nanostructured samples is clearly observed and will affect their magnetocaloric properties.

ture at FWHM just doubles from targets to the produced NPs. Such behavior is also a consequence on the increase of disorder from the reduction of particle size[6,17,134]. In particular, for x = 0.45 composition, the RCP of 289 J/kg is larger than the value obtained by Hadimani *et al.* for the FOMT granular thin film of $Gd_5Si_{1.3}Ge_{2.7}$ obtained by femtosecond PLD[6,17]. Although a bigger average particle size of ∼80 nm was obtained for the thin film, this observation can be related with the absence of hysteresis losses on the nanoparticles produced by ns PLD. Notwithstanding, the relative reduction on the MCE response from the bulk to the nanostructure in the present work averaging 30% is comparable with the 32% observed for $Gd_5Si_{1.3}Ge_{2.7}$ thin film when compared with the system at the macroscale[6]. This indicates that, although the samples were prepared in different conditions, the properties of $Gd_5(Si,Ge)_4$ family compounds at the nanoscale can be somehow related. However, the same compositions should be prepared by ns PLD to finally conclude that. Nevertheless, in order to completely evaluate the MCE on the produced samples, M(T,H) map curves should be carried out at the full range of temperatures; however, for the present work, such procedure could not be performed. Additionally, the M(H) curves at lower temperatures could be used to identify if

Table 8.1: Important magnetic and magnetocaloric features of $Gd_5(Si_xGe_{1-x})_4$ bulk and NPs: Curie temperature (T_C), saturation magnetization (μ_{sat}) obtained at 5 K, the B coefficient from Landau expansion and the maximum entropy change ($-\Delta S_{max}$) for an applied magnetic field of 5 T.

x	Type	T_C (K)	μ_{sat} μ_B/FU	B_{Landau} $(Oe.FU^3/\mu_B^3)$	$-\Delta S_{max}$ (J/kg.K)	RCP (J/kg)	δT_{FWHM} (K)
0.45	Target	240	7.93	-97.0	8.15	363	50.7
	NP	290	7.89	4.16	2.66	289	106
0.55	Target	300	7.89	65.8	6.53	344	49.3
	NP	300	7.84	1.48	1.68	198	118
0.60	Target	310	7.90	67.4	5.87	289	52.6
	NP	310	7.64	4.16	1.95	160	121

the NPs present SPM behaviour as indicates the hysteresis curves at 5 K presented in Fig. 8.6(b).

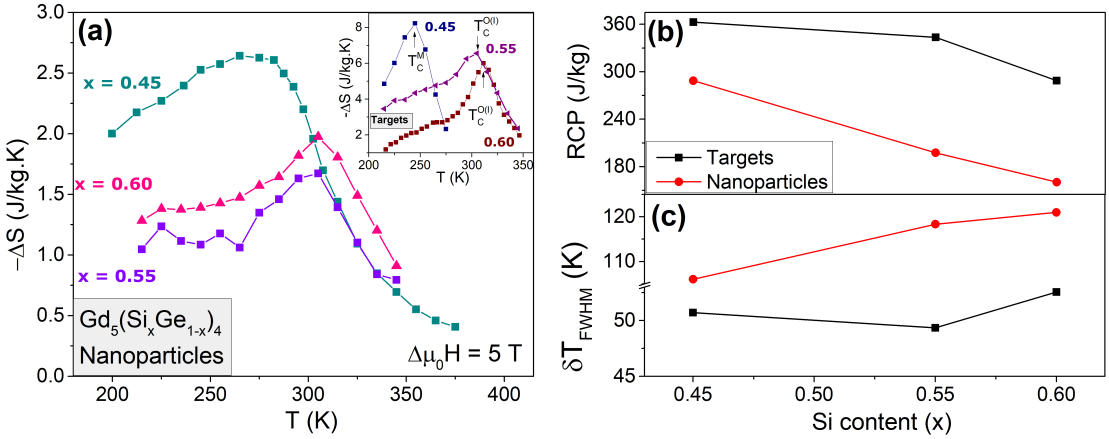

Figure 8.8: **(a)** Magnetic entropy as a function of temperature obtained for $Gd_5(Si,Ge)_4$ nanoparticles and bulks (). From these curves, the RCP and δT_{FWHM} values were calculated and the results are presented in *(b)* and **(c)**, respectively.

8.3 Partial Conclusions

From the results presented on this Chapter, we can conclude that ns PLD using Ar atmosphere is a good approach to obtain $Gd_5(Si_xGe_{1-x})_4$ nanostructures for 0.45<x<0.60 with fine crystallographic and magnetic features. For x = 0.45, the particle size reduction has two related consequences in particular: *(i)* the change in crystallization from a M to an O(I) structure and *(ii)* a second order magnetic transition. This could be a result from surface intrinsic pressure due to the reduction of particle size. As for the close compositions x = 0.55 and 0.60, the morphological and magnetic results point to a structural stabilization in an O(I)-structure. The same crystal structures for these NPs, indicates a similar formation mechanism at this narrow Si:Ge ratio for this family compounds by using ns pulsed ablation in Argon. For all compositions, there is a reduction

on the magnetocaloric response with the gain on the working range temperature. Initial analysis on the results obtained through Synchrotron measurements revealed a NTE around the magnetic transition temperature that could be related with intrinsic pressure originating at the x = 0.45 surface. It is worth to point out that the previous care on the quality of the targets combined with the meticulous gas control inside the chamber during deposition are the reason for such quality on the samples.

Chapter 9

Conclusions & Future Perspectives

A summary of the main conclusions and accomplishments on the thorough study of $Gd_5(Si,Ge)_4$ systems on different scales performed in this work, will be given in this final Chapter. The results and analyses presented along this PhD thesis have answered the remarks exposed in the introduction Chapter bringing into light new questions to explore in the future, which will also be presented below.

9.1 Main Conclusions

The results and analyses presented in this work have demonstrated manifold methods for the production of $Gd_5(Si,Ge)_4$ materials in different scales: from the macro to the nanometric one. Namely, three different experimental processes were followed: bulk alloys, fragmentation to the microscale with implementation into polymeric matrices and nanostructuring using pulsed laser deposition. Structural and magnetic characterization of these systems have answered the questions presented in the Introduction, bringing new perspectives to the development of future work in these family compounds. In short, each modification in the $Gd_5(Si,Ge)_4$ compounds have shown that pressure induced effects is the main responsible mechanism for the observed changes in structural, magnetic and magnetocaloric behaviour.

The first modification was performed by substituting Gd by non-magnetic La atoms in the $Gd_5Si_{1.8}Ge_{2.2}$ bulk sample. It was found that the atoms rearrangement in the unit cell, as the La content increases, led to a change in the symmetry from monoclinic to tetragonal for $Gd_{5-x}La_xSi_{1.8}Ge_{2.2}$ family when $x \geq 2$. This led to an increase in the unit cell volume values which reduced the internal pressure in the structure and, consequently, a reduction on the Curie temperature with $\partial T_C/\partial x \sim -48K/$La and a shift on the magnetic transition order from a first to a second one, as represented in Fig.9.1.

For the implementation into polymeric matrices, the $Gd_5Si_{2.4}Ge_{1.6}$ (GSG) grains were reduced to the microscale through sieving to promote a better dispersion along the composite volume during the synthesis via solvent casting technique. A structural

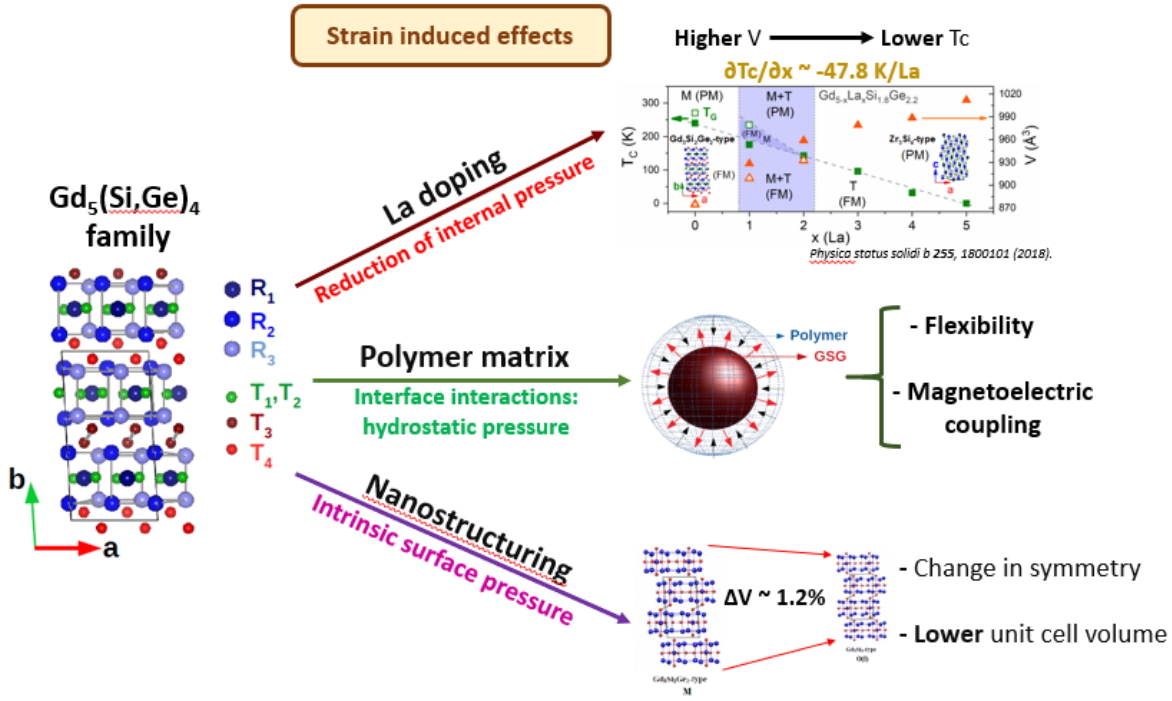

Figure 9.1: Summary on the different systems analysed in this work where the pressure induced effects is the main responsible for the distinct behaviour observed on the $Gd_5(Si,Ge)_4$ systems.

and magnetic characterization in the powder showed that the surface effects became more evident which led to the detection of larger amounts of secondary M-phase as the particle size reduces from 42 μm to 3.4 μm. The introduction of GSG into poly(methyl methacrylate) (PMMA) give rise to surface interactions between particle and polymer wall, revealing that the thermoplastic works as a pressure cell. Magnetic results showed a reduction in the magnetocaloric contribution from the deformed M-phase and the entropy change values correspond mainly to the main orthorhombic structure. Such behaviour is a consequence of the difference between PMMA and GSG thermal expansion that introduces pressure to the M-phase present on the magnetic filler surface[117]. When this powder is introduced into a piezoelectric poly(vinylidene fluorine) (PVDF) matrix, there is an enhancement on the formation and stabilization of electroactive phases of the polymer without further treatments on the composite after solvent casting. For these systems, besides the hydrostatic pressure, there is an improvement on the magnetoelectric coupling driven by the M-phase magnetostriction that is larger for the composite with higher GSG content. Regarding the magnetocaloric evaluation, the pyroelectric character of PVDF should be take into account due to it thermal variation contribution. From these studies, it is possible to conclude that the reinforcement of magnetocaloric materials using polymers can be used to induce multicaloric effects - namely barocaloric, with PMMA blending, and electrocaloric, with the PVDF blended system.

Nanostructuring through ns pulsed ablation has revealed to be a good technique

to obtain structures with good crystalline and magnetic properties. Synchrotron analysis indicates a NTE around the magnetic transition temperature that is a consequence of intrinsic surface pressure on the GSG nanoparticles, as depicted on the scheme of Fig.9.1. Furthermore, a comparison between the structural changes on the produced $Gd_5(Si,Ge)_4$ nanostructures reported on literature and in this PhD thesis revealed a direct relation between it relative unit cell reduction $\Delta V/V$ and the composition isothermal compressibility (κ). As shown in Fig. 9.2, for x = 0 stoichiometry, there is a larger variation of $\sim$2.5% that can be related to it bigger κ values. When the Si content is increased, the relative reduction is decreased as well it compressibility values. However, to complete understand this relation, further investigations are required and is an ongoing work.

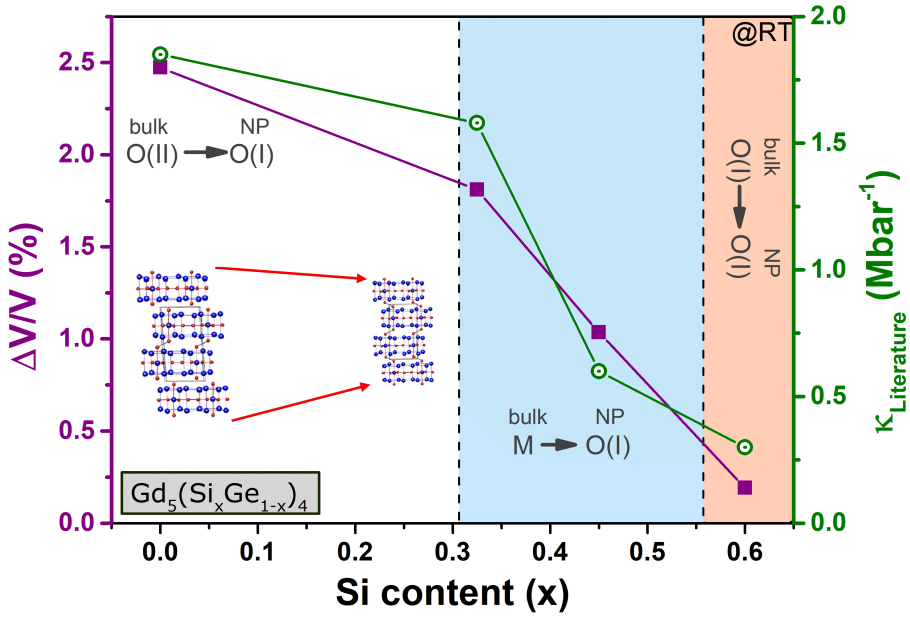

Figure 9.2: Relative unit cell volume ($\Delta V/V$) for $Gd_5(Si_xGe_{1-x})_4$ nanostructures and the compressibility values (κ) as a function of Si content (x). The x = 0 system is a result from a work in progress by our group, x = 0.325 values was obtained from Ref. 6 while x = 0.45 and 0.60 compositions $\Delta V/V$ samples are presented in Chapter 8. As for the κ values, it was obtained from References 6,116,117.

9.2 Future perspectives

This work has presented several approaches aiming to understand the complex behaviour of $Gd_5(Si,Ge)_4$ family compounds through doping and particle size reduction to micro and nanometric scales. The most important findings - summarized previously - can be used to understand and improve the quality of the produced samples, which can then be used for novel technological applications. Some of the future perspectives will be given in the following topics:

- From the reports on the literature, the FOMT can be enhanced on the Ge-rich

compositions for low doping levels, i.e., $0.1 \leq x < 1$ [42,47]. On this matter, we can mention $Tb_5(Si,Ge)_4$ where the structural transition temperature is enhanced from 20 to 25 J/kg.K for La doping of 20%. Mudryk *et al.*, through computational simulation and experimental data, have attributed such behaviour to the preferential occupation of Si/Ge ions on the R_2 positions on the unit cell that play a major role on the magnetic interactions.

- The micro-device proposed by Kitanovski and Egolf consists of a static AMR cycle in a cylinder-shape with several sections, where a magnetocaloric fluid flows from the heat to the hot source [223]. As pointed out by the creators, this type of system can be used for special pumping methods - magneto-hydrodynamic (MHD) - or motionless drives, such as ferro-hydrodynamics (FHD). However, one of the disadvantages of this device is that, for a better performance, different fluids should be used for each section of the device. A way to solve this point, could be by producing the cylinder itself using a magnetocaloric composite with each section based on fillers with sequential T_C's in a cascade to compensate the losses from the fluid. To select the materials, a careful evaluation of mechanical and electric contribution to the caloric effect from the reinforced material should be performed. Calculations using Multiphase Comsol software would be useful to develop new magnetic composites through a simple technique that can be used for biological applications, micro-cooling devices, harvesting energy, and so on [102,279].

- Given the finding that it is possible to obtain $Gd_5(Si,Ge)_4$ nanoparticles using nanosecond laser deposition, to identify the difference between products of same composition by ablating with a ns and a fs pulsed laser. Based on the work of Tarasenka *et al.*, we have built two different setups for Pulsed Laser Ablation in Liquids for the production of $Gd_5(Si,Ge)_4$ nanoparticles using nano- and femtosecond pulses. An optimization of the system can give products with different diameters that can be used to construct the effect of size reduction on the $R_5(Si,Ge)_4$ compounds. A systematic study is required to fully understand the particle formation mechanism of these family nanostructures and is an ongoing work at IFIMUP group.

List of publications

Related with this PhD work

1. V. M. Andrade*, J. H. Belo, M. S. Reis, R. M. Costa, A. M. Pereira, J. P. Araújo. "Lanthanum dilution effects on the giant magnetocaloric $Gd_5Si_{1.8}Ge_{2.2}$". *Physica Status Solid (b)* **255**, 1800101-1800107 (2018).

2. V. M. Andrade*, N. B. Barroca, A. L. Pires, A. M. Pereira, J. P. Araújo. "Induced second-order magnetic transition on $Gd_5(Si,Ge)_4$ family compounds by a polymeric PMMA matrix". To be submitted to *Materials & Design*.

3. V. M. Andrade*, A. A. Amirov, D. M. Yusupov, M. S. Reis, N. B. Barroca, A. L. Pires, J. H. Belo, A. M. Pereira, M. A. Valente, J. P. Araújo. "Multiferroi composite as a multicaloric material: $Gd_5Si_{2.4}Ge_{1.6}$ microparticles embedded into a ferroelectric PVDF matrix". To be submitted to *Scientific Reports*.

4. V. M. Andrade*, N. R. Checca, J. H. Belo, A. L. Rossi, F. Garcia, B. G. Almeida, M. S. Reis, A. M. Pereira, J. P. Araújo. "Critical magnetic and crystallographic behavior of $Gd_5(Si,Ge)_4$ nanoparticles". To be submitted to *Nanomaterials*.

5. J. H. Belo, A. L. Pires, I. T. Gomes, V. M. Andrade*, J. B. Sousa, R. L. Hadimani, D. C. Jiles, Y. Ren, X. Zhang, J. P. Araújo, A. M. Pereira. "Giant Negative Thermal Expansion in Nanogranular $Gd_5Si_{1.3}Ge_{2.7}$ Multifunctional Material". To be submitted to *Physical Review B*.

Unrelated

1. S. S. Pedro, R. J. Caraballo-Vivas, V. M. Andrade*, C. Cruz, L. S. Paixão, C. Contreras, T. Costa-Soares, L. Caldeira, A. A. Coelho, A. Carvalho, A. M. G. Carvalho, D. L. Rocco, M. S. Reis. “Effects of Ga substitution on the structural and magnetic properties of half metallic Fe_2MnSi Heusler compound”. *Journal of Applied Physics*, **117**, 013902, (2015).

2. V. M. Andrade*, S. S. Pedro, R. J. Caraballo-Vivas, D. L. Rocco, M. S. Reis, A. P. C. Campos, A. A. Coelho, M. Escote, A. Zenatti, A. L. Rossif “Magnetocaloric

functional properties of $Sm_{0.6}Sr_{0.4}MnO_3$ manganite due to advanced nanostructured morphology" *Materials Chemistry and Physics*, **172**, 20-25 (2016).

3. J. C. G. Tedesco, S. S. Pedro, R. J. Caraballo-Vivas, C. Cruz, V. M. Andrade*, A. M. dos Santos, A. M. Carvalho, M. Costa, P. Venezuela, D. L. Rocco, M. S. Reis. "Chemical disorder determines the deviation of the Slater–Pauling rule for Fe_2MnSi-based Heusler alloys: evidences from neutron diffraction and density functional theory" *Journal of Physics: Condensed Matter*, **28**, 476002-476008 (2016).

4. V. M. Andrade*, R. J. Caraballo-Vivas, S. S. Pedro, J. C. G. Tedesco, A. L. Rossi, D. L. Rocco, M. S. Reis. "Magnetic and magnetocaloric properties of $La_{0.6}Ca_{0.4}MnO_3$ tunable by particle size and dimensionality." *Acta Materialia (Oxford)* **102**, 49-55 (2016).

References

[1] BP Global. Statistical Review of World Energy. 2018.

[2] D Coulomb, JL Dupon, and A Pichard. The Role of Refrigeration in the Global Economy. *29th Informatory Note on Refrigeration Technologies; Technical Report; International Institute of Refrigeration: Paris, France*, 2015.

[3] J Reilly, R Prinn, H Chen, A Sokolov, X Gao, A Schlosse, J Morris, and S Paltsev. 2018 Food, Water, Energy & Climate Outlook. *MIT Joint Program on the Science and Policy of Global Change*, 2018.

[4] Daryl R Brown, TB Stout, James A Dirks, and Nicholas Fernandez. The prospects of alternatives to vapor compression technology for space cooling and food refrigeration applications. *Energy Engineering*, 109(6):7–20, 2012.

[5] Enric Stern-Taulats, Teresa Castán, Lluís Mañosa, Antoni Planes, Neil D Mathur, and Xavier Moya. Multicaloric materials and effects. *MRS Bulletin*, 43(4):295–299, 2018.

[6] Ravi L Hadimani, Joao HB Silva, Andre M Pereira, Devo L Schlagel, Thomas A Lograsso, Yang Ren, Xiaoyi Zhang, David C Jiles, and Joao P Araújo. $Gd_5(Si,Ge)_4$ thin film displaying large magnetocaloric and strain effects due to magnetostructural transition. *Applied Physics Letters*, 106(3):032402, 2015.

[7] Fleet Appliance Corp. *From ice harvesting to ice making: the history of ice production*.

[8] Emma Greene. *History of Refrigeration, http://www.historyofrefrigeration.com/*, Accessed in August 14, 2018.

[9] Kevin Nwaigwe, CA Okoronkwo, Nnamdi V Ogueke, and EE Anyanwu. Review of nocturnal cooling systems. *International Journal of Energy for a Clean Environment*, 11(1-4), 2010.

[10] Armin Mehdipour and Ali Namazian. Yakhchal; climate responsive persian traditional architecture. In *2nd International Conference on Environment Science and Biotechnology*, volume 48, 2012.

[11] Ellen Leslie. *The ice house uncovered, https://www.countrylife.co.uk/comment-opinion/the-ice-house-uncovered-20789*.

[12] R Radermacher and K Kim. Domestic refrigerators: recent developments. *International Journal of Refrigeration*, 19(1):61–69, 1996.

[13] Montreal Protocol. Montreal protocol on substances that deplete the ozone layer. *Washington, DC: US Government Printing Office*, 26:128–136, 1987.

[14] M S Emani, R Roy, and B K Mandal. Development of Refrigerants: A Brief Review. *Indian J. Sci. Res*, 14(2):175–181, 2017.

[15] United Nations Enviroenment Programme. The importance of energy efficiency in the refrigeration, air-conditioning and heat pump sectors. briefing note a. May 2018.

[16] Andrej Kitanovski, Uroš Plaznik, Urban Tomc, and Alojz Poredoš. Present and future caloric refrigeration and heat-pump technologies. *International Journal of Refrigeration*, 57:288–298, 2015.

[17] V Franco, JS Blázquez, JJ Ipus, JY Law, LM Moreno-Ramírez, and A Conde. Magnetocaloric effect: From materials research to refrigeration devices. *Progress in Materials Science*, 2017.

[18] Anders Smith. Who discovered the magnetocaloric effect? *The European Physical Journal H*, 38(4):507–517, 2013.

[19] Pierre Weiss and Auguste Piccard. Le phénomène magnétocalorique. *J. Phys. Theor. Appl.*, 7(1):103–109, 1917.

[20] Anders Smith, Christian RH Bahl, Rasmus Bjørk, Kurt Engelbrecht, Kaspar K Nielsen, and Nini Pryds. Materials challenges for high performance magnetocaloric refrigeration devices. *Advanced Energy Materials*, 2(11):1288–1318, 2012.

[21] NA De Oliveira and PJ Von Ranke. Theoretical aspects of the magnetocaloric effect. *Physics Reports*, 489(4):89–159, 2010.

[22] GV Brown. Magnetic heat pumping near room temperature. *Journal of Applied Physics*, 47(8):3673–3680, 1976.

[23] Kathryn M Goodenough, Frances Wall, and David Merriman. The rare earth elements: demand, global resources, and challenges for resourcing future generations. *Natural Resources Research*, 27(2):201–216, 2018.

[24] MF Ozaydin and H Liang. Multi-energy conversion of $Gd_5(Si_2Ge_2)$-poly(vinylidene fluoride), a hybrid material. *Applied Physics Letters*, 105(6):062903, 2014.

[25] AM Tishin and YI Spichkin. Recent progress in magnetocaloric effect: Mechanisms and potential applications. *International Journal of Refrigeration*, 37:223–229, 2014.

[26] LJL Love, JF Jansen, TE McKnight, TJ Phelps, and Y Roh. *A Magnetocaloric Pump for Lab-On-A-Chip Technology: Phase I Report*. United States. Department of Energy, 2004.

[27] MP Annaorazov, SA Nikitin, AL Tyurin, KA Asatryan, and A Kh Dovletov. Anomalously high entropy change in FeRh alloy. *Journal of Applied Physics*, 79(3):1689–1695, 1996.

[28] Vitalij K Pecharsky and Karl A Gschneidner Jr. Giant magnetocaloric effect in $Gd_5(Si_2Ge_2)$. *Physical Review Letters*, 78(23):4494, 1997.

[29] Gordon J Miller. Complex rare-earth tetrelides, $RE_5(Si_xGe_{1-x})_4$: New materials for magnetic refrigeration and a superb playground for solid state chemistry. *Chemical Society Reviews*, 35(9):799–813, 2006.

[30] L Morellon, PA Algarabel, MR Ibarra, J Blasco, B García-Landa, Z Arnold, and F Albertini. Magnetic-field-induced structural phase transition in $Gd_5(Si_{1.8}Ge_{2.2})$. *Physical Review B*, 58(22):R14721, 1998.

[31] L Morellon, J Stankiewicz, B Garcıa-Landa, PA Algarabel, and MR Ibarra. Giant magnetoresistance near the magnetostructural transition in $Gd_5(Si_{1.8}Ge_{2.2})$. *Applied Physics Letters*, 73(23):3462–3464, 1998.

[32] Vitalij K Pecharsky and Karl A Gschneidner Jr. $Gd_5(Si_xGe_{1-x})$ 4: An extremum material. *Advanced Materials*, 13(9):683–686, 2001.

[33] RL Hadimani, S Gupta, SM Harstad, VK Pecharsky, and DC Jiles. Investigation of room temperature ferromagnetic nanoparticles of Gd_5Si_4. *IEEE Transactions on Magnetics*, 51(11):1–4, 2015.

[34] JH Belo, AL Pires, IT Gomes, JB Sousa, RL Hadimani, DC Jiles, Y Ren, X Zhang, JP Araujo, and AM Pereira. Giant negative thermal expansion in nanogranular $Gd_5Si_{1.3}Ge_{2.7}$ multifunctional material. *In press*, 2019.

[35] João H Belo, Ana L Pires, João P Araújo, and André M Pereira. Magnetocaloric materials: From micro-to nanoscale. *Journal of Materials Research*, pages 1–24, 2018.

[36] J Romero Gómez, R Ferreiro Garcia, A De Miguel Catoira, and M Romero Gómez. Magnetocaloric effect: A review of the thermodynamic cycles in magnetic refrigeration. *Renewable and Sustainable Energy Reviews*, 17:74–82, 2013.

[37] A Fujita, S Fujieda, Y Hasegawa, and K Fukamichi. Itinerant-electron metamagnetic transition and large magnetocaloric effects in La(Fe_xSi_{1-x})$_{13}$ compounds and their hydrides. *Physical Review B*, 67(10):104416, 2003.

[38] Y Yuan, Y Wu, X Tong, H Zhang, H Wang, XJ Liu, L Ma, HL Suo, and ZP Lu. Rare-earth high-entropy alloys with giant magnetocaloric effect. *Acta Materialia*, 125:481–489, 2017.

[39] O Tegus, E Brück, XW Li, L Zhang, W Dagula, FR De Boer, and KHJ Buschow. Tuning of the magneto-caloric effects in MnFe (P,As) by substitution of elements. *Journal of Magnetism and Magnetic Materials*, 272:2389–2390, 2004.

[40] QY Market Insights. *Global Magnetic Materials Market Professional Survey Report 2018, https://www.qymarketinsights.com/report/global-magnetic-materials-market-professional-survey-report-2018-81227.html*, November 24, 2018 (Accessed in November 26, 2018).

[41] Julia Lyubina, Rudolf Schäfer, Norbert Martin, Ludwig Schultz, and Oliver Gutfleisch. Novel design of La(Fe,Si)$_{13}$ alloys towards high magnetic refrigeration performance. *Advanced Materials*, 22(33):3735–3739, 2010.

[42] JH Belo, AM Pereira, Joao Pedro Araújo, C de la Cruz, AM dos Santos, Joao Nuno Gonçalves, VS Amaral, Luis Morellon, M Ricardo Ibarra, Pedro A Algarabel, et al. Tailoring the magnetism of $Tb_5Si_2Ge_2$ compounds by La substitution. *Physical Review B*, 86(1):014403, 2012.

[43] KP Skokov, D Yu Karpenkov, MD Kuz'min, IA Radulov, T Gottschall, B Kaeswurm, M Fries, and O Gutfleisch. Heat exchangers made of polymer-bonded La (Fe,Si)$_{13}$. *Journal of Applied Physics*, 115(17):17A941, 2014.

[44] VM Andrade, SS Pedro, RJ Caraballo Vivas, DL Rocco, MS Reis, APC Campos, A de A Coelho, M Escote, A Zenatti, and AL Rossi. Magnetocaloric functional properties of $Sm_{0.6}Sr_{0.4}MnO_3$ manganite due to advanced nanostructured morphology. *Materials Chemistry and Physics*, 172:20–25, 2016.

[45] YH Zhuang, JQ Li, WD Huang, WA Sun, and WQ Ao. Giant magnetocaloric effect enhanced by Pb-doping in $Gd_5Si_2Ge_2$ compound. *Journal of Alloys and Compounds*, 421(1-2):49–53, 2006.

[46] Kirk Rudolph, Arjun K Pathak, Yaroslav Mudryk, and Vitalij K Pecharsky. Magnetostructural phase transitions and magnetocaloric effect in ($Gd_{5-x}Sc_x$)$Si_{1.8}Ge_{2.2}$. *Acta Materialia*, 145:369–376, 2018.

[47] Yaroslav Mudryk, Durga Paudyal, Vitalij K Pecharsky, Karl A Gschneidner Jr, Sumohan Misra, and Gordon J Miller. Controlling magnetism of a complex metal-

lic system using atomic individualism. *Physical Review Letters*, 105(6):066401, 2010.

[48] W Imamura, AA Coelho, VL Kupfer, AMG Carvalho, JG Zago, AW Rinaldi, SL Favaro, and CS Alves. A new type of magnetocaloric composite based on conductive polymer and magnetocaloric compound. *Journal of Magnetism and Magnetic Materials*, 425:65–71, 2017.

[49] Manfred Fiebig. Revival of the magnetoelectric effect. *Journal of Physics D: Applied Physics*, 38(8):R123, 2005.

[50] Michael Cleveland and Hong Liang. Magnetocaloric piezoelectric composites for energy harvesting. *Smart Materials and Structures*, 21(4):047002, 2012.

[51] K Khaja Mohaideen and PA Joy. Influence of initial particle size on the magnetostriction of sintered cobalt ferrite derived from nanocrystalline powders. *Journal of Magnetism and Magnetic Materials*, 346:96–102, 2013.

[52] JD Moore, GK Perkins, Y Bugoslavsky, MK Chattopadhyay, SB Roy, P Chaddah, VK Pecharsky, KA Gschneidner Jr, and LF Cohen. Reducing the operational magnetic field in the prototype magnetocaloric system Gd_5Ge_4 by approaching the single cluster size limit. *Applied Physics Letters*, 88(7):072501, 2006.

[53] DM Rajkumar, M Manivel Raja, R Gopalan, and V Chandrasekaran. Magnetocaloric effect in high-energy ball-milled $Gd_5Si_2Ge_2$ and $Gd_5Si_2Ge_2$/Fe nanopowders. *Journal of Magnetism and Magnetic Materials*, 320(8):1479–1484, 2008.

[54] AL Pires, JH Belo, J Turcaud, GNP Oliveira, JP Araújo, A Berenov, LF Cohen, AML Lopes, and AM Pereira. Influence of short time milling in $R_5(Si,Ge)_4$, R= Gd and Tb, magnetocaloric materials. *Materials & Design*, 85:32–38, 2015.

[55] Senthil N Sambandam, Bharath Bethala, Dinesh K Sood, and Shekhar Bhansali. Evaluation of silicon nitride as a diffusion barrier for Gd-Si-Ge films on silicon. *Surface and Coatings Technology*, 200(5-6):1335–1340, 2005.

[56] Natalie Tarasenka, Vladimir Pankov, Andrei Butsen, and Nikolai Tarasenko. Laser assisted synthesis, structural and magnetic characterization of gadolinium germano-silicide nanoparticles in liquid. *Journal of Nanoscience and Nanotechnology*, 16(7):7451–7460, 2016.

[57] Andrew D Maynard, Robert J Aitken, Tilman Butz, Vicki Colvin, Ken Donaldson, Günter Oberdörster, Martin A Philbert, John Ryan, Anthony Seaton, Vicki Stone, et al. Safe handling of nanotechnology. *Nature*, 444(7117):267, 2006.

[58] Florence Sanchez and Konstantin Sobolev. Nanotechnology in concrete–a review. *Construction and building materials*, 24(11):2060–2071, 2010.

[59] Suellen Moraes, David Navas, Fanny Béron, Mariana Proenca, Kleber Pirota, Célia Sousa, and João Araújo. The role of Cu length on the magnetic behaviour of Fe/Cu multi-segmented nanowires. *Nanomaterials*, 8(7):490, 2018.

[60] Rosamund Daw and Joshua Finkelstein. Lab on a chip. *Nature*, 442(7101):367, 2006.

[61] Xin-Xin Chen, Bin Cheng, Yi-Xin Yang, Aoneng Cao, Jia-Hui Liu, Li-Jing Du, Yuanfang Liu, Yuliang Zhao, and Haifang Wang. Characterization and preliminary toxicity assay of nano-titanium dioxide additive in sugar-coated chewing gum. *Small*, 9(9-10):1765–1774, 2013.

[62] Marina E Vance, Todd Kuiken, Eric P Vejerano, Sean P McGinnis, Michael F Hochella Jr, David Rejeski, and Matthew S Hull. Nanotechnology in the real world: Redeveloping the nanomaterial consumer products inventory. *Beilstein Journal of Nanotechnology*, 6:1769, 2015.

[63] Hans-Martin Füssel, André Jol, Andreas Marx, Mikael Hildén, Angel Aparicio, Annemarie Bastrup-Birk, Andrea Bigano, Sergio Castellari, Markus Erhard, Birgit Georgi, et al. Climate change, impacts and vulnerability in Europe 2016: An indicator-based report. *European Environment Agency Report*, 2017.

[64] Haribabu Palneedi, Venkateswarlu Annapureddy, Shashank Priya, and Jungho Ryu. Status and perspectives of multiferroic magnetoelectric composite materials and applications. In *Actuators*, volume 5, page 9. Multidisciplinary Digital Publishing Institute, 2016.

[65] Lluís Mañosa and Antoni Planes. Special issue on caloric materials. *Journal of Physics D: Applied Physics*, 51(7):070201, 2018.

[66] William Imamura, Lucas S Paixão, Érik O Usuda, Nicolau M Bom, Sergio Gama, Éder SN Lopes, and Alexandre Magnus G Carvalho. i-Caloric Effects: a proposal for normalization. *arXiv preprint arXiv:1806.07959*, 2018.

[67] Lluís Mañosa, David González-Alonso, Antoni Planes, Erell Bonnot, Maria Barrio, Josep-Lluís Tamarit, Seda Aksoy, and Mehmet Acet. Giant solid-state barocaloric effect in the Ni–Mn–In magnetic shape-memory alloy. *Nature Materials*, 9(6):478, 2010.

[68] Erell Bonnot, Ricardo Romero, Lluís Mañosa, Eduard Vives, and Antoni Planes. Elastocaloric effect associated with the martensitic transition in shape-memory alloys. *Physical Review Letters*, 100(12):125901, 2008.

[69] Marvin Schmidt, Andreas Schütze, and Stefan Seelecke. Scientific test setup for investigation of shape memory alloy based elastocaloric cooling processes. *International Journal of Refrigeration*, 54:88–97, 2015.

[70] Darin J Sharar, Joshua Radice, Ronald Warzoha, Brendan Hanrahan, and Benjamin Chang. First demonstration of a bending-mode elastocaloric cooling 'loop'. In *2018 17th IEEE Intersociety Conference on Thermal and Thermomechanical Phenomena in Electronic Systems (ITherm)*, pages 218–226. IEEE, 2018.

[71] H Sehitoglu, Y Wu, and E Ertekin. Elastocaloric effects in the extreme. *Scripta Materialia*, 148:122–126, 2018.

[72] AS Mischenko, Qi Zhang, JF Scott, RW Whatmore, and ND Mathur. Giant electrocaloric effect in thin-film $PbZr_{0.95}Ti_{0.05}O_3$. *Science*, 311(5765):1270–1271, 2006.

[73] M Ožbolt, A Kitanovski, J Tušek, and A Poredoš. Electrocaloric refrigeration: thermodynamics, state of the art and future perspectives. *International journal of refrigeration*, 40:174–188, 2014.

[74] Uroš Plaznik, Marko Vrabelj, Zdravko Kutnjak, Barbara Malič, Brigita Rožič, Alojz Poredoš, and Andrej Kitanovski. Numerical modelling and experimental validation of a regenerative electrocaloric cooler. *International Journal of Refrigeration*, 98:139–149, 2019.

[75] Lon E Bell. Cooling, heating, generating power, and recovering waste heat with thermoelectric systems. *Science*, 321(5895):1457–1461, 2008.

[76] PO Castillo-Villa, De E Soto-Parra, JA Matutes-Aquino, RA Ochoa-Gamboa, Antoni Planes, Lluís Mañosa, David González-Alonso, Marcelo Stipcich, Ricardo Romero, D Ríos-Jara, et al. Caloric effects induced by magnetic and mechanical fields in a $Ni_{50}Mn_{25-x}Ga_{25}Co_x$ magnetic shape memory alloy. *Physical Review B*, 83(17):174109, 2011.

[77] Yang Liu, Lee C Phillips, Richard Mattana, Manuel Bibes, Agnès Barthélémy, and Brahim Dkhil. Large reversible caloric effect in FeRh thin films via a dual-stimulus multicaloric cycle. *Nature Communications*, 7:11614, 2016.

[78] S Crossley, ND Mathur, and X Moya. New developments in caloric materials for cooling applications. *Aip Advances*, 5(6):067153, 2015.

[79] WF Giauque. A thermodynamic treatment of certain magnetic effects. a proposed method of producing temperatures considerably below 1 absolute. *Journal of the American Chemical Society*, 49(8):1864–1870, 1927.

[80] WF Giauque and DP MacDougall. Attainment of temperatures below 1^0 absolute by demagnetization of $gd_2(so_4)_3{\cdot}8h_2o$. *Physical Review*, 43(9):768, 1933.

[81] KA Gschneidner Jr and VK Pecharsky. Thirty years of near room temperature magnetic cooling: Where we are today and future prospects. *International Journal of Refrigeration*, 31(6):945–961, 2008.

[82] WA Steyert. Stirling-cycle rotating magnetic refrigerators and heat engines for use near room temperature. *Journal of Applied Physics*, 49(3):1216–1226, 1978.

[83] GV Brown. Practical and efficient magnetic heat pump, Oct 1978. US Patent, LEW-12508.

[84] WA Steyert. Rotating carnot-cycle magnetic refrigerators for use near 2 k. *Journal of Applied Physics*, 49(3):1227–1231, 1978.

[85] Ciro Aprea, Adriana Greco, Angelo Maiorino, and Claudia Masselli. A two-dimensional model of a solid-state regenerator based on combined electrocaloric-elastocaloric effect. *Energy Procedia*, 126:337–344, 2017.

[86] Tino Gottschall, Adrià Gràcia-Condal, Maximilian Fries, Andreas Taubel, Lukas Pfeuffer, Lluís Mañosa, Antoni Planes, Konstantin P Skokov, and Oliver Gutfleisch. A multicaloric cooling cycle that exploits thermal hysteresis. *Nature Materials*, 17(10):929, 2018.

[87] Cooling Post. *Magnetic commercial fridge system launches, https://www.coolingpost.com/world-news/magnetic-commercial-fridge-system-launches/*, 2016 (accessed in November 26, 2018).

[88] C Zimm, A Jastrab, A Sternberg, V Pecharsky, K Gschneidner, M Osborne, and I Anderson. Description and performance of a near-room temperature magnetic refrigerator. In *Advances in Cryogenic Engineering*, pages 1759–1766. Springer, 1998.

[89] A Rowe and A Tura. Experimental investigation of a three-material layered active magnetic regenerator. *International Journal of Refrigeration*, 29(8):1286–1293, 2006.

[90] *Premiere of cutting-edge cooling appliance at CES; 2015.*, 2015 (accessed in November 26, 2018).

[91] Houssem Rafik El-Hana Bouchekara and Mouaaz Nahas. Magnetic refrigeration technology at room temperature. In *Trends in Electromagnetism-From Fundamentals to Applications*. InTech, 2012.

[92] H Wada, T Morikawa, K Taniguchi, T Shibata, Y Yamada, and Y Akishige. Giant magnetocaloric effect of $MnAs_{1-x}Sb_x$ in the vicinity of first-order magnetic transition. *Physica B: Condensed Matter*, 328(1-2):114–116, 2003.

[93] Mohamed Balli, Daniel Fruchart, Damien Gignoux, Cédric Dupuis, Afef Kedous-Lebouc, and R Zach. Giant magnetocaloric effect in $Mn_{1-x}(Ti_{0.5}V_{0.5})_x$As: Experiments and calculations. *Journal of Applied Physics*, 103(10):103908, 2008.

[94] V Franco, JM Borrego, A Conde, and S Roth. Influence of Co addition on the magnetocaloric effect of FeCoSiAlGaPCB amorphous alloys. *Applied physics letters*, 88(13):132509, 2006.

[95] Aleksandra Kolano-Burian, Maciej Kowalczyk, Roman Kolano, Ritta Szymczak, Henryk Szymczak, and Marcin Polak. Magnetocaloric effect in Fe-Cr-Cu-Nb-Si-B amorphous materials. *Journal of Alloys and Compounds*, 479(1-2):71–73, 2009.

[96] Mahmud Khan, Naushad Ali, and Shane Stadler. Inverse magnetocaloric effect in ferromagnetic $Ni_{50}Mn_{37+x}Sb_{13-x}$ Heusler alloys. *Journal of Applied Physics*, 101(5):053919, 2007.

[97] DL Rocco, AA Coelho, S Gama, and M de C Santos. Dependence of the magnetocaloric effect on the A-site ionic radius in isoelectronic manganites. *Journal of Applied Physics*, 113(11):113907, 2013.

[98] V Franco, JS Blázquez, B Ingale, and A Conde. The magnetocaloric effect and magnetic refrigeration near room temperature: materials and models. *Annual Review of Materials Research*, 42:305–342, 2012.

[99] GS Smith, AG Tharp, and W Johnson. Rare earth-germanium and -silicon compounds at 5:4 and 5:3 compositions. *Acta Crystallographica*, 22(6):940–943, 1967.

[100] F Holtzberg, RJ Gambino, and TR McGuire. New ferromagnetic 5:4 compounds in the rare earth silicon and germanium systems. *Journal of Physics and Chemistry of Solids*, 28(11):2283–2289, 1967.

[101] Matthias C Wapler, Jochen Leupold, Iulius Dragonu, Dominik von Elverfeld, Maxim Zaitsev, and Ulrike Wallrabe. Magnetic properties of materials for MR engineering, micro-MR and beyond. *Journal of Magnetic Resonance*, 242:233–242, 2014.

[102] Aaron Hamann and E Dan Dahlberg. High strain magnetostriction in a ferromagnet-polymer composite. *Applied Physics Letters*, 110(9):091906, 2017.

[103] Julie Thévenot, Hugo Oliveira, Olivier Sandre, and Sébastien Lecommandoux. Magnetic responsive polymer composite materials. *Chemical Society Reviews*, 42(17):7099–7116, 2013.

[104] J Stankiewicz, L Morellon, PA Algarabel, and MR Ibarra. Hall effect in $Gd_5(Si_{1.8}Ge_{2.2})$. *Physical Review B*, 61(19):12651, 2000.

[105] KA Gschneidner, VK Pecharsky, AO Pecharsky, VV Ivtchenko, and EM Levin. The Nonpareil $R_5(Si_xGe_{1-x})_4$ Phases. *Journal of Alloys and Compounds*, 303:214–222, 2000.

[106] RL Hadimani, Y Melikhov, DL Schlagel, TA Lograsso, and DC Jiles. Study of the second-order "hidden" phase transition of the monoclinic phase in the mixed phase region of $Gd_5(Si_xGe_{1-x})_4$. *IEEE Transactions on Magnetics*, 48(11):4070–4073, 2012.

[107] AO Pecharsky, VK Pecharsky, and KA Gschneidner Jr. Phase relationships and low temperature heat capacities of alloys in the Y_5Si_4-Y_5Ge_4 pseudo binary system. *Journal of Alloys and Compounds*, 379(1-2):127–134, 2004.

[108] AO Pecharsky, KA Gschneidner Jr, and VK Pecharsky. The giant magnetocaloric effect of optimally prepared $Gd_5Si_2Ge_2$. *Journal of Applied Physics*, 93(8):4722–4728, 2003.

[109] Sumohan Misra. *Structural flexibility in magnetocaloric RE_5T_4 (RE = rare-earth; T = Si,Ge,Ga) materials: Effect of chemical substitution on structure bonding and properties*. PhD thesis, Universidade do Minho, Setember 2013.

[110] C Magen, Z Arnold, L Morellon, Y Skorokhod, PA Algarabel, MR Ibarra, and J Kamarad. Pressure-induced three-dimensional ferromagnetic correlations in the giant magnetocaloric compound Gd_5Ge_4. *Physical Review Letters*, 91(20):207202, 2003.

[111] H Tang, VK Pecharsky, KA Gschneidner Jr, and AO Pecharsky. Interplay between reversible and irreversible magnetic phase transitions in polycrystalline Gd_5Ge_4. *Physical Review B*, 69(6):064410, 2004.

[112] Sumohan Misra and Gordon J Miller. On the distribution of tetrelide atoms (Si,Ge) in $Gd_5(Si_xGe_{1-x})_4$. *Journal of Solid State Chemistry*, 179(8):2290–2297, 2006.

[113] JH Belo, AM Pereira, J Ventura, GNP Oliveira, JP Araújo, PB Tavares, L Fernandes, PA Algarabel, C Magen, L Morellon, et al. Phase control studies in $Gd_5Si_2Ge_2$ giant magnetocaloric compound. *Journal of Alloys and Compounds*, 529:89–95, 2012.

[114] Yevgen Melikhov, RL Hadimani, and Arun Raghunathan. $Gd_5(Si_xGe_{1-x})_4$ system-updated phase diagram. *Journal of Magnetism and Magnetic Materials*, 395:143–146, 2015.

[115] L Morellon, Z Arnold, PA Algarabel, C Magen, MR Ibarra, and Y Skorokhod. Pressure effects in the giant magnetocaloric compounds $Gd_5(Si_xGe_{1-x})_4$. *Journal of Physics: Condensed Matter*, 16(9):1623, 2004.

[116] Ya Mudryk, Y Lee, T Vogt, KA Gschneidner Jr, and VK Pecharsky. Polymorphism of $Gd_5Si_2Ge_2$: The equivalence of temperature, magnetic field, and chemical and hydrostatic pressures. *Physical Review B*, 71(17):174104, 2005.

[117] A Magnus G Carvalho, Cleber S Alves, Ariana de Campos, Adelino A Coelho, Sergio Gama, Flavio CG Gandra, Pedro J von Ranke, and Nilson A Oliveira. The magnetic and magnetocaloric properties of $Gd_5Ge_2Si_2$ compound under hydrostatic pressure. *Journal of Applied Physics*, 97(10):10M320, 2005.

[118] Durga Paudyal, Vitalij K Pecharsky, Karl A Gschneidner Jr, and Bruce N Harmon. Electron correlation effects on the magnetostructural transition and magnetocaloric effect in $Gd_5Si_2Ge_2$. *Physical Review B*, 73(14):144406, 2006.

[119] Ana Lúcia Pires, João Horta Belo, Armandina Maria Lima Lopes, Isabel T Gomes, Luis Morellón, Cesar Magen, Pedro Antonio Algarabel, Manuel Ricardo Ibarra, André Miguel Pereira, and João Pedro Araújo. Phase competitions behind the giant magnetic entropy variation: $Gd_5Si_2Ge_2$ and $Tb_5Si_2Ge_2$ case studies. *Entropy*, 16(7):3813–3831, 2014.

[120] Fèlix Casanova, Xavier Batlle, Amílcar Labarta, Jordi Marcos, Lluís Mañosa, and Antoni Planes. Entropy change and magnetocaloric effect in $Gd_5(Si_xGe_{1-x})_4$. *Physical Review B*, 66(10):100401, 2002.

[121] Felix Casanova, Xavier Batlle, Amilcar Labarta, Jordi Marcos, Lluis Manosa, and Antoni Planes. Change in entropy at a first-order magnetoelastic phase transition: Case study of $Gd_5(Si_xGe_{1-x})_4$ giant magnetocaloric alloys. *Journal of Applied Physics*, 93(10):8313–8315, 2003.

[122] Karl A Gschneidner Jr, Yaroslav Mudryk, and Vitalij K Pecharsky. On the nature of the magnetocaloric effect of the first-order magnetostructural transition. *Scripta Materialia*, 67(6):572–577, 2012.

[123] L Morellon, J Blasco, PA Algarabel, and MR Ibarra. Nature of the first-order antiferromagnetic-ferromagnetic transition in the Ge-rich magnetocaloric compounds $Gd_5(Si_xGe_{1-x})_4$. *Physical Review B*, 62(2):1022, 2000.

[124] Vivian M Andrade, João H Belo, Mario S Reis, Rui M Costa, André M Pereira, and João P Araújo. Lanthanum dilution effects on the giant magnetocaloric $Gd_5Si_{1.8}Ge_{2.2}$ compound. *Physica Status Solidi (b)*, 255(10):1800101–1800107, 2018.

[125] Ilkan Calisir, Abdulkarim A Amirov, Annette K Kleppe, and David A Hall. Optimisation of functional properties in lead-free $BiFeO_3$-$BaTiO_3$ ceramics through La^{3+} substitution strategy. *Journal of Materials Chemistry A*, 2018.

[126] Sumohan Misra and Gordon J Miller. $Gd_{5-x}Y_xTt_4$ (Tt= Si or Ge): Effect of metal substitution on structure, bonding, and magnetism. *Journal of the American Chemical Society*, 130(42):13900–13911, 2008.

[127] Virgil Provenzano, Alexander J Shapiro, and Robert D Shull. Reduction of hysteresis losses in the magnetic refrigerant $Gd_5Si_2Ge_2$ by the addition of iron. *Nature*, 429(6994):853–857, 2004.

[128] Osamu Izumi and Takayuki Takasugi. Mechanisms of ductility improvement in $L1_2$ compounds. *Journal of Materials Research*, 3(3):426–440, 1988.

[129] YI Spichkin, VK Pecharsky, and KA Gschneidner Jr. Preparation, crystal structure, magnetic and magnetothermal properties of ($Gd_xR_{(5-x)}Si_4$, where R= Pr and Tb, alloys. *Journal of Applied Physics*, 89(3):1738–1745, 2001.

[130] J M Elbicki, L Y Zhang, R T Obermyer, W E Wallace, and S G Sankar. Magnetic studies of $Gd_{1-x}M_x)_5Si_4$ alloys (M= La or Y). *Journal of Applied Physics*, 69(8):5571–5573, 1991.

[131] JM Cadogan, DH Ryan, Z Altounian, HB Wang, and IP Swainson. Magnetic Structures of Nd_5Si_4 and Nd_5Ge_4. *Journal of Physics: Condensed Matter*, 14(30):7191, 2002.

[132] André Miguel Trindade Pereira. *Rare-Earth Nanostratified Compounds With Novel Potentialities for Refrigeration and Magnetic Sensors*. PhD thesis, Universidade do Porto, February 2010.

[133] Koichi Momma and Fujio Izumi. Vesta 3 for three-dimensional visualization of crystal, volumetric and morphology data. *Journal of Applied Crystallography*, 44(6):1272–1276, 2011.

[134] Vivian M Andrade, RJ Caraballo Vivas, Sandra S Pedro, Julio César G Tedesco, André L Rossi, Adelino A Coelho, Daniel L Rocco, and Mario S Reis. Magnetic and magnetocaloric properties of $La_{0.6}Ca_{0.4}MnO_3$ tunable by particle size and dimensionality. *Acta Materialia*, 102:49–55, 2016.

[135] Shivakumar G Hunagund, Shane M Harstad, Ahmed A El-Gendy, Shalabh Gupta, Vitalij K Pecharsky, and Ravi L Hadimani. Investigating phase transition temperatures of size separated gadolinium silicide magnetic nanoparticles. *AIP Advances*, 8(5):056428, 2018.

[136] Hmed A El-Gendy, Shane M Harstad, Vimalan Vijayaragavan, Shalabh Gupta, Vitalij K Pecharsky, Jamal Zweit, and Ravi L Hadimani. Ferromagnetic Gd_5Si_4 nanoparticles as T2 contrast agents for magnetic resonance imaging. *IEEE Magnetics Letters*, 8:1–4, 2017.

[137] Pritom J Bora, SM Harstad, S Gupta, Vitalij K Pecharsky, KJ Vinoy, Praveen C Ramamurthy, and RL Hadimani. Gadolinium silicide (Gd_5Si_4) nanoparticles for tuneable broad band microwave absorption. *Materials Research Express*, 2019.

[138] Shane Harstad, Noel D'Souza, Navneet Soin, Ahmed A El-Gendy, Shalabh Gupta, Vitalij K Pecharsky, Tahir Shah, Elias Siores, and Ravi L Hadimani. Enhancement of β-phase in PVDF films embedded with ferromagnetic Gd_5Si_4 nanoparticles for piezoelectric energy harvesting. *AIP Advances*, 7(5):056411, 2017.

[139] Ravi L Hadimani, Yaroslav Mudryk, Timothy E Prost, Vitalij K Pecharsky, KA Gschneidner, and David C Jiles. Growth and characterization of Pt-protected Gd_5Si_4 thin films. *Journal of Applied Physics*, 115(17):17C113, 2014.

[140] Daniel C Mattis. History of magnetism. In *The Theory of Magnetism I*, pages 1–38. Springer, 1981.

[141] Stephen Blundell. Magnetism in condensed matter, 2003.

[142] David J Griffiths. Introduction to electrodynamics, 2005.

[143] MS Reis. Fundamentals of Magnetism, 2013.

[144] Charles Kittel, Paul McEuen, and Paul McEuen. *Introduction to solid state physics*, volume 8. Wiley New York, 1996.

[145] James D Moore, Kelly Morrison, Garry K Perkins, Deborah L Schlagel, Thomas A Lograsso, Karl A Gschneidner, Vitalij K Pecharsky, and Lesley F Cohen. Metamagnetism seeded by nanostructural features of single-crystalline $Gd_5Si_2Ge_2$. *Advanced Materials*, 21(37):3780–3783, 2009.

[146] BK Banerjee. On a generalised approach to first and second order magnetic transitions. *Physics Letters*, 12(1):16–17, 1964.

[147] P Ehrenfest. P. ehrenfest, proc. r. acad. sci. amsterdam 36, 153 (1933). In *Proc. R. Acad. Sci. Amsterdam*, volume 36, page 153, 1933.

[148] M Reis, J Vieira, V Amaral, D Rocco, J Amaral, and N Fernandes. *The Magnetocaloric Project, http://magnetocaloric.web.ua.pt/mce.html*, 2007.

[149] VK Pecharsky and KA Gschneidner Jr. Magnetocaloric effect from indirect measurements: magnetization and heat capacity. *Journal of Applied Physics*, 86(1):565–575, 1999.

[150] JS Amaral and VS Amaral. On estimating the magnetocaloric effect from magnetization measurements. *Journal of Magnetism and Magnetic Materials*, 322(9-12):1552–1557, 2010.

[151] Ekkes Brück. Developments in magnetocaloric refrigeration. *Journal of Physics D: Applied Physics*, 38(23):R381, 2005.

[152] Melvin M Vopson. The multicaloric effect in multiferroic materials. *Solid State Communications*, 152(23):2067–2070, 2012.

[153] Melvin M Vopson. Theory of giant-caloric effects in multiferroic materials. *Journal of Physics D: Applied Physics*, 46(34):345304, 2013.

[154] Antoni Planes, Teresa Castán, and Avadh Saxena. Thermodynamics of multicaloric effects in multiferroic materials: application to metamagnetic shape-memory alloys and ferrotoroidics. *Phil. Trans. R. Soc. A*, 374(2074):20150304, 2016.

[155] Yang Liu, Guangzu Zhang, Qi Li, Laurent Bellaiche, James F Scott, Brahim Dkhil, and Qing Wang. Towards multicaloric effect with ferroelectrics. *Physical Review B*, 94(21):214113, 2016.

[156] K Szałowski, T Balcerzak, and M Jaščur. Thermodynamics of a model solid with magnetoelastic coupling. *Journal of Magnetism and Magnetic Materials*, 445:110–118, 2018.

[157] Zdravko Kutnjak, Brigita Rožič, and Raša Pirc. Electrocaloric effect: theory, measurements, and applications. *Wiley Encyclopedia of Electrical and Electronics Engineering*, pages 1–19, 1999.

[158] Jill Guyonnet. Studies of magnetoelectric coupling in $BiFeO_3$-$CoFe_2O_4$ nanocomposites. Master's thesis, Université de Genève, Switzerland, 2008.

[159] Melvin M Vopson. Reply to" rebuttal of" the multicaloric effect in multiferroic materials". *arXiv preprint arXiv:1611.06262*, 2016.

[160] Krzysztof Marycz, Monika Maredziak, Jakub Grzesiak, Dariusz Szarek, Anna Lis, and Jadwiga Laska. Polyurethane polylactide-blend films doped with zinc ions for the growth and expansion of human olfactory ensheathing cells (oecs) and adipose-derived mesenchymal stromal stem cells (ascs) for regenerative medicine applications. *Polymers*, 8(5):175, 2016.

[161] N Soin, D Boyer, K Prashanthi, S Sharma, AA Narasimulu, J Luo, TH Shah, E Siores, and T Thundat. Exclusive self-aligned β-phase PVDF films with abnormal piezoelectric coefficient prepared via phase inversion. *Chemical Communications*, 51(39):8257–8260, 2015.

[162] Robert Eason. *Pulsed laser deposition of thin films: applications-led growth of functional materials*. John Wiley & Sons, 2007.

[163] Yasuhide Nakayama and Takehisa Matsuda. Surface microarchitectural design in biomedical applications: preparation of microporous polymer surfaces by an excimer laser ablation technique. *Journal of Biomedical Materials Research Part A*, 29(10):1295–1301, 1995.

[164] Natalie Tarasenka, Vladimir Pankov, and Nikolai Tarasenko. Chemical interactions in a mixture of gadolinium and silicon colloidal solutions. *Colloid and Interface Science Communications*, 14:13–16, 2016.

[165] A Inam, MS Hegde, XD Wu, T Venkatesan, P England, PF Miceli, EW Chase, CC Chang, JM Tarascon, and JB Wachtman. As-deposited high T_C and J_C superconducting thin films made at low temperatures. *Applied Physics Letters*, 53(10):908–910, 1988.

[166] X Zeng, XL Mao, R Greif, and RE Russo. Experimental investigation of ablation efficiency and plasma expansion during femtosecond and nanosecond laser ablation of silicon. *Applied Physics A*, 80(2):237–241, 2005.

[167] Boris N Chichkov, C Momma, Stefan Nolte, F Von Alvensleben, and A Tünnermann. Femtosecond, picosecond and nanosecond laser ablation of solids. *Applied Physics A*, 63(2):109–115, 1996.

[168] Han Wu, Chengping Wu, Nan Zhang, Xiaonong Zhu, Xiuquan Ma, and Leonid V Zhigilei. Experimental and computational study of the effect of 1 atm background gas on nanoparticle generation in femtosecond laser ablation of metals. *Applied Surface Science*, 435:1114–1119, 2018.

[169] Hans-Ulrich Krebs, Martin Weisheit, Jörg Faupel, Erik Süske, Thorsten Scharf, Christian Fuhse, Michael Störmer, Kai Sturm, Michael Seibt, Harald Kijewski, et al. Pulsed laser deposition (PLD)-a versatile thin film technique. In *Advances in Solid State Physics*, pages 505–518. Springer, 2003.

[170] Filip Ilievski, T Tepper, and CA Ross. Optical and magnetic properties of γ-iron oxide made by reactive pulsed laser deposition. *IEEE Transactions on Magnetics*, 39(5):3172–3174, 2003.

[171] Isabel Alexandra Domingues Tarroso Gomes. *Manganite thin films deposited on piezoelectric substrates*. PhD thesis, Universidade do Minho, Setember 2013.

[172] David J Smith. Ultimate resolution in the electron microscope? *Materials Today*, 11:30–38, 2008.

[173] Claudionico. *Electron interaction with matter*, 2013 - accessed in August 3, 2018.

[174] *National Programme on Technology Enhanced, https://nptel.ac.in/courses/102103044/module3/lec18/4.html*, 2013 - accessed in August 3, 2018.

[175] Bernard Dennis Cullity and Stuart R Stock. *Elements of X-ray Diffraction*. Pearson Education, 2014.

[176] Harold P Klug and Leroy E Alexander. X-ray diffraction procedures: for polycrystalline and amorphous materials. *X-Ray Diffraction Procedures: For Polycrystalline and Amorphous Materials, 2nd Edition, by Harold P. Klug, Leroy E. Alexander, pp. 992. ISBN 0-471-49369-4. Wiley-VCH, May 1974.*, page 992, 1974.

[177] DL Dorset. X-ray diffraction: a practical approach. *Microscopy and Microanalysis*, 4(5):513–515, 1998.

[178] J K Cockcroft, P Barnes, and M P Attfield. *Advanced Certificate in Powder Diffraction - Birkbeck College, London, http://pd.chem.ucl.ac.uk/pdnn/inst1/optics1.htm*, accessed in August 8, 2018.

[179] Mika Pflüger, Victor Soltwisch, Jürgen Probst, Frank Scholze, and Michael Krumrey. Grazing Incidence Small Angle X-Ray Scattering (GISAXS) on Small Targets Using Large Beams. 2017.

[180] Juan Rodríguez-Carvajal. Recent developments of the program FULLPROF. *Commission on Powder Diffraction (IUCr). Newsletter*, 26:12–19, 2001.

[181] Armando Y Takeuchi. Técnicas de medidas magnéticas. *Editora livraria da Física*, 2010.

[182] Ivar Giaever. Detection of the ac josephson effect. *Physical Review Letters*, 14(22):904, 1965.

[183] R Nave. *SQUID Magnetometer, http://hyperphysics.phy-astr.gsu.edu/hbase/Solids/Squid.html*, accessed in August 6, 2018.

[184] M Knobel, WC Nunes, LM Socolovsky, E De Biasi, JM Vargas, and JC Denardin. Superparamagnetism and other magnetic features in granular materials: a review on ideal and real systems. *Journal of Nanoscience and Nanotechnology*, 8(6):2836–2857, 2008.

[185] L Caron, ZQ Ou, TT Nguyen, DT Cam Thanh, O Tegus, and E Brück. On the determination of the magnetic entropy change in materials with first-order transitions. *Journal of Magnetism and Magnetic Materials*, 321(21):3559–3566, 2009.

[186] M Bradley. *FTIR Sample Techniques - Transmission, https://www.thermofisher.com/us/en/home/industrial/spectroscopy-elemental-isotope-analysis/spectroscopy-elemental-isotope-analysis-learning-center/molecular-spectroscopy-information/ftir-information/ftir-sample-handling-techniques/ftir-sample-handling-techniques-transmission.html*, Accessed in November 20, 2018.

[187] MM Vopson, YK Fetisov, G Caruntu, and G Srinivasan. Measurement techniques of the magneto-electric coupling in multiferroics. *Materials*, 10(8):963, 2017.

[188] AM Pereira, Luis Morellon, C Magen, J Ventura, PA Algarabel, MR Ibarra, JB Sousa, and JP Araújo. Griffiths-like phase of magnetocaloric $R_5(Si_xGe_{1-x})_4$ (R= Gd, Tb, Dy, and Ho). *Physical Review B*, 82(17):172406, 2010.

[189] HF Yang, GH Rao, GY Liu, ZW Ouyang, WF Liu, XM Feng, WG Chu, and JK Liang. Structure dependence of magnetic properties of $Nd_5Si_{4-x}Ge_x$ (x= 1.2 and 2). *Physica B: Condensed Matter*, 325:293–299, 2003.

[190] HF Yang, GH Rao, GY Liu, ZW Ouyang, XM Feng, WF Liu, WG Chu, and JK Liang. Structure dependence of magnetic properties of $Pr_5Si_2Ge_2$. *Journal of Physics: Condensed Matter*, 14(41):9705, 2002.

[191] YF Zhou, Yong Mei Hao, and Zhong Bo Hu. Structure of $Gd_{(5-x)}Ho_xSi_4$ solid solutions. In *Key Engineering Materials*, volume 368, pages 632–634. Trans Tech Publ, 2008.

[192] HF Yang, GH Rao, GY Liu, ZW Ouyang, WF Liu, XM Feng, WG Chu, and JK Liang. Crystal structures of compounds in the pseudobinary system Gd_5Ge_4-La_5Ge_4. *Journal of Alloys and Compounds*, 361(1):113–117, 2003.

[193] Martin Rahm, Roald Hoffmann, and NW Ashcroft. Atomic and ionic radii of elements 1-96. *Chemistry-A European Journal*, 22(41):14625–14632, 2016.

[194] JH Belo, JS Amaral, AM Pereira, VS Amaral, and JP Araújo. On the curie temperature dependency of the magnetocaloric effect. *Applied Physics Letters*, 100(24):242407, 2012.

[195] Jérome Roger, Volodymyr Babizhetskyy, Kurt Hiebl, Jean-François Halet, and Roland Guérin. Structural chemistry, magnetism and electrical properties of binary Gd silicides and Ho_3Si_4. *Journal of Alloys and Compounds*, 407(1):25–35, 2006.

[196] Vladimir V Khovaylo, Valeria V Rodionova, Sergey N Shevyrtalov, and Val Novosad. Magnetocaloric effect in “reduced” dimensions: Thin films, ribbons, and microwires of heusler alloys and related compounds. *Physica Status Solidi (b)*, 251(10):2104–2113, 2014.

[197] Anna G Koniuszewska and Jacek W Kaczmar. Application of polymer based composite materials in transportation. *Progress in Rubber, Plastics and Recycling Technology*, 32(1):1, 2016.

[198] S Ramakrishna, J Mayer, E Wintermantel, and Kam W Leong. Biomedical applications of polymer-composite materials: A review. *Composites Science and Technology*, 61(9):1189–1224, 2001.

[199] Thomas Gereke, Oliver Döbrich, Matthias Hübner, and Chokri Cherif. Experimental and computational composite textile reinforcement forming: A review. *Composites Part A: Applied Science and Manufacturing*, 46:1–10, 2013.

[200] Ja Hoon Koo, Jungmok Seo, and Taeyoon Lee. Nanomaterials on flexible substrates to explore innovative functions: From energy harvesting to bio-integrated electronics. *Thin Solid Films*, 524:1–19, 2012.

[201] *Young's Modulus - Cost, Material selection and processing - Department of Engineering - University of Cambridge, http://www-materials.eng.cam.ac.ukl*, Accessed in September 23, 2018.

[202] GV Stepanov, SS Abramchuk, DA Grishin, LV Nikitin, E Yu Kramarenko, and AR Khokhlov. Effect of a homogeneous magnetic field on the viscoelastic behavior of magnetic elastomers. *Polymer*, 48(2):488–495, 2007.

[203] Y Shen, M Farid Golnaraghi, and GR Heppler. Experimental research and modeling of magnetorheological elastomers. *Journal of Intelligent Material Systems and Structures*, 15(1):27–35, 2004.

[204] AV Chertovich, GV Stepanov, E Yu Kramarenko, and AR Khokhlov. New composite elastomers with giant magnetic response. *Macromolecular Materials and Engineering*, 295(4):336–341, 2010.

[205] Oleg V Stolbov, Yuriy L Raikher, and Maria Balasoiu. Modelling of magnetodipolar striction in soft magnetic elastomers. *Soft Matter*, 7(18):8484–8487, 2011.

[206] Andreas M Menzel. Tuned, driven, and active soft matter. *Physics Reports*, 554:1–45, 2015.

[207] Luiz CA Oliveira, Rachel VRA Rios, Jose D Fabris, V Garg, Karim Sapag, and Rochel M Lago. Activated carbon/iron oxide magnetic composites for the adsorption of contaminants in water. *Carbon*, 40(12):2177–2183, 2002.

[208] TS Sreeprasad, Shihabudheen M Maliyekkal, KP Lisha, and T Pradeep. Reduced graphene oxide-metal/metal oxide composites: facile synthesis and application in water purification. *Journal of Hazardous Materials*, 186(1):921–931, 2011.

[209] Wen Cai, Qi Chen, Nerine Cherepy, Alex Dooraghi, David Kishpaugh, Arion Chatziioannou, Stephen Payne, Weidong Xiang, and Qibing Pei. Synthesis of bulk-size transparent gadolinium oxide-polymer nanocomposites for gamma ray spectroscopy. *Journal of Materials Chemistry C*, 1(10):1970–1976, 2013.

[210] Umar Ali, Khairil Juhanni Bt Abd Karim, and Nor Aziah Buang. A review of the properties and applications of poly (methyl methacrylate)(pmma). *Polymer Reviews*, 55(4):678–705, 2015.

[211] Dae-Hyeong Kim, Jonathan Viventi, Jason J Amsden, Jianliang Xiao, Leif Vigeland, Yun-Soung Kim, Justin A Blanco, Bruce Panilaitis, Eric S Frechette, Diego Contreras, et al. Dissolvable films of silk fibroin for ultrathin conformal bio-integrated electronics. *Nature Materials*, 9(6):511, 2010.

[212] Jong Hyun Park and Sadhan C Jana. The relationship between nano-and micro-structures and mechanical properties in PMMA-epoxy-nanoclay composites. *Polymer*, 44(7):2091–2100, 2003.

[213] Crystal E Porter and Frank D Blum. Thermal characterization of PMMA thin films using modulated differential scanning calorimetry. *Macromolecules*, 33(19):7016–7020, 2000.

[214] Xingqiang Chen, Suxing Fang, and Zhenpin Hou. Preparation and research progress of polymer-based flexible conductive composites. *Journal of Polymer Science and Engineering*, 1(1), 2018.

[215] M Rajabi, M Vahidi, A Simchi, and P Davami. Effect of rapid solidification on the microstructure and mechanical properties of hot-pressed Al–20Si–5Fe alloys. *Materials Characterization*, 60(11):1370–1381, 2009.

[216] H Toraya and S Tsusaka. Quantitative phase analysis using the whole-powder-pattern decomposition method. i. Solution from knowledge of chemical compositions. *Journal of Applied Crystallography*, 28(4):392–399, 1995.

[217] VK Pecharsky and KA Gschneidner. Phase relationships and crystallography in the pseudobinary system Gd_5Si_4-Gd_5Ge_4. *Journal of alloys and compounds*, 260(1-2):98–106, 1997.

[218] VM Andrade, RJ Caraballo-Vivas, T Costas-Soares, SS Pedro, DL Rocco, MS Reis, APC Campos, and A de A Coelho. Magnetic and structural investigations on $La_{0.6}Sr_{0.4}MnO_3$ nanostructured manganite: Evidence of a ferrimagnetic shell. *Journal of Solid State Chemistry*, 219:87–92, 2014.

[219] NR Checca, RJ Caraballo-Vivas, R Torrão, A Rossi, and MS Reis. Phase composition and growth mechanisms of half-metal heusler alloy produced by pulsed laser deposition: From core-shell nanoparticles to amorphous randomic clusters. *Materials Chemistry and Physics*, 196:103–108, 2017.

[220] Karl A GschneidnerJr, VK Pecharsky, and AO Tsokol. Recent developments in magnetocaloric materials. *Reports on Progress in Physics*, 68(6):1479, 2005.

[221] Hu Zhang, YuJie Sun, YaWei Li, YuanYuan Wu, Yi Long, Jun Shen, FengXia Hu, JiRong Sun, and BaoGen Shen. Mechanical properties and magnetocaloric effects in $La(Fe,Si)_{13}$ hydrides bonded with different epoxy resins. *Journal of Applied Physics*, 117(6):063902, 2015.

[222] Xinchun Guan, Xufeng Dong, and Jinping Ou. Magnetostrictive effect of magnetorheological elastomer. *Journal of Magnetism and Magnetic Materials*, 320(3-4):158–163, 2008.

[223] Andrej Kitanovski and Peter W Egolf. Innovative ideas for future research on magnetocaloric technologies. *international Journal of Refrigeration*, 33(3):449–464, 2010.

[224] GC Sih. Thermomechanics of solids: nonequilibrium and irreversibility. *Theoretical and Applied Fracture Mechanics*, 9(3):175–198, 1988.

[225] David A Jesson and John F Watts. The interface and interphase in polymer matrix composites: effect on mechanical properties and methods for identification. *Polymer Reviews*, 52(3):321–354, 2012.

[226] KA Gschneidner Jr and Vitalij K Pecharsky. Magnetocaloric materials. *Annual Review of Materials Science*, 30(1):387–429, 2000.

[227] M Han, Jason A Paulsen, John Evan Snyder, DC Jiles, TA Lograsso, and DL Schlagel. Thermal expansion of single-crystal $Gd_5(Si_{1.95}Ge_{2.05})$ showing unusual first-order transformation. *IEEE Transactions on Magnetics*, 38(5):3252–3254, 2002.

[228] Xi Zhang, Xuezhen Huang, Chensha Li, and Hongrui Jiang. Dye-sensitized solar cell with energy storage function through PVDF/ZnO nanocomposite counter electrode. *Advanced Materials*, 25(30):4093–4096, 2013.

[229] Chung Ming Leung, Jiefang Li, D Viehland, and X Zhuang. A review on applications of magnetoelectric composites: from heterostructural uncooled magnetic sensors, energy harvesters to highly efficient power converters. *Journal of Physics D: Applied Physics*, 51(26):263002, 2018.

[230] DN Astrov. The magnetoelectric effect in antiferromagnetics. *Sov. Phys. JETP*, 11:708, 1960.

[231] TH O'dell. The field invariants in a magneto-electric medium. *Philosophical Magazine*, 8(87):411–418, 1963.

[232] P Tolédano, M Ackermann, L Bohatỳ, P Becker, T Lorenz, N Leo, and Manfred Fiebig. Primary ferrotoroidicity in antiferromagnets. *Physical Review B*, 92(9):094431, 2015.

[233] Jungho Ryu, Alfredo Vazquez Carazo, Kenji Uchino, and Hyoun-Ee Kim. Magnetoelectric properties in piezoelectric and magnetostrictive laminate composites. *Japanese Journal of Applied Physics*, 40(8R):4948, 2001.

[234] Junyi Zhai, Shuxiang Dong, Zengping Xing, Jiefang Li, and D Viehland. Giant magnetoelectric effect in metglas/polyvinylidene-fluoride laminates. *Applied Physics Letters*, 89(8):083507, 2006.

[235] Pierre Ueberschlag. PVDF piezoelectric polymer. *Sensor Review*, 21(2):118–126, 2001.

[236] SG Lu, Z Fang, E Furman, Y Wang, QM Zhang, Y Mudryk, KA Gschneidner Jr, VK Pecharsky, and CW Nan. Thermally mediated multiferroic composites for the magnetoelectric materials. *Applied Physics Letters*, 96(10):102902, 2010.

[237] MS Gaur, Pramod Kumar Singh, Asif Ali, and Rekha Singh. Thermally stimulated discharge current (TSDC) characteristics in β-phase PVDF-$BaTiO_3$ nanocomposites. *Journal of Thermal Analysis and Calorimetry*, 117(3):1407–1417, 2014.

[238] Helena MG Correia and Marta MD Ramos. Quantum modelling of poly (vinylidene fluoride). *Computational Materials Science*, 33(1-3):224–229, 2005.

[239] Zen-Wei Ouyang, Erh-Chiang Chen, and Tzong-Ming Wu. Thermal stability and magnetic properties of polyvinylidene fluoride/magnetite nanocomposites. *Materials*, 8(7):4553–4564, 2015.

[240] Gwang Ho Kim, Soon Man Hong, and Yongsok Seo. Piezoelectric properties of poly (vinylidene fluoride) and carbon nanotube blends: β-phase development. *Physical Chemistry Chemical Physics*, 11(44):10506–10512, 2009.

[241] T Kaura, R Nath, and MM Perlman. Simultaneous stretching and corona poling of PVDF films. *Journal of Physics D: Applied Physics*, 24(10):1848, 1991.

[242] M El Achaby, FZ Arrakhiz, S Vaudreuil, EM Essassi, and A Qaiss. Piezoelectric β-polymorph formation and properties enhancement in graphene oxide-PVDF nanocomposite films. *Applied Surface Science*, 258(19):7668–7677, 2012.

[243] Shansheng Yu, Weitao Zheng, Wenxue Yu, Yujie Zhang, Qing Jiang, and Zhudi Zhao. Formation mechanism of β-phase in PVDF/CNT composite prepared by the sonication method. *Macromolecules*, 42(22):8870–8874, 2009.

[244] Young-Jin Kim, Chang Hyun Ahn, Myung Bok Lee, and Myung-Seok Choi. Characteristics of electrospun PVDF/SiO_2 composite nanofiber membranes as polymer electrolyte. *Materials Chemistry and Physics*, 127(1-2):137–142, 2011.

[245] Mimi Tao, Fu Liu, and Lixin Xue. Hydrophilic poly (vinylidene fluoride)(PVDF) membrane by in situ polymerisation of 2-hydroxyethyl methacrylate (HEMA) and micro-phase separation. *Journal of Materials Chemistry*, 22(18):9131–9137, 2012.

[246] Rinaldo Gregorio Jr. Determination of the α, β, and γ crystalline phases of poly (vinylidene fluoride) films prepared at different conditions. *Journal of Applied Polymer Science*, 100(4):3272–3279, 2006.

[247] Gaurav Mago, Dilhan M Kalyon, and Frank T Fisher. Membranes of polyvinylidene fluoride and PVDF nanocomposites with carbon nanotubes via immersion precipitation. *Journal of Nanomaterials*, 2008:17, 2008.

[248] MG Buonomenna, P Macchi, M Davoli, and E Drioli. Poly (vinylidene fluoride) membranes by phase inversion: the role the casting and coagulation conditions play in their morphology, crystalline structure and properties. *European Polymer Journal*, 43(4):1557–1572, 2007.

[249] Saeid Arabnejad, Koichi Yamashita, and Sergei Manzhos. Defects in crystalline PVDF: a density functional theory-density functional tight binding study. *Physical Chemistry Chemical Physics*, 19(11):7560–7567, 2017.

[250] Marcel Benz and William B Euler. Determination of the crystalline phases of poly (vinylidene fluoride) under different preparation conditions using differential scanning calorimetry and infrared spectroscopy. *Journal of Applied Polymer Science*, 89(4):1093–1100, 2003.

[251] VF Cardoso, Graça Minas, Carlos M Costa, CJ Tavares, and S Lanceros-Mendez. Micro and nanofilms of poly (vinylidene fluoride) with controlled thickness, morphology and electroactive crystalline phase for sensor and actuator applications. *Smart Materials and Structures*, 20(8):087002, 2011.

[252] A Salimi and AA Yousefi. Conformational changes and phase transformation mechanisms in PVDF solution-cast films. *Journal of Polymer Science Part B: Polymer Physics*, 42(18):3487–3495, 2004.

[253] P Martins, AC Lopes, and S Lanceros-Mendez. Electroactive phases of poly (vinylidene fluoride): determination, processing and applications. *Progress in Polymer Science*, 39(4):683–706, 2014.

[254] Piyush Kanti Sarkar, Subrata Maji, Gundam Sandeep Kumar, Krushna Chandra Sahoo, Dipankar Mandal, and Somobrata Acharya. Triboelectric generator composed of bulk poly (vinylidene fluoride) and polyethylene polymers for mechanical energy conversion. *RSC Advances*, 6(2):910–917, 2016.

[255] Xiaomei Cai, Tingping Lei, Daoheng Sun, and Liwei Lin. A critical analysis of the α, β and γ phases in poly (vinylidene fluoride) using FTIR. *RSC Advances*, 7(25):15382–15389, 2017.

[256] Rinaldo Gregorio Jr and Marcelo Cestari. Effect of crystallization temperature on the crystalline phase content and morphology of poly (vinylidene fluoride). *Journal of Polymer Science Part B: Polymer Physics*, 32(5):859–870, 1994.

[257] WL Ong, M Gao, and GW Ho. Hybrid organic PVDF-inorganic M-rGO-TiO_2 (M= Ag, Pt) nanocomposites for multifunctional volatile organic compound sensing and photocatalytic degradation-H_2 production. *Nanoscale*, 5(22):11283–11290, 2013.

[258] João Gomes, J Serrado Nunes, Vitor Sencadas, and Senentxu Lanceros-Méndez. Influence of the β-phase content and degree of crystallinity on the piezo-and ferroelectric properties of poly (vinylidene fluoride). *Smart Materials and Structures*, 19(6):065010, 2010.

[259] VM Laletin, DA Filippov, and TO Firsova. The nonlinear resonance magnetoelectric effect in magnetostrictive-piezoelectric structures. *Technical Physics Letters*, 40(3):237–240, 2014.

[260] Pedro Martins and Senentxu Lanceros-Méndez. Polymer-based magnetoelectric materials. *Advanced Functional Materials*, 23(27):3371–3385, 2013.

[261] M Han, David C Jiles, John Evan Snyder, Thomas A Lograsso, and Deborah L Schlagel. Giant magnetostriction behavior at the Curie temperature of single crystal $Gd_5(Si_{0.5}Ge_{0.5})_4$. *Journal of Applied Physics*, 95(11):6945–6947, 2004.

[262] M Stavrakas, D Triantis, P Photopoulos, A Kanapitsas, and C Tsonos. Thermally stimulated discharge current (TSDC) characteristics in PVDF-graphene nanocomposites. *International Conference Science in Technology . ScinTE 2015*, 2015.

[263] Dwight Hunter, Will Osborn, Ke Wang, Nataliya Kazantseva, Jason Hattrick-Simpers, Richard Suchoski, Ryota Takahashi, Marcus L Young, Apurva Mehta, Leonid A Bendersky, et al. Giant magnetostriction in annealed $Co_{1-x}Fe_x$ thin-films. *Nature Communications*, 2:518, 2011.

[264] Rongrong Wu, Feiran Shen, Fengxia Hu, Jing Wang, Lifu Bao, Lei Zhang, Yao Liu, Yingying Zhao, Feixiang Liang, Wenliang Zuo, et al. Critical dependence of magnetostructural coupling and magnetocaloric effect on particle size in Mn-Fe-Ni-Ge compounds. *Scientific reports*, 6:20993, 2016.

[265] Alberto López-Ortega, Elisabetta Lottini, Cesar de Julian Fernandez, and Claudio Sangregorio. Exploring the magnetic properties of cobalt-ferrite nanoparticles for the development of a rare-earth-free permanent magnet. *Chemistry of Materials*, 27(11):4048–4056, 2015.

[266] P Poddar, J Gass, DJ Rebar, S Srinath, H Srikanth, SA Morrison, and EE Carpenter. Magnetocaloric effect in ferrite nanoparticles. *Journal of magnetism and magnetic materials*, 307(2):227–231, 2006.

[267] Yusuf Yüksel, Ekrem Aydıner, and Hamza Polat. Thermal and magnetic properties of a ferrimagnetic nanoparticle with spin-3/2 core and spin-1 shell structure. *Journal of Magnetism and Magnetic Materials*, 323(23):3168–3175, 2011.

[268] P Dey, TK Nath, PK Manna, and SM Yusuf. Enhanced grain surface effect on magnetic properties of nanometric $La_{0.7}Ca_{0.3}MnO_3$ manganite: Evidence of surface spin freezing of manganite nanoparticles. *Journal of Applied Physics*, 104(10):103907, 2008.

[269] AK Pramanik and A Banerjee. Interparticle interaction and crossover in critical lines on field-temperature plane in $Pr_{0.5}Sr_{0.5}MnO_3$ nanoparticles. *Physical Review B*, 82(9):094402, 2010.

[270] T Zhu, BG Shen, JR Sun, HW Zhao, and WS Zhan. Surface spin-glass behavior in $La_{2/3}Sr_{1/3}MnO_3$ nanoparticles. *Applied Physics Letters*, 78(24):3863–3865, 2001.

[271] M Vasilakaki and KN Trohidou. Numerical study of the exchange-bias effect in nanoparticles with ferromagnetic core/ferrimagnetic disordered shell morphology. *Physical Review B*, 79(14):144402, 2009.

[272] XG Zheng, H Kubozono, H Yamada, K Kato, Y Ishiwata, and CN Xu. Giant negative thermal expansion in magnetic nanocrystals. *Nature Nanotechnology*, 3(12):724, 2008.

[273] TA Mary, JSO Evans, T Vogt, and AW Sleight. Negative thermal expansion from 0.3 to 1050 Kelvin in ZrW_2O_8. *Science*, 272(5258):90–92, 1996.

[274] Dieter Vollath. *Nanoparticles-Nanocomposites-Nanomaterials: An Introduction for Beginners*. John Wiley & Sons, 2013.

[275] RE Camley. Surface spin reorientation in thin Gd films on Fe in an applied magnetic field. *Physical Review B*, 35(7):3608, 1987.

[276] Nicolas Perez, Pablo Guardia, Alejandro G Roca, Maria del Puerto Morales, Carlos J Serna, Oscar Iglesias, Fernando Bartolome, Luis M Garcia, Xavier Batlle, and Amilcar Labarta. Surface anisotropy broadening of the energy barrier distribution in magnetic nanoparticles. *Nanotechnology*, 19(47):475704, 2008.

[277] William Hines, Joseph Budnick, David Perry, Sara Majetich, Ryan Booth, and Madhur Sachan. Nuclear magnetic resonance and magnetization study of surfactant-coated epsilon-Co nanoparticles. *physica status solidi (b)*, 248(3):741–747, 2011.

[278] Fèlix Casanova i Fernàndez. *Magnetocaloric effect in $Gd_5(Si_xGe_{1-x})_4$ alloys*. PhD thesis, Universitat de Barcelona, December 2003.

[279] Zhijie Jia, Zhengyuan Wang, Cailu Xu, Ji Liang, Bingqing Wei, Dehai Wu, and Shaowen Zhu. Study on poly (methyl methacrylate)/carbon nanotube composites. *Materials Science and Engineering: A*, 271(1):395–400, 1999.

[280] Juan Rodríguez-Carvajal. Recent advances in magnetic structure determination by neutron powder diffraction. *Physica B: Condensed Matter*, 192(1):55–69, 1993.

[281] Brian H Toby. R factors in Rietveld analysis: How good is good enough? *Powder Diffraction*, 21(1):67–70, 2006.

Appendix A

Additional information for $Gd_{5-x}La_xSi_{1.8}Ge_{2.2}$ family compounds

A.1 *Le Bail* refinements

The profile matching with relative intensities calculation of the XRD patterns of $(Gd,La)_5Si_{1.8}Ge_{2.2}$ powders were performed using the Fullprof software and the results for all samples are shown in Figs.1-5. An improvement on the refinements was obtained by considering the presence of 1:1 phase, estimated to be less then 15% for all compositions. Lattice parameters, profile U,V,W and R-factors will be summarized after each pattern and calculated curves.

A.2 Arrott plots and Entropy change curves

Using the isothermal curves measured around T_C, the Arrott plot (H/M *versus* M^2) curves were calculated in order to infer the ordering of the FM-PM transition. As can be seen, all the curves present a positive slope which means that the magnetic transition is a second order one, in agreement with the Banerjee criteria[146]. It is worth to point out that such affirmation cannot be applied to x = 1 sample since it presents a mixture phase of M and T structures.

The magnetic entropy change for several applied magnetic fields for all samples are also presented. This curves were also obtained using the isothermal curves and the equations presented on Chapter 3.

Table A.1: Parameters returned from the *LeBail* refinement for $Gd_4La_1Si_{1.8}Ge_{2.2}$ sample.

Type	$Gd_5Si_2Ge_2$	La_5Si_4	$R_1(Si,Ge)_1$
phase fraction (wt.%)	60.8	29.6	9.60
Space group	$P112_1/a$	$P4_12_12$	$Pnma$
a (Å)	7.654(6)	7.844(1)	8.228(3)
b (Å)	14.77(1)	7.844(1)	3.856(1)
c (Å)	7.803(8)	14.53(2)	6.202(2)
V (Å^3)	881.4(1)	894.1(2)	196.8(1)
γ (^{0})	92.07(6)	90.00(0)	90.00(0)
R_p (%)		25.8	
R_{wp} (%)		27.5	
R_{exp} (%)		5.54	
χ^2		24.7	

Table A.2: Lattice parameters and goodness of fit values returned from the LeBail refinement for x = 2, 3, 4 and 5 samples.

	x = 2		**x = 3**		**x = 4**		**x = 5**	
Phase	T $P4_12_12$	O(I) Pnma	T $P4_12_12$	O(I) Pnma	T $P4_12_12$	O(I) Pnma	T $P4_12_12$	O(I) Pnma
	86.4%	13.6%	90.2%	9.80%	92.8%	7.20%	95.2%	4.80%
Space group	$P4_12_12$	$Pnma$	$P4_12_12$	$Pnma$	$P4_12_12$	$Pnma$	$P4_12_12$	$Pnma$
a (Å)	7.928(3)	8.014(2)	7.991(1)	8.029(2)	8.057(3)	8.002(1)	8.113(2)	8.439(0)
b (Å)	7.928(3)	3.769(0)	7.991(1)	3.799(1)	8.057(3)	3.820(0)	8.113(2)	4.059(1)
c (Å)	14.62(1)	5.712(1)	14.83(0)	5.743(4)	15.00(1)	5.739(1)	15.37(4)	6.060(4)
V (Å^3)	918.8(0)	172.5(1)	946.8(2)	175.2(1)	973.8(2)	175.4(3)	1012(1)	207.6(2)
R_p (%)	12.1		14.2		12.9		14.1	
R_{wp} (%)	9.49		11.3		13.2		13.3	
R_{exp} (%)	6.00		5.14		3.48		3.98	
χ^2	2.50		4.80		14.5		11.1	

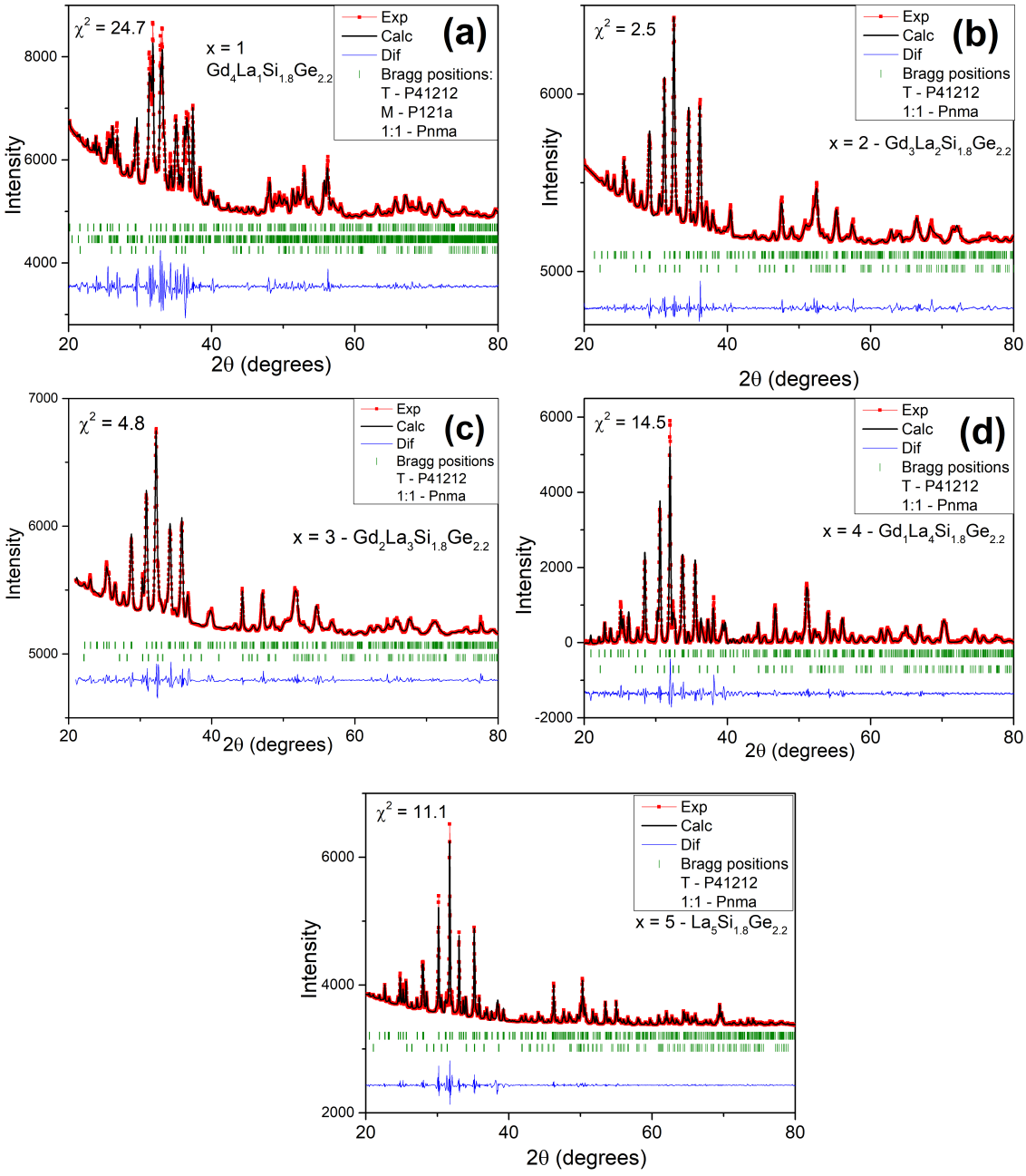

Figure A.1: Le Bail Refinements obtained using the Profile Matching with relative intensities calculation using *FullProf Suite* software[280] for $Gd_{5-x}La_xSi_{1.8}Ge_{2.2}$ compounds with x = 1**(a)**, 2**(b)**, 3**(c)** and 4**(d)**

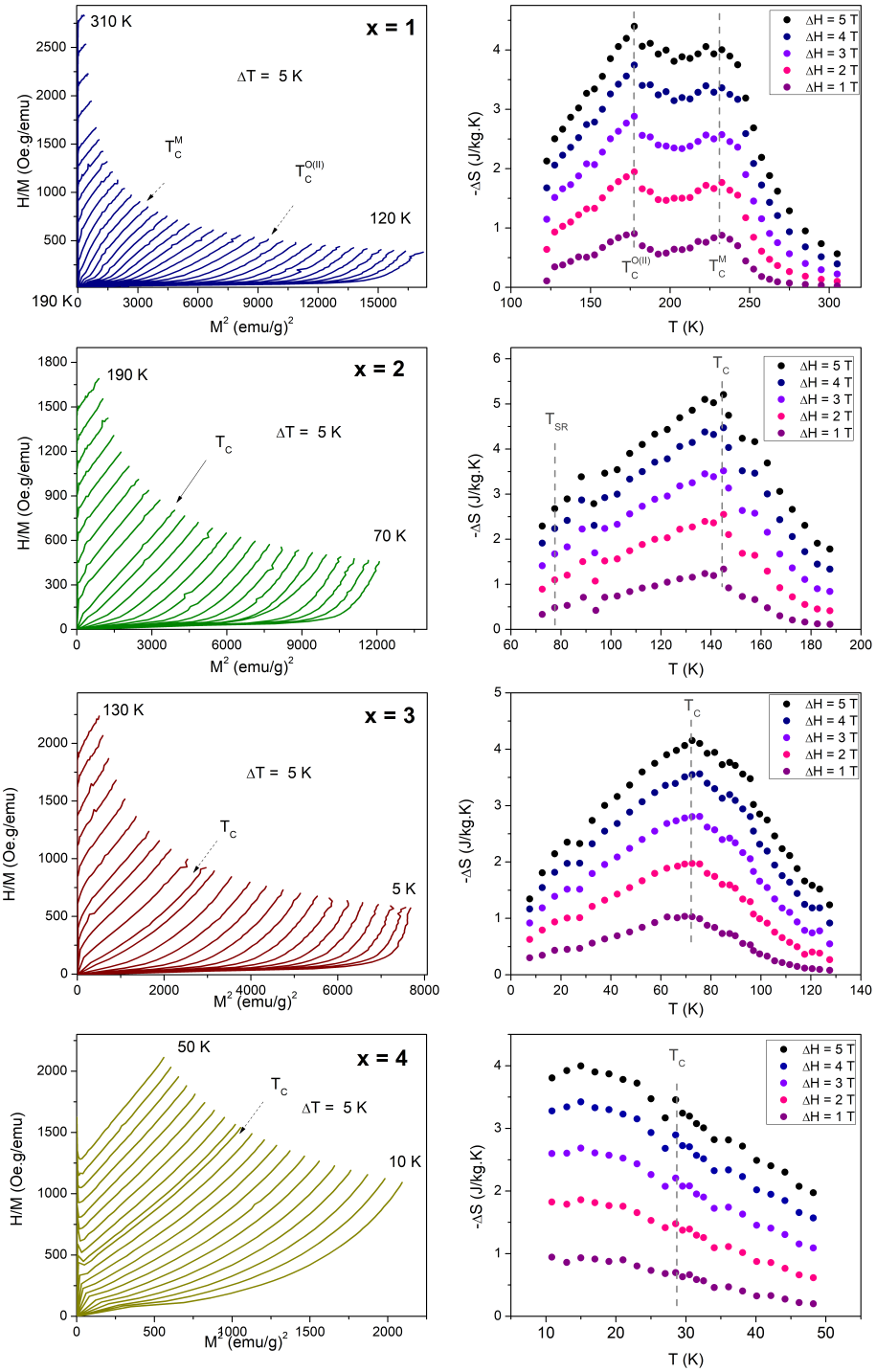
x = 1
310 K
ΔT = 5 K
T_C^M
$T_C^{O(II)}$
120 K
190 K
H/M (Oe.g/emu)
M^2 (emu/g)^2
ΔH = 5 T
ΔH = 4 T
ΔH = 3 T
ΔH = 2 T
ΔH = 1 T
-ΔS (J/kg.K)
T (K)
x = 2
190 K
T_C
ΔT = 5 K
70 K
T_{SR}
x = 3
130 K
ΔT = 5 K
T_C
5 K
x = 4
50 K
T_C
ΔT = 5 K
10 K

Appendix B

Extra information on the $Gd_5Si_{2.4}Ge_{1.6}$ polymers composites

B.0.1 Atomic positions for $Gd_5Si_{2.4}Ge_{1.6}$ sifted powders

The powders used for the production of polymeric composites were obtained by sifting the as-cast milled compound. A *Rietveld* refinement were performed using *Fullprof Suite Software* confirming the formation of orthorhombic-I structure (Gd_5Si_4-type) that belongs to the Pnma space group, monoclinic structure ($Gd_5Si_2Ge_2$-type) belonging to $P112_1/a$ space group and a R_5M_3 phase with a hexagonal symmetry ($P6_3/mcm$ space group). The lattice parameters are summarized on Chapter 5 and are close to the obtained for the PMMA composites on the next section and, for that reason, will not be given on the Appendix. They were found to be unchanged as the particle size reduces, thus, the atomic positions were held as fixed for all samples XRD analysis.

B.0.2 Composites results

The $Gd_5Si_{2.4}Ge_{1.6}$ micrometric powder with poly(methyl methacrylate) (PMMA) composites produced through solvent casting, as described on Chapter 4, were analysed by XRD data collected at room temperature. The initial lattice parameters for *LeBail* calculations were considered to be the same as obtained for the pure powder and the results are shown in FigB.1. And the returned values from the fit are summarized below. Although the PMMA matrix does not change the intrinsic properties of the powder, there is some oscillations on the lattice parameters due to the amorphous layer of the polymer. In particular, for 10 wt.% GSG/PMMA composite, the χ^2 value is below 1, which indicates that the model does not fit the experimental data. Indeed, the quality of the acquired data is really poor duo to the low amount of crystals on the matrix, which justify this fit quality[281].

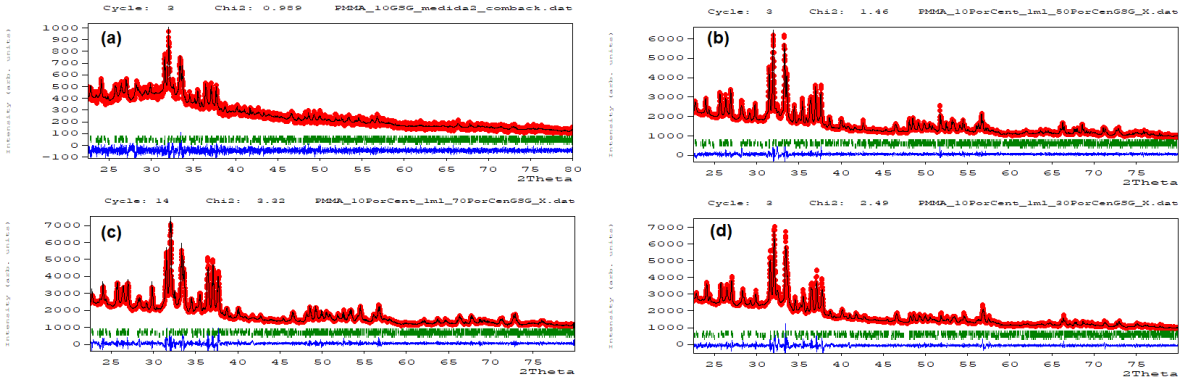

Figure B.1: LeBail refinements for **(a)** 10 wt.%, **(b)** 30 wt.%, **(c)** 50 wt.% and **(d)** 70 wt.% GSG/PMMA composites.

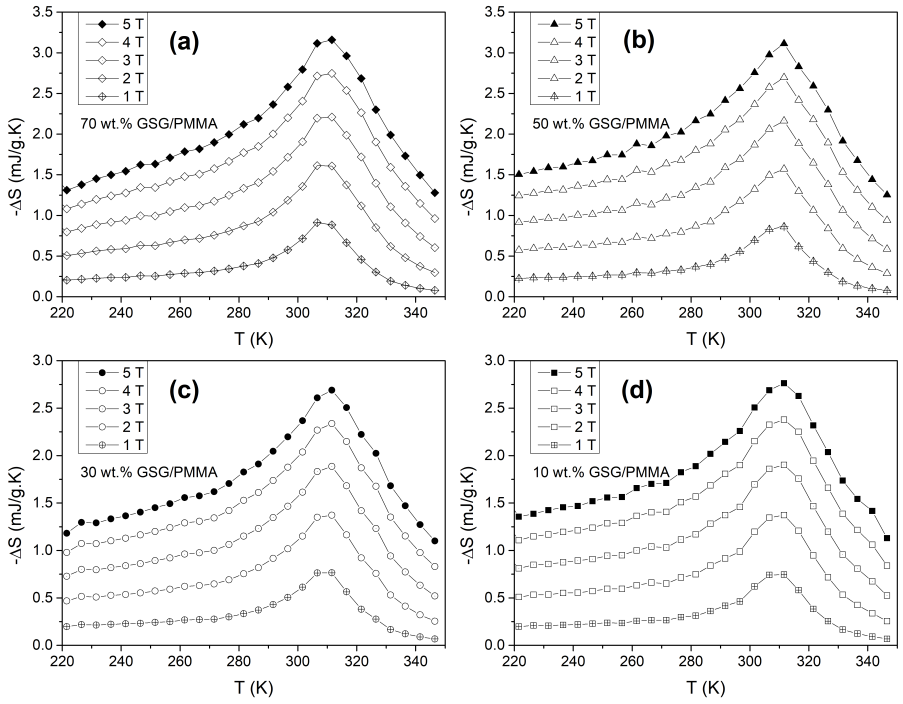

Figure B.2: Entropy change curves for different applied magnetic fields as a function of temperature for **(a)** 10 wt.%, **(b)** 30 wt.%, **(c)** 50 wt.% and **(d)** 70 wt.% GSG/PMMA composites.

Table B.1: Atomic parameters of $Gd_5Si_{2.4}Ge_{1.6}$ powders where it was considered constant for the calculations for different grain sizes.The M correspond to the Si and Ge shared atomic positions and the Occ. values is given for Si atoms.

Atom	Wyck.	x	y	z	Occ
		O(I) - Pnma space group (64)			
Gd1	8d	0.02365	0.40034	0.21243	1.000
Gd2	8d	0.70296	0.37602	0.77315	1.000
Gd3	4c	0.17773	3/4	0.55456	1.000
M1*	8d	0.84816	0.45738	0.52888	0.476
M2	4c	0.01767	3/4	0.08808	0.313
M3	4c	0.32214	3/4	0.7521	0.352
		M - P112$_1$/a space group (14)			
Gd1	4e	0.35665	0.27141	-0.12273	1.000
Gd2a	4e	-0.05133	0.06123	0.31688	1.000
Gd2b	4e	-0.00961	0.45143	0.14003	1.000
Gd3a	4e	0.36979	0.86395	0.27162	1.000
Gd3b	4e	0.32643	0.67472	0.26334	1.000
M1	4e	0.21968	0.18560	0.33898	0.617
M2	4e	0.96450	0.18197	0.79207	0.480
M3a	4e	0.19869	0.9455	0.55311	0.445
M3b	4e	-0.00750	0.66532	0.29763	0.465
		5:3 - P6$_3$/mcm space group (193)			
Gd1	4d	1/3	2/3	0.00000	1.000
Gd2	6g	0.25640	0.00000	1/4	1.000
M	6g	0.11719	0.00000	1/4	0.400

Appendix C

$Gd_5(Si,Ge)_4$ Targets Rietveld Refinements Information

Table C.1: Lattice parameters and the reliability factors obtained from the *Rietveld* refinements for bulk samples used as targets for the NPs production.

Parameters	**x = 0.45**	**x = 0.55**		**x = 0.60**
Space group	M - $P112_1/a$	12% M	88% O(I)	O(I) - $Pnma$
a (Å)	7.594	7.598	7.526	7.512
b (Å)	14.82	14.78	14.80	14.78
c (Å)	7.788	7.802	7.783	7.797
δ (^{0})	93.13	92.97	90.00	90.00
V (Å^3)	873.4	875.1	867.1	865.7
Rp	5.23	6.59		5.46
Rwp	7.15	13.1		7.60
Rexp	3.04	2.86		2.90
χ^2	5.54	21.0		6.86

Table C.2: Atomic positions obtained from Rietveld refinement of $Gd_5Si_{1.8}Ge_{2.2}$ bulk target for the production of its NPs.The M correspond to the Si and Ge shared atomic positions and the occupation values is given for Si atoms, held constant during refinement calculations.

Atom	Wyck.	x	y	z	Occ
		x = 0.45 - P112$_1$/a space group (14)			
Gd1	4e	0.34581	0.24716	0.03774	1.000
Gd2a	4e	0.03225	0.08892	0.12915	1.000
Gd2b	4e	0.01676	0.40149	0.16363	1.000
Gd3a	4e	0.40396	0.87970	0.20038	1.000
Gd3b	4e	0.30818	0.64190	0.17407	1.000
M1	4e	0.15205	0.23572	0.39616	0.450
M2	4e	0.99777	0.28430	0.86873	0.450
M3a	4e	0.18728	0.96554	0.46457	0.450
M3b	4e	0.33855	0.51551	0.43227	0.450

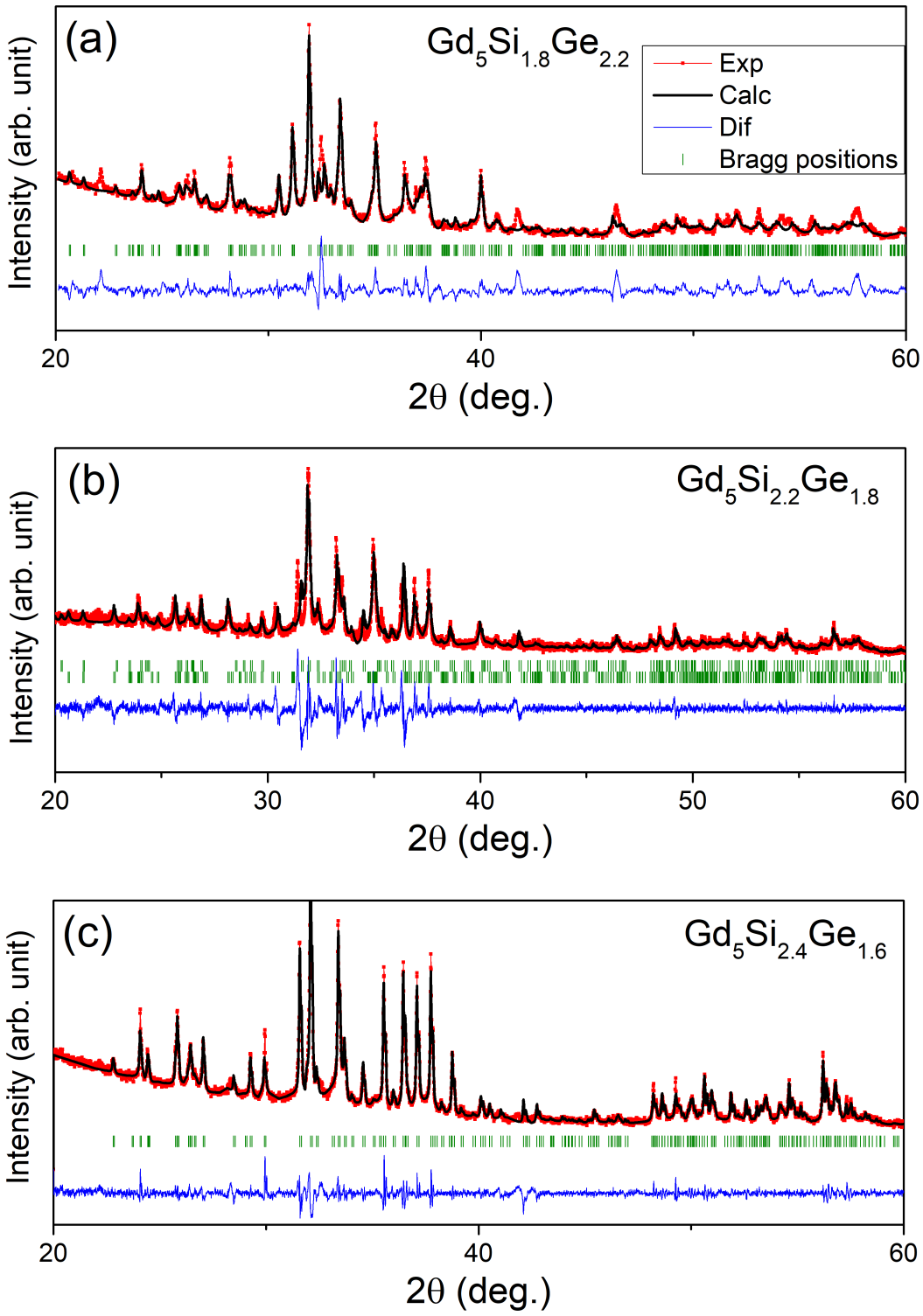

Figure C.1: XRD patterns for the bulk targets of $Gd_5(Si_xGe_{1-x})_4$ with: x = 0.45, that crystallizes in a Monoclinic ($P112_1/a$ space group) phase; x = 0.55, with a mixture of M and Orthorhombic-I ($Pnma$ space group); and, for x = 0.60 in an O(I) structure. The Bragg positions and respective Miller indices for some peaks are indicated for the end compositions target samples, obtained through *Rietveld* refinement.

Table C.3: Atomic parameters of $Gd_5Si_{2.2}Ge_{1.8}$ powders where it was considered constant for the calculations for different grain sizes.The M correspond to the Si and Ge shared atomic positions and the occupation values is given for Si atoms that were held constant during calculations.

Atom	Wyck.	x	y	z	Occ
		O(I) - Pnma space group (64)			
Gd1	8d	0.04656	0.56475	0.07908	1.000
Gd2	8d	0.59980	0.44310	0.81780	1.000
Gd3	4c	0.22622	3/4	0.37806	1.000
M1*	8d	0.96555	0.60511	0.53430	0.550
M2	4c	0.38806	3/4	0.11560	0.550
M3	4c	0.17102	3/4	0.86535	0.550
		M - P112$_1$/a space group (14)			
Gd1	4e	0.34032	0.25390	0.00298	1.000
Gd2a	4e	-0.01098	0.08502	0.18336	1.000
Gd2b	4e	0.01923	0.40304	0.17033	1.000
Gd3a	4e	0.38737	0.18991	0.16199	1.000
Gd3b	4e	0.35632	0.40585	0.17330	1.000
M1	4e	0.16768	0.64383	0.39861	0.550
M2	4e	0.87782	0.18965	0.99002	0.550
M3a	4e	0.20399	0.92028	0.42770	0.550
M3b	4e	0.09561	0.53901	0.46392	0.550